Edge Localized Mode Control in TCV

THÈSE N^O 5311 (2012)

PAR

Jonathan ROSSEL

EPFL

ÉCOLE POLYTECHNIQUE
FÉDÉRALE DE LAUSANNE

Suisse
2012

The electronic version of this dissertation, including hyperlinks for a comfortable document navigation, is available for download from:

http://library.epfl.ch/theses/?nr=5311

Please cite this work as:

J. X. Rossel, **Edge localized mode control in TCV**, Ph.D. thesis, no. 5311, Ecole Polytechnique Fédérale de Lausanne (EPFL), CH-1015 Lausanne, Switzerland, February 2012.

à la Nature, et tout ce qu'elle recèle, suffisamment intelligible pour susciter la curiosité et l'admiration des hommes, suffisamment mystérieuse pour faire taire leur arrogance.

I is very seldom that the same man knows much of science, and about the things that were known before science came.

Lord Dunsany (*1878 – †1957)

Abstract

The Tokamak concept, based on magnetic confinement of a hydrogen plasma, is one of today's most promising paths to energy production by nuclear fusion. The experimental scenarios leading to the largest fusion rate are based on a high confinement plasma regime, the H-mode, in which the energy and particle confinement are enhanced by a transport barrier located at the plasma edge and forming a pedestal in the plasma pressure profile. In standard axisymmetric magnetic configurations, stationary H-mode regimes suffer from instabilities of the plasma edge, the so-called edge localized modes (ELMs), leading to potentially damaging repetitive ejections of heat and particles toward the plasma facing components. In ITER, a Tokamak currently being built to demonstrate net power production from fusion, type I ELMs are expected to occur during high performance discharges. It is expected that the power flux released by these ELMs will cause an intolerable erosion and heat load on the plasma facing components. The control of ELMs, in terms of frequency and energy loss, is therefore of primary importance in the field of magnetic fusion and is subject to an intense research effort worldwide. This thesis, in line with this effort, focuses on two particular ELM control methods: local continuous or modulated heating of the plasma edge, and application of resonant magnetic perturbations (RMP).

In this thesis, the effects of plasma edge heating on the ELM cycle have been investigated by applying electron cyclotron resonant heating (ECRH) to the edge of an H-mode plasma featuring type I ELMs in the *Tokamak à Configuration Variable* (TCV). As the power deposition location is shifted gradually toward the plasma pressure pedestal, an increase of the ELM frequency by a factor 2 and a decrease of the energy loss per ELM by the same factor are observed, even though the power absorption efficiency is reduced. This unexpected and, as yet, unexplained phenomenon, observed for the first time, runs contrary to the intrinsic type I ELM power dependence and provides a new approach for ELM mitigation.

The effects of heating power modulation on the ELM cycle have also been experimentally investigated. It showed that power modulation synchronized in real-time

with the ELM cycle is able to pace the ELMs with low deviation from a given frequency. Experimental results also clearly indicate that the ELM frequency purely remains a function of the heating power averaged over the ELM cycle, so that power modulation itself is not able to drive the ELM frequency and only has a stabilization effect. These results are in qualitative agreement with a simple 0D finite confinement time integrator model of the ELM cycle.

RMP consists in applying a magnetic field perpendicular to the plasma magnetohydrodynamic equilibrium flux surfaces with a spatial variation tuned to align with the equilibrium magnetic field lines. If each coil of an RMP coil system (i.e. a set of toroidally and poloidally distributed coils) is powered with an independent power supply, the coil current distribution can be tuned to optimize the RMP space spectrum. In the course of this thesis, a multi-mode Lagrange method, with no assumption on the coil geometry or spatial distribution, has been developed to determine this optimum, in the limit of the vacuum magnetic field approximation. This method appears to be an efficient way to minimize the parasitic spatial modes of the magnetic perturbation, and the coil current requirements, while imposing the amplitude and phase of a set of target modes. A figure of merit measuring the quality of a perturbation spectrum with respect to RMP independently of the considered coil system or plasma equilibrium is also proposed. To facilitate the application of the Lagrange method, a spectral characterization of the coil system, based on a generalized discrete Fourier transform applied in current space, is performed to determine how spectral degeneracy and side-bands creation limit the number of simultaneously controllable target modes.

Finally, this thesis sets the foundations of experimental research in the particular subject of RMP at CRPP by proposing a physics-based design for a multi-purpose saddle coil system (SCS) for TCV, a coil system located and powered such as to create a helical magnetic perturbation. Using independent power supplies, the toroidal periodicity of this perturbation is tunable, allowing simultaneously ELM control, error field correction and vertical control. Other experimental applications, like resistive wall mode and rotation control, are also in view. In this thesis, the adequacy of two SCS designs, an in-vessel one and an ex-vessel one, is assessed with respect to the desired experimental applications. The current requirements and the system performances are also characterized. The conducting vessel wall is accounted for in a model used to determine the coupled response functions of the SCS, the screening of the magnetic perturbation by the wall, the induced voltages and currents during a plasma disruption and the maximal magnetic forces exerted on the SCS. A scaling

of the SCS parameters with the number of coil turns is presented and the issue of coil heating and cooling is discussed.

Résumé

A l'heure actuelle, la filière de recherche la plus prometteuse pour la production d'énergie par fusion nucléaire est celle du Tokamak, un concept de réacteur basé sur le confinement magnétique d'un plasma d'hydrogène. Les scénarios expérimentaux conduisant aux taux de réactions de fusion les plus élevés sont basés sur un régime plasma à haut confinement, le mode H, dans lequel le confinement de l'énergie et des particules du plasma est amélioré par la présence d'une barrière de transport située au bord du plasma et formant un piédestal dans son profil radial de pression. Dans les configurations magnétiques axisymétriques standards, les plasmas en mode H présentant des régimes stationnaires sont sujets à des instabilités du bord, dénommées ELMs (Edge Localized Modes, i.e. modes localisés au bord), conduisant à des éjections répétitives et potentiellement dommageables de chaleur et de particules sur les surfaces du réacteur faisant face au plasma. Dans ITER, un Tokamak actuellement en construction, et dont le but est de démontrer une production nette de puissance par fusion nucléaire, on s'attend à ce que les décharges à haute performance soient accompagnées d'ELMs de type I. On prévoit également que l'énergie thermique libérée lors des ELMs, et incidente sur les parois du réacteur, dépassera les valeurs autorisées et qu'une érosion intolérable s'en suivra. Le contrôle des ELMs, en termes de fréquence d'apparition et de quantité d'énergie libérée par événement, est donc d'importance primordiale dans le domaine de la fusion par confinement magnétique. En conséquence, ce contrôle est le sujet d'un effort de recherche international intense. Cette thèse contribue à cet effort en se concentrant sur deux méthodes particulières de contrôle des ELMs : le chauffage local, continu ou modulé, du bord du plasma, et l'application de perturbations magnétiques résonantes (Resonant Magnetic Perturbations, RMP).

Dans cette thèse, les effets du chauffage du bord du plasma sur le cycle des ELMs ont été étudiés dans le Tokamak à Configuration Variable (TCV) en chauffant le bord d'un plasma en mode H, sujet à des ELMs de type I, par ECRH (Electron Cyclotron Resonant Heating, i.e. chauffage par résonance avec des ondes cyclotroniques

électroniques). En déplaçant graduellement la position du dépôt de puissance vers le bord du plasma, on observe une augmentation de la fréquence des ELMs d'un facteur 2 et une diminution de l'énergie libérée par ELM du même facteur, même si la puissance injectée est moins bien absorbée. Ce phénomène inattendu, et pour l'instant inexpliqué, observé pour la première fois, s'oppose à la dépendance en puissance intrinsèque aux ELMs de type I, et procure, par ce truchement, une nouvelle approche d'atténuation des ELMs.

Les conséquences de la modulation de la puissance de chauffage sur le cycle des ELMs ont également été étudiées expérimentalement. Ces études ont démontré que la fréquence des ELMs, présentant normalement de fortes déviations par rapport à sa moyenne, est régulée lorsque la modulation de puissance est synchronisée en temps réel avec le cycle des ELMs. Ces expériences indiquent également clairement que la fréquence des ELMs reste purement une fonction de la puissance de chauffage moyennée sur le cycle des ELMs, prouvant ainsi que la modulation de puissance elle-même n'est pas capable d'influencer la fréquence moyenne des ELMs et qu'elle n'a qu'un effet stabilisateur. Ces résultats sont en accord qualitatif avec un modèle zéro-dimensionnel simple du cycle des ELMs basé sur un intégrateur de puissance avec temps de confinement fini.

La RMP consiste à appliquer un champ magnétique perpendiculaire aux surfaces de flux de l'équilibre magnétohydrodynamique du plasma et présentant une variation spatiale qui s'aligne avec les lignes de champ magnétique de cet équilibre. Si chaque bobine d'un système de bobines RMP (c'est-à-dire un ensemble de bobines distribuées toroïdalement et poloïdalement autour du plasma) est alimentée indépendamment, la distribution de courant dans les bobines peut être ajustée pour optimiser le spectre spatial de la RMP produite. Au cours de cette thèse, une méthode d'optimisation de Lagrange a été développée pour déterminer cet optimum. Cette méthode, valable dans la limite de l'approximation du champ magnétique du vide (c'est-à-dire sans réponse du plasma), permet une optimisation simultanée de plusieurs modes spectraux, sans hypothèse sur la géométrie ou la distribution spatiale des bobines. Cette approche permet de minimiser efficacement les modes spectraux parasites de la perturbation magnétique, ainsi que les amplitudes de courant requises dans les bobines, tout en imposant l'amplitude et la phase d'un ensemble choisi de modes spectraux. On propose également ici la définition d'un facteur de qualité permettant de quantifier la qualité d'une perturbation magnétique par rapport à la RMP, et ce indépendamment du système de bobines ou de l'équilibre plasma considéré. Pour faciliter l'application de cette méthode de Lagrange, une caractérisation spectrale

du système de bobines, basée sur une transformation de Fourier discrète généralisée appliquée dans l'espace des courants, est effectuée. Elle permet de déterminer dans quelle mesure la dégénérescence spectrale limite le nombre de modes simultanément contrôlables.

Finalement, cette thèse pose les fondations de la recherche expérimentale dans le domaine particulier de la RMP au CRPP en proposant un design justifié physiquement pour un système multitâche de bobines en forme de selle (SCS, Saddle Coil System) pour TCV. Ce système est positionné et alimenté de manière à créer une perturbation magnétique hélicoïdale. En utilisant des alimentations indépendantes, la périodicité toroïdale de cette perturbation est ajustable, permettant ainsi simultanément le contrôle des ELMs, la correction du champ d'erreur et le contrôle vertical. D'autres applications expérimentales, comme le contrôle des modes résistifs de l'enceinte ou celui de la rotation du plasma, sont également envisagées. Dans cette thèse, l'adéquation de deux designs de SCS, l'un interne et l'autre externe à l'enceinte contenant le plasma, est évaluée par rapport aux applications expérimentales désirées. Les besoins en courant et les performances des systèmes proposés sont également caractérisés. La conductivité de l'enceinte est prise en compte dans un modèle utilisé pour déterminer les fonctions de réponse couplées du SCS interne, l'écrantage de la perturbation magnétique par la paroi, les tensions et courants induits lors d'une disruption du plasma et les forces magnétiques maximales exercées sur ce SCS. La variation des paramètres des SCS en fonction du nombre de spires des bobines est aussi présentée, ainsi qu'une étude sur le problème du chauffage et du refroidissement des bobines.

MOTS CLEFS : mode localisé au bord, contrôle, plasma, confinement magnétique, Tokamak, TCV, bord du plasma, chauffage par résonance avec des ondes cyclotroniques électroniques, puissance modulée, contrôle en temps réel, bobine selle, perturbation magnétique résonante, champ d'erreur, contrôle vertical, Lagrange, ergodique.

Contents

List of Figures

xxi

List of Tables

Chapter 1

Introduction

1.1 Energy production context

Thanks to scientific progress in agriculture and medicine, the world population is growing exponentially, threatening both natural and social equilibria. Not only is the population growing, but the level of resource consumption per capita is also increasing. This continuously growing demand on natural resources usually comes with little interest in the global availability limits of these resources or in the side effects of their massive exploitation. Of course, energy resources are not spared in the process. Presently, the vast majority of the worldwide energy supply relies on fossil fuels (oil, coal and natural gas) [1], renewable energy sources, including hydroelectricity, accounting for less than 10% of the total energy consumption. After the recent nuclear accident in Fukushima, the withdrawal from nuclear energy based on fission has been accelerated in Europe, ignoring the issues of carbon dioxide production and global warming inherent to the fossil fuel-based energy sources chosen as temporary replacements, renewable energy sources being only the long term choice. Apart from hydroelectricity, renewable energy sources, like wind or solar power, are nonetheless subject to two major constraints: low power density (i.e. large area covered per unit of power produced) and circumstantial availability (i.e. power production depending on weather conditions). Nowadays, the challenge of energy supply in an ever growing demand environment is met on one side by the use of fossil fuels, which is only a temporary solution due to the limited available resources and which also causes problematic carbon dioxide emission, and on the other side by resorting to renewable energy sources, which are technically condemned to remain a marginal or small fraction of the global energy production. While nuclear power based on fission does not face a number of these issues, the risks associated

with a nuclear accident and the long term storage of radioactive wastes make this energy source particularly unpopular. In terms of power density, nuclear power is nonetheless unbeatable, since the energy released in nuclear reactions is 6 orders of magnitude larger than the energy released in chemical reactions. It seems therefore reasonable that the energy supply challenge should be met by an energy source based on nuclear reactions, but without the risks of accident or the long term nuclear wastes. With that respect, nuclear fusion is the most promising approach[(*)].

This chapter starts by a brief introduction to nuclear fusion (section 1.2), followed by a presentation of the concept of magnetic confinement (section 1.3), focusing in particular on the Tokamak concept, one of the most promising reactor designs for future nuclear fusion power plants. Finally, the motivations for this thesis are described in section 1.4, and the outline of this document is given in section 1.5.

1.2   Nuclear fusion

The binding energy per atomic nucleus mass is maximum for atoms of intermediate atomic mass. This property explains why energy is released in both the fission of large nuclei (e.g. uranium in nuclear power plants) and the fusion of small nuclei (e.g. hydrogen in stars). However, while fission is easily triggered by neutron bombardment of large nuclei, fusion of two nuclei requires that both nuclei collide with sufficient energy to overcome the repulsive electrostatic force due to the positive charge of the nuclei.

When choosing the fusion reaction reactants for a nuclear fusion power plant, various aspects must be considered: energy required for a high fusion probability, energy released in the reaction, natural abundance of the reactants, etc. In this context, the most promising reaction is the fusion of two hydrogen isotopes, deuterium and tritium, into helium. This reaction is formally written:

$$\,^{2}_{1}\mathrm{D} + \,^{3}_{1}\mathrm{T} \rightarrow \,^{4}_{2}\mathrm{He}\ (3.5\,\mathrm{MeV}) + \,^{1}_{0}\mathrm{n}\ (14.1\,\mathrm{MeV}) \tag{1.1}$$
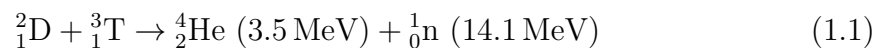
Deuterium has a natural abundance of approximately one atom in 6400 hydrogen atoms and can be easily extracted by physicochemical processes (Girdler sulfide process and vacuum distillation [2]). Tritium does not exist in nature, since it is a radioactive material having a short half-life (12.6 years). It can nonetheless be manufactured by bombarding lithium with neutrons. In a fusion reactor, tritium

---

[(*)]   Leaving contraception aside, of course.

will be bred on-site by incorporating lithium in the reactor vessel mantel and using the neutrons produced by fusion reactions to drive the decay of lithium into helium and tritium. In nature, deuterium is much more abundant than lithium, and the available quantity of lithium is sufficient to cover the global energy consumption for a million years [3].

Energy production by the fusion of hydrogen atoms has several advantages: limitless resources on a human timescale, high power density, uninterrupted power delivery, low resource consumption (less than a kilogram of reactants per day for a 1 GW power plant), no radioactive reaction products, small quantity of radioactive wastes with short-term activity only (mainly the reactor itself, for about 100 years), no greenhouse gases emission, no risks of nuclear accidents or nuclear proliferation.

Unfortunately, fusion reactions are difficult to produce. The high energy at which the reactants must collide, several keV's, and the small probability of a fusion reaction impose harsh constraints on the environment in which these reactions take place. The high energy constraint means that the reactants will be in plasma state, a state where matter takes the form of a gas of ionized atoms and where electrons and ions are only macroscopically coupled. The small probability of fusion reactions means that the reactants must be kept at a sufficiently high temperature and high density for a sufficiently long time to obtain a significant fusion rate. Up to know, these three basic parameters have never simultaneously met the values required to result in a positive power balance, i.e. a fusion power exceeding the plasma heating power.

1.3 Magnetic confinement

As described above, the success of fusion depends on how long a hot and dense plasma can be maintained in a finite volume. The physical properties of the plasma state, in particular the gyration of charged particles about magnetic field lines, can be exploited to increase this confinement time. If the magnetic field amplitude is sufficient, the transport of particles (such as reactant ions) across the field lines is indeed greatly decreased. This technique not only improves the confinement time, but also helps protecting the walls of the vessel containing the plasma by keeping energetic particles away from it. Of course, transport parallel to the field lines is not affected and must be limited externally by a magnetic mirror (i.e. a stronger magnetic field amplitude at the end of the plasma container) or by closing the field lines on themselves. The latter solution is used in the case of Tokamaks, a class of
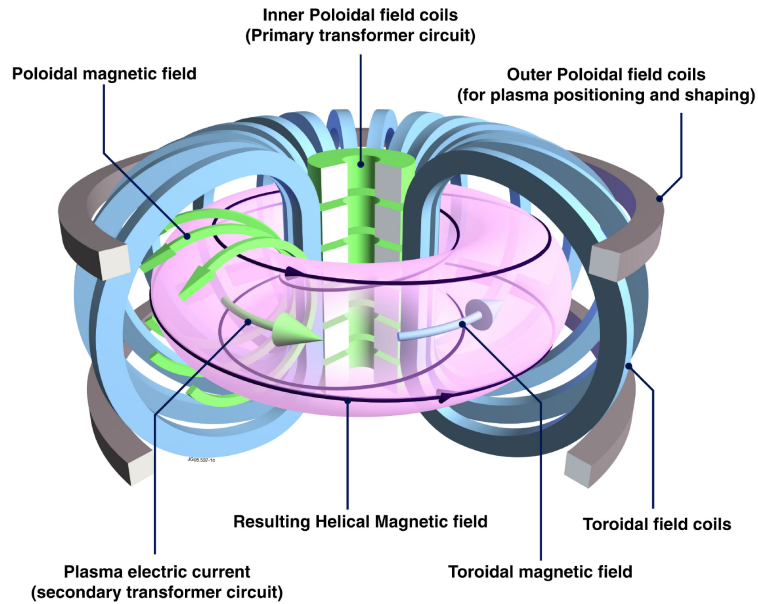
Figure 1.1: The Tokamak concept. A main toroidal magnetic field is created by a set of toroidal field coils. The central column coils serve as the primary of a transformer used to induce a toroidal current in the plasma. This current creates the poloidal magnetic field. Both magnetic field components result in a helical magnetic field configuration. A set of poloidal coils is used to control the plasma shape and position. Figure courtesy of [4].

fusion reactors based on magnetic confinement where the magnetic field lines are closed on themselves toroidally, and where the plasma takes the shape of a torus.

1.3.1   Tokamak concept

Simply closing the magnetic field lines on themselves in a toroidal configuration does not result in good confinement properties. The radial gradient of the magnetic field, inherent to toroidal configurations, leads to a charge-dependent vertical drift of the plasma particles resulting in a vertical electric field. Combined with the toroidal magnetic field, this electric field causes an outward drift of the whole plasma. This issue can be solved by adding a poloidal component to the magnetic field, thereby creating a rotational transform of the field lines about a common magnetic axis. In that case, the resulting magnetic configuration is described by an infinite set of nested flux surfaces along which magnetic field lines follow helical trajectories. This configuration leads to a null average vertical particle drift, because the same number of magnetic flux surfaces is crossed outwards and inwards in the parts of the particle trajectory above and below the magnetic axis, respectively.

In a Tokamak (figure 1.1), the fusion reactor concept invented in the 1950s by Igor Tamm and Andrei Sakharov [5], the main toroidal magnetic field is created

by a set of coils surrounding the vacuum vessel containing the plasma, and the poloidal component of the magnetic field is created by a toroidal current flowing in the plasma. This current is induced by a set of coils located in the central column of the Tokamak. A set of poloidal coils is also necessary to create a radial and vertical magnetic field used to control the plasma position and shape. This control relies on the interaction of the magnetic field with the plasma current through the Laplace force. The term Tokamak is a Russian acronym meaning toroidal chamber with magnetic coils.

As mentioned above, a fusion plasma must not only be well confined, but also heated to high temperatures. In a Tokamak, the most basic source of heat is the Joule effect caused by the plasma current and the finite plasma resistivity η. Unfortunately, η decreases with the plasma temperature, $\eta \propto T^{-3/2}$, and the plasma current density is limited by magnetohydrodynamic (MHD) instabilities. To reach high temperatures, auxiliary heating systems must be used, like neutral-beam injection or radio-frequency heating.

1.4 Motivations for this thesis

In Tokamaks, the experimental scenarios yielding the largest fusion rate are based on a high confinement plasma regime, the H-mode (see section 2.3), in which the energy and particle confinement are enhanced by a transport barrier located at the plasma edge and forming a pedestal in the plasma pressure profile. In standard axisymmetric magnetic configurations, stationary H-mode regimes suffer from instabilities of the plasma edge, the so-called edge localized modes (ELMs) (see section 2.3.1), driven by the steep pressure gradient and the current density in the pedestal region, and leading to potentially damaging repetitive ejections of heat and particles toward the plasma facing components. In ITER, a Tokamak currently being built to demonstrate net power production from fusion, type I ELMs (see section 2.3.1) are expected to occur during high performance discharges. It is expected that the power flux released by these ELMs will cause an intolerable erosion and heat load on the plasma facing components [6–8]. The understanding and control of ELMs [9–11], in terms of frequency and energy loss, will be determinant for the success of ITER and, by extension, will play a major role in the assessment of the viability of the Tokamak approach to fusion power production. It is therefore subject to an intense research effort worldwide.

This thesis, in line with this effort, focuses on two particular ELM control meth-

ods: local continuous and modulated heating of the plasma edge, and application of resonant magnetic perturbations (RMP) (see section 2.3.2). The former is of special interest because of the very limited existing knowledge of its characteristics and potential for ELM control, and the latter particularly attracts attention because of its unique stationary ELM suppression feature.

This thesis sets the foundations of experimental research in the particular subject of RMP at CRPP by proposing a physics-based design for a multi-purpose saddle coil system for TCV (Tokamak à Configuration Variable, see section 2.4), providing not only ELM control, but also error field correction and vertical control. Such an upgrade is motivated by the need to study the effect of plasma shape on the properties of plasmas subject to RMP. Although this effect is significant, in particular in the case of a change of plasma triangularity [12], only few studies have been done so far. With that respect, TCV's unique plasma shaping and positioning capability could significantly extend the study of the dependence of ELM control by RMP on the plasma shape, and contribute to a clearer description of the conditions required for ELM suppression. In the limit of the vacuum magnetic field approximation, this thesis also brings a flexible and robust solution to the problem of optimal coil current distribution determination for generic non-axisymmetric coil systems with independent power supplies, a problem that will be more and more frequent as these coil systems grow in complexity. This solution requires the spectral characterization of the coil system, for which a generic approach is also proposed.

The lack of systematic studies on the capabilities of plasma edge heating to control ELMs calls for additional research in this field. Heating the plasma directly in the pedestal region might indeed have an effect on the ELM cycle by modifying the evolution of the edge pressure and current profiles. ECRH (Electron Cyclotron Resonant Heating, see section 2.4.2) is an optimal tool for this purpose, as it is unparalleled in its degree of localization of the power deposition. Thanks to its highly sophisticated ECRH apparatus and to the recent development of a plasma configuration where power deposition in the edge of a type I ELMing H-mode is possible [13], TCV appeared as a candidate of choice to perform these experiments. These elements motivated the design and conduct of a dedicated experimental mission, whose results are presented in the first part of this thesis. These experiments revealed, for the first time, that the ELM frequency and amplitude depend on the power deposition location. An increase of the ELM frequency by a factor 2 and a decrease of the energy loss per ELM by the same factor are indeed observed as the deposition location is shifted toward the plasma pressure pedestal, even though the

power absorption efficiency is reduced. This unexpected phenomenon runs contrary to the intrinsic type I ELM power dependence and provides a new approach for ELM mitigation. Although the obtained factor of ELM amplitude reduction does not meet the ITER requirements, further studies, on other Tokamaks or with other plasma configurations, might yield larger reduction factors. The power modulation experiments also uncovered a significant number of type I ELM properties: (a) by synchronizing the ECRH power modulation with the ELM cycle so that ELMs always occur during a high power phase, an efficient ELM pacing is achieved; (b) the ELM frequency does not depend, in our experimental conditions, on the exact waveform of the heating power in the ELM cycle, but only on the average heating power; (c) rare transient events with large ELM amplitudes are observed to be less frequent in phases with synchronized power modulation; and (d) each ELM period is individually controllable by acting on the average power delivered during the ELM cycle. These results are consistent with a simple 0D model of the ELMs, detailed in this thesis, where the plasma edge is described as a finite confinement time energy integrator with variable energy threshold. In addition to its physical interest, this ELM pacing technique is also of practical interest. Indeed, regular ELMs facilitate the interpretation of experimental results obtained by statistical approaches like the conditional average sampling method, and ELM pacing is the first step toward an accurate control of ELM timing, which might be used to trigger the measurement of plasma parameters at specific times in the ELM cycle.

1.5 Thesis outline

A brief introduction to nuclear fusion by magnetic confinement, including the description of the motivations for this thesis, was given in this chapter.

Chapter 2 completes this introduction by giving more specific information on the Tokamak physics, including a short presentation of the Tokamak equilibrium and a brief review of the ELM phenomenology and control. The main characteristics of TCV are also detailed.

Chapter 3 describes the experiments of ELM control by edge ECRH conducted in TCV. It shows how ELMs depend on the power deposition location (section 3.3), and how real-time controlled power modulation is a successful ELM pacing tool (section 3.4). The chapter ends by the description of the 0D finite confinement time integrator model of the ELM cycle able to reproduce a large proportion of the experimental results.

The mathematical method developed to calculate the coil current distributions resulting in optimal RMP spectra for generic RMP coil systems is detailed in chapter 4. The efficiency of the method is illustrated in the particular case of the internal saddle coil system proposed for TCV. In addition, a simple approach based on a Fourier decomposition in both real and current spaces is proposed to determine the spectral characterization of non axisymmetric coil systems.

The internal and external saddle coil system designs proposed for TCV are detailed in chapter 5. These designs are reviewed with respect to RMP and error field correction. The electrical response of the in-vessel design is characterized, and the effects of plasma disruptions, as well as the amplitude of magnetic forces, are assessed. The possibility to use the in-vessel coil system for plasma vertical control is also studied. Finally, the issue of coil heating caused by Joule effect is addressed and an estimate of the required cooling time is given.

In chapter 6, a brief summary of the work presented in this thesis is given and the main conclusions are drawn.

Finally, additional material is given in appendices A and B. This comprises technical aspects of the plasma edge ECRH experiments and a number of mathematical derivations necessary for the study of the saddle coil system design.

Chapter 2

Selected chapters of Tokamak physics

2.1 Introduction

This chapter completes the general introduction given in chapter 1 by presenting specific elements of Tokamak physics essential to the understanding of this thesis. It starts with a description of the MHD Tokamak equilibrium (section 2.2), followed by a brief review of the ELM phenomenology and control (section 2.3). Finally, section 2.4 is dedicated to the description of TCV (Tokamak à Configuration Variable), the Tokamak experiment at the heart of this thesis.

2.2 Tokamak equilibrium

The macroscopic properties of Tokamak plasma equilibria are best described in the theoretical frame of ideal MHD [14], a simplified 1-fluid plasma theory, well-suited for the description of slow and large-scale plasma phenomena. In this frame, the plasma equilibrium is determined by the time independent form of the force equation:

$$\nabla p = \mathbf{j} \times \mathbf{B} \tag{2.1}$$

with p the plasma pressure, $\mathbf{j}$ the plasma current density and $\mathbf{B}$ the magnetic field. Equation (2.1) has the important consequence that current flows on isobaric surfaces and that magnetic field lines also lie on the same surfaces. For axisymmetric systems, these magnetic flux surfaces are in addition nested in one another (see figure 2.4), the last closed flux surface, also named the separatrix, being the frontier between the hot confined plasma and the cold scrape-off layer plasma. The magnetic flux

surfaces are usually labelled with the poloidal flux, defined by

$$\psi = \int_{A_{\text{tor}}} \mathbf{B} \cdot d\mathbf{S}, \tag{2.2}$$

or the toroidal flux, defined by

$$\varphi = \int_{A_{\text{pol}}} \mathbf{B} \cdot d\mathbf{S}, \tag{2.3}$$

with A_{tor} the toroidal cross-section delimited by the magnetic axis and the flux surface of interest and A_{pol} the poloidal cross-section of this flux surface. Usually, the radial coordinate $\rho = \sqrt{\psi_{01}}$, with $\psi_{01} = \psi/\psi_{\text{sep}}$ and ψ_{sep} the poloidal flux at the plasma separatrix, is used in the literature.

When characterizing magnetic equilibria, it is convenient to refer to the so-called safety factor q defined by the number of toroidal turns covered by a magnetic field line on a given flux surface per poloidal turn:

$$q(\rho) = \frac{\Delta\phi(\rho)}{2\pi} \tag{2.4}$$

with $\Delta\phi$ the toroidal angle covered by a magnetic field line on surface ρ when the poloidal angle θ covers 2π. q is equivalently expressed in terms of flux with:

$$q(\rho) = \frac{d\varphi}{d\psi} \tag{2.5}$$

For the particular flux surfaces where q takes rational values, the magnetic field lines are closed on themselves. These surfaces, in particular those where q is an integer or a low order rational number, are privileged locations for the development of instabilities, since they allow a constructive interference of perturbations, and are often referred to as resonance surfaces.

2.2.1 Magnetic islands

When a perturbed radial magnetic field is present at a resonance surface with a Fourier component resonant with the equilibrium magnetic field, magnetic reconnection can occur on the resonance surface and form magnetic islands [16]. Magnetic islands, perturbations compatible with MHD theory when the plasma resistivity is included, destroy the equilibrium axisymmetry and increase the level of radial transport. They can be seen as magnetic flux tubes winded around resonance surfaces with the same pitch angle as that of the original equilibrium magnetic field lines on these surfaces (see figure 2.1). The term island comes from the shape formed by the intersection of the poloidal cross-section with the magnetic flux tubes of the magnetic
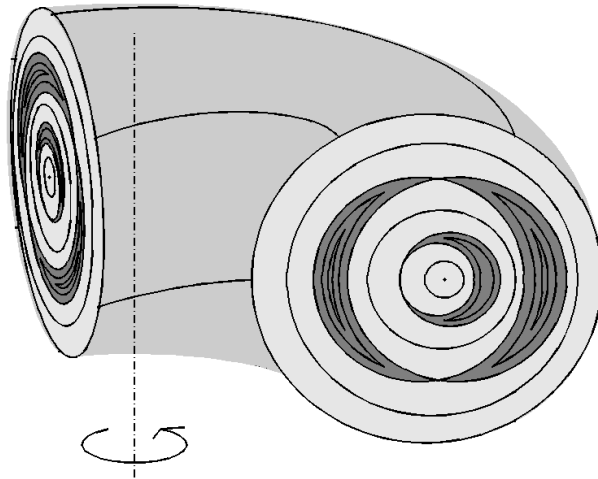
Figure 2.1: Magnetic field topology in the presence of magnetic islands. Both a $q = 1/1$ and a $q = 2/1$ islands are shown (dark grey). Figure courtesy of [15].

equilibrium in the presence of magnetic reconnection. This term is also associated with the fact that plasma inside a magnetic island is insulated from the main plasma. Magnetic islands are driven either by an external resonant magnetic perturbation, or by tearing modes (an MHD instability associated with a non-axisymmetric redistribution of the plasma current). When islands from different resonance surfaces are wide enough to overlap, the magnetic field lines of both islands transit from one island to the other, consequently creating a region of ergodic magnetic field and enhancing greatly heat and particle radial transport.

2.3 High confinement regime and edge localized modes

The high confinement mode (H-mode) [17, 18] is a particular plasma regime characterized by an improved energy and particle confinement time [19]. The transition from the standard low confinement (L-mode) to the high confinement mode is experimentally associated with a threshold P_{LH} on the heating power P_{sep} through (i.e. outward) the separatrix [20]:

$$P_{sep} = P_{input} - \frac{dW}{dt} - P_{rad} \qquad (2.6)$$

with P_{input} the input power (ohmic and auxiliary), W the plasma energy and P_{rad} the power radiated by the plasma. The transport reduction associated with the H-mode is due to a transport barrier located in the plasma edge and forming a pedestal in the pressure profile (i.e. a region of steep pressure gradient).

Operating in H-mode offers the possibility to reduce the size of a Tokamak while keeping equivalent performances. As the cost of a Tokamak is related to its size, Tokamak fusion reactors are planned to work in H-mode.

2.3.1   ELM phenomenology

H-mode plasmas are prone to MHD instabilities driven by the large edge pressure gradient and the edge current density. These instabilities trigger repetitive relaxations of the pedestal profiles, the so-called edge localized modes (ELMs) [21–25]. The ELM cycle is made of two subsequent parts: a build-up phase and a crash phase. During the build-up phase, radial transport is low and the edge pressure grows gradually. Above a certain pressure pedestal gradient and height, an MHD instability develops and replaces the edge transport barrier by a region of turbulent transport, with enhanced radial transport. The pressure pedestal is thereby relaxed and the drive of the instability dies out, allowing for the start of a new ELM cycle. Consistently with pressure profile relaxation, experimental signatures of ELMs include spikes in the H_α emissivity (increased radial transport, see section 2.4.3.1), drops in the toroidal magnetic flux (plasma energy loss, see section 2.4.3.6) and turbulent magnetic perturbations (plasma edge and scrape-off layer current density perturbations). ELM precursors are at times observed in the magnetic diagnostics (see section 2.4.3.5). ELMs of different types are present in Tokamak plasmas, the most frequent types being the type I and type III ELMs.

Type I ELMs are typical from low collisionality plasmas (high temperature, low density) and, being generally associated with the stationary H-mode plasmas presenting the largest energy confinement time [26], expected to occur during high performance discharges in ITER. Their frequency increases with the power through the plasma separatrix:

$$\frac{\mathrm{d}f_{\mathrm{ELM,I}}}{\mathrm{d}P_{\mathrm{sep}}} > 0. \tag{2.7}$$

Type I ELMs are triggered by coupled kink-ballooning[(*)] modes. Both are ideal MHD instabilities, kink modes being associated with the edge current density and ballooning modes with the edge pressure gradient. The ballooning nature of the sta-

---

[(*)]   In the literature, kink-ballooning modes are often wrongly referred to as peeling-ballooning modes. Both peeling and kink modes are destabilized by the edge current density, but peeling modes are unstable only in limited plasma configurations. As H-modes are generally obtained in diverted plasma configurations, the unstable modes associated with the edge current limit are indeed kink modes (see also [27]).

bility limit means that the pedestal parameters are limited by a $T_e \propto 1/n_e$ hyperbola (with n_e the electron density and T_e the electron temperature).

Type III ELMs are typical from high collisionality plasmas (low temperature, high density). Their frequency scales inversely with the power through the plasma separatrix:

$$\frac{\mathrm{d}f_{\mathrm{ELM,III}}}{\mathrm{d}P_{\mathrm{sep}}} < 0. \tag{2.8}$$

They are often associated with coherent precursors observable on internal magnetic probes. Type III ELMs are caused by resistive instabilities.

2.3.2   ELM control in Tokamaks

H-mode plasmas are classified as ELMing (or ELMy) when ELMs are present and ELM-free when they are not. In the absence of dedicated control strategies, an ELM-free H-mode is non stationary. The density and the impurity content grow continuously until the H-mode is lost (because $P_{\mathrm{sep}} \leq P_{\mathrm{LH}}$ [20]) or until a plasma disruption is triggered (because the density stability limit is exceeded [28]). In standard conditions, the only stationary H-mode regime, in terms of density and impurity control, is the ELMing H-mode. This regime is therefore a baseline scenario for ITER. ELMs, by repetitively relaxing the pedestal profiles, nonetheless degrade the plasma confinement and release large fluxes of energy and particles toward the vessel walls. Scaling the current experimental data to ITER predicts that the power flux associated with ELMs will cause an intolerable erosion and heat load on the plasma facing components [6–8], in particular on the divertor where the magnetic field lines of the plasma separatrix intersect the vessel wall. Energy fluxes of 1 – $10 \, \mathrm{MJ/m^2}$ are indeed expected to be released in less than $1 \, \mathrm{ms}$, while the erosion limit corresponds to energy fluxes below $0.5 \, \mathrm{MJ/m^2}$. The control of ELMs [9–11, 29], in terms of frequency and energy loss, is therefore of primary importance in the field of magnetic fusion research.

Nowadays, various methods are available to control ELMs: pellet injection, vertical kicks, lithium coating, resonant magnetic perturbation (RMP) and modulated edge ECRH. These methods are briefly introduced here.

ELM control by pellet injection [29, 30] consists in dropping small deuterium pellets into the plasma to trigger ELMs by a local increase of the plasma pressure. With this technique, ELM pacing is achieved and the ELM frequency (resp. the ELM energy) can be increased (resp. decreased) by a significant factor. This factor, limited by the plasma core fuelling caused by the pellets, might nonetheless be

increased in the future by reducing the size of the pellets.

The technique of vertical kicks, or vertical jogs, consists in applying a fast radial axisymmetric magnetic perturbation to create a vertical push on the plasma. This technique, efficient for ELM pacing [9, 31, 32], is thought to rely on the excitation of the kink-ballooning modes by the additional edge current induced on the plasma surface when the radial field is applied, although this interpretation does not suit all the experimental observations. The ELM frequency increase obtained with this method is nonetheless small.

Lithium coating in NSTX [33] results in a reduction or elimination of ELMs by reduction of the edge pressure gradient. The gradient control is thought to be due to a reduced particle recycling associated with the lithium wall coating. The obtained ELM-free plasma discharges are nonetheless still subject to impurity accumulation [34].

Resonant magnetic perturbation (RMP) consists in applying a magnetic field perpendicular to the plasma equilibrium flux surfaces with a spatial variation tuned to align with the equilibrium magnetic field lines. RMP has been observed to mitigate or suppress ELMs on a number of Tokamaks [10, 11, 35–37] (DIII-D, JET, ASDEX Upgrade, MAST). The physical mechanism at the root of this ELM control technique is nonetheless not yet clearly identified, as experimental results lead to conflicting interpretations (more details on this particular aspect are given in section 4.1.1). The limits of the process, in terms of operation domain, are not yet accurately known, DIII-D being up to now the only Tokamak where a complete suppression of type-I ELMs has been successfully obtained. In addition, experiments in different Tokamaks reveal opposite results for similar conditions, for example RMP can trigger ELMs, though possibly of type III, during ELM-free phases in COMPASS [38], NSTX [39] and MAST [40]. Across these experiments, a number of parameters are particularly relevant to the success of ELM control: the magnetic perturbation amplitude [35], the magnetic perturbation spectrum with respect to the edge safety factor [37, 41, 42], the plasma density or collisionality [11, 41] and the plasma shape [12].

ELM control by application of ECRH in the plasma edge has been, up to now, much less studied than the other control methods described above. Preliminary studies in ASDEX Upgrade [43] have nonetheless shown that the application of modulated ECRH in the plasma edge causes a locking of the ELM frequency to the modulation frequency, as shown in figure 2.2. On DIII-D, it has also been shown that shifting the power deposition outside the plasma separatrix leads to a decrease
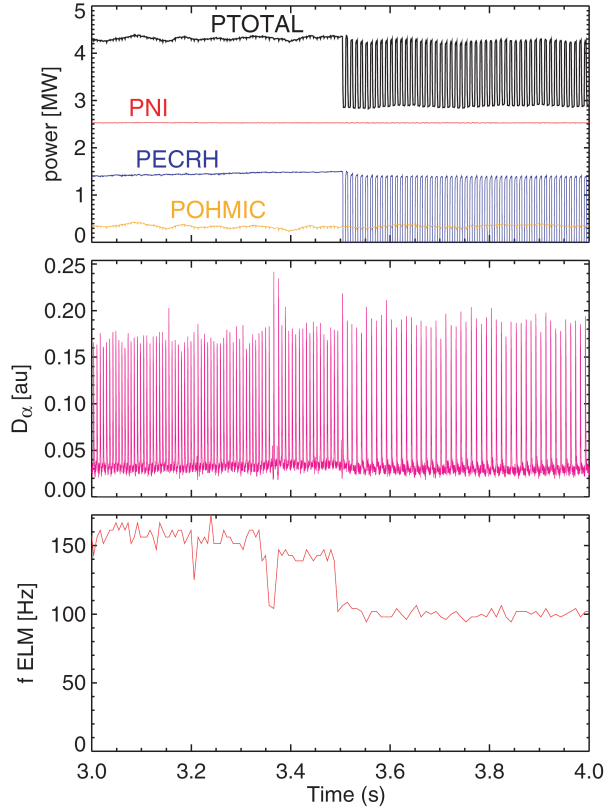
Figure 2.2: Modification of the ELM frequency by the application of the ECRH at the plasma edge. Similar effects are seen with pure heating and with current drive, suggesting that the main modification is to the pressure gradient term rather than directly to the edge current profile. Figure and caption courtesy of [43] (ASDEX Upgrade).

of the type I ELM frequency [44, 45], this frequency reaching values lower than those without additional heating. These results have however not been published because the approach chosen in these experiments did not result in a clear determination of the power deposition location.

To complete this overview of ELM control techniques, one must mention two stationary high confinement regimes that are not subject to ELMs and of interest for ITER: the QH-mode [46, 47] and the I-mode [48]. The QH-mode is a stationary H-mode that relies on a steady, saturated edge instability to eject impurities and maintain edge current and pressure below the kink-ballooning stability limit. This instability is driven by a strong plasma rotation shear in the plasma edge, irrespectively of the rotation direction. The I-mode is a particular confinement regime where the edge transport barrier affects only the energy and not the particles. The transition to this regime, more easily obtained in unfavorable ion drift direction (i.e. away from the X-point), is correlated with the presence of a weakly coherent high frequency edge MHD mode that is thought to control particle transport in the
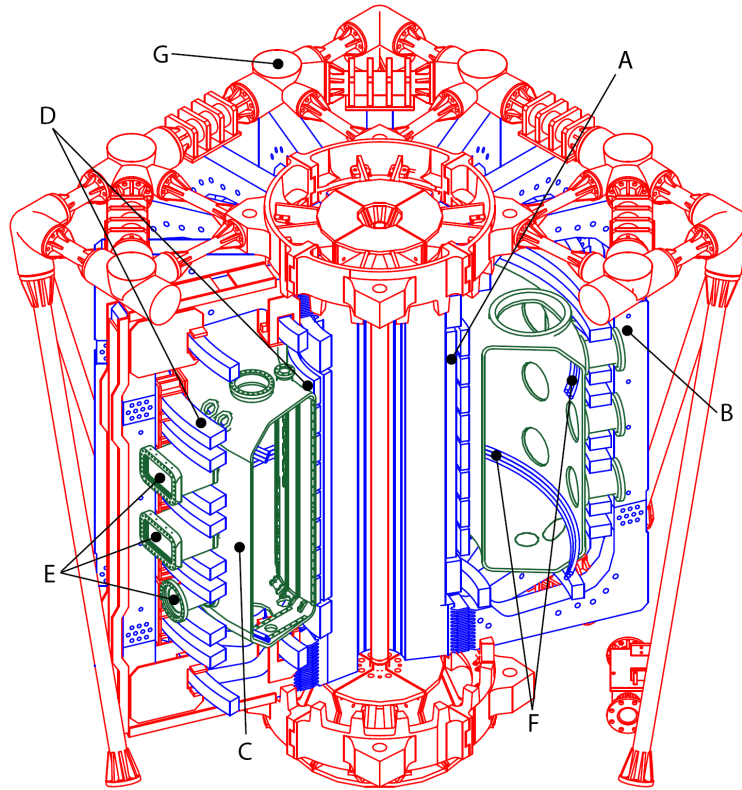
Figure 2.3: Drawing of the main components of the TCV Tokamak: (A) primary transformer circuit (ohmic coils); (B) toroidal field coils; (C) vacuum vessel; (D) poloidal field coils; (E) diagnostic or auxiliary heating portholes; (F) fast internal coils; (G) mechanical support structure. Figure courtesy of [49].

plasma edge.

2.4   Tokamak à Configuration Variable

The studies presented in this thesis have been dedicated to or carried on the TCV (Tokamak à Configuration Variable) Tokamak experiment of the CRPP (Centre de Recherche en Physique des Plasmas) at the EPFL (Ecole Polytechnique Fédérale de Lausanne). In this section, the Tokamak, its auxiliary heating system and the diagnostics relevant to this work are presented. The digital real-time control system, recently implemented on TCV, is also shortly introduced.

2.4.1   The Tokamak

TCV is a medium size Tokamak that has been built with a special attention to flexibility in terms of plasma shape [51] and plasma heating. A 3D schematic view of TCV is shown in figure 2.3 and a poloidal cross-section in figure 2.4. The air core
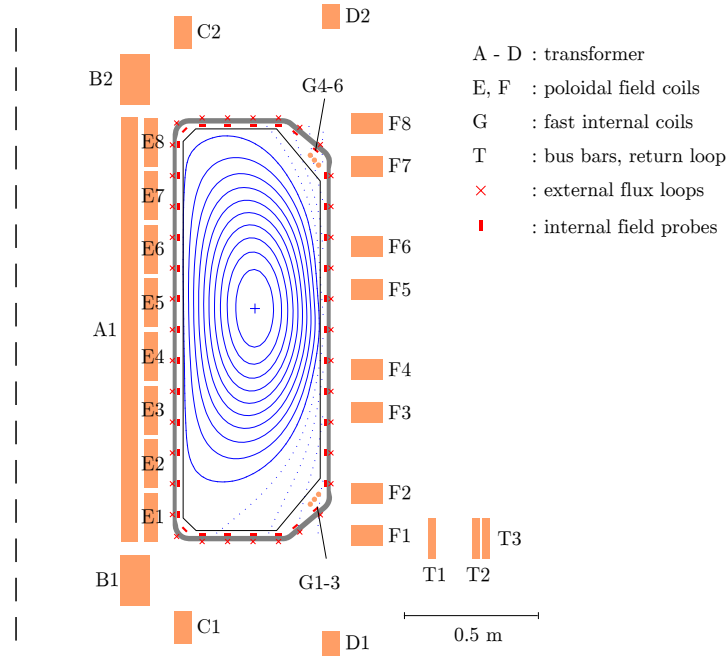
Figure 2.4: Poloidal cross-section of TCV. The magnetic coils (ohmic coils (A-D), poloidal field coils (E-F), fast internal coils (G) and toroidal field coil connections (T)), the location of the magnetic diagnostics (red) and the vacuum vessel (grey) are represented. The black solid line depicts the tile boundary. Magnetic flux surfaces of an elongated limited plasma are shown in blue. The axis of the central column is depicted by a vertical dashed line. Figure courtesy of [50].

transformer (coils A to D) is designed to minimize the perturbation of the poloidal magnetic field inside the vacuum vessel. The poloidal field coils (E1 to E8 and F1 to F8) are powered independently, allowing for a large variety of plasma shapes, as shown in figure 2.5. The internal fast coil (G) extends the operational domain by providing an efficient control of the vertical instability of elongated plasmas. TCV's first wall is covered with 24 mm thick graphite tiles designed to withstand the large power fluxes occurring during ECRH (see section 2.4.2). The main Tokamak and plasma parameters are given in tables 2.1 and 2.2.

2.4.2 Electron cyclotron resonant heating

ECRH (Electron Cyclotron Resonant Heating) [52] is one of the standard auxiliary electron heating sources on Tokamaks. Although the ions are only indirectly heated with ECRH, the high degree of power deposition localization and the high fraction of absorbed power make it an appreciated heating method, in particular for applications such as MHD instability control [53,54] or non-inductive plasma operation [55].

#9849, $t = 0.50$ s   #6010, $t = 0.80$ s   #5650, $t = 0.80$ s   #8856, $t = 0.29$ s

(a)   (b)   (c)   (d)

Limited $\kappa = 1.2$, $\delta = 0.0$, $I_{\mathrm{p}} = 230$ kA   **SND upper** $I_{\mathrm{p}} = 330$ kA   **SND lower** $I_{\mathrm{p}} = 335$ kA   **DND** $I_{\mathrm{p}} = 325$ kA

#11368, $t = 0.65$ s   #18548, $t = 1.50$ s   #6442, $t = 0.50$ s   #10159, $t = 0.01$ s

(e)   (f)   (g)   (h)

Highest current, $I_{\mathrm{p}} = 1.06$ MA   **Highest fully ECCD driven current**, $I_{\mathrm{p}} = 210$ kA   **Pear shape** $I_{\mathrm{p}} = 360$ kA   **Doublet shape** $I_{\mathrm{p}} = 115$ kA

#19373, $t = 0.42$ s   #8890, $t = 0.75$ s   #11928, $t = 0.67$ s   #11962, $t = 1.00$ s

(i)   (j)   (k)   (l)

Highest elongation, $\kappa = 2.80$ **Highest triangularity**, $\delta = 0.86$ **Lowest triangularity**, $\delta = -0.77$ **Highest squareness**, $\lambda = 0.5$

Figure 2.5: Range of plasma shapes achieved on TCV. Figure courtesy of [50].

Parameter	Symbol	Value
Major radius	R_0	$0.88\,\mathrm{m}$
Minor radius	a	$0.25\,\mathrm{m}$
Aspect ratio	$\epsilon^{-1} = R_0/a$	$\simeq 3.5$
Vacuum vessel elongation	κ_{TCV}	2.9
Toroidal vessel resistance	Ω_{TCV}	$45\,\mathrm{m\Omega}$
Toroidal field on axis	B_0	$\leq 1.54\,\mathrm{T}$
Plasma current	I_P	$\leq 1\,\mathrm{MA}$
Loop voltage	V_{loop}	$\leq 10\,\mathrm{V}$
X2 ECRH	$P_{\mathrm{ECH,X2}}$	$\leq 2.7\,\mathrm{MW}$
X3 ECRH	$P_{\mathrm{ECH,X3}}$	$\leq 1.5\,\mathrm{MW}$
Discharge duration		$< 4\,\mathrm{s}$

Table 2.1: Main TCV parameters.

Parameter	Symbol	TCV values
Central electron density	n_{e0}	$1 - 20 \cdot 10^{19}\,\mathrm{m^{-3}}$
Central electron temperature	T_{e0}	$< 1\,\mathrm{keV}$ (ohmic)
		$< 15\,\mathrm{keV}$ (ECRH)
Central ion temperature	T_{i0}	$< 1\,\mathrm{keV}$
Electron plasma frequency	f_{pe}	$28 - 120\,\mathrm{GHz}$
Electron cyclotron frequency	f_{ce}	$41\,\mathrm{GHz}$
Plasma elongation	κ_a	$0.9 - 2.8$
Plasma triangularity	δ_a	$-0.8 - 0.9$

Table 2.2: Typical TCV plasma parameters with ohmic and ECRH/ECCD heating.

TCV is equipped with a uniquely flexible ECRH setup [56], consisting in up to $1.5\,\mathrm{MW}$ of heating at the third harmonic of the electron cyclotron resonance in extraordinary mode (X3, $118\,\mathrm{GHz}$, $n_{e,\mathrm{cut\text{-}off,X3}} = 11.5 \cdot 10^{19}\,\mathrm{m^{-3}}$) and up to $2.7\,\mathrm{MW}$ of heating at the second harmonic (X2, $82.7\,\mathrm{GHz}$, $n_{e,\mathrm{cut\text{-}off,X2}} = 4.25 \cdot 10^{19}\,\mathrm{m^{-3}}$). The X2 power is delivered from the equatorial (up to $0.9\,\mathrm{MW}$) and the upper lateral (up to $1.8\,\mathrm{MW}$) launchers, while the X3 power is delivered from the top launcher to maximize the length of the absorption layer crossed by the beam, as illustrated in
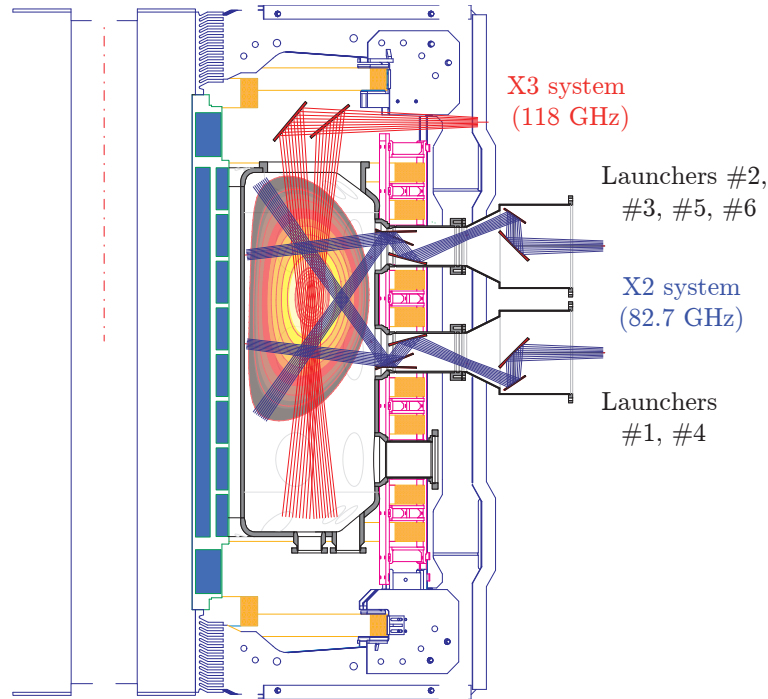
Figure 2.6: Poloidal cross-section of TCV and its ECRH system. The steerability of the launcher mirrors is illustrated by a superposition of both extreme mirror positions for each launcher location.

figure 2.6[†].

The X3 gyrotrons can only be operated at full or null power. Intermediate power levels are only possible through power modulation schemes, with a maximal modulation frequency of 400 Hz at 50% duty cycle. The X3 launcher has two degrees of freedom: the radial position of the mirror (fixed during a plasma discharge) and the poloidal angle of the mirror (steerable during a discharge).

The X2 gyrotrons are much more flexible. Similarly to the X3 gyrotrons, the X2 gyrotrons cannot be operated at intermediate power levels in the range 0-200 kW (with 1 ms required to reach either power level), but in the range 200–450 kW, any intermediate power level is allowed. In standard operation, a 0.1 ms sampling time is used for the gyrotron feed-forward power time traces. This sets the limit for the maximal time derivative of the gyrotron power in the range 200–450 kW. When using the real-time control system (see section 2.4.4), this limit is lowered to 0.02 ms. The X2 launchers have two degrees of freedom: the toroidal and poloidal angles. The

---

[†]   The nominal powers are 465 kW for the X2 gyrotrons and 480 kW for the X3 gyrotrons. However, the calibration curves vary slightly between gyrotrons. In addition, when operating the gyrotrons through the real-time control loop, small differences occur in the gyrotron cathode voltage setting which result in slightly higher output powers. Altogether, the full output power of the gyrotrons vary from 450 to 500 kW.

poloidal angle can be changed rapidly during a shot (with a limit of $1°/10\,\mathrm{ms}$) but the toroidal angle can only be steered between shots. When the toroidal launcher angle is set to obtain a non perpendicular injection of the ECRH beam, energy is preferentially transferred to electrons having a parallel velocity in the same direction as the beam. This results in a net plasma current, the process being referred to as ECCD (Electron Cyclotron Current Drive) [57].

The ECRH beam trajectories and power deposition locations can be calculated with the ray-tracing code TORAY-GA [58]. The nearly perpendicular X2 power injection (with respect to the electron cyclotron resonance layer) generally results in a low sensitivity of the TORAY-GA simulations to small errors on the mirror parameters. For X3, the nearly tangential power injection implies that a small error on the mirror parameters (e.g. $0.5\,\mathrm{cm}$) can have a dramatic effect on the consistency of the experimental and simulated values of the absorbed power fraction. The poloidal angle of the X3 launcher mirror is usually well determined, but its radial position is subject to drifts and must be verified experimentally by comparing the mirror parameters leading to the highest electron temperature with the mirror parameters leading to optimal absorption in TORAY-GA. At the time of the experiments reported in this thesis, an offset of 1–$1.5\,\mathrm{cm}$ was measured.

2.4.3   Selected TCV diagnostics

TCV is equipped with a set of diagnostics used to characterize the plasma parameters and the evolution of plasma instabilities. This section gives a brief description of the diagnostics essential to this thesis.

2.4.3.1   Photodiodes

Visible light spectroscopy of TCV plasmas is carried out by a set of 18 photodiodes distributed poloidally on the portholes of a toroidal sector of TCV, and acquired at $50\,\mathrm{kHz}$. A set of filters is installed in front of the diodes to selectively measure the radiation amplitude in spectral bands corresponding to transitions between well-identified electronic energy levels of bound electrons of partly ionized or neutral atoms. Amongst the variety of atomic spectral lines radiated by the plasma, the emissivity in the so-called H_α line is of particular interest. Its amplitude is related to the recombination rate of hydrogen atoms and is therefore sensitive to transport events in the edge, like ELMs.

2.4.3.2   XTE

Tokamak plasmas are sources of X-rays. At sufficiently high energies (i.e. above the ionization potential energy of the heaviest plasma impurities), the X-ray emission spectrum is made of recombination and Brehmstrahlung radiation, and is a simple function of the plasma electron temperature and density. By combining the measurements of the X-ray radiation amplitude at two different energy levels, the dependence on the plasma density can be cancelled and the electron temperature deduced.

On TCV, the XTE diagnostic relies on this principle to give an estimate of the plasma core temperature. The diagnostic consists of four X-ray detectors placed in a top porthole of the vacuum vessel, behind four different X-ray absorbers. These different absorbers result in the radiation energy level discrimination necessary to determine the electron temperature. The signals are acquired at 10 kHz.

2.4.3.3   Thomson scattering system

Thomson scattering, the scattering of an electromagnetic wave by a free electron, is a phenomenon commonly used to measure the plasma electron temperature and density. These quantities are determined by measuring the spectrum line of the light scattered by a well-defined plasma volume when a laser beam is fired through it. The width of the spectral line associated with the scattered light is related to the electron temperature (Doppler broadening), while its integral is proportional to the electron density.

As described in [60], the Thomson scattering system [61–63] is the main diagnostic for the measurement of the spatial profiles of the electron temperature and density on TCV. The profiles are measured along the line of sight of a laser beam passing vertically through the plasma at $R = 0.9\,\mathrm{m}$ (mid radius of the TCV vacuum vessel, see figure 2.7). Wide-angle camera lenses collect the scattered light from the observation volumes in the plasma and focus it onto sets of fiber bundles. There are 35 observation positions covering the region from $Z = -17\,\mathrm{cm}$ to $Z = 66\,\mathrm{cm}$ with a spatial vertical integration length that depends on the channel location. Spatial channels with higher resolution (integration length of 12 mm) are positioned near the top (TS-edge system) for observation of the pedestal in H-mode plasmas (see section 2.3). The sampling rate of the measurements is determined by the repetition rate of the high-power Nd:YAG lasers, emitting at a wavelength of 1.06 microns. There are 3 lasers combined in a cluster to build a beam which traverses the plasma
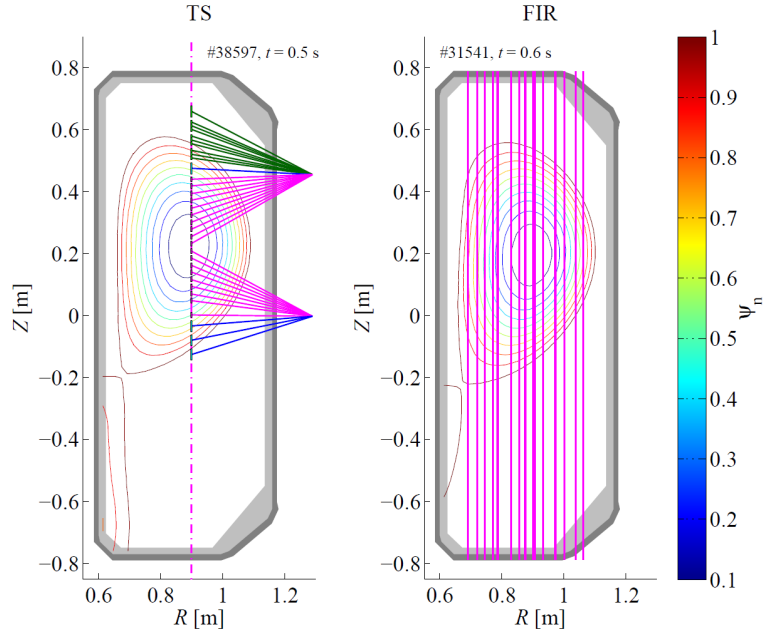
Figure 2.7: Thomson scattering (TS) system and Far Infra-Red (FIR) interferometer lines-of-sight. **Left**: TS setup. The 23 main chords are divided in two groups, with low spatial resolution (blue, $\Delta Z = 36\text{--}37\,\text{mm}$) and high spatial resolution (magenta, $\Delta Z = 16\text{--}17\,\text{mm}$). The TS-edge system chords cover the plasma edge with high spatial resolution (green, $\Delta Z = 12\,\text{mm}$ and $\Delta Z = 36\,\text{mm}$ for the top chord). **Right**: FIR interferometer. 14 vertical chords. The central chord (#9, thick line, $R \simeq 0.9\,\text{m}$) is used for the line-averaged density measurement. The line-of-sights are drawn on top of a poloidal cross-section of the flux surfaces of a typical diverted plasma (the values of the normalized poloidal flux ψ_n are indicated by a color code), enclosed by the vacuum vessel (grey). Figure courtesy of [59].

as a narrow fan. It appears as a single laser beam when viewed by the detection optics. Each laser operates at a fixed repetition rate of $20\,\text{Hz}$. The signal to noise ratio can be increased, for example in the case of low density or ECRH heated plasmas, by triggering the lasers simultaneously.

2.4.3.4 FIR

As described in [64, 65], a 14-channel Mach-Zehnder type interferometer is used to measure the line-integrated plasma electron density along parallel vertical chords (see figure 2.7). The system comprises a FIR (Far InfraRed) laser emitting a continuous wave at $214\,\mu\text{m}$, and a multi-element detector unit (InSb hot-electron bolometer). The laser beam is divided into a reference beam, which is frequency shifted by a rotating grating, and 14 probe beams crossing the plasma at different radial positions. When the probe beams pass through the plasma, the difference in refractive index causes a phase delay with respect to the reference beam. Since the reference beam is

frequency shifted, the phase delay can directly be obtained from a comparison of the detector signals at the difference frequency (beat frequency). At the wavelength and for the polarization of the FIR beams, the refractive index of the plasma is directly related to the electron density. Therefore, the system provides continuous measurements of the line-integrated density along 14 chords. The system is fully automated and part of the basic and essential diagnostic set in operation for each TCV shot. The measurement along the central chord (#9) is used for real time control of the plasma density, as well as to measure the line-averaged plasma electron density. The signals are acquired at 20 kHz.

2.4.3.5   Magnetic diagnostics

TCV is equipped with a large number of magnetic probes and flux loops [66] (see figure 2.4). The magnetic probes are located inside the vacuum vessel and measure the time derivative of the poloidal magnetic field tangent to the vacuum vessel. Their signals are not only used for real-time plasma shape and position control and for plasma equilibrium reconstruction, but also for the analysis of MHD modes. Magnetic probes are spatially distributed poloidally (4 arrays of 38 probes) and toroidally inside the vacuum vessel (3 arrays of 8 probes on the high field side and 3 arrays of 17 probes on the low field side). The flux loops are located outside the vacuum vessel and measure the time derivative of the poloidal magnetic flux. They are used for the plasma equilibrium reconstruction.

2.4.3.6   DML

The DML (DiaMagnetic Loop) [67] is a conducting loop poloidally encircling the plasma. It measures the time derivative of the toroidal magnetic flux, from which the plasma contribution to the toroidal flux can be derived. Ideal MHD shows that this flux is closely related to the total plasma energy. The DML signal is therefore an important constraint in the plasma equilibrium reconstruction code LIUQE [68] used to analyze TCV shots.

2.4.4   Real-time control

In addition to, and as a future replacement of, the so-called "hybrid" control system[‡], a new real-time digital Distributed Control System (SCD, Système de Con-

---

[‡]   The name "hybrid" comes from a hybrid combination of analog and digital processes in the system.

trôle Distribué) [69–71] has been installed on TCV. It offers, in particular, the possibility to control the ECRH actuators (power and launcher angles) in real-time. The real-time algorithms are programmed with the flexible and powerful block programming software Simulink. The SCD is described in details in [71].

Chapter 3

ELM control by ECRH

3.1 Introduction

As mentioned in section 2.3.1, type I ELMs are associated with a stability limit involving the edge pressure gradient and the edge current density [26], which jointly drive the so-called kink-ballooning modes. Due to the dependence of the ELM frequency on the power flux, it has been assumed up to now that neither the deposition location nor the heating mix could directly affect type I ELMs. Heating the plasma directly in the pedestal region might nevertheless have an effect on the ELM cycle by modifying the evolution of edge profiles. Electron cyclotron resonance heating (ECRH) is an optimal tool for this purpose, as it is unparalleled in its degree of localization of the power deposition.

As described in section 2.3.2, preliminary studies have shown that the application of modulated ECRH in the plasma edge causes a locking of the ELM frequency to the modulation frequency in ASDEX Upgrade [43] and that the ELM dynamics might be influenced by the power deposition location in DIII-D [44,45]. These preliminary results called for a more thorough investigation of the effect of ECRH in the plasma edge in conditions of optimal ECRH control. Thanks to its highly sophisticated ECRH apparatus (see section 2.4.2), TCV appeared as a candidate of choice to perform experiments where ECRH would be applied to the edge of type I ELMing plasmas.

This chapter starts by a description of the experimental setup used in the plasma edge heating experiments (section 3.2). ELM control by the application of ECRH is demonstrated in section 3.3, where it is shown that, in our setup, the ELM frequency increases by a factor 2 and that the ELM energy loss decreases in the same proportion when the power deposition location is scanned from well inside the pedestal
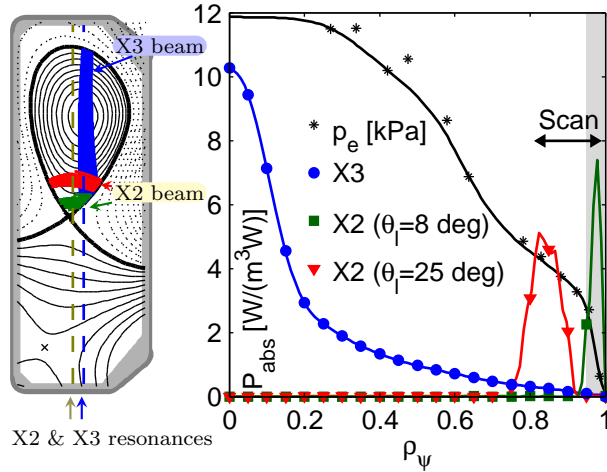
Figure 3.1: Left: poloidal cross-section of the TCV vacuum vessel with ECRH-X3 and ECRH-X2 beam trajectories and magnetic flux surfaces. The X2 beams for two possible antenna orientations are shown for illustration. The cold resonances are indicated by dashed lines. Right: ECRH power density absorbed by the plasma, by unit of input power, as a function of ρ_ψ for X3 and X2 for both antenna orientations. A representative electron plasma pressure profile, $p_e(\rho_\psi)$, is also shown (Thomson scattering data and spline fitting). The pedestal region is indicated in grey.

to the plasma boundary, an effect that is independent of the total input power. Section 3.4 shows how power modulation synchronized in real-time with the ELM cycle is able to pace the ELMs with low deviation from a given frequency. Experimental results clearly indicate that, for a given deposition location, the ELM frequency is only a function of the average power over the ELM cycle. This section also includes results of feed-forward power modulation experiments demonstrating that power modulation itself is not able to drive the ELM frequency. A simple 0D finite confinement time integrator model of the ELM cycle, capturing most of the observed features of the ELMs, is then discussed in section 3.5.

3.2   Experimental setup

3.2.1   Plasma target and heating schemes

The ELM control experiments are all performed with the same plasma target (figure 3.1 (left)): a lower single null diverted plasma with major radius $R_0 = 0.89\,\mathrm{m}$, vertical location $Z_0 = 0.36\,\mathrm{m}$, a plasma current of $290\,\mathrm{kA}$, a toroidal magnetic field on the magnetic axis of $1.43\,\mathrm{T}$, an edge safety factor q_{95} (at 95% of the poloidal flux) of 2.3, a central density of $5 \cdot 10^{19}\,\mathrm{m}^{-3}$, normalized pressures $\beta_{pol} = 0.35 - 0.5$ and $\beta_{tor} = 1 - 1.3\,\%$, and shape parameters $\kappa_{95} = 1.6$, $\delta_{95,top} = 0.17$ and $\delta_{95,bot} = 0.15$.

The $\mathbf{B} \times \nabla B$ ion-drift points toward the magnetic null point (favorable with respect to the H-mode power threshold). The baseline heating scheme consists of 0.1-0.2 MW of Ohmic power and 1 MW of third harmonic extraordinary mode (X3) ECRH launched from the top of the vacuum vessel and mainly absorbed in the plasma core. This power is sufficient to maintain an ELMing H-mode. The low field side launchers are used to inject second harmonic ECRH (X2) at various angles and powers. The launcher angle θ_l, defined as the angle between the X2 beam and a horizontal line, and the X2 input power $P_{\text{input,X2}}$ can be varied in the course of a plasma discharge. The beam trajectories and power deposition profiles shown in figure 3.1 are calculated with the ray-tracing code TORAY-GA [58]. Deposition profiles are given as a function of ρ_ψ, the square root of the normalized poloidal flux ψ. Using TORAY-GA simulations, a mapping from θ_l to $\rho_{\psi,\text{max}}(X2)$, the location of the maximum of the X2 absorbed power density, is deduced. The X3 waves are absorbed in the plasma core with an efficiency of 70±10%, resulting in an effective X3 heating power of 0.7±0.1 MW. The X2 waves are absorbed in a narrow region of the plasma edge at a rate ranging from 100% for $\theta_l \gtrsim 20°$ down to 70% for $\theta_l \simeq 8°$. The launcher angle has an upper limit set by the point in the density profile where the X2 propagation cut-off is encountered (25-30°) and a lower limit set by the plasma boundary (8°). The X2 power is injected in various ways. To avoid confusion, a glossary is given below:

Stationary : constant power or launcher angle, depending on context, on a given time interval.

Scanned or swept : power or launcher angle, depending on context, undergoes a linear ramp up or down on a given time interval.

RT : power modulated between a low and a high power level with low power phases triggered by the ELMs.

invRT : equivalent to RT mode but with inverted modulation phase (i.e. ELMs trigger high power phases).

FF : feed-forward power modulation. The power is modulated with a predefined frequency and duty cycle, irrespective of the ELM cycle.

Note that the contribution of the fraction of X2 power that has not been absorbed during the first pass, approximately 30% in the worst cases, has not been considered in the analysis of the results presented here. Figure 3.1 clearly shows that for small launcher angles, when the absorption is poorest, the non-absorbed part of the beam

Figure 3.2: Power ramp at constant launcher angle ($\theta_l = 14°$): (a) X2 input power; (b) ELM frequency; (c) relative plasma energy loss per ELM, as measured by the DML. Averages (for the stationary phases) and linear fits (for the ramp) are depicted by solid lines.
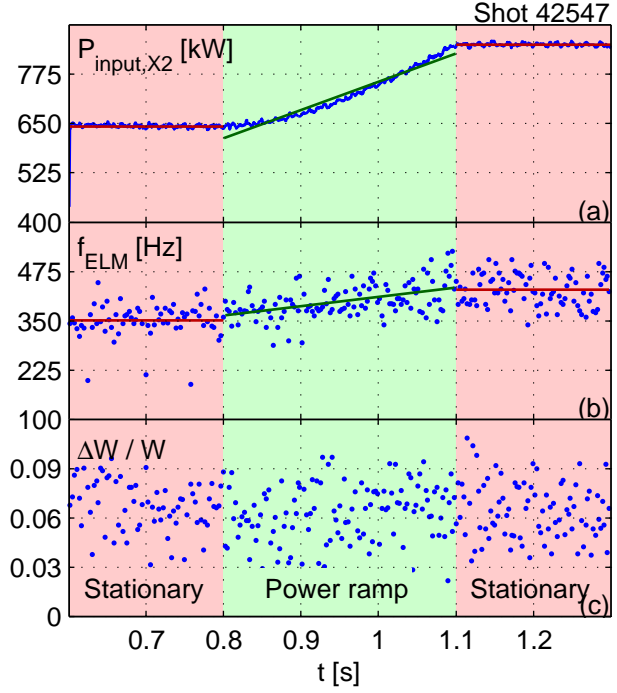
will be reflected toward the bottom of the vacuum vessel by the wall. The following multiple reflections against the vessel wall will increase the isotropy of the beam polarization and result in an unpredictable mixture of X and O modes. Because of refraction, the X-mode part, having the largest absorption factor, will only be absorbed in the divertor region, and only if the incidence angle is adequate. Since only a fraction of these 30% will fulfill these requirements, the impact of these secondary passes has been neglected. Of course, the wall itself will also absorb a fraction of this power.

Figure 3.2 shows the time evolution of the ELM frequency and relative plasma energy loss per ELM $\Delta W/W$ as the X2 input power is increased in the baseline plasma target while keeping a constant launcher angle. Since $\mathrm{d}f_{\mathrm{ELM}}/\mathrm{d}P_{\mathrm{input,X2}}$ is positive and $\Delta W/W$ does not vary significantly with power, and since no detectable magnetic precursor oscillations are present (not shown here), the type I character of these ELMs [21] is established. This characterization is also supported by ideal MHD edge stability calculations. The plasma target used here indeed corresponds to the so-called snowflake-like single null configuration, identified in [13] as kink-ballooning unstable.

3.2.2 Experimental constraints and limitations

X2 accessibility is an important aspect of the experiments reported here. The plasma target shown in figure 3.1 is the only known target on TCV which allows efficient edge heating of H-mode plasmas by X2 waves, thanks to an X2 beam nearly perpendicular to the flux surfaces and to a large flux expansion at the heating location which reduces the density gradient. Both are key factors in limiting beam refraction. The large flux expansion also contributes to a better localization of the power deposition in flux coordinates. In addition, the electron plasma density must stay below a level under which beam refraction remains tolerable. This level depends on the launcher angle, but the experiments are generally safely performed when a central density close to $5 \cdot 10^{19}\,\mathrm{m}^{-3}$ is maintained. In the series of experiments reported here, the primary goal is to apply pure ECRH in the plasma edge. ECCD is not considered because TORAY-GA simulations show that the level of current drive is insignificant in the range of toroidal beam angle in which refraction is tolerable (less than 1% of the ohmic current density). Experimentally, a small toroidal angle is nonetheless often necessary to avoid large stray power on the portholes of TCV in case of unexpected excursions of density. A study presented in Appendix A.2 shows that this small angle has theoretically and experimentally no significant effect.

Plasma density control is not only necessary to avoid X2 beam refraction, but also to maintain a stable type I ELMing H-mode. For line-averaged densities exceeding $5.1 \cdot 10^{19}\,\mathrm{m}^{-3}$, ELMs display a different behaviour, consistent with large type III ELMs [63, 72]. During a type I ELMing phase, a drop of density often leads to a back-transition to L-mode, and an increase of density often triggers an ELM-free phase. In the experiments, plasma density control has been successfully achieved by increasing the pre-shot glow duration and using the feedback control of the gas injection valve.

The particularly high location of the plasma in the vacuum chamber comes with a number of restrictions in terms of diagnostics. The CXRS, for example, is not available and ion temperature profiles are therefore not measured. The edge system of the Thomson scattering diagnostic is also inadequately positioned for this plasma location and a high resolution measurement of the pressure pedestal is hence not possible. In addition, ECRH increases the noise level in Thomson scattering measurements. To improve the signal quality, the Thomson lasers must therefore be triggered simultaneously, which considerably decreases the sampling frequency (down to 20 Hz). Consequently, the number of Thomson points in each phase of the ELM cycle for each experimental scenario is small and does not allow a fine analysis

of changes in the evolution of the pedestal across the scenarios.

3.2.3   Data analysis procedure

3.2.3.1   ELM and heating parameters

Various diagnostics (see section 2.4.3) are used to analyse the ELM response to plasma edge heating. The photodiodes measuring H_α radiation are used to determine the ELM crash times, from which the ELM period T_{ELM} and frequency f_{ELM} are deduced. The loss of energy per ELM, ΔW, is calculated in the small diamagnetism approximation, using the variation of toroidal flux $\Delta\varphi$ measured by the DML, and assuming that the Shafranov surface integrals do not change during the ELM crash [73]:

$$\Delta W = 3\frac{\pi}{\mu_0}R_0 B_{0,\phi}\Delta\varphi \tag{3.1}$$

where $B_{0,\phi}$ is the toroidal component of the vacuum magnetic field measured at R_0. The total plasma energy W is deduced from a full MHD equilibrium reconstruction using the LIUQE code [68] constrained by the magnetic diagnostics and DML data.[(*)] The line-integrated electron plasma density is measured by the FIR along a line-of-sight passing vertically through the plasma core and the conversion to a line-averaged density is deduced from the LIUQE reconstruction. The TORAY-GA simulations used to determine the power absorption and the power deposition location are run using electron temperature and density profiles measured by the Thomson scattering diagnostics, with density scaled to be consistent with FIR data. The X2 and X3 input powers are deduced from the gyrotron cathode voltage (and anode voltage, in the case of the triode-type X3 gyrotrons). The central electron temperature deduced from the XTE diagnostic has also been used when a higher time resolution was required.

3.2.3.2   Time interval selection for database generation

The time interval selection process is based on the following criteria:

[(*)] The maximal time resolution of LIUQE reconstructions is limited to $5\,\mathrm{kHz}$, the sampling frequency of the magnetic diagnostics on TCV. This frequency is too low to resolve the ELM crash, explaining why the DML signal alone, acquired at $10\,\mathrm{kHz}$, is used to determine ΔW. A comparison of the variation of plasma energy in the case of a slowly growing tearing mode [74] however shows that the LIUQE results are 50% larger than the values computed with (3.1), a discrepancy caused by the assumptions of constant Shafranov integrals and small diamagnetism.

- Baseline heating: 1 MW of X3 ECRH with constant launcher parameters

- Line-averaged density below $5.1 \cdot 10^{19}\,\mathrm{m}^{-3}$

- Stationary underlying plasma parameters: shape, temperature, density, energy

- Identical power deposition location if more than one X2 launcher are used

- Stationary heating scheme parameters, apart from linear scans in power or launcher angle

- Phase long enough for statistics to be representative

- Avoidance of time intervals where the ELM behaviour is anomalous with respect to other phases having identical operation parameters

This selection results in a database comprising 208 ELM phases with an average of 49 ± 31 and a median of 44 ELMs per phase, ranging from 11 to 289 ELMs per phase.

3.3 ELM control by plasma edge ECRH

3.3.1 Introduction

This section demonstrates how ELM control is achieved in TCV by applying ECRH in the plasma edge (i.e. in the pressure pedestal region). More specifically, it shows that, in our experimental conditions, the ELM frequency increases by a factor 2 and that the ELM energy loss decreases in the same proportion when the power deposition location is scanned from well inside the pedestal to the plasma boundary, an effect that is independent of the total input power. Since ECRH power is more poorly absorbed in the plasma edge, this behaviour is opposite to that expected from power scaling alone and must therefore be imputed to an unknown physics mechanism. Evidence ruling out variations in the underlying plasma parameters as the cause of the ELM modification is also presented. The degree of robustness of ELM control within a range of input power is documented, thus laying the foundation for the practical employment of this technique as a control tool. It is also important to stress that the standard assumption for ITER type I ELMing H-mode predictions is that neither the heating method nor the deposition location is important with respect to the H-mode physics [26]. The results presented here challenge this assumption and new experiments will be required in order to validate the scaling laws predicting the ELM behaviour in ITER.

Figure 3.3: (a) X2 launcher angle θ_l and location of the maximum of the X2 absorbed power density $\rho_{\psi,\max}(X2)$; (b) absorbed X2 power ($P_{\mathrm{input,X2}} = 510\,\mathrm{kW}$); (c) H_α emission detected by a wide-angle filtered photodiode located at the top of the vessel; (d) ELM frequency; (e) relative plasma energy loss per ELM, as measured by the DML; (f) energy confinement time (ratio of the plasma energy to the total absorbed power); (g) confinement time normalized to the ITER-IPB98(y,2) scaling law [26]; (h) line-averaged electron plasma density. Averages (for the stationary phase) and linear fits (for the angle sweep) are depicted by solid lines.
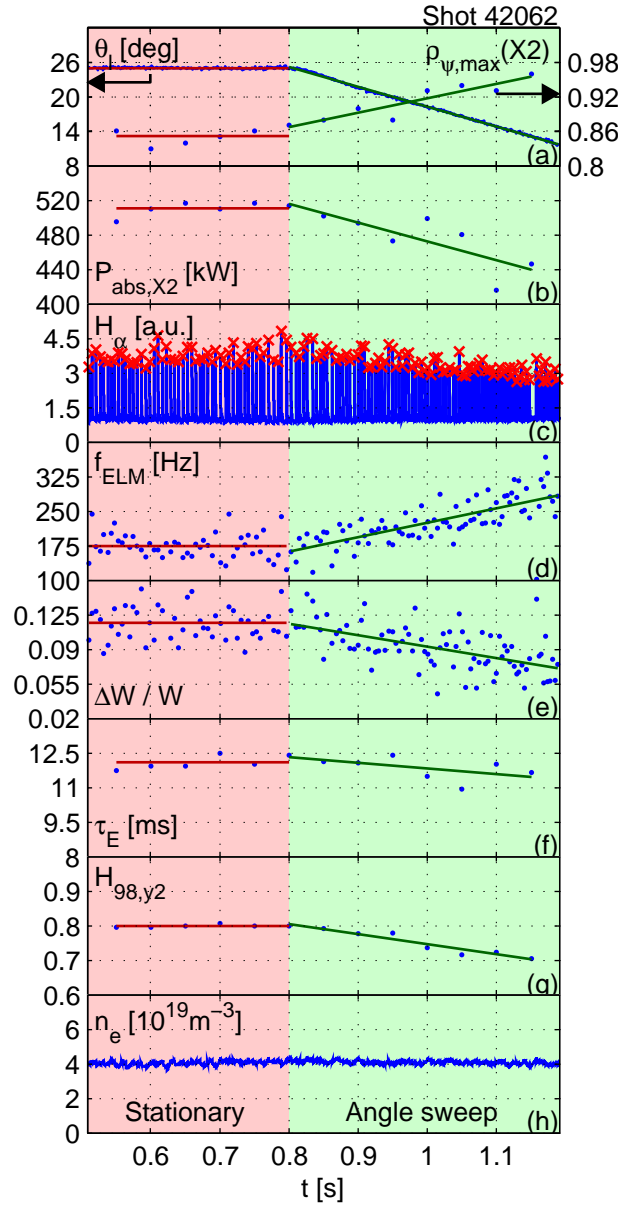
3.3.2 Launcher angle sweep at constant power

The control of ELMs by deposition of ECRH in the plasma edge is demonstrated by figure 3.3. In this shot, the launcher angle θ_l is swept toward the plasma edge at constant input power. The decrease in the absorbed power during the sweep is due to lower temperature and density values toward the edge. The increase in ELM frequency and decrease in their amplitude are visually apparent in figure 3.3(c), showing the typical spike signature of ELMs in H_α radiation from the plasma edge, and quantified by figures 3.3(d) and (e). In the stationary phase, the energy confinement time (figure 3.3(f)) is 20% lower than the value predicted by the standard scaling law (figure 3.3(g)). In comparison, the $H_{98,\mathrm{y2}}$-factor for a similar shot with
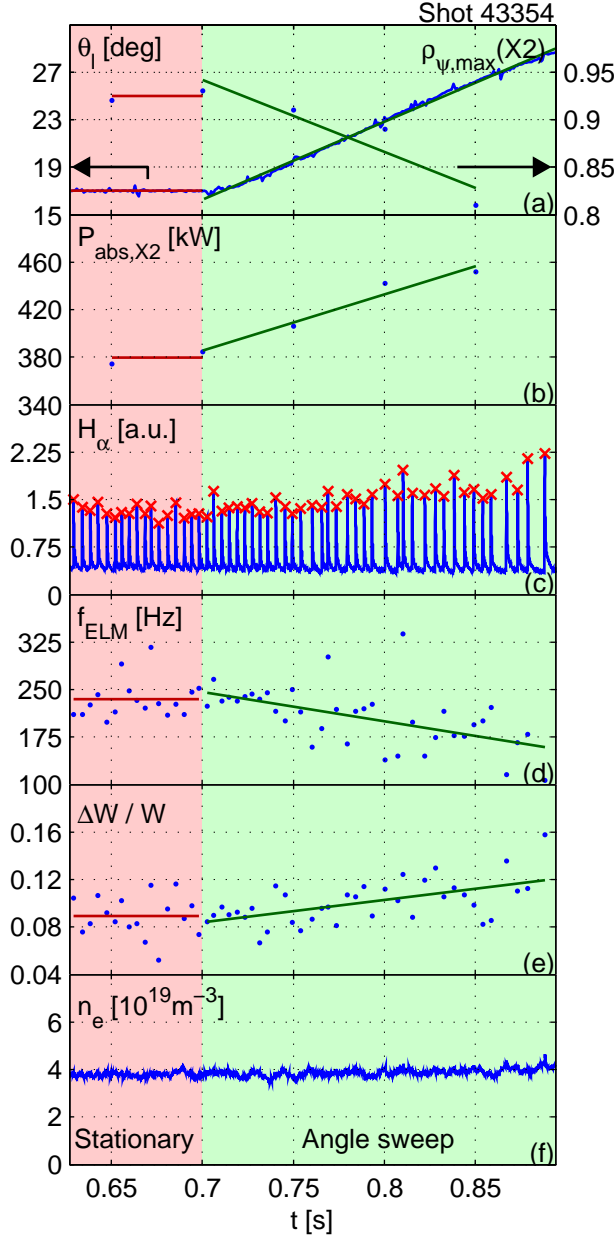
Figure 3.4: (a) X2 launcher angle θ_l and location of the maximum of the X2 absorbed power density $\rho_{\psi,\max}(X2)$; (b) absorbed X2 power ($P_{\text{input,X2}} = 465\,\text{kW}$); (c) H_α emission; (d) ELM frequency; (e) relative plasma energy loss per ELM, as measured by the DML; (f) line-averaged electron plasma density. Averages (for the stationary phase) and linear fits (for the angle sweep) are depicted by solid lines.

no X2 power is approximately 1. As expected, the well-known confinement degradation with power is therefore worsened further as X2 power is deposited close to the edge. Note that the increase of f_{ELM} due to the scan of θ_l does not contribute to a significant change in confinement time since ΔW decreases in the same (or larger) proportion. In addition to power, triangularity and density are known to have an effect on the ELM frequency, amplitude and type [72, 75]. Here, the measured line-averaged electron plasma density is entirely stationary, with extrema within 11% of the mean value, as shown in figure 3.3(h), excluding it as a possible cause of the observed change in f_{ELM}. Since the plasma target is kept identical in these experiments, triangularity effects are also excluded.

When sweeping the launcher angle inward, the results are similar to those obtained for outward sweeps, as shown in figure 3.4. This absence of hysteresis suggests that f_{ELM} and ΔW purely depend on θ_l and $P_{\text{input,X2}}$, with no dependence on the history of the plasma.

3.3.3 ELM and plasma parameters as functions of power and launcher angle

3.3.3.1 Results and discussion

The ELM frequency and relative energy loss are plotted in figure 3.5 as functions of X2 input power and launcher angle (or, equivalently, deposition radius; this is indicated by a color code), all other parameters being kept constant. Reference points with no X2 power are also shown. Figure 3.5(a) clearly confirms the increase of f_{ELM} as the X2 beam is moved outward, as well as the type I nature of the ELMs. The increase of f_{ELM} appears as a change of slope in the dependence on the input power and not as a constant offset.

The decrease of $\Delta W/W$ when the X2 beam is moved outward is also confirmed (figure 3.5(b)), although the statistical deviations are larger. Contrary to the ELM frequency, the variation of $\Delta W/W$ with X2 input power appears to saturate above a certain power threshold. ΔW and W are shown separately in figure 3.6. Identical results are found for ΔW and $\Delta W/W$, even though the relative reduction as a function of launcher angle is slightly larger for the former (~ 2.5). W suffers a loss of 20-30% when the power deposition location is scanned toward the plasma separatrix. The fact that ECRH power absorption decreases toward the edge is not sufficient to account for this loss, and the degradation of the confinement of power deposited further away from the core must be invoked.

The average power lost through ELMs, $P_{\text{ELM}} = f_{\text{ELM}}\Delta W$, is plotted in figure 3.7. The observed linear dependence of P_{ELM} on P_{input}, with $P_{\text{ELM}} \simeq 0.25 P_{\text{abs,X2+X3}}$, is consistent with the ASDEX Upgrade results [22]. The dependence of P_{ELM} on θ_l is more ambiguous. Although data would suggest that P_{ELM} slightly decreases with θ_l, accounting for the lower power absorption at higher θ_l would lead to a realignment of the low θ_l points on the $P_{\text{ELM}}(P_{\text{abs,X2+X3}})$ line and suggest that P_{ELM} is independent of θ_l.

For the sake of completeness, the line-averaged electron plasma density and the estimated core electron temperature are given in figure 3.8. The small scattering present in figure 3.8(a) (standard deviation of less than 10%) confirms the adequacy
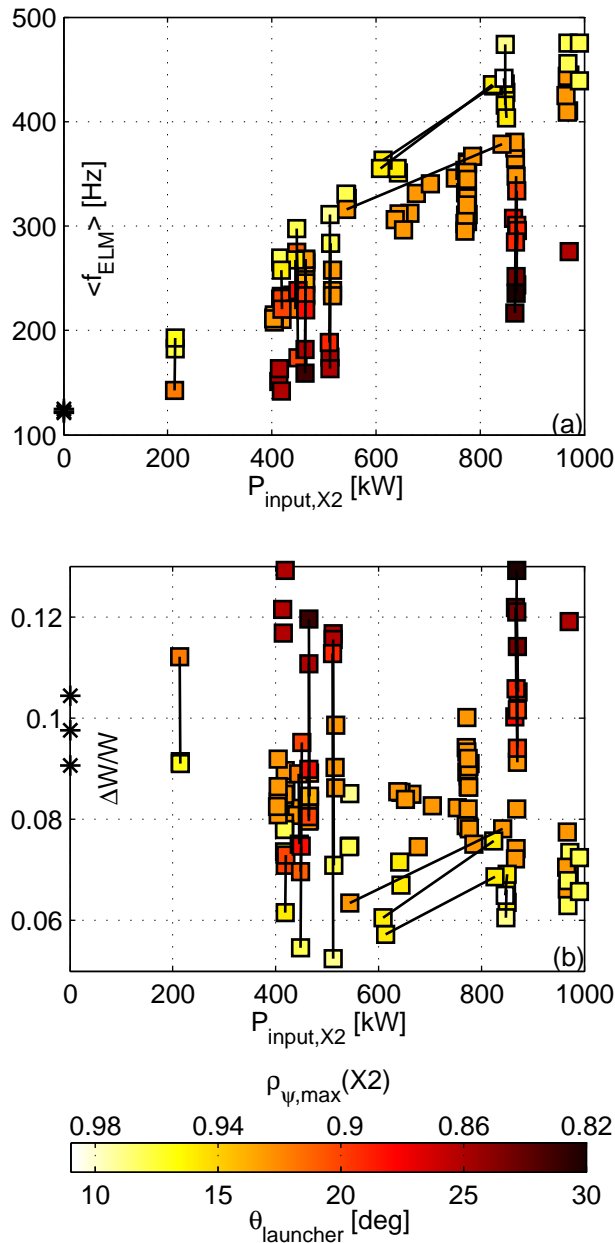
Figure 3.5: Statistics of (a) ELM frequency and (b) relative plasma energy loss per ELM (measured by the DML) as functions of X2 input power and launcher angle. The solid lines denote linear fits over power or angle scans, whereas the unconnected points are averages over stationary phases. Stars indicate values obtained for shots with no X2 power. The mapping between $\rho_{\psi,\max}(X2)$ and θ_l is obtained from the fits in figure 3.3(a).

(a) Energy loss per ELM
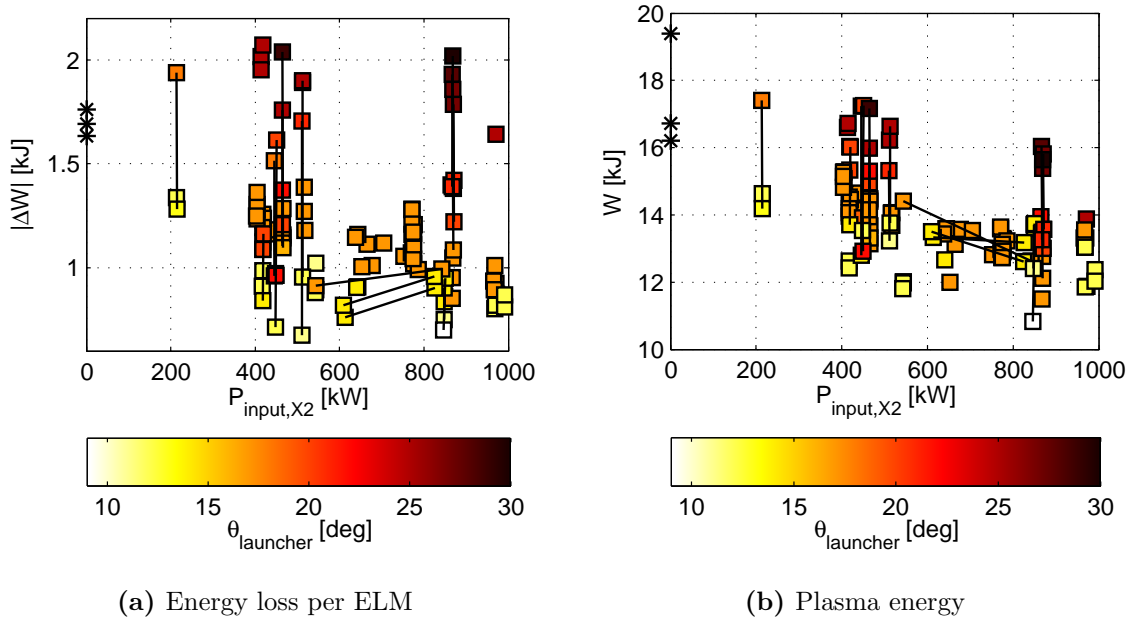
(b) Plasma energy

Figure 3.6: Statistics of (a) absolute energy loss per ELM (measured by the DML) and (b) total plasma energy as functions of X2 input power and launcher angle. The solid lines denote linear fits over power or angle scans, whereas the unconnected points are averages over stationary phases. Stars indicate values obtained for shots with no X2 power.
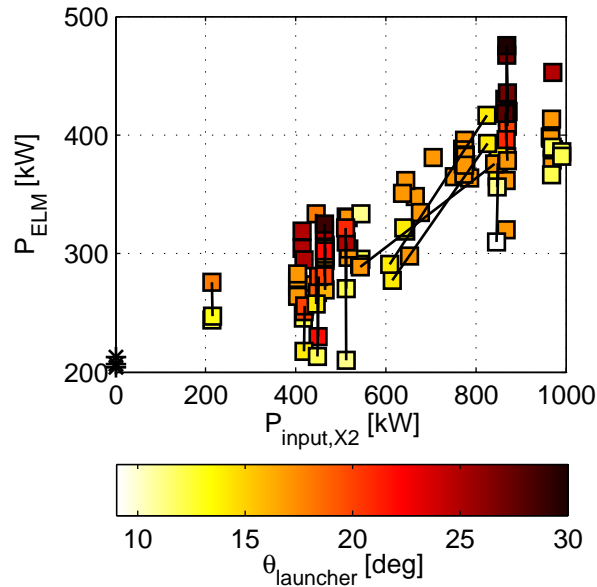
Figure 3.7: Statistics of $P_{\mathrm{ELM}} = f_{\mathrm{ELM}}\Delta W$, the average power lost through ELMs, as a function of X2 input power and launcher angle. The solid lines denote linear fits over power or angle scans, whereas the unconnected points are averages over stationary phases. Stars indicate values obtained for shots with no X2 power.

(a) Electron density   **(b)** Electron temperature
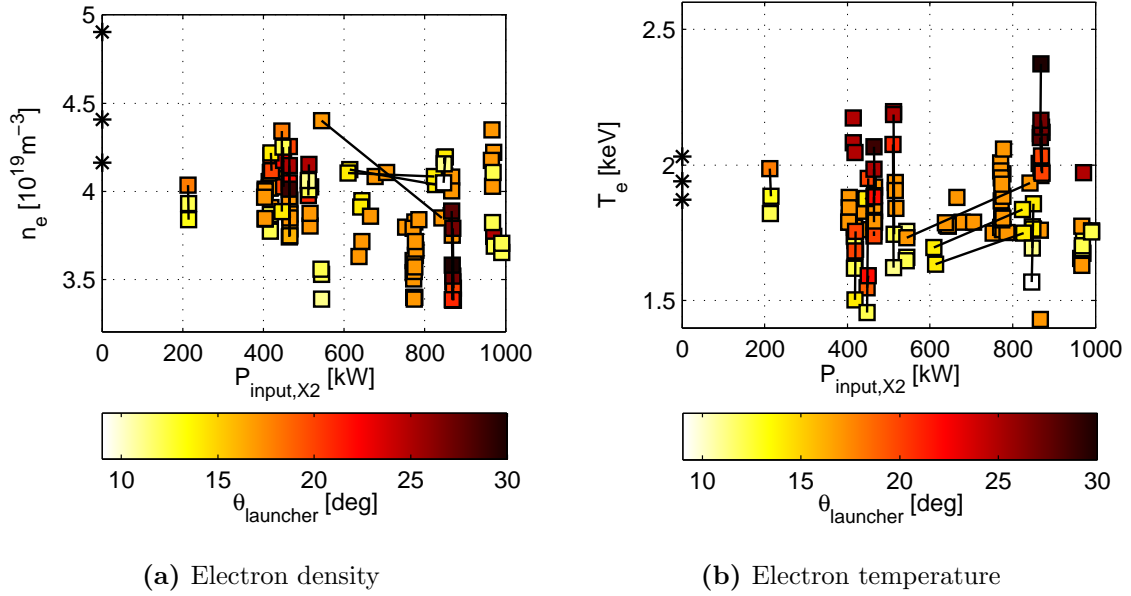
Figure 3.8: Statistics of (a) line-averaged electron plasma density, measured by the FIR, and (b) core electron temperature, estimated with the 2-filter method applied to x-ray emission measurements, as functions of X2 input power and launcher angle. The solid lines denote linear fits over power or angle scans, whereas the unconnected points are averages over stationary phases. Stars indicate values obtained for shots with no X2 power.

of the ELM phase selection procedure. Since these experiments are performed with feedback control of the density, dependencies of n_e on $P_{\text{input,X2}}$ or θ_l are not observable. In practice, density drops when f_{ELM} increases and gas injection is necessary to compensate this loss. The dependence of temperature on θ_l (figure 3.8(b)) is consistent with that observed for W, with the same loss of 20-30% across the angle scan. The similarities between the dependences of temperature and energy on power are not as clear, but the density contribution must be also taken into account. This explains, for example, the opposite trends in the case of the power scan between 540 and 840 kW at $\theta_l = 17°$.

3.3.3.2   Interpretation

The increase of f_{ELM} and decrease of ΔW as the X2 beam moves toward the plasma separatrix are contrary to the documented behaviour of type I ELMs. Indeed, when the beam moves, the fraction of absorbed X2 power decreases and the pedestal pressure gradient should grow less rapidly after an ELM. As the time required for the gradient to reach the kink-ballooning instability threshold increases, f_{ELM} should decrease, contrary to observations. In general, an increase in ELM frequency can be attributed either to a faster evolution of the pedestal to the same instability

threshold or to the triggering of kink-ballooning modes having a different dominant wavenumber, with an intrinsically shorter time cycle. In the former case, it could be expected that ΔW remains constant, as seen in the case of power scans; therefore a variation in ΔW, as observed in the angle scans (figure 3.5(b)), would rather suggest the latter explanation. The triggering of different unstable modes can only be the result of a different time evolution of the pedestal parameters (pressure and current density), which in turn would also be consistent with a change in power deposition location thanks to a finite energy diffusion time effect. The evolution of the edge current density might, for example, also be modified due to a lower local resistivity in the early phase of the ELM cycle. These conjectures may guide the theoretical work that will be required to interpret the challenging and counter-intuitive results obtained for the ELM frequency and amplitude as functions of power deposition location. Finally, even though the $q = 2$ surface, which is often associated with strong resonant MHD instabilities, is in the region heated by the X2 beam ($\rho_\psi(q = 2) = 0.95$, i.e. at 90% of the poloidal flux), no changes are observed during the angle scan in the MHD activity detected by magnetic probes. Such modes can thus be safely ruled out as an explanation for the ELM modification.

3.3.4   Summary of the ELM control experiments

ECRH has been applied to the edge of type I ELMing H-mode plasmas in TCV. Power and deposition location scans have been performed. These experiments show that the ELM frequency increases and the relative plasma energy loss per ELM decreases significantly when the ECRH beam is moved in the pressure pedestal region toward the plasma separatrix, an effect that is independent of the total input power. This result is opposite to the expected one for type I ELMs, since the absorbed power progressively decreases when approaching the separatrix, and constitutes a promising tool for ELM control and mitigation in reactor-relevant scenarios. Note that the current experimental setup does not allow one to study the dependence of the ELM parameters on θ_l for values exceeding 25-30°. It is nonetheless expected that the observed effects saturate as the X2 beam reaches the core region of the plasma. Finally, the results presented here contradict the preliminary DIII-D results, but the heating scheme used to obtain those results did not lead at that time to a clear determination of the exact power deposition location. Their relevance is therefore debatable.

3.4 ELM pacing by modulated ECRH

3.4.1 Introduction

ELM pacing, understood here as a stabilization of the ELM frequency around a controlled average value, is of interest for a number of reasons: ELM pacing might be used to avoid very large excursions in ΔW; the success and limitations of a particular method are important sources of information for understanding the ELM cycle and constraining an *ad hoc* model; regular ELMs facilitate the interpretation of experimental results obtained by statistical approaches like the conditional average sampling method; finally, ELM pacing is the first step toward an accurate control of ELM timing, which might be used to trigger the measurement of plasma parameters at specific times in the ELM cycle.

The preliminary results from ASDEX Upgrade [43] suggest that it is possible to pace the ELMs by applying modulated ECRH power to the edge of an ELMing plasma. These results motivate a more thorough experimental investigation of the limits of this control method. In particular, it must be determined whether the ELM frequency can be driven, and ultimately increased, by delivering a fixed amount of energy in a short pulse. If successful, this pacing method would imply that power modulation in itself acts as an ELM trigger, similar to a "kick" effect induced by a fast power rise and physically understood as a rapid and large local increase of the temperature gradient triggering the ELMs.

While demonstrating a successful ELM pacing technique by ECRH power modulation, this section also shows that the ELM frequency purely remains a function of the average input power over the ELM cycle (at constant launcher angle) and that power modulation only has a stabilization effect, consequently ruling out the "kick effect" interpretation of the ASDEX Upgrade results. More specifically, section 3.4.2 describes how ELM pacing is achieved using power modulation synchronized in real time with the ELM cycle, including a succinct study of the robustness of the control as a function of the power deposition location. Section 3.4.3 demonstrates how inverting the phase of the power modulation in the ELM cycle maintains the same dependence of the ELM frequency on the average power, while increasing significantly the standard deviation of the ELM period. Finally, section 3.4.4 details a set of feed-forward power modulation experiments, whose main results are that the ELMs lock to the modulation cycle only at their natural frequency (i.e. their frequency at the equivalent stationary input power) and that the resulting locking is less robust than the real-time one.
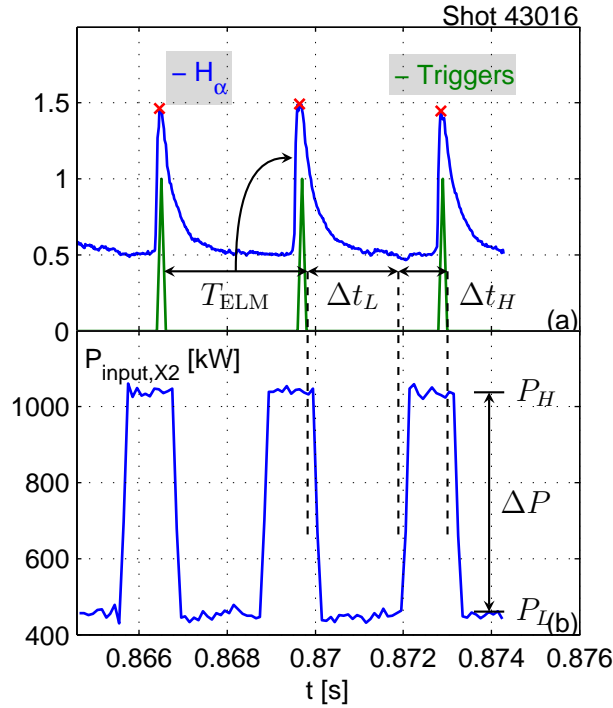
Figure 3.9: Real-time control scheme used in the ELM pacing experiments. (a) H_α emission. Resulting ELM times, determined by the control system, are used as triggers for the power modulation. The crosses mark the peaks of the H_α signal. The ELM period, T_{ELM}, and the ELM to which it is assigned are indicated. (b) X2 input power. The power is modulated between P_L and P_H. The ELMs trigger a low power phase of controlled duration Δt_L, followed by a high power phase of duration Δt_H which lasts until the next ELM.

3.4.2   ELM pacing by real-time controlled power modulation

3.4.2.1   Real-time control scheme

The real-time control experiments are performed with the SCD (real-time control system described in section 2.4.4), using the H_α signal as input and the X2 power as actuator. The real-time control scheme is illustrated in figure 3.9. X2 power is modulated between two power levels, $\Delta P = P_H - P_L$. The modulation is synchronized in real-time with the ELM cycle, each ELM triggering a low power phase when the time derivative of the H_α signal crosses a pre-defined threshold. The duration of the low power phase, Δt_L, is the controlled parameter, while the duration of the high power phase, Δt_H, is a free parameter, self-determined by the plasma.

In feed-forward mode, Δt_L is set *a priori*, irrespectively of the plasma response[†]. This scheme will be referred to as the ff-RT scheme. In feed-back mode, Δt_L is determined in real-time by a control algorithm that adjusts the value of Δt_L until a predefined value of f_{ELM} is reached. This scheme will be referred to as the fb-RT scheme. Its control law for Δt_L is written in terms of the ELM period as:

$$\Delta t_{L,k} = \Delta t_{L,k-1} + K_i(T_{\text{ref}} - T_{\text{ELM,k-1}}) + \Delta t_{L,ff,k} - \Delta t_{L,ff,k-1} \qquad (3.2)$$

where k is the current ELM cycle index, K_i the integral gain, T_{ref} the reference ELM period, $T_{\text{ELM,k-1}}$ the ELM period of the last ELM cycle and $\Delta t_{L,ff}$ a pre-programmed feed-forward value. This control law is of integral type, Δt_L being incremented proportionally to the error. The cycle time of the control loop varies from 0.1 to 0.02 ms across the experiments [‡].

3.4.2.2 Real-time control results

This section describes the results of the real-time ELM pacing experiments. In particular, it shows that ELM pacing is successfully achieved by real-time controlled power modulation. In optimal cases, a standard deviation of the ELM period of less than 0.1 ms and a minimal relative deviation of 2.4% are achieved. The control of the ELM frequency in fb-RT mode is also demonstrated. Using an advanced heating scenario where Δt_L is varied "randomly" from ELM to ELM, it is shown that ELMs are individually controllable, proving that history only has a weak effect on the ELMs. A statistical analysis demonstrates that the dependence of the ELM frequency on the average input power in RT mode is identical, within error bars, to that in stationary mode. This fact is then illustrated in two particular plasma discharges, confirming that while the power modulation is necessary to pace the

---

[†] In this chapter, two different heating schemes are referred to as "feed-forward": the real-time controlled power modulation scheme with Δt_L set *a priori* (and thus in feed-forward), and the feed-forward power modulation scheme where the power time trace is entirely set *a priori*. The acronyms ff and FF are used, respectively, for the former and the latter cases. This should prevent any confusion.

[‡] In a first series of experiments, the sampling rate of the SCD was not optimized and the cycle time was limited to 0.1 ms. This limit has then been decreased to 0.02 ms by grouping all the real-time processes on a single real-time node. This setup modification did not result in significant changes of the ELM pacing properties. Further analysis (see below) revealed that the parameter controlling the ELM pacing efficiency is the instantaneous power at the ELM time. A small delay in the synchronization has therefore no importance as long as the power level at which ELMs occur is controlled.

Figure 3.10: Real-time control experiment in feed-forward mode with X2 power modulated in $[400,1000]$ kW. (a) H_α emission, with peaks marked by crosses, and corresponding real-time control triggers; (b) X2 input power ($\theta_l = 17°$): stationary phase followed by three ff-RT phases, with $\Delta t_L = 2.5$ ms, $\Delta t_L = 2$ ms and $\Delta t_L = 1.5$ ms respectively; (c) ELM period T_{ELM} and low power phase duration Δt_L (relevant to RT phases only); (d) ELM frequency f_{ELM}. In (b) and (d), solid lines depict averages over the respective phases.
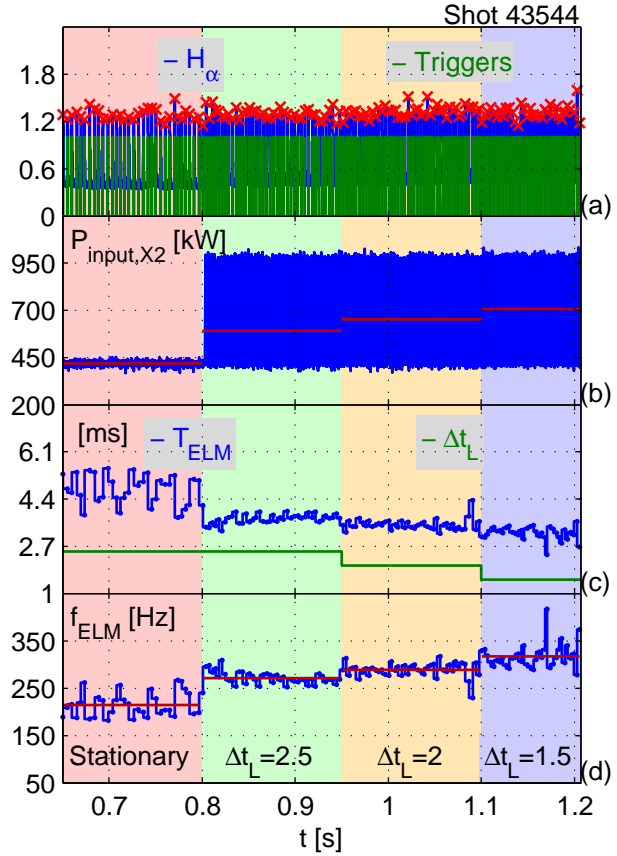
ELMs, the actual ELM frequency is only determined by the average input power (at constant launcher angle). By studying the dependence of the standard deviation of the ELM period on the input power, the ELM pacing by synchronized power modulation is then explained. Finally, it is shown that real-time control has no significant effect on the standard deviation of ΔW, even if very large anomalous excursions of ΔW due to small ELM-free phases might be prevented by it.

Note that for all the results presented in this section, a constant intermediate launcher angle $\theta_l = 17°$ has been chosen.

Feed-forward real-time control Figure 3.10 shows the results obtained for a step-scan of Δt_L in ff-RT mode, using X2 power modulation in the range 0.4-1 MW after a phase of stationary power. When comparing the stationary heating phase with the ff-RT phases, the stabilization of the ELM period T_{ELM}, figure 3.10(c), by the real-time controlled modulated power is patent, even if T_{ELM} still undergoes a few medium-size excursions for smaller values of Δt_L. In addition, each value of Δt_L (figure 3.10(c)) corresponds to a value of f_{ELM} (figure 3.10(d)) and $\langle P_{\mathrm{input,X2}} \rangle$ (figure 3.10(b)), with a monotonic dependence. Similar conclusions can be drawn from figure 3.11, where X2 power modulation is, this time, in the range 0-1 MW,
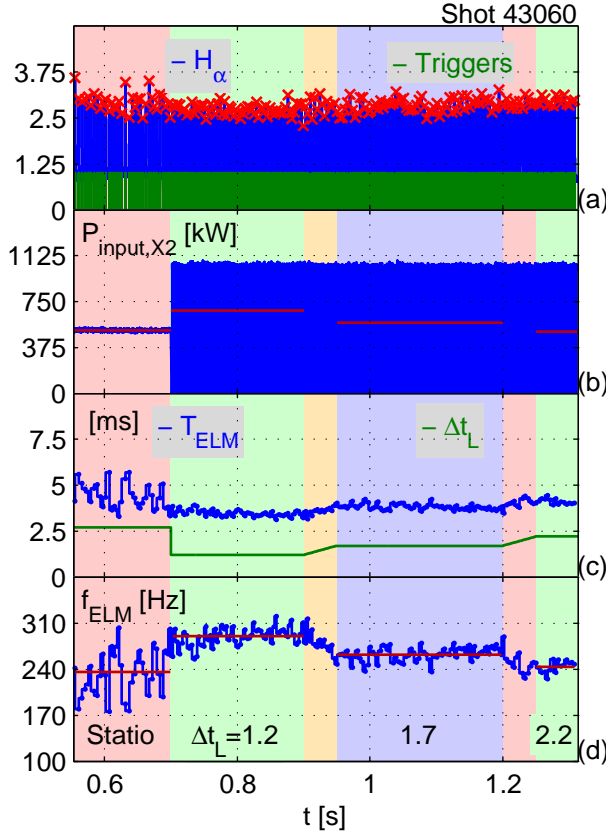
Figure 3.11: Real-time control experiment in feed-forward mode with X2 power modulated in $[0,1000]$ kW. (a) H_α emission, with peaks marked by crosses, and corresponding real-time control triggers; (b) X2 input power ($\theta_l = 17°$): stationary phase followed by three ff-RT phases, with $\Delta t_L = 1.2$ ms, $\Delta t_L = 1.7$ ms and $\Delta t_L = 2.2$ ms respectively, including two short transition phases; (c) ELM period T_{ELM} and low power phase duration Δt_L (relevant to RT phases only); (d) ELM frequency f_{ELM}. In (b) and (d), solid lines depict averages over the respective phases.

after a phase of stationary heating. The observed bijective relation between Δt_L and f_{ELM} is exploited for the real-time control of the ELM frequency described below.

Feed-back real-time control   Figures 3.12 and 3.13 show the results obtained for step-scans of the reference ELM frequency f_{ref} in fb-RT mode, using X2 power modulation in the range 0.4-1 MW between two phases of ff-RT mode and after a stationary heating phase, respectively. The real-time adjustment of Δt_L (figures 3.12(c) and 3.13(c)) by the control algorithm to reach the planned ELM frequency in each phase is effective, as demonstrated by figures 3.12(d) and 3.13(d). Δt_L is therefore a good control parameter for obtaining a desired ELM frequency, as long as the inequality $f_{\mathrm{ELM}}(P_L) < f_{\mathrm{ref}} < f_{\mathrm{ELM}}(P_H)$ holds. In figure 3.12(c), T_{ELM} appears to vary more at low values of Δt_L, as previously observed in figure 3.10(c). Since this phenomenon is not reproduced in figure 3.13(c), a statistical analysis is required to have a clearer understanding of this matter. Similarly to the feed-forward case, the bijective relation between f_{ELM} and $\langle P_{\mathrm{input,X2}} \rangle$ remains.

Real-time control using "random" Δt_L   In this experiment, the X2 power is in ff-RT mode, but instead of keeping Δt_L constant over a time interval, Δt_L is

Figure 3.12: Real-time control experiment in feed-back mode. (a) H_α emission, with peaks marked by crosses, and corresponding real-time control triggers; (b) X2 input power ($\theta_l = 17°$), consisting of three fb-RT phases, with $f_{\text{ref}} = 310\,\text{Hz}$, $f_{\text{ref}} = 369\,\text{Hz}$ and $f_{\text{ref}} = 348\,\text{Hz}$ respectively, preceded and followed by two ff-RT phases having $\Delta t_L = 2\,\text{ms}$; (c) ELM period T_{ELM} and low power phase duration Δt_L; (d) ELM frequency f_{ELM} and reference ELM frequency f_{ref} (relevant to fb-RT phases only). In (b), solid lines depict averages over the respective phases. *Note:* the choice of frequency is musically relevant.
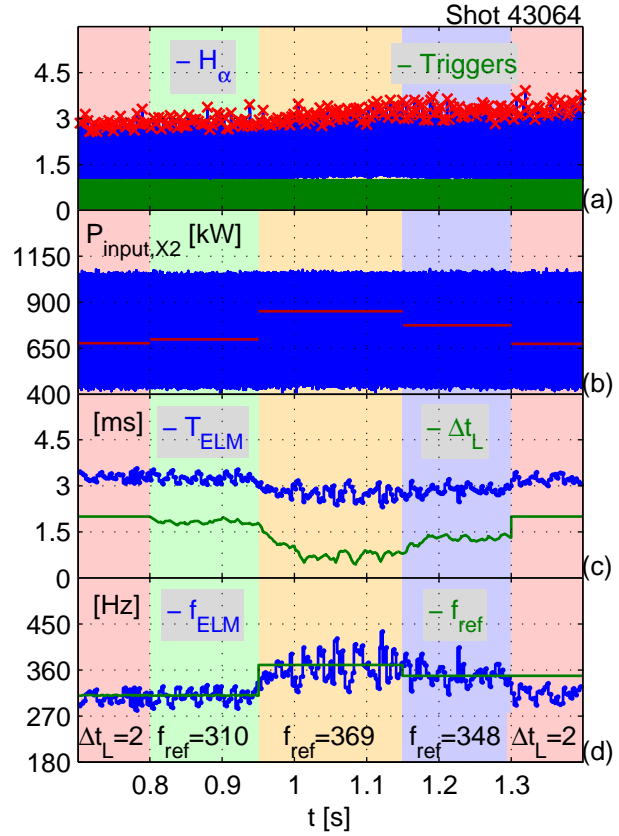
Figure 3.13: Real-time control experiment in feed-back mode (bis). (a) H_α emission, with peaks marked by crosses, and corresponding real-time control triggers; (b) X2 input power ($\theta_l = 17°$): stationary phase followed by four fb-RT phases, with $f_{\text{ref}} = 300\,\text{Hz}$, $f_{\text{ref}} = 337\,\text{Hz}$, $f_{\text{ref}} = 378\,\text{Hz}$ and $f_{\text{ref}} = 300\,\text{Hz}$ respectively; (c) ELM period T_{ELM} and low power phase duration Δt_L (relevant to RT phases only); (d) ELM frequency f_{ELM} and reference ELM frequency f_{ref} (relevant to fb-RT phases only). In (b), solid lines depict averages over the respective phases. *Note:* the choice of frequency is musically relevant.
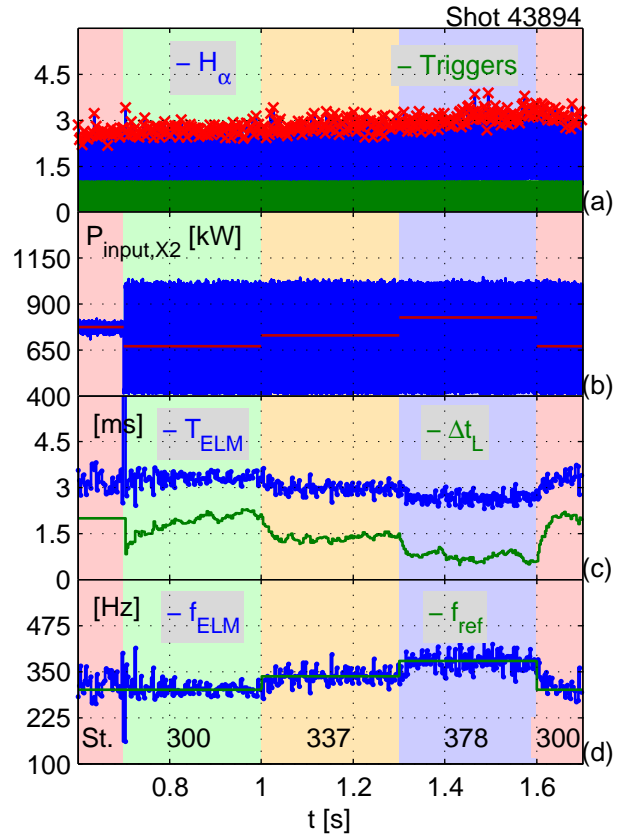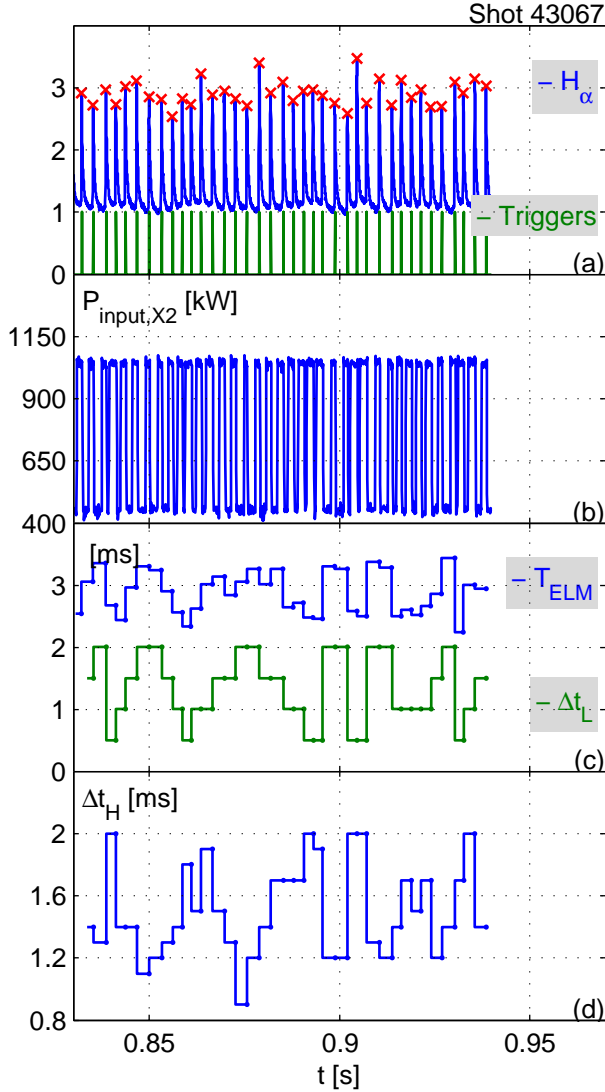
Figure 3.14: Real-time control experiment using random values of Δt_L. (a) H_α emission, with peaks marked by crosses, and corresponding real-time control triggers; (b) X2 input power ($\theta_l = 17°$): ff-RT phase, Δt_L being assigned another value, "randomly" taken from the set $\{0.5, 1, 1.5, 2\}$ ms, after each ELM; (c) ELM period T_{ELM} and low power phase duration Δt_L; (d) high power phase duration Δt_H.

assigned another value after each ELM. These values are taken "randomly" within the set $\{0.5, 1, 1.5, 2\}$ ms. A constant ELM period in this experiment would mean that the power averaged over several ELM cycles is decisive for the determination of the ELM period, therefore indicating that ELMs are sensitive to events preceding their own cycle, referred here as a history effect. On the contrary, an ELM period following the power averaged over the individual ELM cycles would mean that only the power injected during the own cycle of an ELM is decisive for the determination of its period, therefore indicating that ELMs are not (or weakly) sensitive to history. The results of this experiment, presented in figure 3.14, appear to favor the latter interpretation, since T_{ELM} follows Δt_L with little effect of history. The important fact that the ELM period can be set individually for each ELM is hence experimentally demonstrated. In the past [76, 77], deterministic chaotic behaviour in type III ELM time series was reported. According to these studies, a chaotic behaviour is
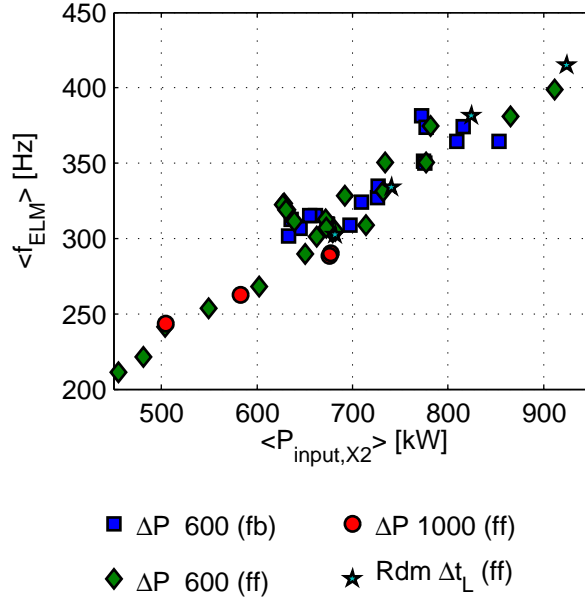
Figure 3.15: ELM frequency versus average X2 input power in fb-RT mode with $(P_L, P_H) = (400, 1000)$ kW (squares), in ff-RT mode with $(P_L, P_H) = (400, 1000)$ kW (diamonds), in random Δt_L ff-RT mode $(P_L, P_H) = (400, 1000)$ kW (using CAS analysis, indicated by stars) and in ff-RT mode with $(P_L, P_H) = (0, 1000)$ kW. $\theta_l = 17°$.

observable on the deviation of groups of consecutive ELM periods from their average, proving that short-lived time correlation of the ELMs exists. Note however that the arguments published in [76, 77] for type III ELMs have not been confirmed for type I ELMs. At any rate, the two results do not necessarily contradict each other. Indeed, while the average period of the ELMs is only determined by the average of the input power over their cycle, the standard deviation of this period remains finite and the presence of a higher order time correlation between ELMs is not excluded. The real-time synchronized power modulation, by strongly reducing this standard deviation, decreases further the experimental footprint of the time correlation of the ELMs. To summarize, the experiments presented here demonstrate that the ELM period depends predominantly on the input power injected during the ELM cycle, without excluding a weak, short-lived, time correlation of the ELMs.

Since the values of Δt_L are taken out of a small set of values, a CAS (Conditional Average Sampling) analysis of each corresponding class of ELMs from this plasma discharge is appropriate. The classes represent respectively $\{53, 88, 59, 79\}$ ELMs and this analysis is therefore statistically sound. The results of this analysis are labelled "Rdm Δt_L (ff)" in the figures and are compared below to other real-time control results.
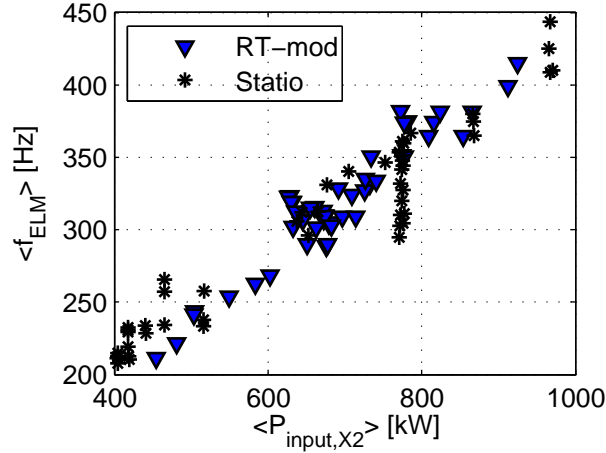
Figure 3.16: ELM frequency versus average X2 input power, in stationary heating mode (stars) and in RT mode (triangles), including ff-RT, fb-RT and random Δt_L control schemes. $\theta_l = 17°$.

Dependence of f_{ELM} on $\langle P \rangle$ in RT mode A statistics of the ELM frequency as a function of input power in all the RT modes covered so far is presented in figure 3.15. Note that, apart from random Δt_L cases, the average power is calculated over the whole phases, not over individual ELM cycles. The most important observation is the conservation of a linear dependence of f_{ELM} on $\langle P_{\text{input,X2}} \rangle$, suggesting that the energy input rather than the modulation determines the ELM frequency. Of course, a comparison with stationary cases must be done to further establish this point. While the alignment of ff-RT and fb-RT data for identical values of ΔP is not surprising, the alignment of $\Delta P = 1000\,\text{kW}$ data with data from other heating schemes is comforting. Indeed, this particular scheme has no X2 power in the low power phase $((P_L, P_H) = (0, 1000)\,\text{kW})$ and the dependence of f_{ELM} on θ_l might have discriminated these points from the others. Another important result presented in this figure is the excellent agreement of the points obtained by CAS analysis of the random Δt_L discharge with data from other heating schemes. Such an agreement is a compelling evidence of the weak sensitivity of ELMs to history and the success of individual ELM control in the random Δt_L experiment. Should it be otherwise, a flattening of the $f_{\text{ELM}}(\langle P_{\text{input,X2}} \rangle)$ curve passing by these particular points would indeed be observed thanks to an averaging of the ELM frequency between classes of ELMs having different values of Δt_L.

ELM frequency versus power in RT and stationary mode A statistics of the ELM frequency as a function of input power, with and without real-time control, is presented in figure 3.16. Taking into account the data scattering, the linear dependence of f_{ELM} on $\langle P \rangle$ not only remains true in RT mode, but remains identical

Figure 3.17: Evolution of ELM parameters for real-time controlled and equivalent stationary heating. (a) H_α emission, with peaks marked by crosses, and corresponding real-time control triggers. (b) X2 input power ($\theta_l = 17°$), in five consecutive phases: first in stationary mode, then in ff-RT mode with $\Delta t_L = 2\,\text{ms}$, followed by a stationary phase whose power level is determined in real-time to equal the average power of the previous phase. Both phases are then repeated using $\Delta t_L = 1\,\text{ms}$. (c) ELM period T_{ELM} and low power phase duration Δt_L (relevant to RT phases only). (d) ELM frequency f_{ELM}. In (b) and (d), solid lines depict averages over the respective phases.
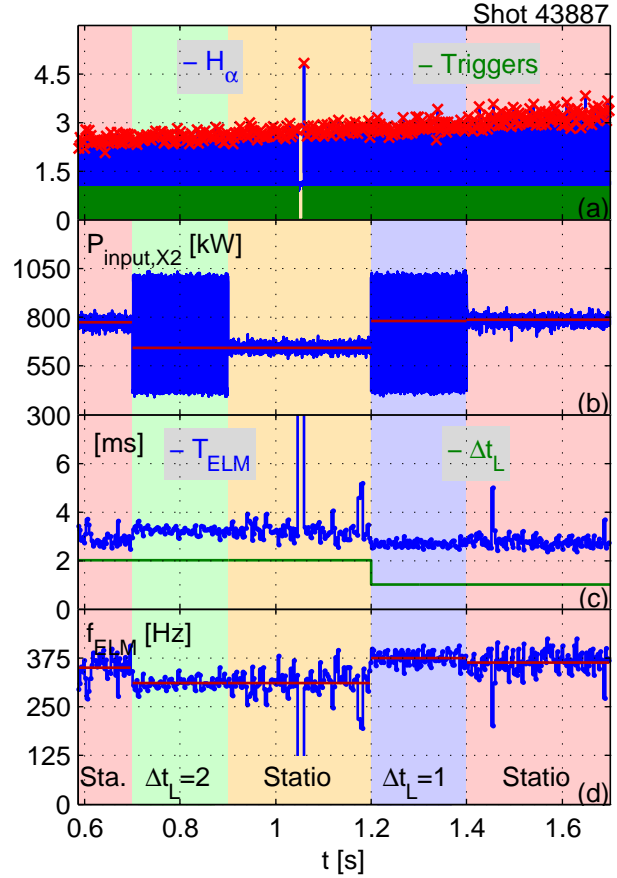
to the dependence measured in stationary mode. This important result is illustrated in two particular plasma discharges using yet another application of real-time power control. In the first discharge (figure 3.17), a phase of ff-RT heating is followed by a phase of stationary heating, using a power level determined in real-time to equal the average power of the ff-RT phase. Both phases are then repeated using a lower value of Δt_L (i.e. a larger power). As expected, for both pairs of phases, a constant average power leads to insignificant changes in ELM frequency when passing from a RT phase to a stationary phase. As before, the control system efficiently stabilizes the ELM period in the ff-RT phases. Significantly, in this example the very large excursions of f_{ELM} and their associated large ΔW occurring in stationary mode disappear during the RT phases. In the second discharge (figure 3.18), a phase of fb-RT heating is followed by a phase of continuous heating (no modulation), where the power is adjusted in real-time to reach the same reference ELM frequency as in the previous phase. Both phases are then repeated using a higher value of f_{ref} (i.e. a larger power). The control law (3.2) is also used here, replacing Δt_L by $P_{\text{input,X2}}$ and using a negative gain. While the first discharge aimed at keeping the power constant across phases, the second discharge aims at keeping the ELM frequency
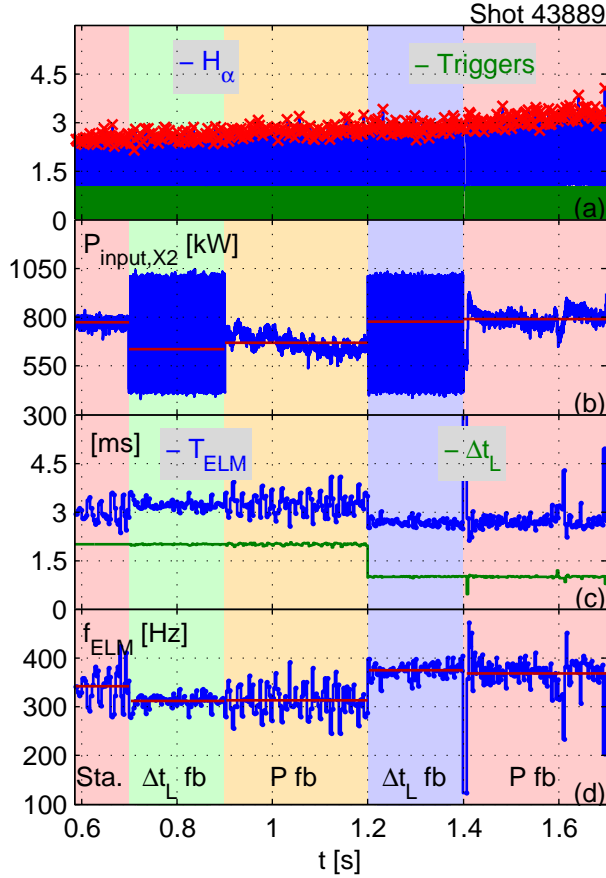
Figure 3.18: Evolution of ELM parameters for real-time controlled frequency with feedback on Δt_L or $P_{X2,input}$. (a) H_α emission, with peaks marked by crosses, and corresponding real-time control triggers. (b) X2 input power ($\theta_l = 17°$), in five consecutive phases: first in stationary mode, then in fb-RT mode with $f_{ref} = 310\,Hz$, followed by a phase with CW but feedback-controlled power level ($f_{ref} = 310\,Hz$). Both phases are then repeated using $f_{ref} = 370\,Hz$. (c) ELM period T_{ELM} and low power phase duration Δt_L (relevant to fb-RT phases only). (d) ELM frequency f_{ELM}. In (b) and (d), solid lines depict averages over the respective phases.

constant. Equivalently, for both pairs of phases, a constant ELM frequency leads to insignificant changes in average power when passing from a RT phase to a stationary phase. It is therefore confirmed that while the power modulation is necessary to pace the ELMs, the actual ELM frequency is only determined by the average input power (at constant launcher angle). Note that in the fb-RT phases of figure 3.18, Δt_L remains rather constant because the ELM period at the chosen feed-forward values was already very close to the reference value.

High power phase duration analysis   In terms of modulated power, an increase of $\langle P \rangle$ corresponds to an increase of the modulation duty cycle. It does not *a priori* mean that Δt_H increases in absolute value, at least for the upper part of the covered range of $\langle P \rangle$. If Δt_H remained constant, the interpretation of the ELM triggering would be affected, even though the results presented above already indicate that the trigger mechanism in RT mode is rather an energy threshold than a kick effect. It is therefore of interest to study the characteristics of the high power phase duration Δt_H. In the random Δt_L experiment, figure 3.14(d) shows that Δt_H follows the evolution of Δt_L, but in the opposite direction. This result is confirmed by figure 3.19
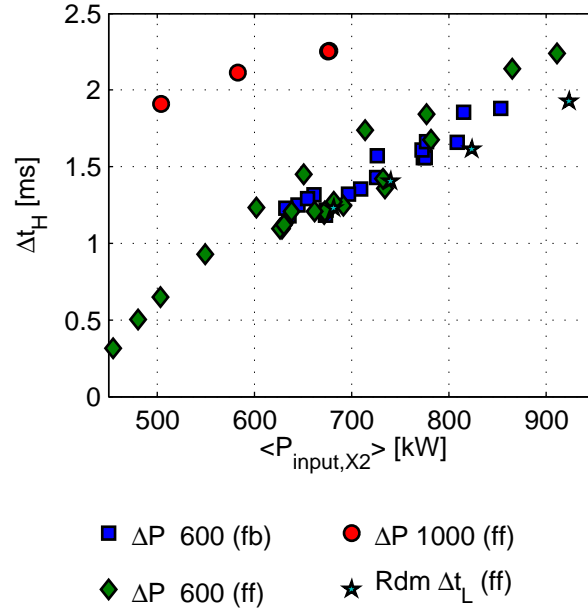
Figure 3.19: High power phase duration versus average X2 input power in fb-RT mode (squares), in ff-RT mode (diamonds), in random Δt_L ff-RT mode (using CAS analysis, indicated by stars) and in ff-RT mode with a modulation in the range [0,1000] kW instead of [400,1000] kW (circles). $\theta_l = 17°$.

where Δt_H is plotted versus $\langle P \rangle$ for all the RT experiments. The increase of Δt_H as Δt_L is decreased implies that the energy lacking from the low power phase needs to be recovered in the high power phase, confirming that the control of f_{ELM} in fb-RT mode is achieved by a real-time tuning of the average X2 input power. The [0,1000] kW ff-RT data also corroborate this statement, Δt_H being much larger than for the standard modulation range cases (i.e. in [400,1000] kW).

It has been previously mentioned that excursions of the ELM period are often observed to be larger for smaller values of Δt_L in RT mode. This effect is studied in figure 3.20 where the standard deviation of the ELM period, σ_T, is plotted versus Δt_H (not Δt_L, to include [0,1000] kW modulation data). Although data scattering is significant and even though the variation is small in absolute value, the increase of σ_T with Δt_H seems real. Since the data scattering about the linear fit line is not too different from the range of σ_T covered by that line, a larger number of data points would nonetheless be preferable to confidently state this conclusion. Note that the lower bound of Δt_H, $\Delta t_{H,\text{min}}$, is not zero, since a minimal finite value is required to ensure that ELMs are all controlled (i.e. all occurring during a high power phase), which is a requirement for a meaningful comparative study. Its upper bound, however, is the smallest ELM period itself, $T_{\text{ELM,min}}$, since there is no difference, in terms of input power at the ELM time, between a phase with stationary full power
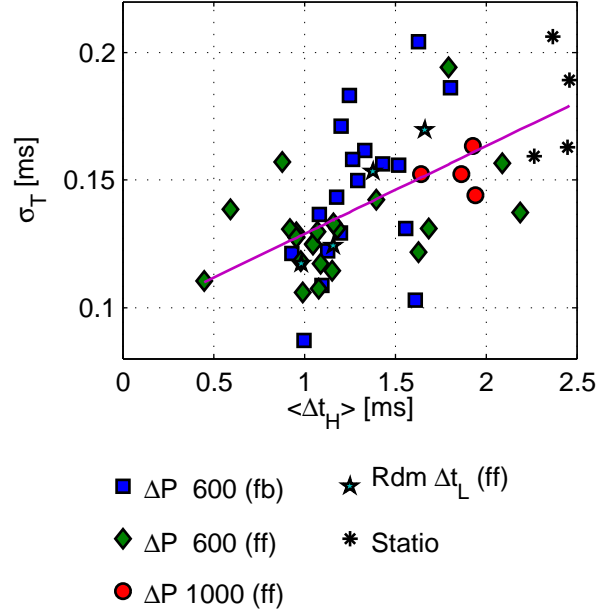
Figure 3.20: Standard deviation of the ELM period versus high power phase duration for X2 input power in fb-RT mode (squares), in ff-RT mode (diamonds), in random Δt_L ff-RT mode (using CAS analysis, indicated by stars) and in ff-RT mode with a modulation in the range $[0,1000]\,\mathrm{kW}$ instead of $[400,1000]\,\mathrm{kW}$ (circles). $1000\,\mathrm{kW}$ stationary phases are plotted with asterisks, Δt_H being equal to T_{ELM} in that case. $\theta_l = 17°$. The solid line depicts a linear fit of the data.

or a phase in RT mode.

ELM period stabilization by real-time control The standard deviation of the ELM period over an ELMing phase, σ_T, is the parameter of choice to assess the efficiency of the ELM pacing provided by the real-time controlled power modulation method. Figure 3.21(a) shows σ_T versus f_{ELM} for X2 input power in stationary and RT mode. It clearly confirms the qualitative assessments made on the time traces discussed above (e.g. figure 3.10(c)), proving that synchronizing the power modulation with the ELM cycle to ensure that ELMs occur during the high power phase is an effective ELM pacing method. In stationary mode, σ_T decreases more than proportionally with f_{ELM} (or, equivalently, input power) (figures 3.21(a) and 3.21(b)). In RT mode, in the range of frequencies where real-time control is effective (i.e. where the inequality $\Delta t_{H,\mathrm{min}} < \Delta t_H < T_{\mathrm{ELM,min}}$ holds), σ_T remains rather constant, with an upper bound given by the value it takes in stationary heating mode at full power, i.e. $\sigma_T(\mathrm{RT}) \lesssim \sigma_T(P_H)$. σ_T reaches a value as low as $0.1\,\mathrm{ms}$ in the best cases. This value remains larger than the limit imposed by the time resolution of the real-time system and is therefore not imposed by technical constraints. When comparing RT to stationary mode results, it is clear that the possible dependence of

(a) Standard deviation of T_{ELM} **(b)** Relative deviation of T_{ELM}
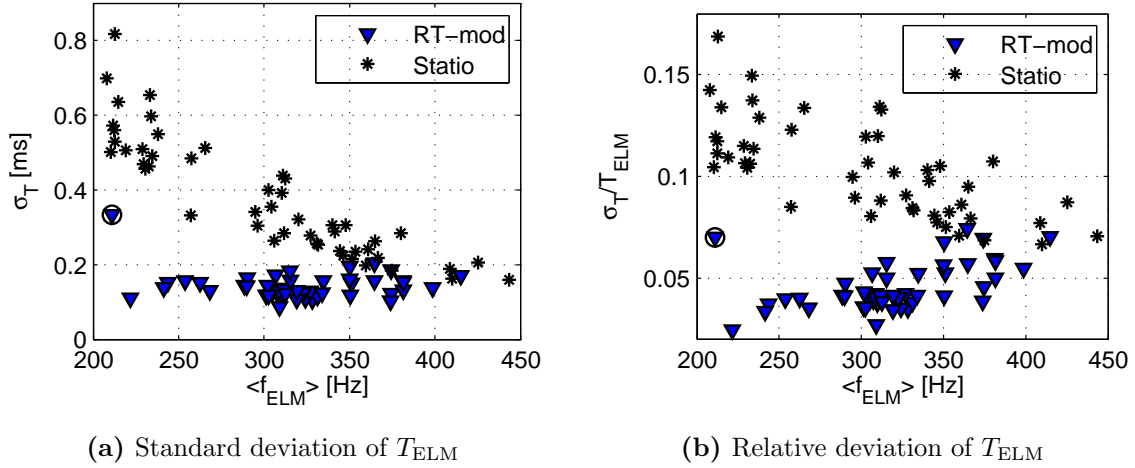
Figure 3.21: Standard (a) and relative (b) deviation of T_{ELM} versus f_{ELM} with X2 input power in stationary heating mode (stars) and in RT mode (triangles), including ff-RT, fb-RT and random Δt_L control schemes. Circled triangles indicate phases where control is only partly effective (Δt_L is at times larger than T_{ELM}). $\theta_l = 17° \pm 1°$.

σ_T on Δt_H discussed in the previous paragraph can be ignored when searching the reasons explaining the success of ELM pacing. Altogether, these arguments suggest that σ_T is predominantly determined by the instantaneous power level at the ELM time. In this perspective, ELM pacing is simply the result of a smart distribution of the input power in the ELM cycle, adjusting Δt_L to set the ELM frequency and delivering the largest available power at the ELM time to reduce σ_T. As long as the power level at the ELM time is controlled, the time resolution of the real-time system is not a limiting factor and the accuracy of the ELM pacing is theoretically only limited by the value of P_H.

ELM amplitude versus ELM frequency in RT and stationary modes In large Tokamaks, such as ITER, the technical requirements for heat flux tolerance are dictated by the energy loss per ELM, rather than their frequency. Moreover, these requirements must account for the variability of the ELM amplitude about its average. It is therefore of interest to inspect whether a reduction of the ELM period variability leads to a reduction of the ELM amplitude variability.

$\Delta W/W$ and its standard deviation are plotted as functions of f_{ELM} for stationary and RT heating in figures 3.22 and 3.23 respectively. As expected, the loss of energy per ELM is identical in both modes. More interestingly, the ELM paced by real-time control show no signs of reduction of the energy loss variability, at least statistically (figure 3.23). Very rare large ELM period events happening in stationary mode, like those appearing on figure 3.17, are indeed not statistically significant, even though
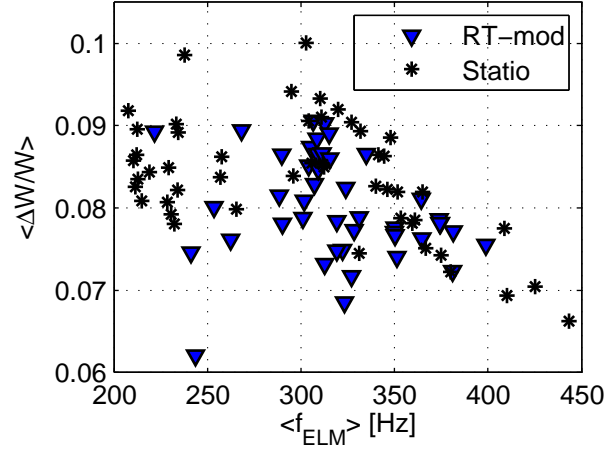
Figure 3.22: $\Delta W/W$ versus f_{ELM} with X2 input power in stationary heating mode (stars) and in RT mode (triangles), including ff-RT, fb-RT and random Δt_L control schemes. $\theta_l = 17° \pm 1°$.
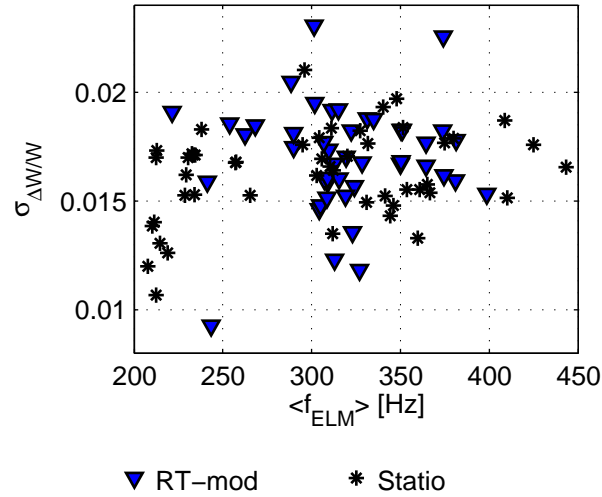
Figure 3.23: $\sigma_{\Delta W/W}$ versus f_{ELM} with X2 input power in stationary heating mode (stars) and in RT mode (triangles), including ff-RT, fb-RT and random Δt_L control schemes. $\theta_l = 17° \pm 1°$.

they are often associated with large values of ΔW. Since, contrary to σ_T, $\sigma_{\Delta W/W}$ does not decrease with $P_{\mathrm{input,X2}}$ (or, equivalently, f_{ELM}) in stationary mode, it is not surprising that the power modulation has no effect on it either. The control mechanism that works for the ELM period can therefore not be applied to the ELM amplitude.

3.4.2.3   Dependence of ELM pacing on power deposition location

In the real-time control results shown above, a constant launcher angle $\theta_l = 17°$ has been used. This section addresses the question of the dependence of the ELM pacing efficiency on the power deposition location. This study is however limited

(a) ELM frequency

(b) Relative ELM amplitude
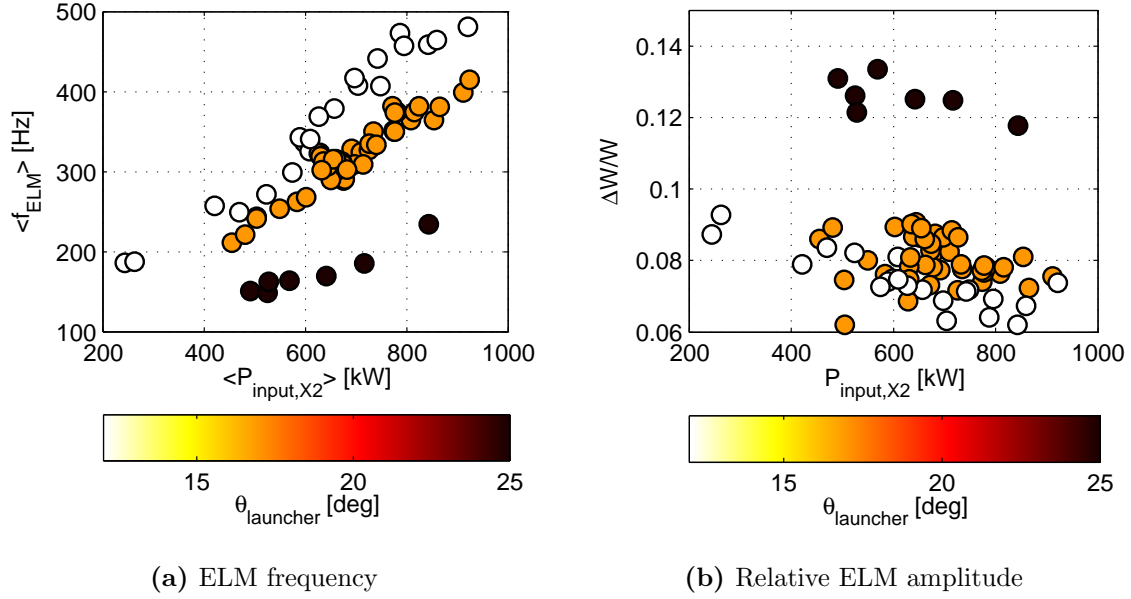
Figure 3.24: Statistics of (a) ELM frequency and (b) relative plasma energy loss per ELM (measured by the DML) as functions of X2 input power (RT mode) and launcher angle.

by experimental constraints, mainly the limited range of allowed X2 launcher angles (i.e. power deposition location) and the fact that X3 power supplies are not part of the real-time control system. It has consequently been limited to a comparison between the results obtained for RT heating mode at $\theta_l \in \{12°, 17°, 25°\}$. These values correspond to limit values toward the edge (12°) and the core (25°), while 17° is the reference launcher angle.

The first step of this study is to validate the ELM control results (section 3.3). The dependence of the ELM frequency and amplitude on the X2 input power and launcher angle in RT mode is shown in figure 3.24. When comparing with the stationary heating results (figure 3.5), it is indubitable that real-time control has no impact on the increase of f_{ELM} and decrease of ΔW when depositing the power closer to the plasma separatrix. The two methods can therefore be readily combined.

According to the results presented in the previous section ($\theta_l = 17°$), the efficiency of ELM pacing by real-time controlled power modulation is related to the decrease of the standard deviation of the ELM period, σ_T, with input power. Figure 3.25(a) shows that σ_T not only decreases with input power, but also increases with launcher angle in stationary heating mode. This double dependency can be replaced by a single one, using the ELM frequency as the scaling parameter (figure 3.25(b)). Following this scaling, one would expect the real-time control to result in the best ELM pacing (i.e. the lowest σ_T) at low values of θ_l.

A comparison of the standard deviation of the ELM period for RT heating at

(a) σ_T as a function of $P_{\mathrm{input,X2}}$ and θ_l

(b) σ_T as a function of f_{ELM} and θ_l
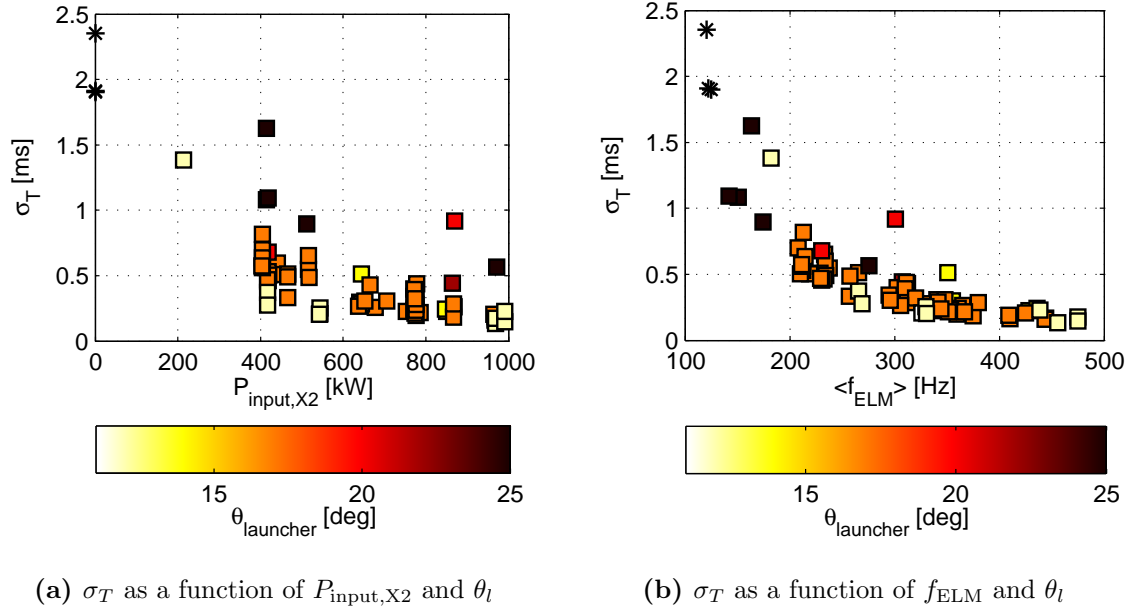
Figure 3.25: Statistics of the standard deviation of the ELM period as a function of launcher angle and (a) X2 input power and (b) ELM frequency. Stars indicate values obtained for shots with no X2 power.

three different deposition locations is plotted in figure 3.26. While the expected ordering of the ELM pacing efficiency with respect to power deposition location is experimentally confirmed in a number of cases, a class of $\theta_l = 12°$ data points take surprisingly large values of σ_T, indicating a less efficient pacing in that case. When considering the relative deviation (figure 3.26(b)), the two distinct classes of $\theta_l = 12°$ data points clearly stand out, one matching the good $\theta_l = 17°$ results with half the deviation of the other. Concerning the $\theta_l = 25°$ results, even if the statistics is scarce, it is encouraging to note that the best result is comparable in relative value to the results obtained for the other deposition locations.

A comparison with stationary heating data is presented in figure 3.27 for both limiting cases. Although statistics are scarce, if the anomalous $\theta_l = 12°$ data points are discarded, the features described for the $\theta_l = 17°$ case (figure 3.21(a)) remain true, in particular the inequality $\sigma_T(\mathrm{RT}) \lesssim \sigma_T(P_H)$ seems to hold. When analysing these results, one must keep in mind that $\theta_l \in \{12°, 25°\}$ correspond to limit cases where changes in plasma density have an impact on the power absorption or plasma regime. In particular, at small angles, a density rise often triggers an ELM-free phase. Operating close to a bifurcation point might explain why an inconsistent dependence of σ_T on $P_{\mathrm{input,X2}}$ is observed for $\theta_l = 12°$. The larger density measured for the anomalous points (figure 3.28) supports this interpretation, although more data points would be required to clearly establish this fact.
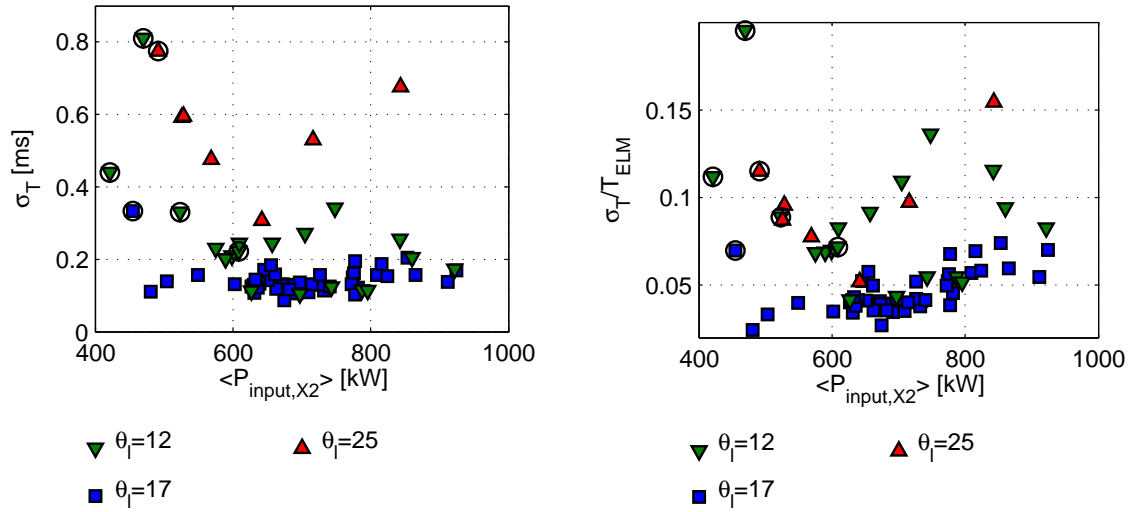
(a) σ_T as a function of $P_{\text{input,X2}}$ and θ_l

(b) σ_T/T_{ELM} as a function of $P_{\text{input,X2}}$ and θ_l

Figure 3.26: Statistics of (a) the standard deviation and (b) the relative deviation of the ELM period as functions of launcher angle and X2 input power in RT mode. Circled data points indicate phases where control is only partly effective (Δt_L is at times larger than T_{ELM}).
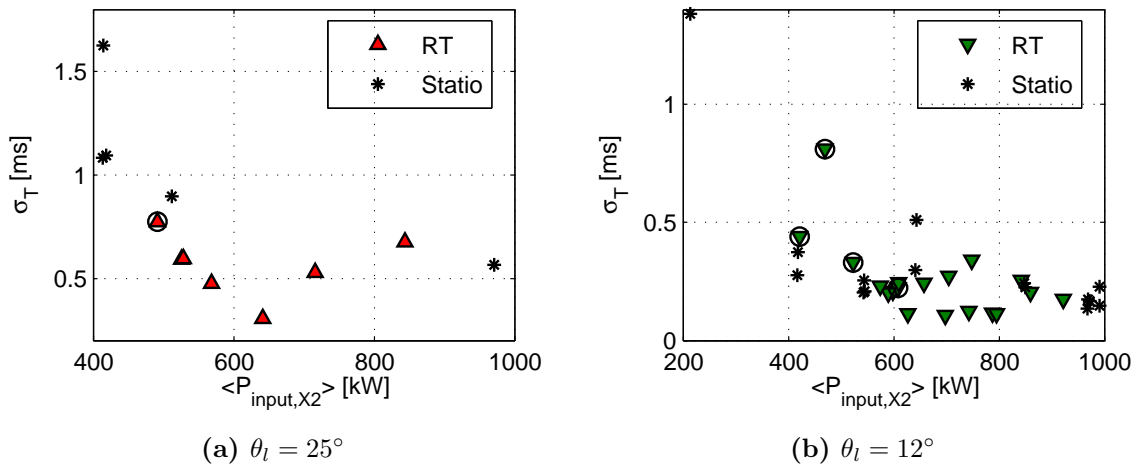
(a) $\theta_l = 25°$

(b) $\theta_l = 12°$

Figure 3.27: Statistics of the standard deviation of the ELM period as a function of X2 input power in RT mode (triangles) and stationary heating mode (stars), at two launcher angles. Circled data points indicate phases where control is only partly effective (Δt_L is at times larger than T_{ELM}).
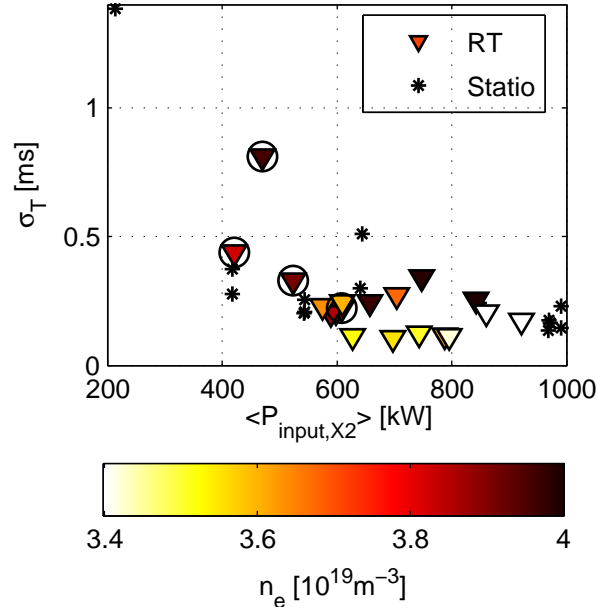
Figure 3.28: Statistics of the standard deviation of the ELM period as a function of X2 input power in RT mode (triangles) and stationary heating mode (stars), at $\theta_l = 12°$. The line-averaged electron plasma density of each phase is indicated by a color code. Circled data points indicate phases where control is only partly effective (Δt_L is at times larger than T_{ELM}).

3.4.3 Real-time control with inverted modulation phase

The best way to confirm the understanding of the ELM characteristics inferred in section 3.4.2 is to use a waveform orthogonal to that used in the original real-time control scheme. In the experiments presented here, ELMs are used to trigger the power modulation cycle, as in section 3.4.2, but this time a high power phase of controlled duration Δt_H is triggered, followed by a low power phase lasting until the next ELM. In this section, the original modulation scheme will still be referred to as the RT mode, while the inverted modulation scheme will be referred to as the invRT mode. All these experiments are performed with a constant launcher angle $\theta_l = 17°$.

Figure 3.29 shows the results obtained for a step-scan of Δt_H in invRT mode, using X2 power modulation in the range 0.4-1 MW, preceded and followed by two phases of stationary power. As expected, increasing Δt_H results in an increase of $\langle P_{\text{input,X2}} \rangle$ (figure 3.29(b)) with an associated increase of f_{ELM} (figure 3.29(d)). Heating in invRT mode clearly results in larger excursions of the ELM period, as seen in figure 3.29(c). This change of σ_T even seems to increase with Δt_H, until the limit of effective control, where some ELMs have $T_{\text{ELM}} < \Delta t_H$, is reached ($\Delta t_H = 2.25$ ms here).

The dependence of the ELM frequency on the average power for invRT modula-

Figure 3.29: Real-time control experiment in inverted modulation mode with X2 power modulated in [400,1000] kW. (a) H_α emission, with peaks marked by crosses, and corresponding real-time control triggers; (b) X2 input power ($\theta_l = 17°$): four invRT phases, with $\Delta t_H = 0.75$ ms, $\Delta t_H = 1.25$ ms, $\Delta t_H = 1.75$ ms and $\Delta t_H = 2.25$ ms respectively, preceded and followed by two stationary phases; (c) ELM period T_{ELM} and high power phase duration Δt_H (relevant to invRT phases only); (d) ELM frequency f_{ELM}. In (b) and (d), solid lines depict averages over the respective phases.
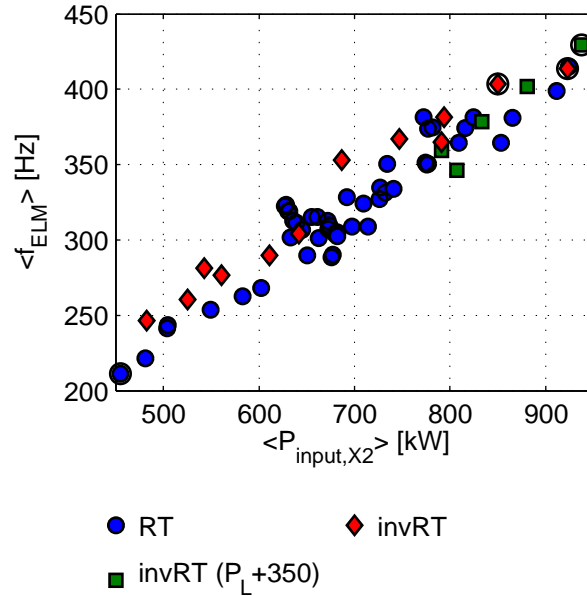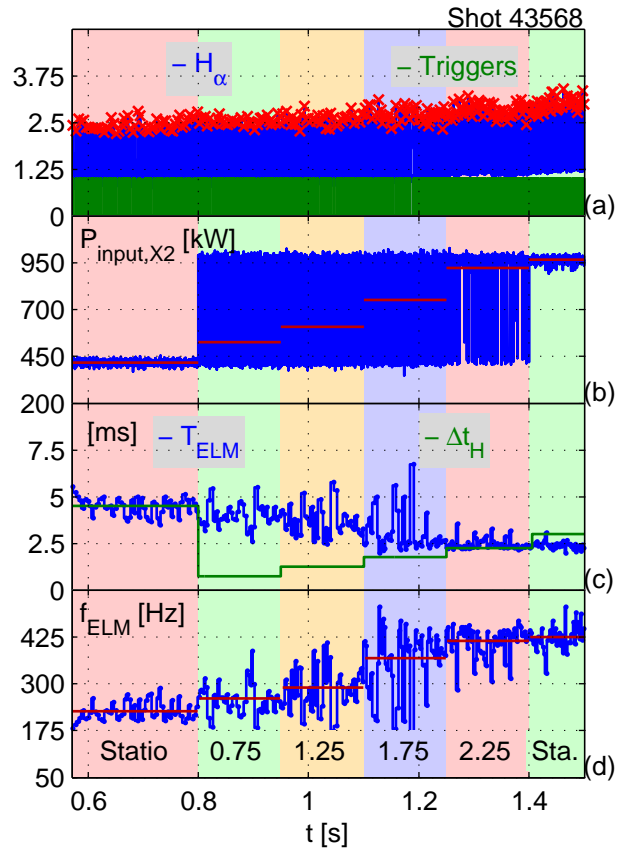
Figure 3.30: f_{ELM} versus $\langle P_{\text{input,X2}}\rangle$ for real-time control in standard RT mode (circles) and invRT mode (inverted modulation phase), for modulation in [400,1000] kW (diamonds) and in [750,1000] kW (squares). $\theta_l = 17°$.
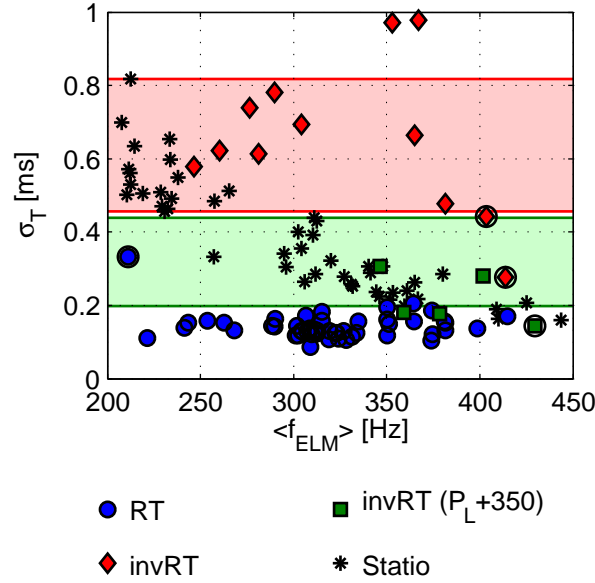
Figure 3.31: Standard deviation of T_{ELM} versus f_{ELM} with X2 input power in stationary heating mode (stars), standard RT mode (circles) and invRT mode (inverted modulation phase), for modulation in $[400,1000]\,\text{kW}$ (diamonds) and in $[750,1000]\,\text{kW}$ (squares). Circled symbols indicate phases where control is only partly effective (Δt_L or Δt_H is at times larger than T_{ELM}). $\theta_l = 17° \pm 1°$.

tion is compared to the standard RT modulation in figure 3.30. The figure includes a few data points corresponding to invRT modulation with a higher low power level, i.e. with modulation in $[750,1000]\,\text{kW}$. No significant difference between the $f_{\text{ELM}}(\langle P_{\text{input,X2}} \rangle)$ curves of each mode is observed, therefore confirming that the ELM frequency depends on the average power only (at constant launcher angle) and that no "kick effect" due to the power modulation is observed, as observed in the RT experiments.

Finally, figure 3.31 shows σ_T versus f_{ELM} for X2 input power in stationary, RT and invRT modes. It clearly confirms that the orthogonality of the waveforms used in RT and invRT modes mainly affects the regularity of the ELM period. While RT heating decreases σ_T, invRT heating increases it. As discussed in section 3.4.2, the RT results are consistent with σ_T being only a function of the power at the ELM time. In the case of the invRT mode, one would therefore expect that $\sigma_T(\text{invRT})$ is equal or close to $\sigma_T(P_L)$ in stationary mode. To validate this point, the range of values taken by σ_T in stationary mode at powers close to the low power level of the modulation are indicated by color patches in the figure. Most of the data points where control is effective fall into or are very close to these intervals, consistently with the RT results. Nonetheless, the scattering of σ_T is large, leading to rather

large intervals. Due to this significant scattering, it is hard to determine whether the increase of $\sigma_T(\text{invRT})$ with Δt_H (or, equivalently, f_{ELM}), observed qualitatively on figure 3.29(c) and also appearing on the invRT data points (with modulation in $[400,1000]\,\text{kW}$) on figure 3.31, is real or only the result of poor statistics.

3.4.4   Feed-forward power modulation experiments

3.4.4.1   Introduction

This section describes the results of the feed-forward power modulation experiments. In this heating mode, the FF mode, X2 power is modulated between $400\,\text{kW}$ and $900\,\text{kW}$, irrespectively of the ELM cycle. The duty cycle, determining the average input power, and the modulation frequency, f_{mod}, are the only varied parameters (a constant launcher angle $\theta_l = 17°$ is used). This section shows that the ELM frequency cannot be driven by power modulation and that the ELMs are locked to the power modulation only if $f_{\text{mod}} = f_{\text{ELM,nat}}$, where $f_{\text{ELM,nat}}$ is the natural ELM frequency, i.e. the ELM frequency at a stationary power equal to the average of the modulated power. The term "locking" itself is also put into question, since a simple synchronicity of the modulation and ELM cycles would give similar results.

3.4.4.2   Analysis method

In this study, ELMs are said to be locked to the power modulation when there is exactly one ELM per modulation cycle. ELM locking also implies the existence of a drive and therefore supposes that ELMs are triggered reproducibly at a well-defined time point in the modulation cycle. The parameters of interest for locking analysis are consequently the time elapsed from a known time point in the modulation cycle to the next ELM, as well as the number of ELMs per modulation cycle. Since, due to their kink-ballooning nature, ELMs are more likely to be triggered by high power phases, the rise time of the power modulation is chosen as the reference time in the analysis shown below. To facilitate the interpretation of the results, in particular when f_{mod} is swept during the shot, the relative time $t_{\text{ELM,rel}}$ of the ELMs in the modulation cycle is used. It is defined as:

$$t_{\text{ELM,rel}} = \frac{t_{\text{ELM}} - t_{\text{Rise}}}{T_{\text{mod}}} \tag{3.3}$$

where t_{Rise} is a power modulation rise time, t_{ELM} the time of the subsequent ELM and T_{mod} is the power modulation period.
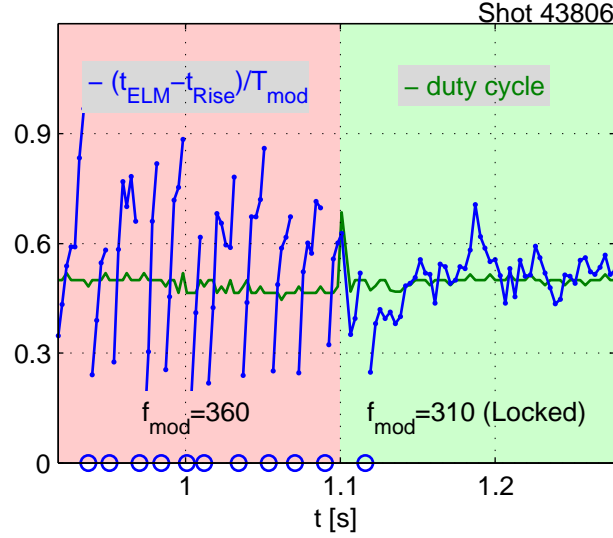
Figure 3.32: Relative ELM time in modulation cycle and duty cycle versus X2 power rise time. The X2 input power is modulated between $400\,\mathrm{kW}$ and $900\,\mathrm{kW}$ with a 50% duty cycle. $f_{\mathrm{mod}} = 360\,\mathrm{Hz}$ in the first phase of the shot and $310\,\mathrm{Hz}$ in the second phase. The natural ELM frequency at the equivalent average power ($650\,\mathrm{kW}$) is approximately $310\,\mathrm{Hz}$. Circles indicate modulation cycles with no ELM.

3.4.4.3   Results and discussion

In figure 3.32, the relative ELM time is plotted versus the power modulation rise time for a phase where f_{mod} is $50\,\mathrm{Hz}$ higher than $f_{\mathrm{ELM,nat}}$, followed by a phase where $f_{\mathrm{mod}} = f_{\mathrm{ELM,nat}}$. In the first phase, there is a clear drift of the ELM time within the modulation cycle. The positive slope indicates that ELMs occur later and later in the modulation cycle, up to the point where no ELMs occur in a whole cycle. This succession of parallel lines, interrupted by cycles with no ELMs (or with several ELMs, if the slope is inverted), is the result of a frequency mismatch between the ELM and the modulation cycles, therefore proving the absence of locking. In the second phase, the relative ELM times remain rather constant, with exactly one ELM per modulation cycle in the vast majority of cases. This phase therefore corresponds to a phase of ELM locking. In this example, locking occurs only when $f_{\mathrm{mod}} = f_{\mathrm{ELM,nat}}$.

The locking of the ELM frequency along the natural $f_{\mathrm{ELM,nat}}(P_{\mathrm{input,X2}})$ curve is experimentally demonstrated in figure 3.33, where both the modulation frequency and the duty cycle are simultaneously swept to follow the natural curve. In particular, figure 3.33(c) shows that f_{ELM} matches f_{mod} along the sweep, and figure 3.33(d) shows that locking remains effective for the vast majority of ELMs.

Unfortunately, ELM locking only occurs in a small range of modulation frequen-
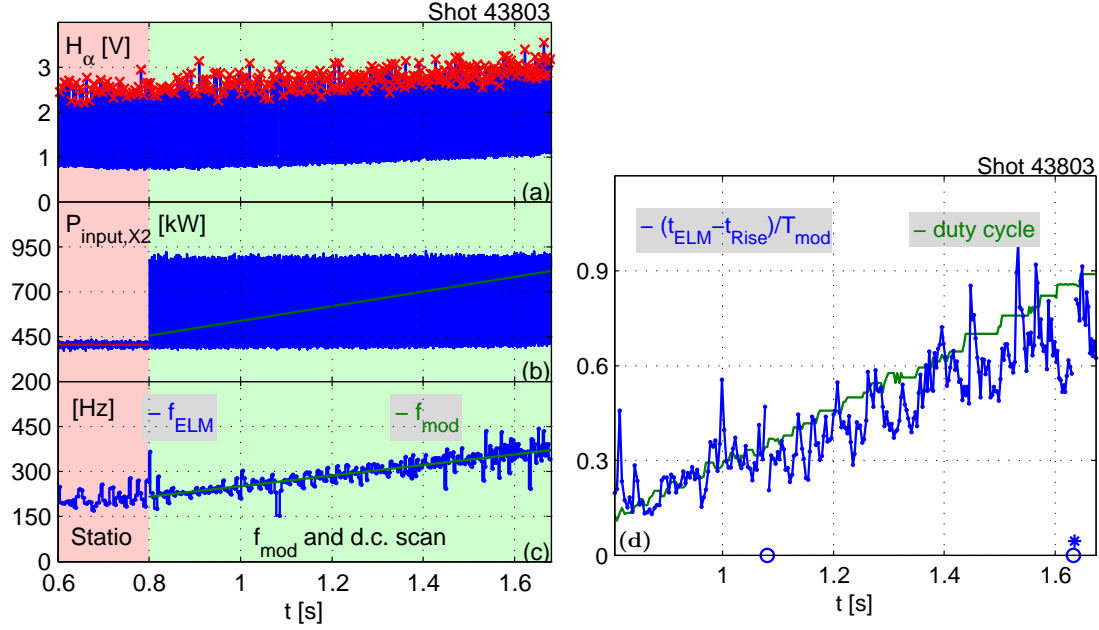
Figure 3.33: Sweep of f_{mod} and duty cycle along the $f_{ELM,nat}(P_{input,X2})$ curve. (a) H_α emission, with peaks marked by crosses; (b) X2 input power ($\theta_l = 17°$): stationary phase followed by a FF phase with simultaneous sweeps of f_{mod} (215-375 Hz) and duty cycle (10-90%) to follow the $f_{ELM,nat}(P_{input,X2})$ curve; (c) ELM frequency f_{ELM} and power modulation frequency f_{mod}; (d) Relative ELM time in modulation cycle and duty cycle versus X2 power rise time. In (b), solid lines depict the average followed by the linear fit over the respective phases. In (d), circles and stars indicate modulation cycles with, respectively, no ELMs and more than one ELM.

cies close to the natural ELM frequency, as proven by the modulation frequency sweep performed at constant duty cycle in the vicinity of the natural ELM frequency shown in figures 3.34 and 3.35. The sweep does not affect the (local) average value of the ELM frequency, but only regularizes it in the phase where $f_{mod} \simeq f_{ELM,nat}$, i.e. in the ELM locking phase (figures 3.34(c) and 3.35(a)). In this phase, the use of the term locking is maybe even an overstatement. The relative ELM time would indeed be expected to remain constant in the case of locking, whereas a clear downward drift is observable on figure 3.35(b). The observed stabilization of the ELM frequency in the locked phase is consistent with the fact that a majority of ELMs occur during the high power phase of the modulation in this period.

A statistics of f_{ELM} versus f_{mod} at various duty cycles is plotted in figure 3.36. It clearly confirms that $f_{mod} = f_{ELM,nat}$ is a necessary condition for ELM locking and that the average input power drives the ELM frequency, not the power modulation. The preliminary ASDEX Upgrade results [43] conform to this representation of the effect of power modulation on ELMs and consequently appear to be the result of a somewhat fortunate choice of experimental parameters rather than a demonstration
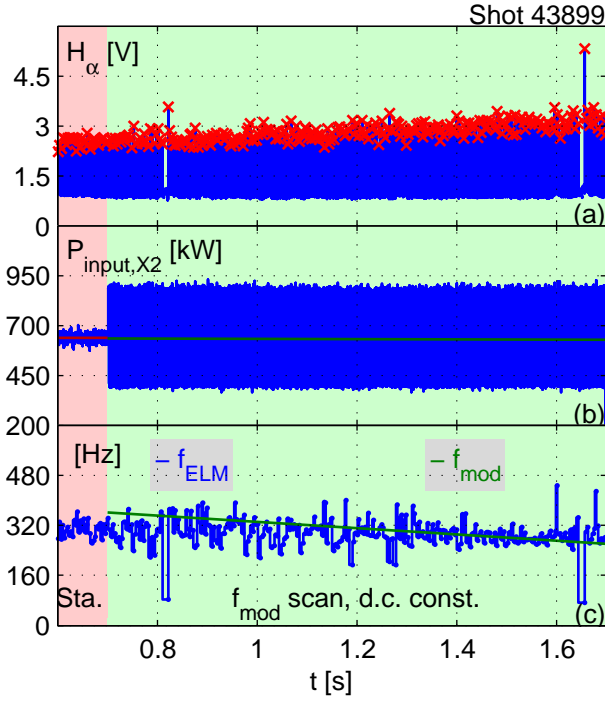
Figure 3.34: Sweep of f_{mod} at a constant 50% duty cycle in the vicinity of $f_{\mathrm{ELM,nat}} = 290\,\mathrm{Hz}$. (a) H_α emission, with peaks marked by crosses; (b) X2 input power ($\theta_l = 17°$): a stationary phase followed by a FF phase with a sweep of f_{mod} (360-260 Hz) at constant duty cycle (50%); (c) ELM frequency f_{ELM} and power modulation frequency f_{mod}; In (b), solid lines depict the average followed by the linear fit over the respective phases.
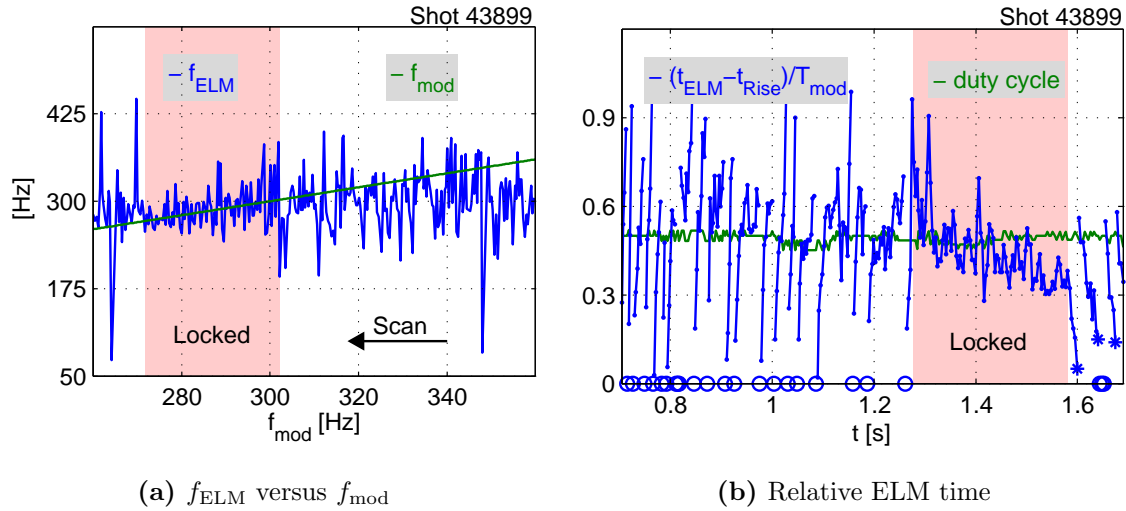
(a) f_{ELM} versus f_{mod}

(b) Relative ELM time

Figure 3.35: Sweep of f_{mod} in the vicinity of $f_{\mathrm{ELM,nat}} = 290\,\mathrm{Hz}$. The X2 input power is modulated between $400\,\mathrm{kW}$ and $900\,\mathrm{kW}$ with a 50% duty cycle. (a) f_{ELM} and f_{mod} as functions of f_{mod}; (b) Relative ELM time in modulation cycle and duty cycle versus X2 power rise time. In (b), circles and stars indicate modulation cycles with, respectively, no ELMs and more than one ELM.
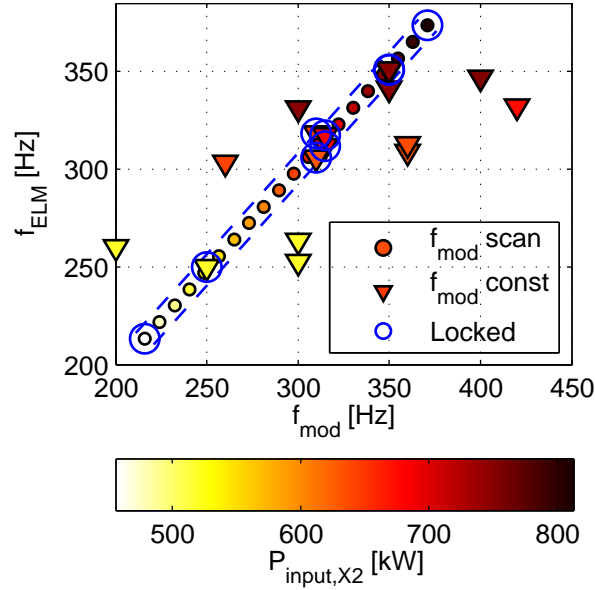
Figure 3.36: Statistics of f_{ELM} versus f_{mod} at various duty cycles. The X2 input power is modulated between $400\,\text{kW}$ and $900\,\text{kW}$. Its average is indicated by a color code. The simultaneous f_{mod} and duty cycle scan along the $f_{\text{ELM,nat}}(P_{\text{input,X2}})$ curve (see figure 3.33) is represented by circles, surrounded by dashed lines indicating ELM locking. Averages over ELMing phases with constant modulation parameters are depicted by triangles. Circled symbols represent locked phases.

of ELM locking by feed-forward power modulation.

The distinction between locking and synchronicity of the ELM and modulation frequencies is better addressed by the analysis of the standard deviation of the ELM period, σ_T. Real locking should indeed be distinguished by a clear decrease of σ_T. Figure 3.37 shows the statistics of σ_T corresponding to the data plotted in figure 3.36. While ELM locking is clearly a sufficient condition to obtain lower values of σ_T, it is unclear whether it is also a necessary condition, in particular for cases with intermediate duty cycle. In addition, σ_T presents no significant dependence on the sign of $f_{\text{mod}} - f_{\text{ELM}}$, at least in the studied range. σ_T is plotted versus ELM frequency and input power for the stationary, real-time controlled and feed-forward heating schemes in figure 3.38. While the best cases of ELM locking in FF mode reach the lower range of equivalent stationary cases, a significant number of ELM locking cases show no improvement of σ_T compared to stationary cases. If locking is real, it is therefore not very robust. Since power modulation cannot drive the ELM frequency, the controversy of locking versus synchronicity of the ELMs is of no importance as figure 3.38 shows that real-time control is incontestably a more efficient ELM pacing tool. Finally, the global decrease of σ_T with input power in FF mode can be attributed to the increased duty cycle. Increasing the duty cycle
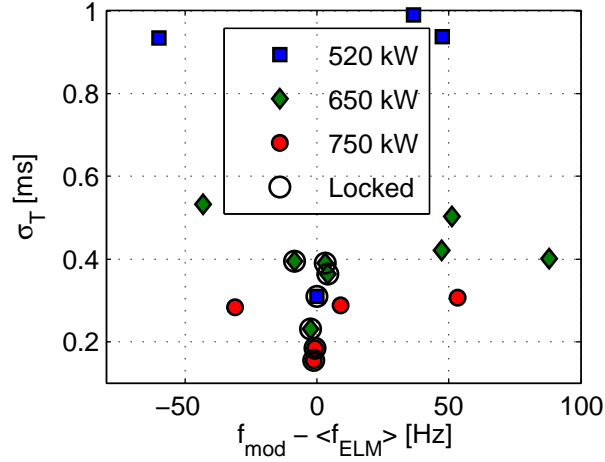
Figure 3.37: Statistics of σ_T versus $f_{\mathrm{mod}} - f_{\mathrm{ELM}}$ at various duty cycles (25%, 50%, 75%). The X2 input power is modulated between $400\,\mathrm{kW}$ and $900\,\mathrm{kW}$. Circled symbols represent locked phases. The average power is indicated in the legend.

(a) σ_T as a function of f_{ELM}

(b) σ_T as a function of $P_{\mathrm{input,X2}}$
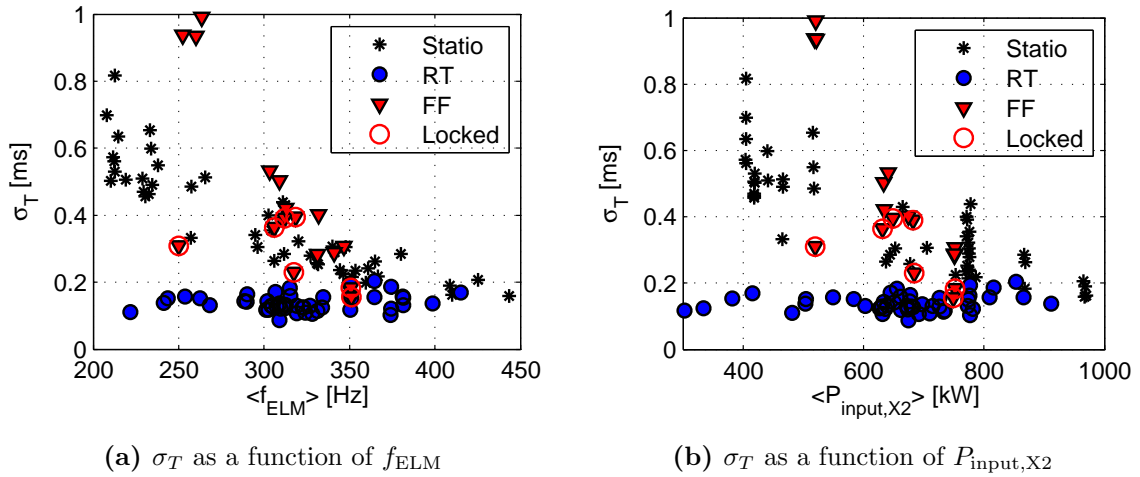
Figure 3.38: Statistics of σ_T versus (a) f_{ELM} and (b) $P_{\mathrm{input,X2}}$ for the stationary (stars), RT (circles) and FF (triangles) heating schemes. In FF mode, the X2 input power is modulated between $400\,\mathrm{kW}$ and $900\,\mathrm{kW}$ at various duty cycles, circled symbols representing locked phases.

indeed results in a larger proportion of ELMs occurring during a high power phase, which is known from the real-time experiments to decrease σ_T.

3.4.5 Interpretation of the ELM pacing experiments

The linear relation between f_{ELM} and $\langle P_{\mathrm{input,X2}} \rangle$, identical for stationary and modulated heating schemes, the balancing of a smaller Δt_L by a larger Δt_H in RT mode, and the results of the random Δt_L experiment suggest that ELMs are triggered when an energy threshold is exceeded rather than through a kick effect. This interpretation is confirmed by the feed-forward power modulation experiments, where average power and modulation frequency are not intrinsically correlated, showing no sign of ELM triggering by power modulation and describing the same $f_{\mathrm{ELM}}(\langle P_{\mathrm{input,X2}} \rangle)$ curve as the other heating schemes. The various real-time experiments also show that ELM pacing by ELM-synchronized power modulation only works because σ_T is a decreasing function of the instantaneous power at the ELM time.

3.4.6 Summary of the ELM pacing experiments

ELM pacing by deposition of modulated ECRH power in the edge of an ELMing H-mode plasma has been studied using diverse power modulation schemes: the RT mode (power modulation synchronized in real-time with the ELM cycle, including the feed-forward ff-RT and the feedback fb-RT modes), the invRT mode (equivalent to the RT mode, but inverting the modulation phase), and the FF mode (purely feed-forward power modulation). While the results of all the tested schemes converge toward a demonstration of the independence of the ELM frequency on the exact waveform of the power in the ELM cycle, only the RT scheme results in a significant and robust reduction of the ELM period variability, theoretically only limited by $\sigma_T(P_H)$, the standard deviation of the ELM period at the high power level of the modulation. While the standard deviation of the ELM amplitude, $\sigma_{\Delta W}$, is not affected by a stabilization of the ELM period, rare transient events with large ELM amplitudes are observed to be less frequent in real-time controlled phases. In feedback mode, the RT scheme also displays an efficient control of the ELM frequency itself. The random Δt_L experiment clearly demonstrates that each ELM is individually controllable by acting on the average power delivered during the ELM cycle. While the results of these pacing experiments are not thought to be dependent on the power deposition location, it has been shown here that ELM pacing is more robust when operating away from power and/or density limits, in terms of plasma

regime.

3.5 0-D model of the ELM cycle

3.5.1 Introduction

This section aims at identifying an ELM cycle model able to encompass the richness of the results presented in sections 3.3 and 3.4, in order to draw a clearer picture of the physical mechanisms lying behind the ELM phenomenon. The experimental results are summarized in the list given below:

- The ELMs under consideration are of type I: $f_{\mathrm{ELM}} \nearrow$ if $P \nearrow$.

- The standard deviation of the ELM period decreases more than proportionally with the input power: $\sigma_T \searrow$ and $\sigma_T/T_{\mathrm{ELM}} \searrow$ if $P \nearrow$.

- The relative ELM amplitude $\Delta W/W$ and its standard deviation $\sigma_{\Delta W/W}$ are mostly independent of the input power at constant launcher angle and for $P_{\mathrm{input,X2}} > 400\,\mathrm{kW}$.

- The ELM frequency increases and the ELM amplitude decreases when power is deposited closer to the plasma separatrix: $f_{\mathrm{ELM}} \nearrow$ and $\Delta W/W \searrow$ if $\theta_l \searrow$.

- The ELM frequency depends only on the average of the input power, and not on the details of its waveform within an ELM cycle: $f_{\mathrm{ELM}} = f_{\mathrm{ELM}}(\langle P \rangle)$.

- Power modulation does not result in a drive or an acceleration of the ELMs, so that no associated "kick effect" is observed.

- Using power modulation synchronized in real-time with the ELM cycle, so that ELMs occur during the high power phase P_H, significantly stabilizes the ELM period: $\sigma_T(\mathrm{RT}) \simeq \sigma_T(P_H)$.

  - An increase of σ_T with Δt_H, though much weaker, is also not excluded.

- Inverting the phase of the real-time power modulation, so that ELMs occur during the low power phase P_L, significantly destabilizes the ELM period: $\sigma_T \simeq \sigma_T(P_L)$.

  - Other weaker dependencies, not excluded by rather poor statistics, might be present: in particular, a possible increase of σ_T with Δt_H.

- The period of an ELM is mainly determined by the power delivered in its own cycle, ELMs being therefore essentially uncorrelated with one another and independently controllable.

- ELM pacing by real-time control works thanks to:
  - The control of the average ELM period by the average input power.
  - The stabilization of the ELM period due to the high power phase present when the ELMs occur.

This section shows how an integrator model of the ELM cycle is able to reproduce most of the experimental results. Starting from the simplest possible model, the perfect integrator model, and from the most easily understood experimental results, the ELM pacing results, a basic understanding of the ELM cycle is proposed. This is then refined into the finite confinement time integrator model to move towards a more comprehensive reproduction of the experimental results and to satisfy physics constraints; this model is also tested versus experiments. Finally, it will be shown that, by defining the energy threshold for ELM triggering as a function of the power deposition location, the ELM control results are also reproduced. Of course, this model does not aim at providing an accurate theoretical explanation of the ELM cycle. Replacing the full kink-ballooning mode description by a simple, loosely equivalent energy threshold model is certainly not an appropriate theoretical approach. Nonetheless, this simple model does succeed in facilitating the understanding of the experimental results and forms a useful practical basis for further experimentation in ELM control.

3.5.2   Perfect integrator model

The linear dependence of f_{ELM} on P_{input} (e.g. figure 3.16) and the insignificant dependence of $\Delta W/W$ on P_{input} (figure 3.22) favors the description of the ELM cycle by a power integrator model with constant energy threshold E_{thres}:

$$\frac{\mathrm{d}E_{\mathrm{ped}}}{\mathrm{d}t} = P_{\mathrm{X2}}(t) + P_{\mathrm{X3}} + P_{\mathrm{OH}} - P_{\mathrm{rad}} \tag{3.4}$$

where E_{ped}, the "pedestal energy", is used here to refer to the energy accumulated up to E_{thres}, the energy threshold where an ELM is triggered. P_{X2}, P_{X3} and P_{OH} are the X2, X3 and Ohmic heating sources, respectively. P_{rad} represents the radiation loss channel. In this context, E_{thres} is equal to the ELM amplitude ΔW, independently of the input power. Combining all the power terms into the variable P, the relation

$$\langle P \rangle = \frac{1}{T_{\mathrm{ELM}}} \int_0^{T_{\mathrm{ELM}}} \frac{\mathrm{d}E}{\mathrm{d}t}\mathrm{d}t = \frac{E_{\mathrm{thres}}}{T_{\mathrm{ELM}}} \tag{3.5}$$

ensures the linear relation between the ELM frequency and the input power. A source of variability must also be included to yield finite values of σ_T and $\sigma_{\Delta W/W}$.
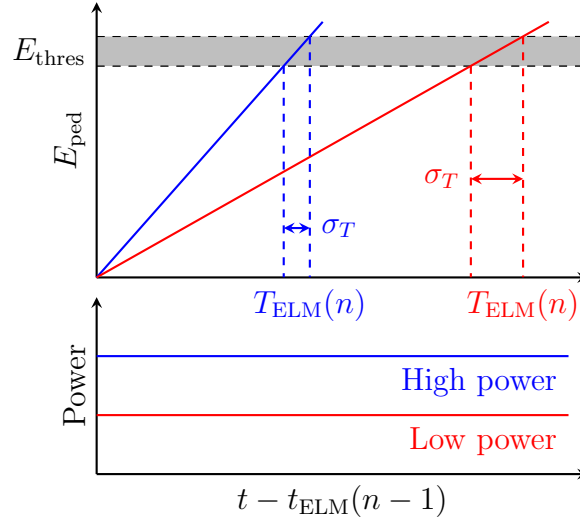
Figure 3.39: Illustration of the perfect integrator model with variable energy threshold in the cases of stationary low and high power heating. E_{ped} is the energy accumulated from the last ELM crash and E_{thres} the energy threshold at which the next ELM is triggered.

This source is subjected to the constraints that σ_T decreases with input power (figure 3.21(a)) and that $\sigma_{\Delta W/W}$ does not depend on input power (figure 3.23). Replacing the fixed energy threshold by a variable one is consistent with all these requirements. Equivalent results would be obtained by using a variable offset in the integration. This approach, although physically more sound (the initial conditions of the integration being blurred by the chaotic events occurring at the ELM crash), would muddle the model illustrations shown in this section and has therefore not been retained. Note however that even though the interpretation capabilities of the model are not affected by this choice, the correlation between successive ELMs is. Indeed, in the variable offset approach, the ΔW of the last ELM contributes to the determination of the period of the next ELM, while it does not in the variable threshold approach. The model of the perfect integrator with variable energy threshold is illustrated in figure 3.39 in the cases of stationary low and high power heating. The variability in E_{thres}, independent of input power, corresponds to $\sigma_{\Delta W/W}$ and is noted here σ_{thres}. As illustrated in the figure, increasing the input power results in a proportional decrease of σ_T.

As illustrated in figure 3.40, the perfect integrator model is consistent with the observed stabilization of the ELM period by real-time controlled power modulation. While T_{ELM} is only determined by $\langle P \rangle$, σ_T depends on the slope of $E_{\text{ped}}(t)$, i.e. the input power, at the ELM time. In this picture, the ELM period is therefore stabilized by a faster crossing of the metastable region at the energy threshold. Reciprocally, the model is also consistent with the observed destabilization of the
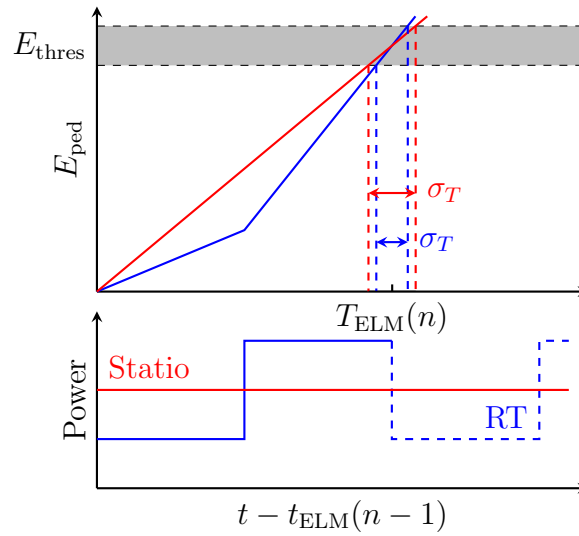
Figure 3.40: Stationary versus real-time controlled heating illustrated in the frame of the perfect integrator model with variable energy threshold. $\langle P \rangle$ and T_{ELM} are identical for both heating schemes, but σ_T differs.
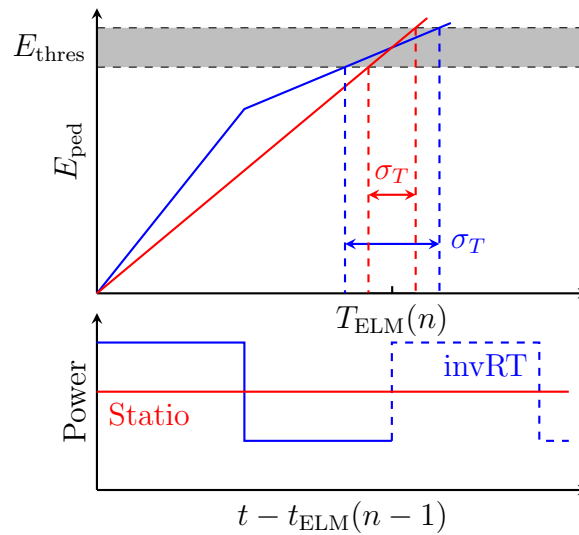
Figure 3.41: Stationary versus real-time controlled heating with inverted modulation phase illustrated in the frame of the perfect integrator model with variable energy threshold. $\langle P \rangle$ and T_{ELM} are identical for both heating schemes, but σ_T differs.
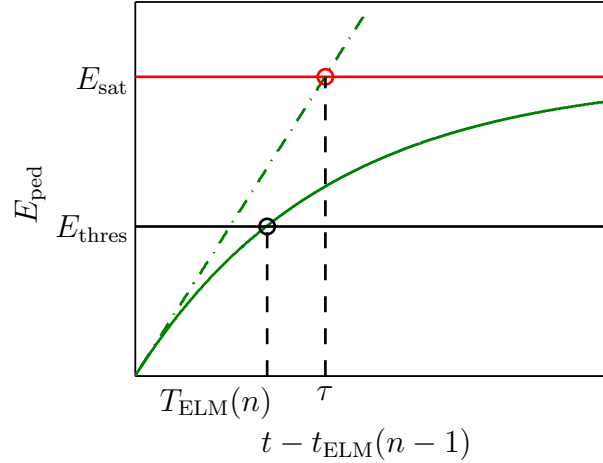
Figure 3.42: Perfect (green dash-dotted line) versus finite confinement time (green solid line) integrator model, with τ the confinement time of the inter-ELM phase in the pedestal region and E_{sat} the saturation energy. Threshold variability is not shown.

ELM period in the case of real-time controlled heating with inverted modulation phase, as illustrated in figure 3.41. Nonetheless, in stationary heating, the model predicts a constant σ_T/T_{ELM}, inconsistent with the experimental results. Note that if the variable offset approach were used instead of the variable energy threshold approach, the same conclusions would hold.

3.5.3   Finite confinement time integrator model

As mentioned above, the decrease of σ_T/T_{ELM} with input power in stationary mode is not captured by the simple perfect integrator model. In addition, it is all too well-known in fusion science that the energy confinement time is finite. The model complexity therefore needs to be increased to accommodate a finite confinement time term:

$$\frac{\mathrm{d}E_{\text{ped}}}{\mathrm{d}t} = P_{\text{X2}}(t) + P_{\text{X3}} + P_{\text{OH}} - P_{\text{rad}} - \frac{E_{\text{ped}}}{\tau} \qquad (3.6)$$

where τ is the energy confinement time of the inter-ELM phase in the pedestal region. τ is therefore not the usual global energy confinement time. The solution of (3.6) for a stationary input power is plotted in figure 3.42. The finite confinement time term results in the appearance of a saturation level $E_{\text{sat}} = P\tau$, where $P = P_{\text{X2}}(t) + P_{\text{X3}} + P_{\text{OH}} - P_{\text{rad}}$. The effect of a finite value of τ is stronger when E_{thres} is close to E_{sat}. Equivalently, if $T_{\text{ELM}} \ll \tau$, the perfect integrator assumption holds, while if $T_{\text{ELM}} \gtrsim \tau$, T_{ELM} is larger than in the ideal case. Of course, this effect is stronger at high E_{ped} for low $P_{\text{X2,input}}$. The finite τ contribution is therefore minimized in standard RT modulation and maximized in invRT modulation.

3.5.3.1 Choice of model parameters for ELM cycle simulations

In order to determine whether the finite confinement time model is able to reproduce the observed experimental trends, realistic parameters must be used to feed the model and run simulations. Since the aim of this study is not to provide quantitative results, the choice of model parameters is only based here on a set of reasonable arguments. Of course, a more in-depth study could be performed, trying to identify the set of parameters that provide the best fit to all the experimental results, but the outcome of such a study would likely bring limited additional insight.

The primary model parameters are the confinement time τ, the energy threshold E_{thres} and its variability σ_{thres}. To account for the undetermination of P_{rad} and the error bars on P_{X3} and P_{OH}, another free parameter $C = P_{\text{X3}} + P_{\text{OH}} - P_{\text{rad}}$ is added to the model.

Experiments show no difference between the $f_{\text{ELM}}(\langle P \rangle)$ curves obtained in RT and invRT modes. According to the arguments given above (section 3.5.3), $T_{\text{ELM}} \ll \tau$ or $T_{\text{ELM}} < \tau$ therefore apply. Assuming, for a moment, a perfect integrator, the constraint $E_{\text{thres}} = (P_{\text{X2}} + C)T_{\text{ELM}}$ can be used in association with a linear fit of the $f_{\text{ELM}}(\langle P \rangle)$ curve to determine E_{thres} and C. When using a finite τ, C must then be increased to maintain a constant energy threshold, now given by $E_{\text{thres}} = (P_{\text{X2}} + C)\tau(1 - \exp(-T_{\text{ELM}}/\tau)$, as a function of power. This also results in a more realistic value of C. The parameters are determined from the $f_{\text{ELM}}(\langle P \rangle)$ data for stationary heating at $\theta_l = 17°$ (figure 3.16). Altogether, the resulting self-consistent set of parameters is given by $\tau = 10\,\text{ms}$, $C = 500\,\text{kW}$ and $E_{\text{thres}} = 3.2\,\text{kJ}$. Using $\sigma_{\text{thres}} = 0.15\,\text{kJ}$ reproduces the experimental results well. The value chosen for τ is justified experimentally by the lower limit of $5\,\text{ms}$ set by the invRT experiments and the upper limit of $22\,\text{ms}$ corresponding to the global confinement time of a purely X3 heated plasma. It must also be recalled that τ corresponds to the inter-ELM confinement time of the plasma edge, and therefore excludes the confinement loss due to the ELM crash.

An independent verification of the validity of the parameter set can be sought through a comparison between the obtained value of E_{thres} and the average energy loss per ELM. We find that the value $E_{\text{thres}} = 3.2\,\text{kJ}$ obtained above does not match well the typical $\Delta W = 1.1\,\text{kJ}$ obtained experimentally at $\theta_l = 17°$ (see figure 3.6(a)). The underestimation of ΔW occurring when computing its value from the DML signal (see footnote in section 3.2.3.1) only partly accounts for this discrepancy (factor 1.5 instead of 3). This issue can be addressed by directly setting E_{thres} to its experimental value, the remaining model parameters being then adjusted to account
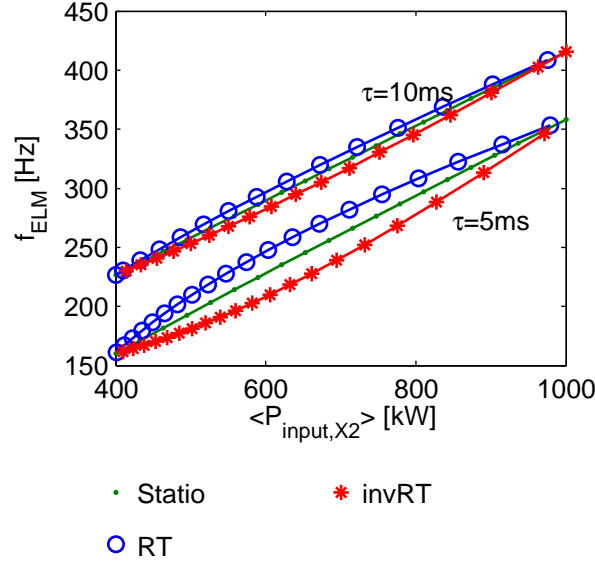
Figure 3.43: Simulations of $f_{\mathrm{ELM}}(\langle P \rangle)$ by the finite confinement time integrator in the RT (circles), invRT (stars) and stationary (dots) modes, for $\tau = 5\,\mathrm{ms}$ and $\tau = 10\,\mathrm{ms}$. $C = 500\,\mathrm{kW}$ and $E_{\mathrm{thres}} = 3.2\,\mathrm{kJ}$ in all cases. To be compared with figures 3.16 and 3.30.

for this additional constraint. In that case, the optimal (C, τ) pair is identified by looking for the minimum of the error e on the energy threshold:

$$ e^2(C, \tau) = \frac{1}{N_P} \sum_{k=1}^{N_P} \left[E_{\mathrm{thres}} - (P_{\mathrm{X2},k} + C)\tau(1 - \exp(-T_{\mathrm{ELM},k}/\tau)) \right]^2. \qquad (3.7) $$

Due to the coupling of C and τ in this model, the minimum of e is an area along a curve $\tau_{\mathrm{optim}} \propto 1/C_{\mathrm{optim}}$. At low values of E_{thres}, e.g. $1.1\,\mathrm{kJ}$, none of the $(C_{\mathrm{optim}}, \tau_{\mathrm{optim}})$ pairs are simultaneously realistic. Including the 1.5 correction factor is not sufficient to overcome this difficulty. In addition, the error e is a factor 5 larger for $E_{\mathrm{thres}} = 1.65\,\mathrm{kJ}$ than for $E_{\mathrm{thres}} = 3.2\,\mathrm{kJ}$. Since the linear dependence of f_{ELM} on P_{X2} is well demonstrated experimentally, the value $E_{\mathrm{thres}} = 3.2\,\mathrm{kJ}$ has been kept for the analysis below. Various arguments could be mentioned to explain this discrepancy, among which the assumption of independence of τ on the input power or inaccuracies in the calibration of the DML.

3.5.3.2 RT, invRT and stationary heating simulations

To justify further the choice of $\tau = 10\,\mathrm{ms}$ made above and to illustrate the expected experimental results in case of smaller values of τ for the RT, invRT and stationary heating schemes, the respective simulated $f_{\mathrm{ELM}}(\langle P \rangle)$ curves are plotted in figure 3.43 for $\tau = 5\,\mathrm{ms}$ and $\tau = 10\,\mathrm{ms}$, keeping all the other parameters constant. As expected, the curves are clearly distinguishable when τ takes values similar to T_{ELM}, confirming
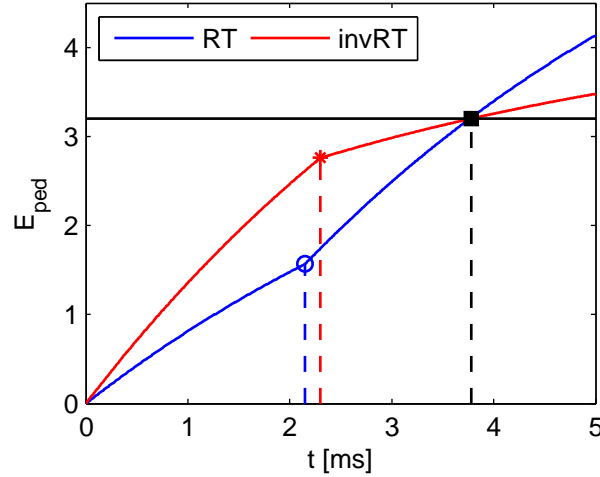
Figure 3.44: Simulations of $E_{\mathrm{ped}}(t)$ by the finite confinement time integrator in the RT (circle) and invRT (star) modes, for $\tau = 5\,\mathrm{ms}$ and Δt_L, resp. Δt_H, tuned to yield the same ELM period. The duration of the high power phase is longer in the invRT mode. $C = 500\,\mathrm{kW}$ and $E_{\mathrm{thres}} = 3.2\,\mathrm{kJ}$ in both cases.

the $\tau > T_{\mathrm{ELM}}$ interpretation of the experimental results. The difference of power consumption at equal ELM frequency predicted for low values of τ for the RT and invRT modes is explained by figure 3.44. The RT mode smartly distributes the power in the ELM cycle so that the low power phase is active where it is least sensitive to finite τ effects, consequently reducing the duty cycle of the modulation while maintaining the same ELM period. In the frame of the finite confinement time model, the fact that the ELM frequency only depends on the average power over an ELM cycle therefore only holds because, in the range of studied plasma parameters, the inequality $T_{\mathrm{ELM}} < \tau$ holds. If the ELM period were longer, the RT modulation scheme would result in a higher ELM frequency than the stationary heating, but in any case this would not be related to a "kick effect".

The simulations of $\sigma_T(P_{\mathrm{input,X2}})$ and $\sigma_T/T_{\mathrm{ELM}}(P_{\mathrm{input,X2}})$ for various values of τ are plotted in figures 3.45(a) and 3.45(b), respectively. As expected, σ_T considerably increases as τ gets closer to T_{ELM}. The decrease of $\sigma_T/T_{\mathrm{ELM}}$ with power, observed experimentally but not reproduced by the perfect integrator model, is now clearly apparent when using a realistic value of τ. The effect is visible even if $\tau > T_{\mathrm{ELM}}$ (see the $\tau = 10\,\mathrm{ms}$ case) and is therefore consistent with previously described constraints on τ.

(a) Simulated $\sigma_T(P_{\mathrm{input,X2}})$ **(b)** Simulated $\sigma_T/T_{\mathrm{ELM}}(P_{\mathrm{input,X2}})$
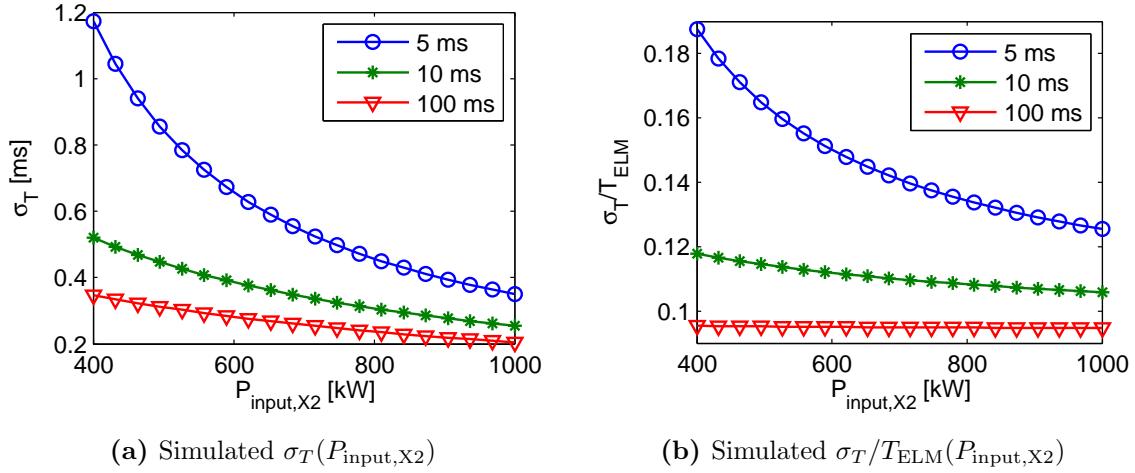
Figure 3.45: Simulations of σ_T and $\sigma_T/T_{\mathrm{ELM}}$ versus $P_{\mathrm{input,X2}}$ by the finite confinement time integrator in stationary mode, for $\tau = 5\,\mathrm{ms}$ (circles), $\tau = 10\,\mathrm{ms}$ (stars) and $\tau = 100\,\mathrm{ms}$ (triangles). $C = 500\,\mathrm{kW}$, $E_{\mathrm{thres}} = 3.2\,\mathrm{kJ}$ and $\sigma_{\mathrm{thres}} = 0.15\,\mathrm{kJ}$ in all cases. To be compared with figure 3.21.

(i) Based on $f_{\mathrm{ELM}}(P_{\mathrm{input,X2}},\theta_l)$ **(ii)** Based on $\Delta W(P_{\mathrm{input,X2}},\theta_l)$
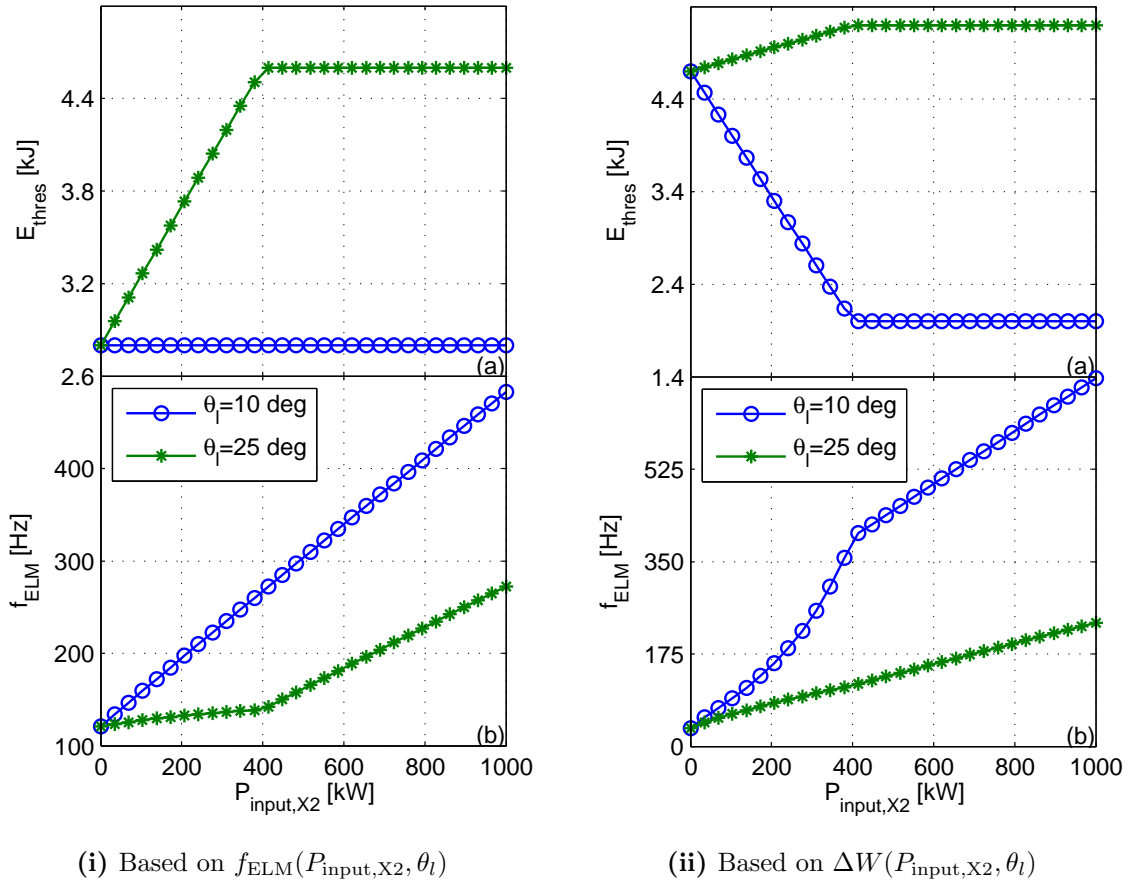
Figure 3.46: Bottom figures: simulations of $f_{\mathrm{ELM}}(P_{\mathrm{input,X2}})$ by the finite confinement time integrator model in stationary mode for $\theta_l = 10°$ (circles) and $\theta_l = 25°$ (stars). **(i)** $E_{\mathrm{thres}}(P_{\mathrm{input,X2}},\theta_l)$ (fig. **(i)**(a)) optimized to reproduce $f_{\mathrm{ELM}}(P_{\mathrm{input,X2}},\theta_l)$ data (figure 3.5(a)). **(ii)** $E_{\mathrm{thres}}(P_{\mathrm{input,X2}},\theta_l)$ (fig. **(ii)**(a)) obtained by scaling $\Delta W(P_{\mathrm{input,X2}},\theta_l)$ data (figure 3.6(a)) consistently with $E_{\mathrm{thres}}(400\,\mathrm{kW},17°) = 3.2\,\mathrm{kJ}$. $\tau = 10\,\mathrm{ms}$ and $C = 500\,\mathrm{kW}$ in all cases.

3.5.4   Dependence on the launcher angle

It has been experimentally demonstrated that the ELM frequency increases and the ELM amplitude decreases when the launcher angle is decreased (i.e. when power is deposited closer to the plasma separatrix, see section 3.3). The finite confinement time integrator model can reproduce these results if, in agreement with the experimental results, the energy threshold is expressed as a function of the launcher angle. To ensure continuity of the ELM frequency at $P_{X2} = 0$, E_{thres} must, in that case, also be a function of P_{X2}, at least close to $P_{X2} = 0$, where the same ELM frequency must be obtained for any value of the launcher angle. This last requirement, however, can only be true for a limited range of P_{X2} to remain consistent with the results discussed above. From figures 3.5(a) and 3.6(a), it is reasonable to limit this range to $[0,400]$ kW. A simulation of $f_{ELM}(P_{input,X2})$ for $\theta_l = 10°$ and $\theta_l = 25°$ is presented in figure 3.46, where E_{thres} has been tuned to reproduce the $f_{ELM}(P_{input,X2}, \theta_l)$ data shown in figure 3.5(a) (figure 3.46(i)) or to respect the scaling of the $\Delta W(P_{input,X2}, \theta_l)$ data shown in figure 3.6(a) (figure 3.46(ii)). In the former case, the tuning of E_{thres} does not respect the experimental results: E_{thres} is constant for the $\theta_l = 10°$ branch and increases linearly in the $[0,400]$ kW domain for the $\theta_l = 25°$ branch. When respecting the scaling of the experimental data for ΔW, the resulting simulation of f_{ELM} (figure 3.46(ii)) shows trends that are somewhat different from the experimentally observed ones. The origin of these inconsistencies has not been clearly identified. A possible explanation is the assumption that τ depends neither on the input power nor on the launcher angle. The guess made for the values of the model parameters might also be too imprecise, these inconsistencies revealing here the problem of correlations present between these parameters. The model itself might also not be capable of capturing all the physics at play. If the origin of the experimentally observed (figure 3.5(a)) change of slope occurring in the $\theta_l = 25°$ branch of $f_{ELM}(P_{input,X2})$ were understood, the modelling of the dependence on θ_l could possibly be more robust. Note that the variation of the absorbed power between $\theta_l = 10°$ and $\theta_l = 25°$ has not been taken into account in these simulations.

Finally, a simulation of $\sigma_T(P_{input,X2}, \theta_l)$ by the finite confinement time integrator model is plotted in figure 3.47. The input parameters are identical to those used in figure 3.46(i) with, in addition, a linear increase of σ_{thres} with E_{thres}. Even though a finite value of τ is sufficient to reproduce a variation of σ_T with θ_l, the experimental results (figure 3.25(a)) are better matched if the threshold variability is proportional to E_{thres}.
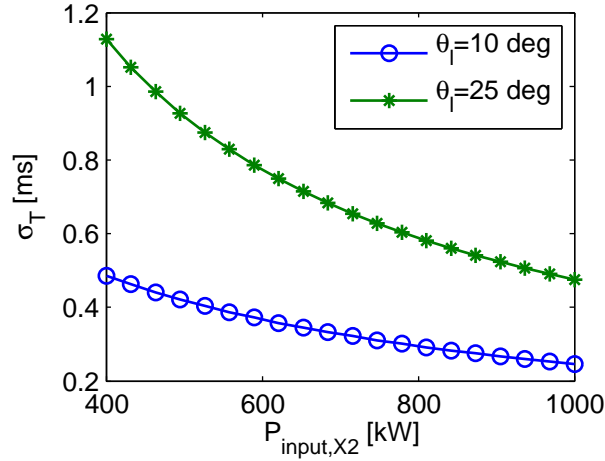
Figure 3.47: Simulations of $\sigma_T(P_{\text{input,X2}})$ by the finite confinement time integrator in stationary mode for $\theta_l = 10°$ (circles) and $\theta_l = 25°$ (stars). Model parameters are identical to those used in figure 3.46(i) ($E_{\text{thres}}(\theta_l = 10°) = 2.8\,\text{kJ}$, $E_{\text{thres}}(\theta_l = 25°) = 4.6\,\text{kJ}$, $\tau = 10\,\text{ms}$ and $C = 500\,\text{kW}$), with in addition $\sigma_{\text{thres}}(\theta_l = 10°) = 0.15\,\text{kJ}$ and $\sigma_{\text{thres}}(\theta_l = 10°) = 0.25\,\text{kJ}$. To be compared with figure 3.25(a).

3.5.5 Summary of the 0-D model results

This section aimed at identifying a simple 0-D model of the ELM cycle able to reproduce most of the observed experimental results and to guide their interpretation. It has been shown that the perfect integrator model, where ELMs are triggered by the crossing of an energy threshold subject to a small variability, successfully reproduces a large fraction of these results (type I ELMs, $\sigma_T \searrow$ if $P \nearrow$, ΔW and $\sigma_{\Delta W}$ mostly independent of the input power at constant θ_l, f_{ELM} independent of the waveform of the input power within an ELM cycle, σ_T decreases in RT mode and increases in invRT mode, no or weak correlation between ELMs). Note that, in this model, the variability of the energy threshold is equivalent to a variable offset on the initial conditions of the energy integration. To reproduce the decrease of σ_T/T_{ELM} with input power, and to be more physically realistic, a finite confinement time term has been added to the model. Comparing simulations to experiments, it appeared clearly that the inequality $\tau > T_{\text{ELM}}$, valid in the plasma and heating configurations studied here, explains why f_{ELM} is independent of the waveform of the input power within an ELM cycle. Finally, the model has been tested against the ELM control experiments by adding a dependence on θ_l in E_{thres} and σ_{thres}. While the overall trends are reproduced, inconsistencies appear in the detail of the simulations, showing either the limits of the model itself or the limits of the crude estimation of the model input parameters used here.

3.6　　Conclusions and outlook

The experiments of ELM control by the application of ECRH to the edge of a type I ELMing H-mode plasma in TCV have led to a rich variety of results, many novel to the field.

The ELM control experiments, consisting mainly of scans of power deposition location, have revealed that the ELM frequency increases and the relative plasma energy loss per ELM decreases significantly when the ECRH beam is moved in the pressure pedestal region toward the plasma separatrix, an effect that is independent of the total input power. Although the power deposited in the edge is poorly confined compared to core heating, a decrease of the energy loss per ELM is of enormous value for machines such as ITER where the power peaks at the divertor due to unmitigated ELMs cannot be tolerated. The energy cost of this method could well be tolerable if its effectiveness is confirmed. These new results also put into question the common assumption that heating methods and deposition location are not important with regards to ELMing H-mode physics [26] and present a new challenge to models claiming to explain the ELM dynamics, as well as to scaling laws used to predict ITER scenarios. Contrary to RMP (see section 2.3.2), where ELMs are mitigated or suppressed under certain plasma conditions, ELM control by plasma edge ECRH does not lead to a complete ELM suppression. However, the range of plasma parameters for which the ELM mitigation works is as yet unknown and might be less restrictive than that of RMP. In addition, contrary to in-vessel coils, which represent a significant engineering problem in a burning plasma environment, ECRH systems have been present in Tokamaks for a long time and have always been considered as essential parts of ITER. ELM control by plasma edge ECRH, only requiring a dedicated launcher and sufficient input power, is therefore a technically interesting solution to the ELM problem.

The ELM pacing experiments, based on input power modulation with and without real-time synchronization with the ELM cycle, revealed that pacing is possible with ECRH, but that only real-time synchronized power modulation succeeds in providing a robust pacing of the ELMs. Comparison with various modulation schemes clearly established that the standard deviation of the ELM period depends primarily on the instantaneous power at the ELM time. It is therefore clear that the ELM pacing technique, by synchronizing the high power phase with the ELM time, relies on this physical property. Another property revealed by these experiments is the independence of the ELM frequency on the exact waveform of the power in the ELM

cycle. The hope of using ECRH power modulation to trigger ELMs with reduced power consumption cannot therefore be realized, at least in the conditions of these experiments. The feed-forward power modulation experiments not only confirm this fact, but also explain the preliminary ASDEX Upgrade results [43] as a special case of ELM and power modulation synchronicity caused by a particularly fortunate choice of experimental parameters. While the standard deviation of the ELM amplitude is not affected by a stabilization of the ELM period, rare transient events with large ELM amplitudes are observed to be less frequent in real-time controlled phases. Although no systematic study has been done on this particular aspect, a reliable avoidance of large amplitude ELMs by real-time ELM pacing would be of significant value for Tokamaks of fusion reactor scale. Finally, the random Δt_L experiment clearly demonstrates that each ELM is individually controllable by combining a controlled level of average power delivered during the ELM cycle with a high power phase at the ELM time.

A large proportion of these experimental results are consistent with a simple 0D model of the ELMs where the plasma edge is described as a finite confinement time energy integrator with variable energy threshold. This crude model, although over-simplifying the physical mechanism at play here, reproduces the experimental results rather accurately, particularly for the ELM pacing experiments and for the lack of dependence of the ELM frequency on the input power waveform.

The study presented here opens various paths of experimental research. Although global plasma parameters have mainly been used here to analyze the experimental data, accurate density and temperature profile measurements are necessary to investigate the physical mechanisms at the root of ELM control by plasma edge heating. These measurements would require long stationary phases of ECRH injection at various locations, so that CAS methods can be applied to the Thomson scattering data. To achieve an optimal space resolution, a modification of the lines of sight of the Thomson scattering system would be necessary. Another possibility, consistent with TCV's poloidal coils, would be to turn the plasma configuration upside down. This configuration would allow the usage of the X2 launchers located on the upper lateral ports, increasing the available input power. In addition, the heating setup would allow more flexibility on the vertical location of the plasma, which would not only be helpful for the Thomson scattering diagnostics, but also for the CXRS diagnostics (to measure the ion temperature). However, the power flux on the low field side tiles, in particular on the corner tiles for CXRS measurements, might be a limiting factor. This configuration also requires a reversal of the toroidal magnetic

field, to keep the same favorable $\mathbf{B} \times \nabla B$ ion-drift direction. Among the list of research subjects potentially linked to the study presented here, the following areas are of particular interest:

- An extension of the studies conducted here in type III ELM regime. Type III ELMs are indeed met at higher densities in an otherwise identical experimental setup. The small range of densities resulting in type III ELMs without refracting the X2 beams will certainly be a significant limiting factor.

- The use of X3 power modulation to pace the ELMs. Even though the total input power would remain the same in this scenario, the impact on the central electron temperature when modulating X3 power would be significantly different. The delay due to the transport of energy from the core to the edge of the plasma might also cause differences in the ELM response. This study would be of importance for comparison with other Tokamaks, where edge heating is not possible. Note that the limited flexibility of the X3 gyrotrons with regard to power modulation might restrict the range of possible duty cycles and modulation frequencies.

- On a longer term, when the X3 power upgrade [78] is implemented, X3 beams will be available from the low field side launchers and more power will be available from the top launchers. The additional X3 power (top launchers) will be useful to determine the ratio of edge to core heating necessary to control the ELMs. As for the side launchers firing X3 beams, they will allow the completion of the power deposition location scan toward the plasma core.

Chapter 4

Magnetic perturbation spectrum optimization

4.1 Introduction

4.1.1 Principle of RMP

As described in section 2.3.2, resonant magnetic perturbation (RMP) consists in applying a magnetic field perpendicular to the plasma equilibrium flux surfaces with a spatial variation tuned to align with the equilibrium magnetic field lines. RMP has been observed to mitigate or suppress ELMs on a number of Tokamaks [10,11,35,36]. The magnetic perturbation is generally created by a set of poloidally and toroidally distributed coils having mainly a radial field contribution. As, in DIII-D, the ELM suppression only occurs for a window of q_{95} values (edge safety factor) corresponding to a resonant magnetic perturbation situation [79], the name RMP has been retained for this ELM control technique. In addition, the condition of minimal width of the ergodization layer at the plasma edge [80] (vacuum magnetic field calculation states $\Delta\psi_{01} = 0.17$, with ψ_{01} the normalized poloidal flux) suggests that ELM mitigation or suppression by RMP is related to the overlap of the magnetic islands created by RMP (see section 2.2.1). In the frame of this interpretation, the ergodic zone created in the plasma edge increases the outward transport and thereby limits the pedestal gradients to values below the instability limits. There are nonetheless a number of arguments against this simple description of the RMP mechanism. A direct application of stochastic diffusion theory, for example, does not reproduce the modification of the pedestal profiles observed experimentally [41]. The crucial aspect of magnetic perturbation screening due to plasma rotation is also not included

in this description. Even though research is still on going in this particular area, it is certain that global plasma rotation, or electron fluid rotation, leads to a significant reduction of the resonant perturbation amplitude [81–83], possibly exceeding an order of magnitude [84] or even close to total screening [85]. Experimentally, the ELM mitigation requirements based on the DIII-D results are only partially confirmed on MAST [37, 86], where, similarly to DIII-D, a significant increase of the type I ELM frequency is obtained in a narrow interval of q_{95} values, but, contrary to DIII-D, the width of the ergodized edge layer also satisfies the DIII-D criterion outside this interval of q_{95} values. Even more significantly, recent experiments have demonstrated that ELM mitigation is achieved on a wide safety factor range on ASDEX Upgrade [11], weakening the assumed necessity of resonant perturbation. Note however that the DIII-D and the ASDEX Upgrade results differ in the plasma regime at which ELM control is achieved, the DIII-D results being valid at low plasma collisionality while the ASDEX Upgrade results are valid at high plasma collisionality.

In this chapter, a generic magnetic perturbation spectrum optimization method based on vacuum field calculation (i.e. where the perturbation field is calculated in vacuum and added to the unperturbed axisymmetric equilibrium field) is described. It is then applied to the special case of RMP, using in addition the optimization of a dedicated figure of merit. While this approach relies on the initial interpretation of the DIII-D results, the recent ASDEX Upgrade results and the expected large perturbation screening, although calling for a change of paradigm, do not entirely depreciate it. Despite the ASDEX Upgrade results, the DIII-D, MAST and even JET [42] results still support a physical interpretation where resonance plays a significant role. While the vacuum magnetic perturbation spectrum might not be the most relevant parameter to understand the effect of magnetic perturbations on ELMs, the new paradigm will certainly have to include it. Being able to act on it in an optimal way would then be a precious experimental tool.

4.1.2   Principles of RMP spectrum optimization

When applying asymmetric magnetic perturbations to generate RMP, the spectrum of the perturbation should be optimized for what is thought to be efficient for ELM mitigation [87, 88]: (a) minimal resonant mode amplitude in the core to avoid triggering of MHD instabilities, (b) maximal resonant mode amplitude near the edge to obtain the ergodization of the edge region, (c) minimal non resonant mode amplitude to avoid parasitic effects such as plasma braking or acceleration due to neoclassi-

cal toroidal viscosity [82, 89, 90] and (d) no or minimal side-band modes to avoid parasitic effects that could impair the interpretation of the experimental results. Technically realistic coil current requirements must also be maintained in the process. All these aspects justify the development of the optimization method presented in this chapter.

Error fields are another aspect of toroidally asymmetric magnetic fields. They are typically due to construction tolerances in Tokamak coil positions and shapes. These fields, dominated by low values of the toroidal mode number, induce plasma braking and locked modes [91], themselves responsible for disruptions. Their effects can be corrected by applying an asymmetric field of opposite phase. Despite the distinction often present in the literature, error field correction (EFC) and RMP are strongly related, since they both rely on effects due to the component of a non axisymmetric perturbation magnetic field perpendicular to the flux surfaces. In the case of EFC, both non resonant and resonant perturbations are present. In the case of RMP, the focus is on resonant perturbations, but non resonant ones generally dominate in amplitude. Both concepts can and should therefore be studied with the same set of tools.

When EFC or RMP coil systems are fed with independent power supplies, the effectiveness of the created perturbation may be enhanced by a fine tuning of the relative distribution of currents in the coils. Hanson [92, 93] has developed a method of optimization of the correction coil currents based on a least square approach and working with Fourier components in the current space, consequently limited to evenly-spaced coil systems. We present here (section 4.2) a method of optimization of the currents of generic coil systems based on Lagrange multipliers and working in real current space. This method is not limited to evenly-spaced identical coil systems and allows simultaneous multi-mode optimization. It would therefore also be adequate if one of the coils becomes unavailable. Using a Lagrange method allows to distinguish between constraints to satisfy exactly – e.g. the corrected error field – and optimization of cost functions – e.g. the minimization of core islands in the case of ELM mitigation. We show (section 4.2.5) that the Lagrange method is an efficient way to minimize parasitic modes and current requirements while imposing the amplitude and phase of a set of target modes. For example, the relative amplitude of edge modes can be increased at the cost of lower absolute amplitudes, demonstrating a degree of controllability on the localization of the magnetic perturbation. In this process, a figure of merit may be used to quantify the optimization of the magnetic spectrum. Section 4.2.3 shows how the Lagrange method is used to
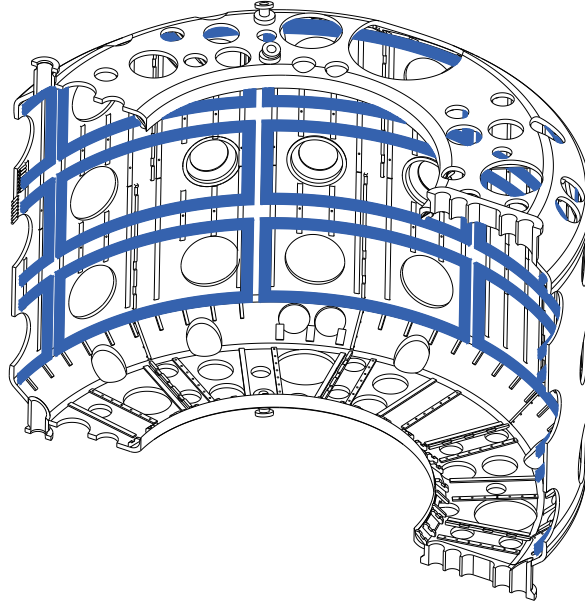
Figure 4.1: Perspective view of the in-vessel design of the SCS project (in blue) for TCV, drawn on top of the vacuum vessel (in black). The system consists of 3 rows of 8 internal saddle coils located on the low field side of the torus. The coils are toroidally juxtaposed and vertically aligned. The number of turns per coil in the figure is illustrative only.

maximize such a figure of merit. The dependence of the figure of merit on the value of the edge safety factor and the robustness of an optimal current distribution to a change in the plasma equilibrium are analysed in section 4.2.6. Finally, linear optimization methods, as the least square or Lagrange ones, cannot directly minimize the maximal current required in the coil system but rather the norm of the vector made of all the coil currents. The implications of this simplification are described in section 4.2.2 and a workaround is given. We show that in some cases, up to 40% of mode amplitude can be gained for the same maximal coil current (section 4.3.3).

The characterization of a coil system in terms of spectral degeneracy, number of simultaneously controllable target modes, availability of optimization for a given set of target modes and efficiency in each toroidal mode is crucial in order to apply the Lagrange method. The study presented in section 4.3 describes a simple method to obtain such a characterization, using a generalized discrete Fourier transform.

The Lagrange method is illustrated in the special case of a multi-purpose in-vessel saddle coil system (SCS) proposed as part of a future upgrade of TCV (figure 4.1 and chapter 5). This system consists of 3 rows of 8 internal coils, each coil having independent power supplies.

4.2   Optimization method

In the frame of the vacuum field calculation approach, the RMP modelling is based on the calculation of the width of the magnetic islands generated on resonant flux surfaces by $B_\perp$, the component of the perturbation magnetic field perpendicular to the flux surfaces. An analytical derivation of the width of the islands is given in [92,93] for non circular Tokamak plasmas. We express it here in a form consistent with [94]. The straight field line coordinates (ρ, θ^*, ϕ) [95] are used to describe the perturbation: $\rho = \sqrt{\psi_{01}}$ is the normalized radius (ψ_{01} being the normalized poloidal flux), ϕ the toroidal angle and $\theta^*(\rho, \theta)$ is such that the equilibrium field $\mathbf{B}_0$ follows straight lines in a (θ^*, ϕ)-plane. The Biot-Savart law is used to calculate the vacuum magnetic field perturbation due to the SCS in 3-D. The various coordinate transformations and vector projections are performed in the framework of the ψ-toolbox [95]. The width of the islands is given by:

$$\Delta\rho_s = 4\sqrt{\frac{2|\tilde{b}(\rho_s, m, n)|q_s^2}{|mq_s'|}} \tag{4.1}$$

with m the poloidal mode number, n the toroidal mode number, s the resonant flux surface index, $q' = \mathrm{d}q/\mathrm{d}\rho$ the radial derivative of the safety factor q, and b the locally normalized perpendicular vacuum magnetic perturbation due to the coil system:

$$b(\rho, \theta^*, \phi) = \frac{B_\perp R\|\nabla\rho\|}{B_{0,\phi}} \tag{4.2}$$

with R the major radius coordinate and $B_{0,\phi}$ the toroidal component of the equilibrium magnetic field. In equation (4.1), $\tilde{b}$ is the Fourier transform of b along θ^* and ϕ:

$$\tilde{b}(\rho, m, n) = \frac{1}{(2\pi)^2}\iint_0^{2\pi} \mathrm{d}\phi\mathrm{d}\theta^* b(\rho, \theta^*, \phi)\mathrm{e}^{\mathrm{i}(-m\theta^* - n\phi)} \tag{4.3}$$

The Chirikov parameter [96] σ used to characterize the degree of overlapping of magnetic islands is defined by:

$$\sigma_{s+1/2} = \frac{\Delta\rho_s + \Delta\rho_{s+1}}{2(\rho_{s+1} - \rho_s)} \tag{4.4}$$

The criterion of ergodization is given by $\sigma_{s+1/2} \geq 1$. Equations (4.1) and (4.4) show that $|\tilde{b}|$ is the parameter of interest for studying the efficiency of a given magnetic perturbation.

The cost function f minimized in the Lagrange approach is defined as a linear combination of the current cost function f_{cur} and the cost functions f_k related to

sets of optimized modes S_k:

$$f(\{I_c\}) = f_{\text{cur}}(\{I_c\}) + \sum_k w_k f_k(\{I_c\}) \tag{4.5}$$

with I_c the coil currents. w_k are relative weights, with $w_k > 0$ (resp. $w_k < 0$) for a minimization (resp. maximization) of f_k. The weight on f_{cur} is used as reference and is set to 1. f_k and its normalization factor N_k are chosen as:

$$f_k = \frac{1}{N_k} \sum_{p \in S_k} \left[\left(\sum_c \tilde{b}_{cp,r} I_c - \Re(a_p e^{i\alpha_p}) \right)^2 + \left(\sum_c \tilde{b}_{cp,i} I_c - \Im(a_p e^{i\alpha_p}) \right)^2 \right] \tag{4.6}$$

$$N_k = \sum_{p \in S_k} A_p^2 \tag{4.7}$$

$$A_p = \left[\left(\sum_c |\tilde{b}_{cp,r}| \right)^2 + \left(\sum_c |\tilde{b}_{cp,i}| \right)^2 \right]^{1/2} \tag{4.8}$$

with p the index on the modes in S_k (each value of p corresponds to a point (ρ, m, n)), $\tilde{b}_{cp,r}$ (resp. $\tilde{b}_{cp,i}$) the real (resp. imaginary) part of mode p due to a unit current in coil c and $a_p e^{i\alpha_p}$ the target value to be approached for mode p, with amplitude a_p and phase α_p. A_p is a measure of the natural distribution of the amplitude of the modes created by the SCS. Note that even though a maximization of f_k is possible when using a negative weight, f, as a quadratic form, must remain positive definite to ensure that its constrained extremum is neither a maximum nor a saddle point. Consequently, a negative weight should always be chosen so that the maximized cost function, i.e. that with $w_k < 0$, does not dominate the overall cost.

The exact target modes, i.e. the constraints of the Lagrange method, are a set of modes whose amplitudes a_t and phases α_t must be exactly matched by the coil system. They are introduced by defining:

$$g_{t,r}(\{I_c\}) = \sum_c \tilde{b}_{ct,r} I_c - \Re(a_t e^{i\alpha_t}) \tag{4.9}$$

$$g_{t,i}(\{I_c\}) = \sum_c \tilde{b}_{ct,i} I_c - \Im(a_t e^{i\alpha_t}) \tag{4.10}$$

with t the index on the target modes. The constraints are fulfilled if:

$$g_{t,r}(\{I_c\}) = 0 \qquad g_{t,i}(\{I_c\}) = 0 \qquad \forall t \tag{4.11}$$

Note that the constraint part depends linearly on the currents. If the phases of the approximative or exact target modes are free parameters, an iterative process is used to select the phase combination leading to the lowest total cost f.

Finally, the Lagrange method requires an auxiliary function h defined by:

$$h(\{I_c\}, \{\lambda_t\}) = f(\{I_c\}) + \sum_t [\lambda_{t,r} g_{t,r}(\{I_c\}) + \lambda_{t,i} g_{t,i}(\{I_c\})] \qquad (4.12)$$

with Lagrange multipliers λ_t. The constrained optimum is found by solving:

$$\nabla_{\{I_c\},\{\lambda_t\}} h = 0 \qquad (4.13)$$

The solution must then be checked to be a minimum. A simple approach consists in exploring the affine sub-space of solutions around the optimal coil current vector $\mathbf{I}_{\text{opt}}$. Defining the constraint matrix $\mathbf{C}$ as:

$$\mathbf{C} = \left(\begin{array}{c} \left(\tilde{b}_{ct,r} \right) \\ \left(\tilde{b}_{ct,i} \right) \end{array} \right), \qquad (4.14)$$

the coil current vectors fulfilling the constraints are given by: $\mathbf{K} + \mathbf{I}_{\text{opt}}$ where $\mathbf{K} \in \ker(\mathbf{C})$, the null space of $\mathbf{C}$. $\mathbf{I}_{\text{opt}}$ is a minimum of f if $f(\mathbf{I}_{\text{test}}) > f(\mathbf{I}_{\text{opt}})$ for any $\mathbf{I}_{\text{test}} = \mathbf{I}_{\text{opt}} \pm \epsilon \|\mathbf{I}_{\text{opt}}\| \mathbf{k}_i$ where $\mathbf{k}_i$ is the i-th base vector of $\ker(\mathbf{C})$ and ϵ is small.

Note: if some of the coils have a fixed connection, their respective magnetic fields must be combined prior to the application of the optimization method. The subset of connected coils should then appear as a single equivalent coil.

4.2.1 Linear approach

In the linear approach, $\nabla_{\{I_c\}} f$ must be a linear combination of the coil currents. The current cost function is therefore defined as:

$$f_{\text{cur}} = \frac{1}{N_{\text{coils}}} \sum_c I_c^2 \qquad (4.15)$$

where N_{coils} is the total number of coils. In this case, solving (4.13) is equivalent to inverting a full rank linear system of equations.

4.2.2 Non linear approach

The linear method presented in section 4.2.1 minimizes the norm of the current vector, a simplified version of the non linear real technical constraint: $\max_c(|I_c|)$. A non linear algorithm has been created to minimize f_{nl}, the non linear cost function given by using $\max_c(I_c^2)$ instead of $\sum_c(I_c)^2$ in f_{cur}. This algorithm is based on the exploration of the affine space of currents fulfilling the constraints, starting from the solution provided by the linear approach. It calculates the cost in each orthogonal

direction and moves to the combination of directions minimizing the cost. Note that when using the non linear cost for evenly spaced coil systems, side-band modes must be introduced in the cost function to force their minimization, otherwise the system would be underdetermined.

If the target mode phases are free parameters, an efficient approach consists in using the linear solution for each (discrete) phase combination, but using the non linear cost function to select the optimal phase combination. This approach has been retained as the standard resolution method.

4.2.3　RMP spectrum optimization

The choice of the sets S_k of optimized modes and their respective cost function weights w_k in (4.5) is usually driven by physical requirements: low coil currents or high relative amplitude of a certain region of the magnetic spectrum. In certain cases, the requirements can be summarized by a figure of merit, qualifying to which extent these requirements are met. In some ways, this approach replaces the arbitrary choice of weights by an arbitrary definition of a figure of merit. In this section, the choice of the cost function used for RMP spectrum optimization is described. A figure of merit is also defined to measure the level of spectrum optimization and guide the choice of the relative cost function weights.

4.2.3.1　Cost functions and target modes

In the case of RMP, the spectrum of b must be optimized to obtain minimal resonant core mode amplitudes, maximal edge ergodization and minimal non resonant mode amplitudes. These conditions are satisfied with an approach based on two sets of modes: the first set, S_e, consists of the resonant edge modes. The second set, S_g, includes all the modes of the spectrum. Formally, S_e and S_g are written:

$$S_e = \{(\rho, m, n) \mid \rho_{\lim} \leq \rho \leq \rho_{95}, \ q(\rho) = m/n, \ n = n_t\} \tag{4.16}$$

$$S_g = \{(\rho, m, n) \mid \rho \leq \rho_{95}, \ -20 \leq m \leq 20, \ n = n_t\} \tag{4.17}$$

with n_t the target value of n, and $\rho_{\lim}$ the inner radius of the selected ergodized zone. The interval $[-20, 20]$ appearing in S_g is chosen as integration boundaries since the mode amplitudes outside this interval are negligible in our application. $\rho_{95} = \sqrt{0.95}$ is used as an upper limit to avoid the singularity due to the X-point at the last closed flux surface. The optimization of the edge mode amplitudes is based on the Chirikov criterion. By analogy with (4.4), the separate contribution of each mode

to the Chirikov parameter is defined as $C_s = \Delta\rho_s/(\rho_{s+1} - \rho_{s-1})$, with an equivalent approximative ergodization criterion given by $C_s = 1/2$. Using (4.1), the minimal mode amplitudes required to ergodize the edge are then given by:

$$a_e = \frac{|mq'_e|(\rho_{e+1} - \rho_{e-1})^2}{128 q_e^2}. \tag{4.18}$$

These values are considered as lower limits for each edge mode in the optimization procedure. When expressed as a function of a_e for the edge modes, C_s is given by $C_e = \frac{1}{2}\sqrt{|\tilde{b}_e|/a_e}$, therefore indicating that it is the relative, and not the absolute, deviation of $|\tilde{b}_e|$ from a_e that matters for the ergodization of the edge (when $|\tilde{b}_e| < a_e$), and that the associated cost function must be based on relative deviations.

The Lagrange method is applied here by associating two cost functions, as defined in (4.6), to both S_e and S_g, respectively f_e and f_g, and by using the mode labelled by $e_{\max}$, the index of the resonant edge mode having the highest a_e, as unique exact target mode[*]. The total cost function f is therefore defined as:

$$f_{\mathrm{RMP}}(\{I_c\}) = f_{\mathrm{cur}}(\{I_c\}) + w_e f_e(\{I_c\}) + w_g f_g(\{I_c\}) \tag{4.19}$$

where f_e acts on modes included in S_e with approximate target amplitudes given by (4.18) and f_g acts on modes included in S_g with null target amplitudes ($a_g = 0$). Note that f_e is only useful in situations where resonant edge mode amplitudes are too small ($|\tilde{b}_e| < a_e$). For the other situations, f_e would decrease the amplitude of these modes, which would be unnecessary and detrimental in terms of edge ergodization. Consequently, an iterative process is used to activate f_e only on the subset of resonant edge modes having $|\tilde{b}_e| < a_e$. In addition, a supplementary normalization of each individual term is necessary in f_e to minimize the relative distance to a_e instead of the absolute one, consistently with the argument mentioned above. Formally, f_e is written as:

$$f_e = \frac{1}{N_e} \sum_{p \in S_e^{sub}} \frac{1}{a_p^2} \left[\left(\sum_c \tilde{b}_{cp,r} I_c - \Re(a_p e^{i\alpha_p}) \right)^2 + \left(\sum_c \tilde{b}_{cp,i} I_c - \Im(a_p e^{i\alpha_p}) \right)^2 \right] \tag{4.20}$$

$$N_e = \sum_{p \in S_e^{sub}} \frac{A_p^2}{a_p^2} \tag{4.21}$$

where $S_e^{sub} = \{p \in S_e \mid |\tilde{b}_p| < a_p\}$.

---

[*] Conceptually, setting an exact target mode ensures that a sensible solution (i.e. $|\tilde{b}| > 0$) is found for any set of weights, in particular for the set $(w_g, w_e) = (0, 0)$.

4.2.3.2   Figure of merit

A definition of a figure of merit r quantifying the quality of a spectrum with respect to RMP is given below:

$$
r = \left[\frac{|\tilde{b}_{e_{\max}}|^2}{\left(1 + \max_{|\tilde{b}_e| < a_e} \left\{ \left((|\tilde{b}_e| - a_e)/a_e \right)^2 \right\} \right) \int_{S_g} |\tilde{b}|^2 \mathrm{d}\rho} \right]^{1/2}
\tag{4.22}
$$

The main term in (4.22) is the ratio between the amplitude of the resonant edge mode requiring the strongest excitation and the integral of the spectrum. This ratio increases as $|\tilde{b}_{e_{\max}}|$ becomes relatively larger and as the spectrum becomes more peaked, so that an increase in r does reflect an increase of quality of the spectrum, as defined in the frame of RMP. The factor $\left(1 + \max_{|\tilde{b}_e| < a_e} \left\{ \left((|\tilde{b}_e| - a_e)/a_e \right)^2 \right\} \right)$ in r is a correction factor which impairs the figure of merit if one of the resonant edge modes has an amplitude lower than the minimal amplitude required for ergodization. The link between r and f_{RMP} is direct, since f_g and f_e are respectively associated with the main term and the correction factor in r.

The optimization of r is obtained by iteratively calculating $r(w_g, w_e)$, increasing w_g, and w_e if necessary, up to a point where the evolution of r becomes insignificant. When increasing w_g, the integral of the spectrum decreases whereas $|\tilde{b}_{e_{\max}}|$ remains constant, therefore increasing r. In this process, if modes with $|\tilde{b}_e| < a_e$ are detected, f_e is activated on this subset of weak modes to limit their negative impact on r.

The approach described above has several advantages: (a) the iterative process of weight selection to optimize r acts on at most two parameters, independently of the considered coil system; (b) the minimization of the coil current is included in f_{RMP}, allowing a direct estimation of the gain in r with respect to the increase in required current; (c) both f_e and f_g are minimized in the proposed process, which means that the existence of a global minimum of f_{RMP} is always guaranteed; (d) the definition of r proposed in (4.22) involves only normalized or relative quantities and is therefore a good candidate to measure the adequacy of a coil system for a range of magnetic equilibria.

4.2.4   Current requirement determination

According to Fenstermacher [80], a $\Delta\psi_{01} = 0.17$ wide ergodization layer at the plasma edge is sufficient to obtain type I ELM suppression on DIII-D. This is equivalent to setting the inner radius of the ergodized zone at $\rho_{\lim} = 0.911$. The minimal

coil current I_{req} required to obtain an ergodization of the edge down to ρ_{lim} is a parameter complementary to r, as it reveals whether the optimal r current distribution is technically feasible. The calculation of this current is based on the satisfaction of the Chirikov criterion in the edge. At ρ_{lim}, a sufficient condition is that the first edge island ($\rho_{\mathrm{first}} > \rho_{\mathrm{lim}}$) overlaps either ρ_{lim} or the last core island ($\rho_{\mathrm{last}} < \rho_{\mathrm{lim}}$). The minimal I_{req} is then determined with (4.1).

4.2.5   Optimization method results

In the case of RMP, the toroidal modes of interest for the TCV SCS are $n = 2$, $n = 3$ and $n = 4$. $n = 1$ could also be considered, but this mode number is more prone to trigger locked modes and disruptions, and is associated with a poor edge ergodization for the typical values of q_{95} on TCV. The results presented here are obtained for a standard diverted H-mode plasma centered on the mid-plane of the machine and characterized by a density on axis $n_e = 7.5 \cdot 10^{19}\,\mathrm{m}^{-3}$, a plasma current $I_p = 415\,\mathrm{kA}$, a toroidal magnetic field on axis $B_{\phi,\mathrm{axis}} = 1.4\,\mathrm{T}$, a major radius $R_{\mathrm{axis}} = 0.91\,\mathrm{m}$, a minor radius $a = 0.22\,\mathrm{m}$, a triangularity $\delta_{95} = 0.4$, an elongation $\kappa_{95} = 1.7$, a normalized pressure $\beta_p = 0.65$ and an edge safety factor $q_{95} = 2.6$.

4.2.5.1   Dependence of r and I_{req} on the cost function weights

Figure 4.2 (solid lines) shows the figure of merit r as a function of the weight w_g for the different values of n_t. The maximum of r has an asymptotic character. This feature is inherent to the method since the current distribution converges to a fixed distribution as the f_e and f_g terms dominate in f_{RMP}, leading to a saturation of r. The asymptotic value will be referred to as the optimal r in the remainder of this chapter. The experimental equilibrium used for the calculation of r shown in figure 4.2 does not require the activation of f_e because the resonant edge modes stay at amplitudes above the Chirikov criterion for all values of w_g. A synthetic equilibrium case requiring the activation of f_e is presented in figure 4.3. The same saturation mechanism occurs, but its location now depends on the ratio of w_e and w_g. Due to the very small gradient of r around its asymptotic maximum, any set of weights chosen in this area can be considered as satisfactory.

Figure 4.2 (dash-dotted lines) shows I_{req} as a function of w_g. As expected, the lowest current is obtained when w_g is close to zero. The slight offset in the location of the minimum of the current, observable for $n_t = 2$ and $n_t = 3$, is a consequence of the semi-linear approach used to define the current cost function f_{cur}, as described
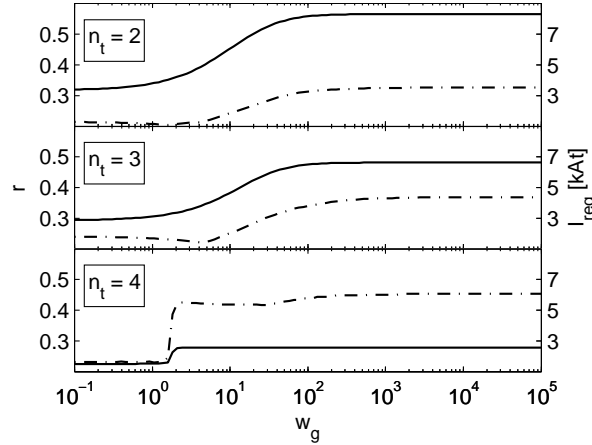
Figure 4.2: Figure of merit r (solid lines) and required current for edge ergodization I_{req} (dash-dotted lines) as a function of the weight w_g in the cases $n_t = 2$, $n_t = 3$ and $n_t = 4$. For the reference plasma equilibrium considered here, r is independent of w_e.
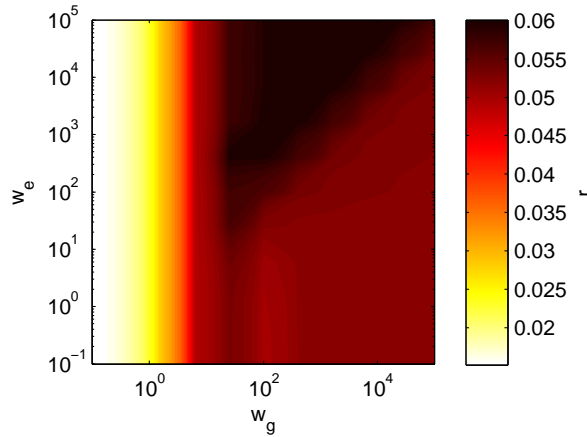
Figure 4.3: Figure of merit r as a function of the weights for a synthetic equilibrium case ($n_t = 3$, $q_{95} = 8.3$). The dependence of r on w_e appears for $w_g > 20$.

in section 4.2.2: minimizing the norm of the current vector does not guarantee to obtain the lowest maximal current. Figure 4.2 also shows that I_{req} remains within acceptable values when r is optimal. It must be noted that the edge ergodization criterion is satisfied at much lower currents if larger non resonant components are allowed, leaving some margin on the coil current requirement.

4.2.5.2   Optimal cases for $n_t = 2$, $n_t = 3$ and $n_t = 4$

For each value of n_t, the current distribution minimizing the current requirements and the current distribution maximizing the figure of merit represent both optimal cases, from the technical or the physical point of view. Each case is associated with a set of weights, respectively $(w_e, w_g) = (0, 0)$ and $(w_e, w_g) = (0, 10^5)$ (see figure 4.2,

noting that r is independent of w_e here). The optimization method efficiency is assessed here by means of the perturbation spectra and ergodization maps. The latter are obtained by plotting the location of the generated islands as a function of the SCS current and the flux surface coordinate on a 2D map, and are useful to visualize the localization of the ergodized regions. This method of analysis is similar to a radial profile of the Chirikov parameter but solves the issue of island pairing inherent to the Chirikov approach.

Figures 4.4(a) to 4.4(f) show $|\tilde{b}|$ for the different values of n_t in both optimal cases. In each case, a maximal coil current of $1\,\mathrm{At}$ is used to facilitate the comparison of the perturbation amplitudes. The associated ergodization maps are shown in figures 4.5(a) to 4.5(f), where the maximal current used in each case corresponds to a maximal value of $B_\perp$ at the plasma separatrix of $5.3\,\mathrm{mT}$, equivalent in relative value to the perturbation applied in DIII-D. For each toroidal mode number target, the method proves its efficiency at either minimizing the currents (observed here by a higher absolute amplitude of the modes) or optimizing the spectrum, i.e. increasing the relative amplitude of the resonant edge modes. For $n_t = 3$ (figures 4.4(c) and 4.4(d)), the optimization of the spectrum has the side effect of increasing the relative amplitude of non resonant edge modes. This reveals that despite the clear advantage of using the optimization method, the low number of degrees of freedom imposes limits on the process. Even though $n = 3$ is not a natural mode of the coil system, the edge mode amplitudes are comparable to those of $n_t = 2$ (figure 4.4(b)), proving the flexibility of the system and allowing this configuration for experimental studies. It should also be noted that the obtained perturbation is a pure $n = 3$ mode (i.e. no $n = 0$, $n = 1$, $n = 2$ or $n = 4$ components), within the limit of the degeneracy described in section 4.3.

The case $n_t = 4$ (figures 4.4(e) and 4.4(f)) is a special case for the coil system considered here, as it corresponds to $n_t = N_s/2$ where N_s is the number of coils per row. In this case, the system has a higher order of symmetry ($b(-\phi) = b(\phi)$) which results in a symmetrical spectrum with respect to $m = 0$, and hence a lower number of available degrees of freedom. Using a higher value of n_t has two downsides in terms of RMP: first the activated edge modes have a lower amplitude since the values of m required for the same value of q are higher, second the width of the islands is smaller due to the factor m in (4.1). However, in the case $n_t = N_s/2$, each coil in the same row is powered with the same current amplitude, resulting in a larger perturbation than for the other cases, and the number of resonant flux surfaces, therefore the number of islands, is also larger. Altogether, these effects

compensate each other and result in good performances of the system for $n_t = 4$, as shown in figure 4.5(f). Such a configuration is also interesting as the corresponding degenerate modes are extremely weak (see section 4.3).

The current distributions corresponding to both $n_t = 2$ cases are displayed in figures 4.6(a) and 4.6(b). In the case where r is optimized, the bottom and top rows of coils, less efficient in terms of magnetic perturbation amplitudes, have much larger currents. This behaviour is consistent with the optimization of r, which shapes the perturbation spectrum using all the available degrees of freedom, without taking the current consumption into consideration.

4.2.6   Edge safety factor dependence and robustness analysis

The results shown in section 4.2.5 have all been generated with the same experimental equilibrium. It is of interest to study how the optimal figure of merit and its associated required current evolve with respect to a change in the magnetic equilibrium, since such a study contributes to the assessment of the adequacy of a RMP coil system. Amongst the different equilibrium parameters that impact the effects of a coil system, q_{95} is certainly the most important one since it determines which components of the perturbation spectrum must have the largest amplitudes, and consequently has a strong influence on r and I_{req}. For this study, a series of synthetic equilibria generated with the free boundary code FBTE [97] are used to simulate a scan on q_{95} while keeping other parameters as constant as possible. These equilibria are characterized by: $q_{95} \in [2.0, 8.3]$, $q_{\mathrm{axis}} = 0.8$, $I_p \in [575, 125]\,\mathrm{kA}$, $\beta_p = 0.36$, $\delta_{95} \in [0.42, 0.30]$, $\kappa_{95} \in [1.70, 1.58]$, $B_{\phi,\mathrm{axis}} = 1.4\,\mathrm{T}$, $R_{\mathrm{axis}} = 0.89\,\mathrm{m}$ and $a = 0.23\,\mathrm{m}$.

4.2.6.1   Dependence of r and $I_{\mathbf{req}}$ on q_{95}

The solid lines in figures 4.7 and 4.8 show the optimal figure of merit r_{opt} and its associated I_{req} as a function of q_{95}. One can observe that $r_{\mathrm{opt}}(q_{95})$ mainly decreases as q_{95} or n_t increases, consistently with the naturally low amplitude of higher m modes. The small undulations of r_{opt} along q_{95} are due to the regular crossing of higher amplitude ridges naturally appearing in the spectra (see figures 4.4(b), 4.4(d) and 4.4(f)) as the locus of resonant surfaces moves to higher values of m. $I_{\mathrm{req}}(q_{95}, r_{\mathrm{opt}})$ displays various behaviours as q_{95} increases. At low q_{95}, I_{req} manifests oscillations whose amplitude decreases with n_t and q_{95}. For these values of q_{95}, I_{req} is always determined by the first edge island ($\rho_{\mathrm{first}} > \rho_{\mathrm{lim}}$) and the oscillations are hence due to variations in the distance between the ergodized region limit ρ_{lim} and

(a) $n_t = 2$, minimal current

(b) $n_t = 2$, optimal spectrum

(c) $n_t = 3$, minimal current

(d) $n_t = 3$, optimal spectrum

(e) $n_t = 4$, minimal current

(f) $n_t = 4$, optimal spectrum
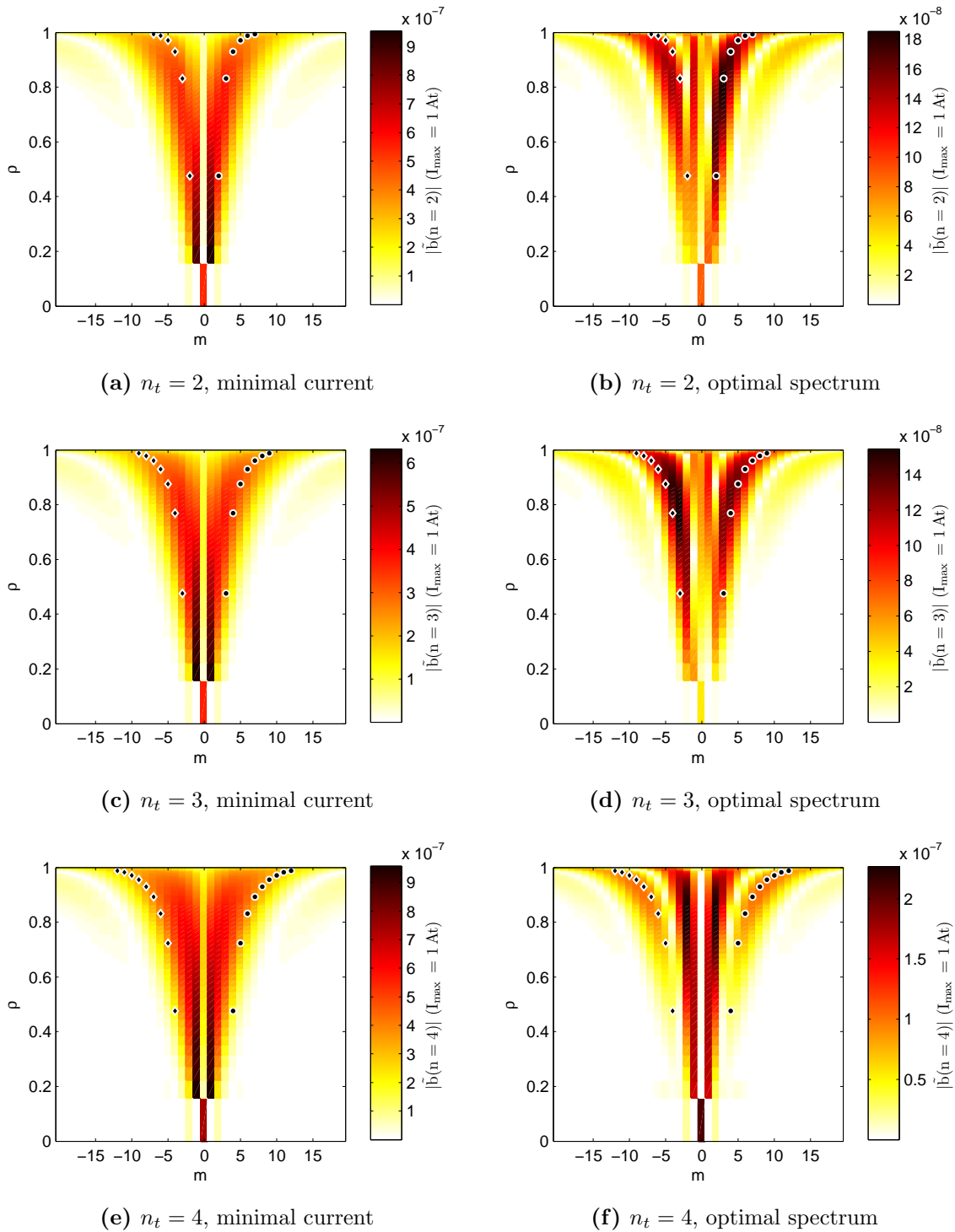
Figure 4.4: $\left| \tilde{b}(\rho, m, n \in \{2; 3; 4\}) \right|$. Target: outside $\rho_{\mathrm{lim}} = 0.911$. ● : resonant flux surface locations, ◆ : symmetrical non resonant counterparts. Case: in-vessel, $z_{\mathrm{mag}} = 0$.

(a) $n_t = 2$, minimal current

(b) $n_t = 2$, optimal spectrum

(c) $n_t = 3$, minimal current

(d) $n_t = 3$, optimal spectrum

(e) $n_t = 4$, minimal current

(f) $n_t = 4$, optimal spectrum
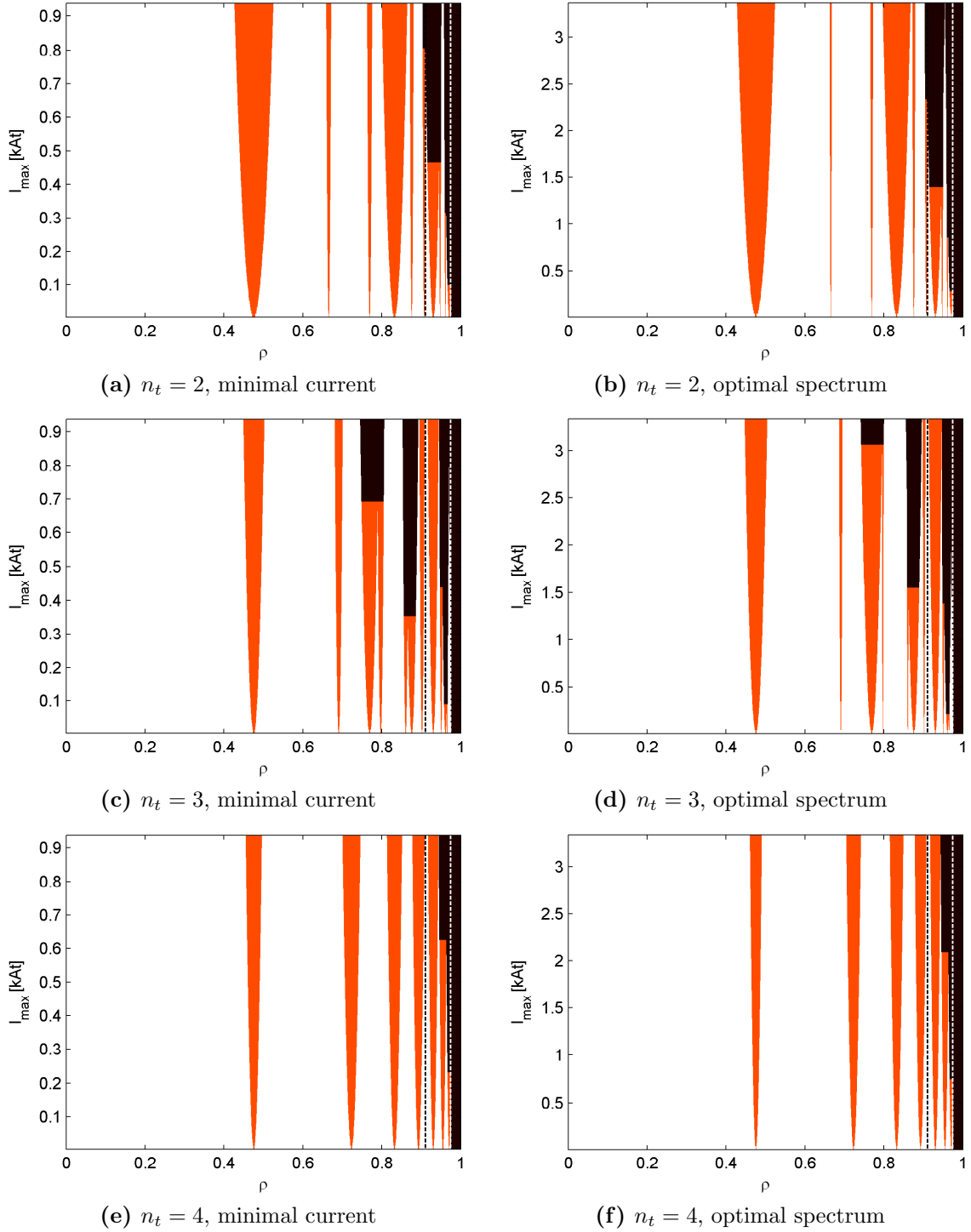
Figure 4.5: Ergodization maps. Target: outside $\rho_{\text{lim}} = 0.911$. Island width (red) and ergodic regions (dark brown) shown as a function of the maximal current fed in the SCS. Vertical black dashed line: inner limit of the required ergodic zone according to the $\rho_{\text{lim}} = 0.911$ limit. Vertical white dashed line: $\psi_{01} = 0.95$. Case: in-vessel, $z_{\text{mag}} = 0$. The small islands are due to the degenerate Fourier components.

(a) Minimal current

(b) Optimal spectrum
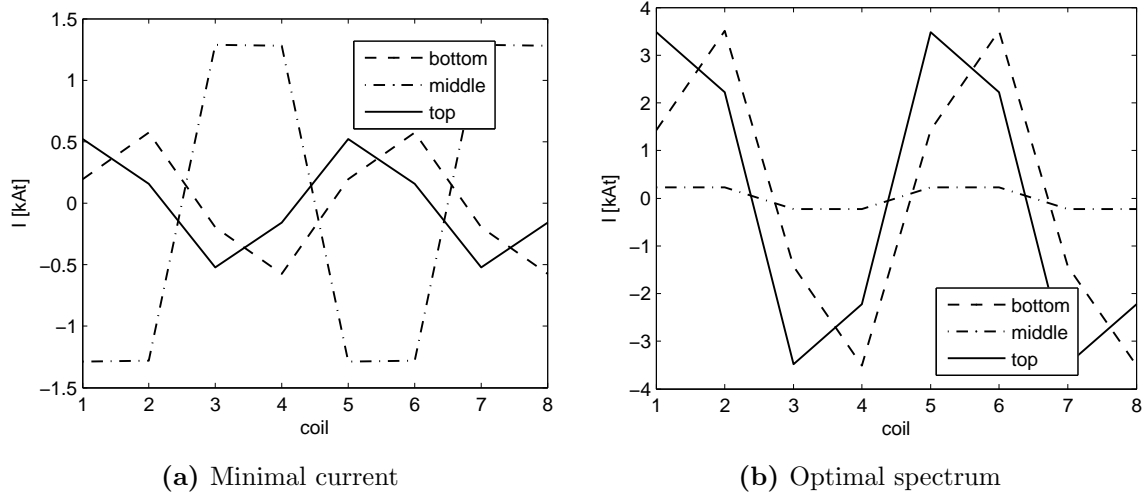
Figure 4.6: Current distributions of the 3 coil rows of the in-vessel TCV SCS for a $n_t = 2$ target and a set of weights optimizing (a) the current amplitude, $(w_e, w_g) = (0, 0)$, and (b) the figure of merit r, $(w_e, w_g) = (0, 10^5)$. In both cases, the current distribution is scaled to satisfy the condition of edge ergodization (see figure 4.2).

the first island position. These oscillations decrease in amplitude as the number of islands in the edge increases, consistently with increasing n_t or q_{95}. At higher q_{95}, I_{req} presents larger wavelength (in terms of q_{95}) oscillations. They typically occur when the q profile passes over an inter-ridge spectral zone within the edge region, therefore leading to a large required current in order to satisfy the edge ergodization constraint. When filtering out the low and high q_{95} oscillations, I_{req} displays a global minimum at $q_{95} \simeq 7$ for $n_t = 2$, at $q_{95} \simeq 4.5$ for $n_t = 3$ and at $q_{95} \simeq 3.5$ for $n_t = 4$. This reflects a trade-off between the number of islands, increasing with q_{95}, and the size of the islands, decreasing with q_{95}. In terms of RMP coil system qualification, the obtained results show that, for the proposed SCS, $I_{\text{req}}(q_{95}, r_{\text{opt}})$ remains technically reasonable in the typical operational interval $q_{95} \in [2, 6]$. Of course, lower I_{req} are possible if an optimal r is not required. The decrease of r_{opt} when the resonant edge modes have high values of m could only be counteracted by a modification of the SCS design, for example by increasing the number of rows and decreasing the height of each row, both options leading to technical difficulties related to the increased current consumption and the higher number of feed-throughs.

4.2.6.2 Robustness of an optimal current distribution against a change in q_{95}

Having in view the experimental application of the method developed here, one can raise the question of the robustness of an optimal current distribution with respect to
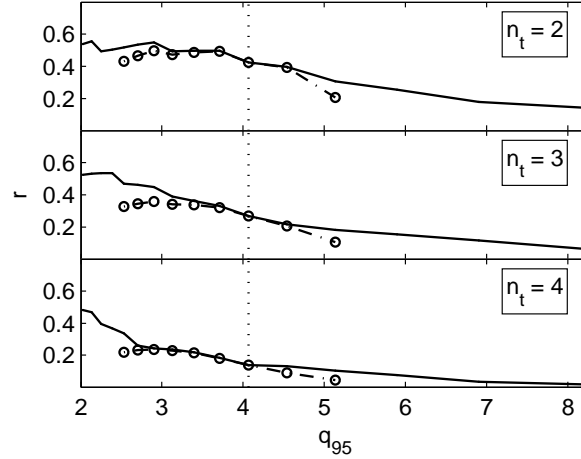
Figure 4.7: Solid lines (—): optimal figure of merit r_{opt} as a function of the edge safety factor q_{95} for targets $n_t = 2$, $n_t = 3$ and $n_t = 4$. Dash-dotted lines (- ⊙): $r(q_{95})$ calculated for a constant relative current distribution $\{I_c\}_{q_{95}=4.1}$, the current distribution optimizing r at $q_{95} = 4.1$ (vertical dotted line).

a change in the magnetic equilibrium, for example a variation of q_{95}. This question is addressed here by taking a reference equilibrium, $q_{95} = 4.1$, calculating its optimal relative current distribution $\{I_c\}_{q_{95}=4.1}$ and applying this distribution to the other equilibria in order to evaluate its figure of merit and required current. The results are displayed in figures 4.7 and 4.8 (dash-dotted lines). Figure 4.7 shows that the optimum is stable for $n_t = 2$ and $n_t = 3$, but only asymmetrically stable for $n_t = 4$. This asymmetry appears because at $q_{95} = 4.1$, the q profile is aligned with the edge of a spectral ridge for $n_t = 4$. Experimentally, the variation of I_{req} with q_{95}, also present for the optimal current distribution case, might be another source of difficulties. Both observations suggest that the whole space of possible equilibria should be explored before the experiments in order to assess the robustness of the selected current distribution and the overall required current. Real-time control of the coil currents would therefore have to rely on real-time plasma equilibrium reconstruction and comparison with a library of equilibria for which pre-calculated sets of optimal current distributions would be available.

4.3   Coil system characterization

The spectrum of the magnetic field perturbation, as defined in (4.3), is a function of the coil geometry, the coil location and the relative coil currents. Due to the small number of coil rows and to the identical geometry of the coils, spectral degeneracy occurs, consequently limiting the number of simultaneously controlled modes pro-
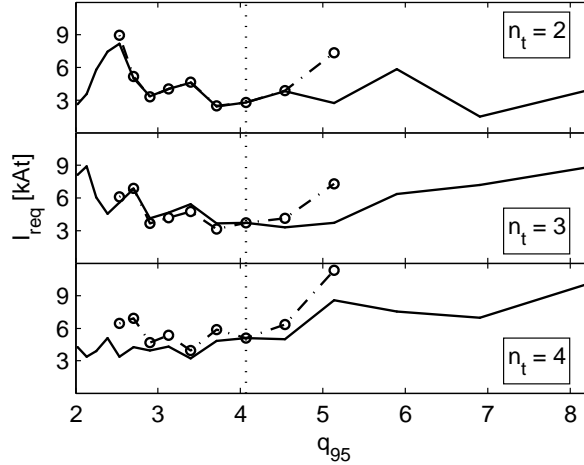
Figure 4.8: Solid lines (—): required current $I_{\rm req}$ as a function of the edge safety factor q_{95} for optimal figures of merit in the cases $n_t = 2$, $n_t = 3$ and $n_t = 4$. Dash-dotted lines (- ⊙): $I_{\rm req}(q_{95})$ calculated for a constant relative current distribution $\{I_c\}_{q_{95}=4.1}$, the current distribution optimizing r at $q_{95} = 4.1$ (vertical dotted line).

vided by the coil system. A simple theory, based on the combination of the real-space Fourier transform of the magnetic perturbation due to a single coil with the current-space Fourier transform of the current distribution of a set of equivalent coils, is used to entirely characterize the spectral limitations of a coil system. This section describes this theory, addressing in particular the questions of spectral degeneracy, number of simultaneously controlled target modes, availability of optimization and efficiency in each toroidal mode.

4.3.1 General coil system

The most general approach to characterize a coil system consists in grouping coils in sets s of equivalent coils (i.e. identical coils on the same row, with arbitrary toroidal spacing) and reducing the expression of the magnetic perturbation spectrum to a combination of the spectrum of a single coil per set with the Fourier transform of the currents flowing in the associated coil set:

$$
\begin{aligned}
\tilde{b}(\rho, m, n) &= \sum_s \sum_c \tilde{b}_c^s(\rho, m, n) I_c^s \\
&= \sum_s \tilde{b}_0^s(\rho, m, n) \sum_c I_c^s e^{-in\phi_c^s} \\
&= \sum_s \tilde{b}_0^s(\rho, m, n) \hat{I}^s(n)
\end{aligned}
\tag{4.23}
$$

$$
\hat{I}^s(n) = \sum_c I_c^s e^{-in\phi_c^s}
\tag{4.24}
$$

with $\tilde{b}_c^s$ the space Fourier transform of the magnetic perturbation due to a unit current in coil c of set s, I_c^s the current in coil c of set s, ϕ_c^s the toroidal shift from the reference coil 0 to the coil c of set s, and $\hat{I}^s$ the generalised discrete Fourier transform of I_c^s in the current space (ϕ_c^s does not necessarily describe a regular grid). From equation (4.23), it follows that at most one target mode can be imposed per set of equivalent coils per value of n. The advantage of independent coil powering within a coil row therefore mainly appears as a gain of degrees of freedom in the simultaneous and, if degeneracy allows, controlled excitation of modes with different values of n. Note that a row of coils could contain different coil sets, so that the "one mode per row" statement is not general.

4.3.2 Evenly-spaced coil system

In the case of evenly spaced coils (or, more accurately, coils separated by an integer multiple of the smallest angle between two adjacent coils), ϕ_c^s is written $\phi_c^s = (2\pi/N_s)c$, with $c \in \{0, N_s - 1\}$ (all the values must not necessarily be taken by c here) and N_s the highest possible number of coils in the set s. The mode degeneracy is characterized by:

$$\hat{I}^s(n + pN_s) = \hat{I}^s(n) \qquad \forall p \in \mathbb{N} \tag{4.25}$$

$$\hat{I}^s(N_s - n) = \hat{I}^{s*}(n) \tag{4.26}$$

These equations only impose an upper limit on the number of modes that can be simultaneously controlled. In the case of an incomplete coil row, this number would be further reduced by the coupled activation of modes with different values of n occurring in that situation. In addition, the fact that $\hat{I}^s(n)$ is purely real when $n = N_s/2$ or $n = N_s$, i.e. $\Im\left(\hat{I}^s(n \in \{N_s/2, N_s\})\right) = 0$, limits arbitrary phase setting of target modes with $n_t \in \{N_s/2, N_s\}$ to situations where multiple coil sets are available.

4.3.3 Complete evenly-spaced coil system

Finally, in the case of complete evenly-spaced coil sets, $\hat{I}^s$ is equal to the standard discrete Fourier transform of I_c^s, so that modes with different values of n can be orthogonally activated by using Fourier components for the currents in each coil row. The feature of orthogonal activation in even geometries implies the necessity to use a cross-mode cost function in the implementation of the Lagrange method, such as the cost based on the current amplitude. In the linear approach, the norm of the

current vector is used. As it is proportional to $\sum_{s,n} |\hat{I}^s(n)|^2$ (the Fourier transform conserves the norm), it is independent of the phase of the current modes. On the contrary, when using the non linear cost, based on the maximum of the current, an optimization of this phase is achieved, generally leading to a localization of the extrema of the current mode in the middle of two consecutive coils (see figure 4.6(a)). Defining the gain due to a coil set, i.e. the gain in perturbation amplitude due to the use of N_s coils instead of 1, as

$$g^s(n) = \frac{|\hat{I}^s(n)|}{\max_c(|I_c^s|)}, \tag{4.27}$$

such an optimization can lead to a gain $g(2) = 5.6$ instead of the expected $g(2) = 4$, i.e. an increase of 40% of the mode amplitude for $n_t = 2$, in the case of the TCV SCS.

4.3.3.1 Characterization of the SCS proposed for TCV

In the case of the coil system proposed for TCV, 3 rows of 8 evenly-spaced identical coils (see section 4.1.2), equations (4.25) and (4.26) lead to the conclusion that 5 orthogonal classes of n are available $\{0; 1; 2; 3; 4\}$, with main degenerate pairs $\{0; 8\}$, $\{1; 7\}$, $\{2; 6\}$ and $\{3; 5\}$. For classes $n = 1$, $n = 2$ and $n = 3$, the 3 coil rows allow a maximum of 3 simultaneous targets (i.e. 3 points (ρ, m, n) for which $\tilde{b}$ is controlled) per class, while for classes $n = 0$ and $n = 4$, only 1 target per class is allowed (with simultaneous spectrum optimization). The maximal gains due to the toroidal periodicity of the coil system are as follows: $g(\{0; 4\}) = 8$, $g(\{1; 3\}) = 4.3$ and $g(\{2\}) = 5.6$. For the class $n = 3$, the degeneracy between $n = 3$ and $n = 5$ and the small spectral distance between these modes implies a non negligible effect of $n = 5$ modes when working in $n_t = 3$ configurations. Figure 4.5(d) shows how the small islands created by the $n = 5$ component of the perturbation overlap with the larger $n = 3$ islands and ergodize them.

4.3.4 Loss of a coil in an evenly-spaced coil system

It is of practical interest to theoretically assess the impact of the loss of a coil on the control of the magnetic perturbation spectrum, in the case of an evenly-spaced coil system. From the theory above, the main result of such a loss is the loss of the orthogonal activation of the modes. If the number of remaining coils is sufficient, the activation of side-band modes can nonetheless be mitigated by using optimal current distributions, as those calculated with the method described in section 4.2. If the

current amplitude cost function is too global to minimize these modes with sufficient control, a dedicated cost function can be used, as described in equation (4.5). If the target mode phase is a free parameter and if $n_t \notin \{0, N_s/2\}$, the side-band modes can be completely avoided by adjusting the phase of the current Fourier component so that it crosses zero at the location of the missing coil.

Note from equation (4.23) that for a single set of coils, whichever their toroidal spacing, the activation of the different toroidal modes only depends on $\hat{I}^s(n)$, which is independent of the plasma parameters. In general, for a given n, $\hat{I}^s(n)$, as a vector in the complex plane, is univocally represented by a linear combination of two orthogonal base vectors, each of them corresponding to a coil current distribution. A rough, but computationally efficient, method of side-band mode minimization consists in identifying, for each value of n, a pair of orthogonal base vectors that individually minimize the amplitude of side-band modes (in the current space). Any linear combination of these vectors will in turn result in weak side-band mode activation. This approach reduces the dimension of the overall optimization problem to 2 unknown per coil set (i.e. the factors of each base vector), if no explicit cross-mode optimization is required (i.e. only one value of n is considered). Of course, for complete sets of evenly-spaced coils, these base vectors are made of sine and cosine components. For the other cases, e.g. when a coil is missing, a Lagrange method can be used to find the base vectors that minimize coupling with other values of n while assuring that their generalized Fourier transforms are orthogonal. Mathematically, if n_t is the toroidal mode number of the target mode, the associated cost function is written:

$$f = \sum_{n \neq n_t} \left| \hat{I}^s(n) \right|^2 \tag{4.28}$$

and the associated target $\hat{I}^s(n_t) = a_t \exp(\mathrm{i}\alpha_t)$. The phase α_t leading to the lowest cost is selected, giving $\alpha_{t,1}$. This yields the first base vector. The second base vector is given by the same procedure, but this time an imposed phase $\alpha_{t,2} = \alpha_{t,1} + \pi/2$ is used to ensure orthogonality. The case of 1 coil missing out of a row of 8 coils is taken as an example. The generalized spectra of both basis vectors are shown in figure 4.9 for the case $n_t = 2$. As expected, the current distribution associated with the first base vector totally decouples the $n = 2$ component from the others, by adjusting the phase of the current mode to require a null current at the missing coil position. The drawback, compared to a complete coil set, is that the maximal gain is reduced to 4. The second vector, whose phase is adjusted to force orthogonality of both base vectors in Fourier space, is associated with a current distribution that
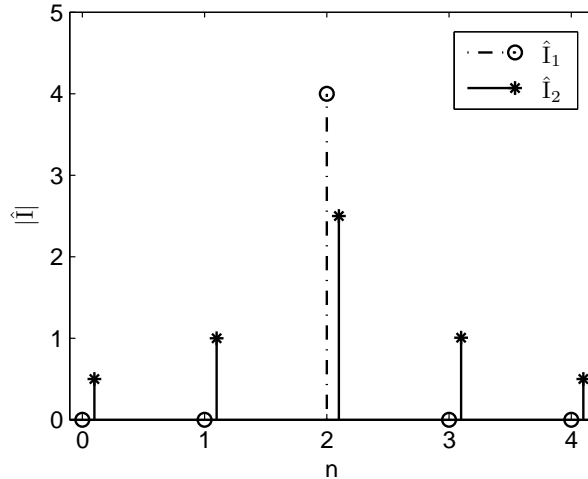
Figure 4.9: Generalized spectra of coil currents for one row of 8 coils where 1 coil is missing. Both associated current distributions are optimal for $n_t = 2$, according to the method described in section 4.3.4.

strongly couples the toroidal components with one another.

The simple approach described here has the advantage of leading to technically important results, while remaining at the current space level, i.e. excluding any additional complexity due to the plasma. In the example detailed here, it appears clearly that the loss of only 1 coil out of 8 coils leads to a significant deterioration of the magnetic perturbation spectrum purity, even for a small wave number (i.e. large wavelength) such as $n = 2$, unless a strong limitation is imposed on the perturbation phase.

4.4 Conclusion

In this chapter, a comprehensive study of RMP calculation and optimization, based on vacuum magnetic perturbation calculation and independent powering of the coils, has been presented. The optimization method relies on a semi-linear generic Lagrange approach that can handle a large variety of optimization requests for any coil system topology, providing in particular the mean to balance the quality of the magnetic perturbation spectrum optimization with the coil current requirement. By associating a cost function with a figure of merit quantifying the quality of a magnetic perturbation spectrum with respect to RMP, the efficiency of the method in this particular application has been proven on a number of experimentally relevant cases: $n = 2$, $n = 3$ and $n = 4$ targets for a typical H-mode plasma. A general procedure for spectral characterization of coil systems has also been developed and

its application to common special cases detailed. This work could be applied to any existing coil system, with a special dedicated application to the SCS proposed for ASDEX Upgrade [98] since two different subsets of coils are planned for the mid-plane row, resulting in the potential activation of deleterious side-band modes.

As discussed in the introduction (section 4.1.1), it is yet unclear to which extent the vacuum magnetic perturbation calculation is physically relevant. Nonetheless, thanks to the experimental results supporting the resonant characteristics of the magnetic perturbations resulting in ELM suppression, it is reasonable to think that the perturbation spectrum plays a significant role in the process. While the arguments guiding the optimization requirements might still evolve as the understanding of the mechanism of ELM suppression improves, it is not excluded that a direct connection to the vacuum perturbation spectrum will remain. In this case, the possibility to calculate an optimal tuning of this spectrum will be valuable.

Chapter 5

Physics design of a saddle coil system for TCV

5.1 Introduction

5.1.1 Project overview

The upgrade project for TCV includes the installation of a set of saddle coils, namely the saddle coil system (SCS), located and powered such as to create a helical magnetic perturbation. The toroidal periodicity of this perturbation is tunable in order to allow simultaneously ELM control, error field correction and vertical control. Other experimental applications, like resistive wall mode and rotation control, are also in view.

5.1.2 Motivations

5.1.2.1 ELM control

As described in sections 2.3.2 and 4.1.1, the application of asymmetric magnetic perturbations to ELMing H-mode plasmas results in ELM mitigation or stabilization in a number of Tokamaks [10, 11, 11, 36, 37]. Although the condition of resonance of these perturbations with the plasma equilibrium magnetic field is still questioned, this ELM control technique is widely referred to as RMP (Resonant Magnetic Perturbation). Even though the question of ELM control by RMP is subject to an important worldwide scientific effort, the physical mechanism explaining how ELM control is obtained remains unclear. As discussed in section 4.1.1, the initial physical interpretation, based on edge gradient control by magnetic field line ergodization,

appears to be questionable, although the resonance condition is experimentally supported in a large number of cases.

In the frame of this worldwide effort, few studies of the dependence of ELM control by RMP on the plasma shape have been done. Experiments on DIII-D [12, 99] nonetheless show that the plasma shape is an important parameter, leading to "significant differences in the RMP requirements and in the properties of the ELM suppressed plasmas" when the plasma triangularity, for example, is changed. With that respect, TCV's unique plasma shaping and positioning capability could significantly extend the study of the dependence of ELM control by RMP on the plasma shape and contribute to a clearer description of the conditions required for ELM suppression.

5.1.2.2   Error field correction (EFC)

As described in section 4.1.2, error fields are asymmetric magnetic fields associated with construction tolerances in Tokamak coil positions and shapes, and detrimental to Tokamak operation, causing locked modes [91] and disruptions. Their effects can be corrected by applying an asymmetric field of opposite sign, as provided by a SCS. Measurements [100] have shown that these fields are non negligible on TCV and that their correction could be beneficial to the operation of the machine.

5.1.2.3   Vertical control

Vertical control (VC) is required to stabilize the highly unstable vertical position of the plasma. It is obtained by applying an axisymmetric radial magnetic field. The growth rate of vertical modes is such that the vertical control coils need to be located inside the Tokamak vessel to avoid screening of the control field. TCV already has a vertical control system, namely the internal G-coils. Due to the lack of free space inside the vessel and to the required number of feed-throughs, it would be difficult to have both a new SCS and the actual internal coil systems coexisting in the machine. Therefore, the G-coils must be removed and the SCS must be designed to provide the vertical control functionality.

5.1.2.4   Rotation control

Generally, stationary asymmetric magnetic fields result in a toroidal plasma braking, as observed in the case of strong error fields. For higher toroidal harmonics, perturbation fields can also lead to counter-current toroidal acceleration, as reported

on DIII-D [82,89,90]. This effect could be of particular interest for TCV, since there is presently no external source of momentum on the machine, due to the absence of NBI heating.

Tearing modes [74,101] are regularly present in Tokamaks. In TCV, their frequency is typically in the range of 5 kHz. A SCS powered with a high bandwidth source could, taking into account the vessel screening, open a field of research on the interaction of these modes with rotating perturbations, especially on the question of stability and phase locking of the modes.

5.1.2.5 RWM control

Resistive wall modes [102,103] (RWM) are ideal MHD instabilities that are not stabilized by the vessel wall because their growth rate is slower than the resistive time of the vacuum vessel. A SCS covering a sufficient portion of the wall could be used as a way to actively reproduce an ideal wall screening on slower time scales, following the smart shell principle [104] demonstrated on RFX [105].

5.1.3 Chapter outline

In this chapter, a description and a characterization of two proposed SCS designs, namely the in-vessel and ex-vessel SCS, are given. The physical arguments at the root of the proposed designs are detailed in section 5.2, where the geometry of the designs, the current requirement for RMP and the expected perturbation spectra and ergodization features, based on vacuum magnetic perturbation calculation, are also presented. The study on error field control (EFC) is presented in section 5.3, including the determination of the current requirement for the error field correction on TCV. The questions of inductance and wall coupling are dealt with in section 5.4. This section also details the determination of the SCS response function. The requirements for vertical control are established in section 5.5, using a principle of equivalence with the system currently used on TCV. The voltage and current induced in the in-vessel SCS during a plasma disruption are calculated in section 5.6. The maximal magnetic force exerted on the SCS and the type of force gradients that may be expected are calculated in section 5.7. A discussion on the impact of the number of turns per coil and a scaling of different parameters with this parameter are presented in section 5.8. The issue of coil heating due to Joule effect and the questions of cooling time and necessity of active cooling are addressed in section 5.9. This chapter ends with a short conclusion on the studies presented here. Note that

the ex-vessel design has been studied for a limited number of aspects, namely RMP, EFC and self-inductance. Also note that the spectral characterization of both SCS designs has been detailed in the previous chapter, section 4.3.3.1.

5.2 RMP and coil system design

This section first describes the method used to establish the current requirements and the approaches used to qualify a SCS with respect to RMP. Physical arguments are then given to optimize the coil system topology in terms of poloidal coil location, poloidal and toroidal coil distribution, individual coil shape and dimensions, number of coils and toroidal phase shift between coil rows. Finally, two coil designs are proposed and discussed with respect to their expected performances, using vacuum field calculation in a number of situations.

Note: Since the RMP coil systems are generally made of saddle-shaped coils, the generic name of saddle coil system (SCS) will be used in the remaining part of this chapter.

5.2.1 Current requirement determination

The determination of the minimal current amplitude required for RMP is based on two complementary approaches. In the first approach, the required perturbation amplitude is given by the condition of creating a radial magnetic field at the plasma separatrix that has the same amplitude, with respect to the toroidal field, as in DIII-D or JET. This condition corresponds to a perturbation of 0.4%, i.e. $5.7\,\mathrm{mT}$ for TCV. The second approach is based on the criterion of magnetic island overlap in the plasma edge, as described in section 4.2.4, and corresponds to the condition $\sigma(0.83 \leq \psi_{01} \leq 1) \geq 1$ where ψ_{01} is the normalized poloidal flux and $\sigma(\psi_{01})$ the Chirikov parameter. As σ is a function of the amplitude of the current in the SCS, the current required to satisfy the edge ergodization condition can be deduced.

Since the physical mechanism at the root of ELM control by RMP is still unclear, the justification of the second approach is not obvious. While being mostly related to the initial, and now contested, interpretation of RMP, it is nonetheless supported by a number of arguments: (a) the vacuum calculation approach is consistent with the condition of resonance observed on a number of Tokamaks; (b) it has been used to determine the current requirement of the ASDEX Upgrade coil system [98], where a successful observation of ELM mitigation has been observed; (c) ignoring a possible magnetic perturbation amplification by the plasma, it is reasonable to

think that if no significant plasma equilibrium perturbation is observable when the plasma response is neglected, then the perturbative effect will be even less significant when the plasma response is considered, therefore identifying the vacuum calculation results as minimal requirements. Note that this approach has also been used for the current requirement determination for the JET [106] and ITER [87] coil system projects.

In what follows, the vacuum magnetic perturbation calculation will be the approach of reference for all the aspects of coil system qualification.

5.2.2 Qualifying a SCS with respect to RMP

As described in chapter 4, the magnetic perturbation created by a SCS can be characterized by the space spectrum $\tilde{b}(\rho, m, n)$ of the perpendicular component of the magnetic perturbation at the equilibrium magnetic flux surfaces. This spectrum depends on the plasma equilibrium, on the coil system geometry and on the coil current distribution. Two coil current distributions are of particular interest: the current distribution resulting in the largest peaking of the spectrum around the resonant edge modes, named here the "optimal spectrum" situation, and the current distribution corresponding to a minimal current requirement while maintaining a finite activation of the edge modes, named here the "minimal current" situation. The method used to determine these optimal current distributions is detailed in chapter 4. A SCS is then qualified with respect to a variety of elements:

Spectrum quality: a figure of merit is attributed to the optimal spectra obtained for each controlled value of the toroidal mode number n of the perturbation. An equivalent figure of merit is also attributed to the minimal current spectra in each case.

Ergodization localization: by plotting the location of the generated islands as a function of the SCS current and the flux surface coordinate on a 2D map, the location of the ergodized regions can be visualized. This method of analysis is similar to a radial profile of the Chirikov parameter but solves the issue of island pairing inherent to the Chirikov approach.

Poincaré plots: the vacuum magnetic field perturbation is added to the equilibrium field and a large number of field lines are followed in space. A Poincaré plot is obtained by marking the position of the field lines on a poloidal cross-section after each toroidal turn. They provide an independent way of determining the location of the ergodized regions. Although they require a much

longer computation time than the previous method, the obtained result is more robust since they require less intermediate calculations and do not assume a constant perturbation amplitude across the islands.

5.2.3   Optimal coil system topology

In order to limit the range of studied coil systems, it is useful to formulate a number of generic arguments serving as reflection guides. These arguments are then used to propose a number of possible SCS designs, which are in turn qualified with respect to a given plasma equilibrium using the methods described above.

5.2.3.1   Toroidal distribution

As far as RMP is concerned, there is no theoretical constraint on the toroidal distribution of coils in the coil setup. However, a number of arguments must be considered:

- A system that is not evenly-spaced toroidally activates a whole family of toroidal modes, with little control on the relative amplitudes in each value of the toroidal mode number n, although the perturbation spectrum is usually peaked on modes with low n values. This may seriously impair the experimental usage of the coil system, as well as the physical interpretation of the experimental results. For example, it becomes very difficult to limit the magnetic field line ergodization to the plasma edge in such a case.

- A coil system can therefore be used for error field correction only if it is evenly-spaced toroidally.

- In vertical control operation, the pure $n = 0$ correction is much better mimicked if the coils cover the whole toroidal circumference, i.e. if they are juxtaposed with one another.

- If the coils are juxtaposed with one another and evenly-spaced, the toroidal spectrum of the perturbation displays less activation of side-band modes. It also means that the coil current requirements to obtain a given perturbation amplitude are smaller.

The optimal toroidal distribution is therefore made of evenly-spaced juxtaposed coils.

5.2.3.2 Poloidal location and distribution

Concerning the poloidal location and distribution of the coil system, the following arguments should be considered (see [94] and equation (4.2)):

- Since the edge safety factor is usually large in Tokamaks, a perturbation must activate modes with high values of the poloidal mode number m in order to be resonant. Sharp poloidal variations of the magnetic perturbation are therefore necessary. This constraint can be somewhat lessened on the low field side since the poloidal angle between two successive turns of a field line is larger in that particular location.

- A magnetic perturbation located close to a region of the plasma where the poloidal flux expansion is small has a larger effect. Since Tokamak plasmas are vertically elongated, such a region is present on the median plane of the plasma. In addition, the flux expansion is further reduced by the Shafranov shift on the low field side of the machine.

- The relatively smaller toroidal magnetic field on the low field side contributes to a larger effect of a magnetic perturbation located there.

From these arguments, it appears clearly that the coil system must be located on the low field side of the machine, spread on as many rows as possible.

5.2.3.3 Individual coil shape and dimension

The exact shape of each coil has small significance in terms of perturbation spectrum. A saddle-like shape is nonetheless preferred to other possible shapes since it maximizes the amplitude of the perturbation field for a given coil area and, in case of juxtaposed coil systems, minimizes the effect of spatial discretization when the coils are combined to mimic systems having smaller spatial mode numbers. In a system made of juxtaposed coils, the coil dimension is determined by the poloidal and toroidal number of coils. Otherwise, the coils should be as large as possible to minimize the current requirement.

5.2.3.4 Number of coils

The number of coil rows is determined as a trade-off between current requirements and spectrum shaping. A higher number of rows allow more control on modes with high values of m, but comes with smaller coils requiring more current. The number of coils in the toroidal direction, $N_{\mathrm{coils},t}$, defines $n_{\max}$, the highest controllable value of

n. Again, a trade-off between current requirements and coil system features must be chosen. Important aspects in this matter are the number of available feed-throughs, the cost of power supplies and the natural geometry of the Tokamak.

5.2.3.5   Mechanical toroidal phase shift between coil rows

When using independent coil powering, the phase of the perturbation created by each row of coils can be tuned for all the values of n smaller than n_{max}. In the case where $N_{\mathrm{coils},t}$ is even and for $n = n_{\mathrm{max}}$, this statement does not hold and the spectrum of the perturbation can only be optimized by adjusting the relative current amplitude between coil rows, which might be insufficient. In that case, the alignment of the magnetic perturbation with the magnetic field lines in the edge of the plasma may be optimized by a mechanical toroidal phase shift between coil rows. Such a design raises a number of issues:

- The optimization is rigid and might be optimal with respect to a narrow experimental domain, in particular limited by the value of q_{95}, the sign of the helicity, the plasma position and the plasma shape.

- The optimization rigidity may be alleviated by increasing the number of coils in one or more rows and changing the coil connections in these rows depending on the desired phase shift. However, such a solution requires a much larger number of coils and the development of multiple coil designs. Space occupation might also be an issue.

5.2.4   Optimal coil system topology for TCV

The particular geometry of TCV, approximately 3 rows of 16 evenly-spaced portholes, and the requirement of flexible plasma positioning dictate most of the topology choices for the SCS project. The positioning flexibility requires the conservation of the mid-plane symmetry of the machine. Since small elongation plasmas located in the top or bottom half of the machine are commonly created, a mid-plane coil row is also necessary. Therefore, at least (and at most, due the portholes) 3 coil rows must be installed. The choice of n_{max}, the highest controllable value of n, is driven by the toroidal symmetry of the machine: $n_{\mathrm{max}} \in \{1; 2; 4; 8\}$. RMP requires at least $n_{\mathrm{max}} = 2$, but $n_{\mathrm{max}} = 4$ is certainly preferable to ensure a certain flexibility during experimental studies. $n_{\mathrm{max}} = 8$ would not only represent an important cost, but also be less interesting in terms of resonant mode control since the corresponding values of m are too high with respect to the capabilities of a 3-row system.

Concerning the question of mechanical toroidal phase shift between coil rows, in a $n_{max} = 4$ design and taking the vessel geometry into account, only a $2\pi/16$ phase shift of the mid-plane row would be sensible. For $n = 4$, such a phase shift actually worsens the magnetic perturbation alignment since the field line pitch angle is usually much flatter than the pitch angle of the perturbation that would then be created.

Following the arguments stated above, the optimal coil system topology for TCV consists in 3 rows of 8 evenly-spaced coils. If possible, these coils should be juxtaposed with one another and the rows should be vertically aligned.

5.2.4.1   In-vessel coil system

An in-vessel coil system would be the most interesting option in terms of potential experimental usage of the system since all the intended applications would be possible. A number of important restrictions are nonetheless present for such a system, as shown in the list below:

- The coils must be passed through the manhole during the installation procedure. As a result:

    - The toroidal extent of the coils is limited by the height of the vessel. This is compatible with a choice $n_{max} = 4$, i.e. a coil encircling 2 portholes.
    - The height of the coil is limited by the diameter of the manhole, giving a final height of approximately $38\,cm$.

- The number of portholes for feed-throughs limits the number of coils ($n_{max} \leq 4$).

- The coils must be as thin as possible to fit in a narrow space between the vessel and the tiles.

- The coils must be as far away as possible from the vessel to limit the screening of the perturbation and as close as possible to the plasma in order to minimize the required coil current and maximize the amplitude of modes with high values of m.

- The coil support must be strong enough to endure the mechanical shocks associated with plasma disruptions.

- The coil design must be vacuum-compatible.

- The coil design must account for the coil temperature increase due to Joule
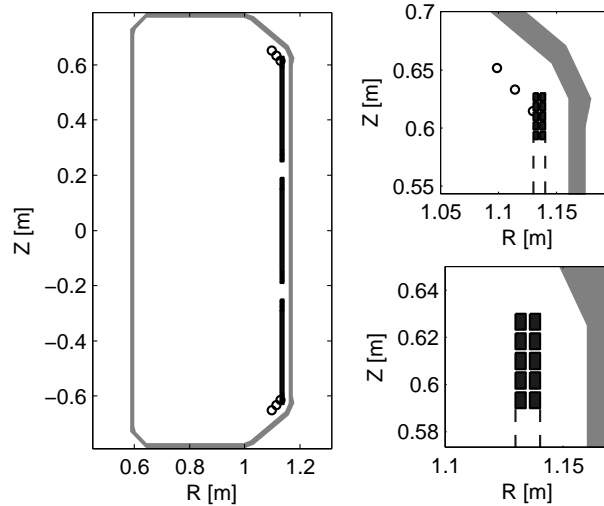
Figure 5.1: Poloidal cross-section of the 10-turn in-vessel SCS design. On the LHS, the toroidal projection of the coils is shown, as well as the actual position of the internal fast coils, also known as G-coils ($\circ$). On the RHS, a zoom on the coil is shown.

effect in the absence of active cooling and due to vessel baking during conditioning phases.

A possible design is shown in figure 4.1, chapter 4. This design is compatible with all the requirements stated above and follows the optimization guidelines. The 10-turn design used for numerical applications throughout this chapter is shown in figures 5.1 and 5.2.

5.2.4.2   Ex-vessel coil system

An ex-vessel coil system might prove interesting in terms of cost reduction. The restrictions specifically related to an ex-vessel system are listed below:

- The vertical control and mode rotation control features are lost due to the vessel wall screening of any high frequency perturbation. Resistive wall mode control becomes very limited or impossible.

- The coils are further away from the plasma. As a result, the amplitude of modes with high values of m is decreased, with a possible detrimental effect on ELM control by RMP, and the current requirement is increased.

- The current induced in the coils due to a disruption is reduced, thanks to the vessel wall screening.

- The space occupation outside the vessel limits considerably the possible coil geometry. A "chair-like" design might be envisaged to minimize the distance
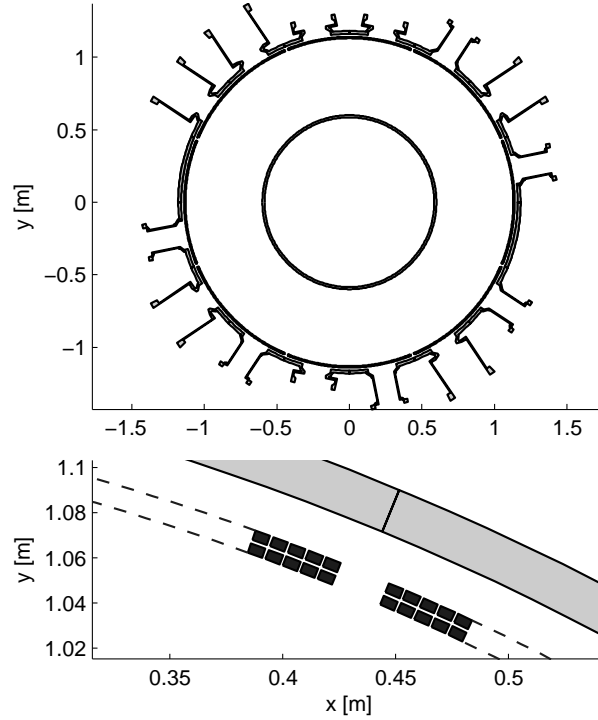
Figure 5.2: Toroidal cross-section of the 10-turn in-vessel SCS design. Top: overview of the TCV vessel with the coil array (nearly continuous circle). Bottom: zoom on a particular pair of coils. NB: the tangential porthole is missing on the figure.

between the coils and the plasma. The toroidal juxtaposition of coils is not possible in that case.

A possible design is shown in figure 5.3. The design is compatible with the restrictions stated above but some portholes might need to be re-engineered in order to accommodate such a system. A configuration with only 4 coils toroidally, generating a perturbation with $n_{max} = 2$, would fit more easily into the current TCV setup. The single-turn design used for numerical applications throughout this chapter is shown in figures 5.4 and 5.5.

5.2.5 RMP performances and current requirement of the in/ex-vessel SCS

In this section, the performances of the proposed in- and ex-vessel SCS in terms of RMP are assessed following the principles given in section 5.2.2. The current requirements (see section 5.2.1) are also given.
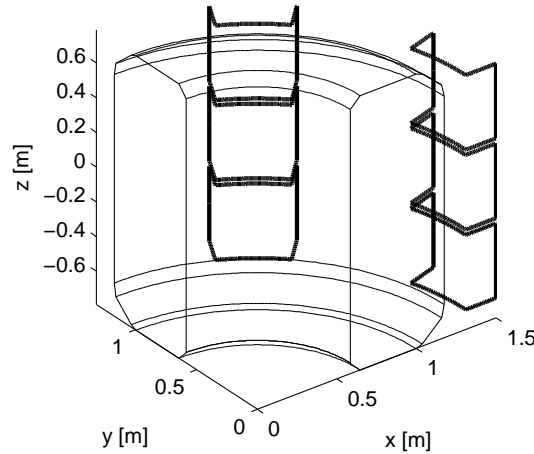
Figure 5.3: Perspective view of the optimal ex-vessel design for the SCS project for TCV, drawn on top of the vacuum vessel. The system consists of 3 rows of 8 external saddle coils located on the low field side of the torus. The coils are vertically aligned.
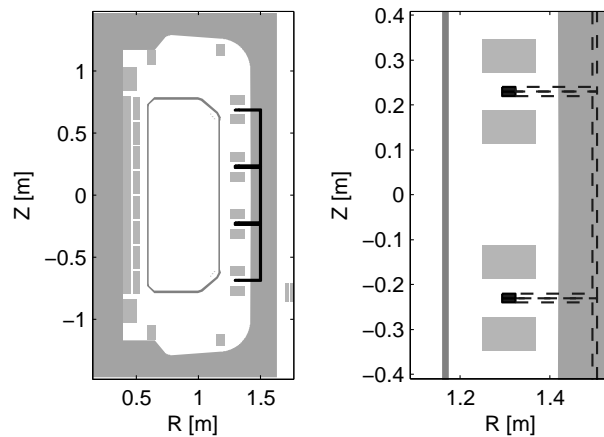
Figure 5.4: Poloidal cross-section of the ex-vessel SCS design. On the LHS, the toroidal projection of the coils is shown, as well as the position of the TCV coil system. On the RHS, a zoom on the coil is shown.

5.2.5.1   Equilibrium description

A typical ELMy H-mode plasma equilibrium is used to calculate the different parameters used in the design quality assessment. The same equilibrium is used at two different vertical positions of the magnetic axis: $z_{mag} = 0$ and $z_{mag} = 0.23\,\mathrm{m}$. The plasma is characterized by a density on axis $n_e = 7.5 \cdot 10^{19}\,\mathrm{m}^{-3}$, a plasma current $I_p = 415\,\mathrm{kA}$, a toroidal magnetic field on axis $B_{\phi,\mathrm{axis}} = 1.4\,\mathrm{T}$, a major radius $R_{mag} = 0.91\,\mathrm{m}$, a minor radius $a = 0.22\,\mathrm{m}$, a triangularity $\delta_{95} = 0.4$, an elongation $\kappa_{95} = 1.7$, a normalized pressure $\beta_p = 0.65$ and a safety factor $q_{95} = 2.6$.
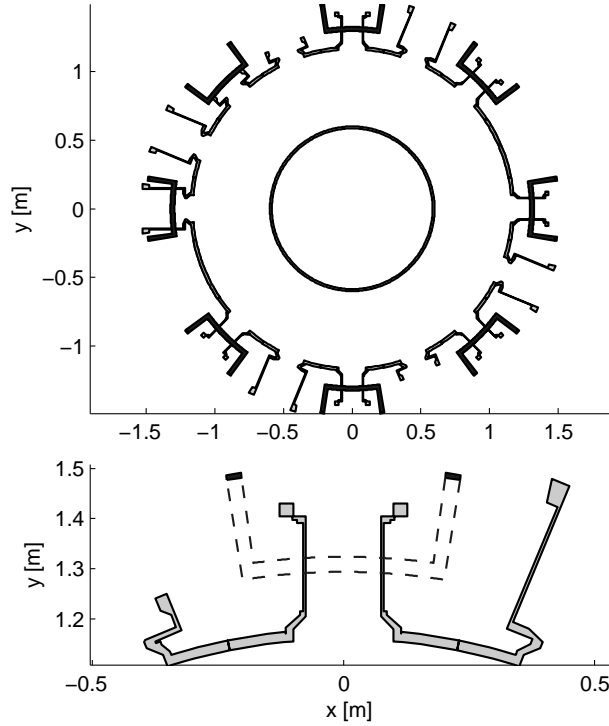
Figure 5.5: Toroidal cross-section of the ex-vessel SCS design. Top: overview of the TCV vessel with the coil array. Bottom: zoom on a particular coil. NB: the tangential porthole is missing on the figure.

5.2.5.2 Current requirements and figure of merit

The figures of merit and the required currents, based on the overlap of magnetic islands, are shown in figures 5.6 and 5.7 for all the cases of interest. Both parameters are shown as a function of the cost function weight w_g indicating a scan between the current requirement minimization and the spectrum optimization (see section 4.2.3).

The general aspects of the dependence of the figure of merit and the required current on the weight w_g are discussed in section 4.2.5. The focus is brought here on the comparison between the different cases (design and plasma location).

Vertical position: $z_{\mathbf{mag}} = 0$ vs $z_{\mathbf{mag}} = 0.23\,\mathrm{m}$

- The figure of merit r generally takes a higher value at $z_{\mathrm{mag}} = 0.23$ for w_g small. At this position, the location of the transition from the equatorial coil row to the upper coil row coincides with the plasma magnetic axis and the SCS therefore naturally produces perturbations with high values of m without increasing the value of the current cost function.

- The overall current requirements are higher (factor 2 to 3) at $z_{\mathrm{mag}} = 0.23$, especially for optimal spectra. This is due to the weak contribution of the

(a) $z_{\mathrm{mag}} = 0$ **(b)** $z_{\mathrm{mag}} = 0.23\,\mathrm{m}$
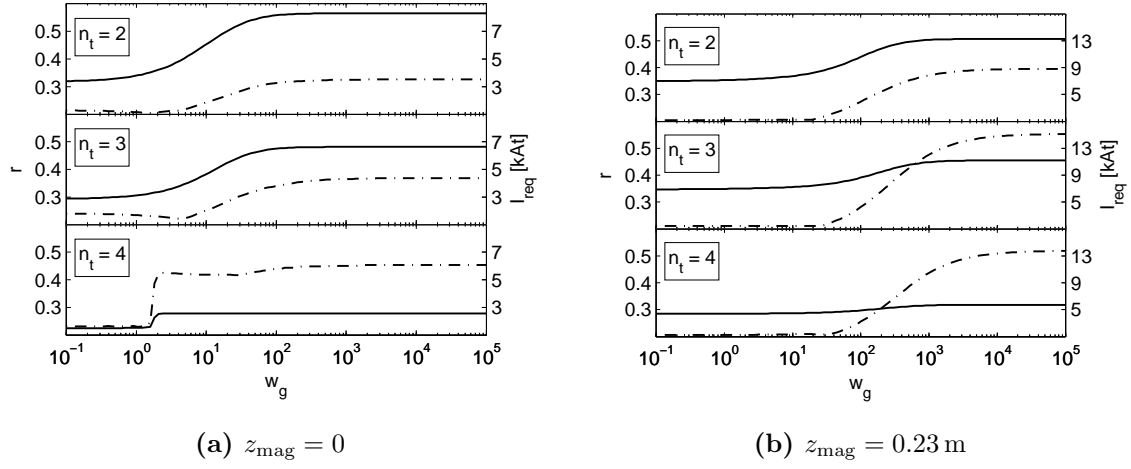
Figure 5.6: Figure of merit r (solid lines) and required current for edge ergodization I_{req} (dash-dotted lines) as a function of the weight w_g in the cases $n_t = 2$, $n_t = 3$ and $n_t = 4$ for the in-vessel SCS and both plasma locations.

(a) $z_{\mathrm{mag}} = 0$ **(b)** $z_{\mathrm{mag}} = 0.23\,\mathrm{m}$
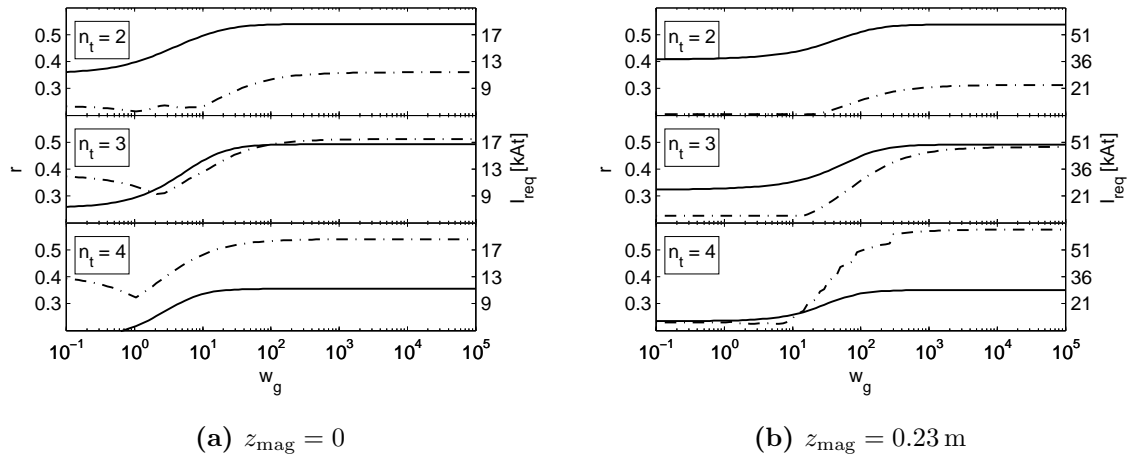
Figure 5.7: Figure of merit r (solid lines) and required current for edge ergodization I_{req} (dash-dotted lines) as a function of the weight w_g in the cases $n_t = 2$, $n_t = 3$ and $n_t = 4$ for the ex-vessel SCS and both plasma locations.

bottom coil row.

SCS location: in-vessel vs ex-vessel

- Despite the extra distance to the plasma, the ex-vessel design displays spectral features close to the values given by the in-vessel system. However, in the case of the in-vessel SCS, a realistic multi-turn coil design has been used to calculate the spectra, whereas a single-turn design has been used for the ex-vessel system. This choice might have an impact on the presented results, since a multi-turn system produces a perturbation with less activation of the modes with high values of m.

- As expected, the current requirements for the ex-vessel system are much larger than those for the in-vessel system. This result is explained by the limited toroidal extent and the larger distance to the plasma in the ex-vessel case.

Current requirements As shown in figures 5.6 and 5.7, the current requirements based on magnetic island overlap vary greatly as a function of the degree of optimization of the spectra. To determine the DIII-D and JET equivalent current (see section 5.2.1), only the relative current distribution giving an optimal spectrum at $z_{\mathrm{mag}} = 0$ has nonetheless been retained. This choice is justified by a too weak activation of the bottom and top coil rows in the minimal current configuration, leading to a nearly insignificant contribution to the total perturbation in that case. For the in-vessel system, a DIII-D and JET equivalent is given by a current of approximately $4\,\mathrm{kAt}$. As shown in figure 5.6, such a current would be sufficient for non-optimal spectra at both vertical locations. At $z_{\mathrm{mag}} = 0$, the reserve of current dedicated to the error field correction (approximately $3\,\mathrm{kAt}$) could be used to reach the optimal spectra. At $z_{\mathrm{mag}} = 0.23$, the optima would not be reached unless the current limit for RMP only is increased to $12\,\mathrm{kAt}$. For the ex-vessel system, the DIII-D and JET equivalent is reached for a current of $14\,\mathrm{kAt}$. As before, the error field correction current can be used for RMP and offers an additional $7\,\mathrm{kAt}$. Here again, the optimal spectra at $z_{\mathrm{mag}} = 0.23$ are reachable only at the cost of a large increase of the current requirement for RMP.

5.2.5.3 Spectra

The magnetic perturbation spectra corresponding to both optimal current distributions, i.e. to both extremes of w_g, for each SCS design and each plasma location are

plotted in figures 4.4, 5.8, 5.9 and 5.10. These detailed views show that the figure of merit captures correctly the main features of the spectra. As expected from the previous discussion, the flexibility in spectrum shaping and the perturbation amplitude are greater at $z_{\mathrm{mag}} = 0$. In addition, the $z_{\mathrm{mag}} = 0$ spectra of the in-vessel system exhibit sharper variations along m than those of the ex-vessel system, consistently with the smaller distance to the plasma of the in-vessel system. This is an example of a local feature that is not rendered by the figure of merit. In most cases, it can be concluded that the alignment of the perturbation with the q-profile is sufficient and that the optimization of the spectra is efficient, particularly in terms of reduction of core mode amplitudes.

(a) $n_t = 2$, minimal current

(b) $n_t = 2$, optimal spectrum

(c) $n_t = 3$, minimal current

(d) $n_t = 3$, optimal spectrum

(e) $n_t = 4$, minimal current

(f) $n_t = 4$, optimal spectrum
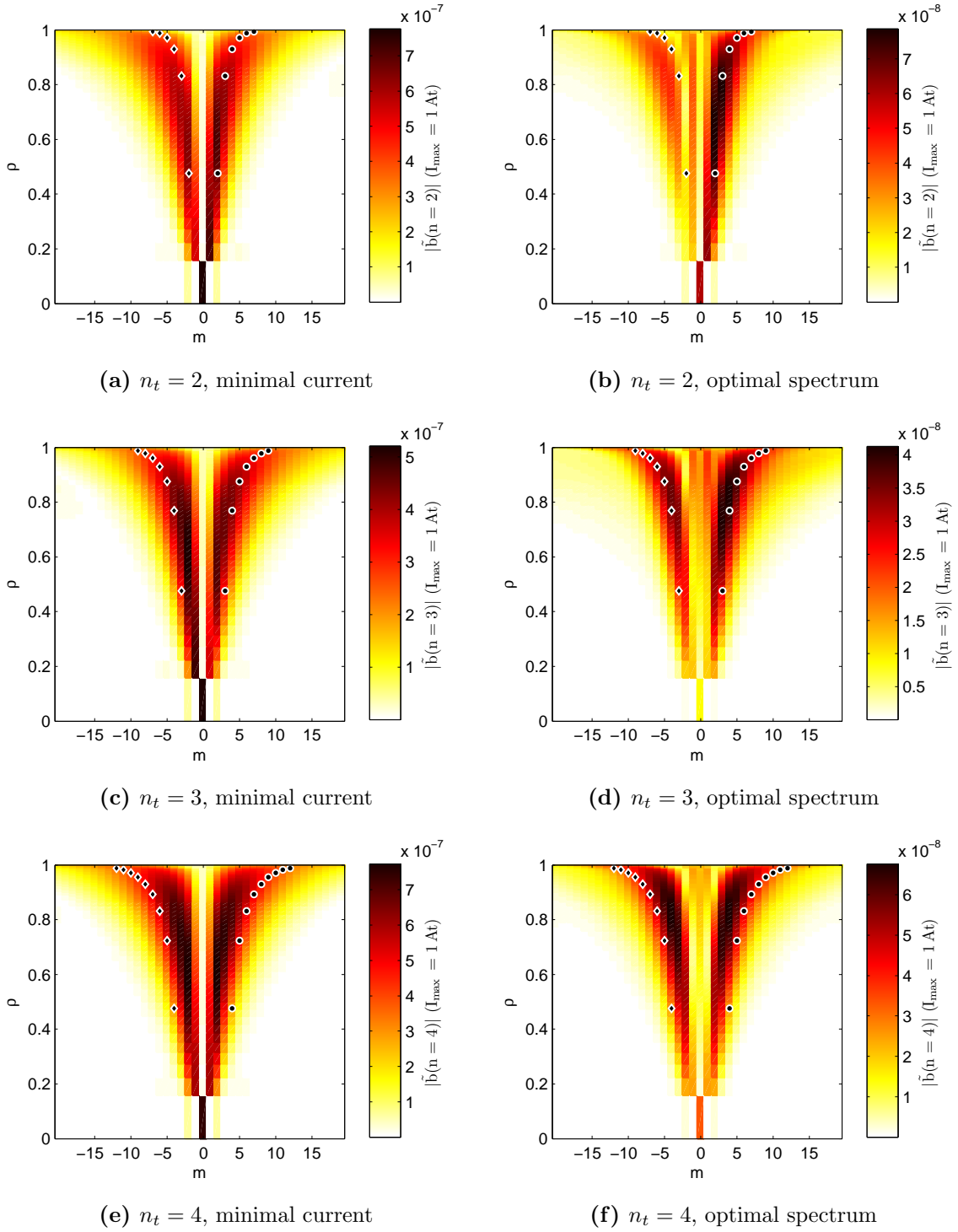
Figure 5.8: $\left| \tilde{b}(\rho, m, n \in \{2; 3; 4\}) \right|$. Target: outside $\rho_{\text{lim}} = 0.911$. ● : resonant flux surface locations, ◆ : symmetrical non resonant counterparts. Case: in-vessel, $z_{\text{mag}} = 0.23\,\text{m}$.

(a) $n_t = 2$, minimal current

(b) $n_t = 2$, optimal spectrum

(c) $n_t = 3$, minimal current

(d) $n_t = 3$, optimal spectrum

(e) $n_t = 4$, minimal current

(f) $n_t = 4$, optimal spectrum
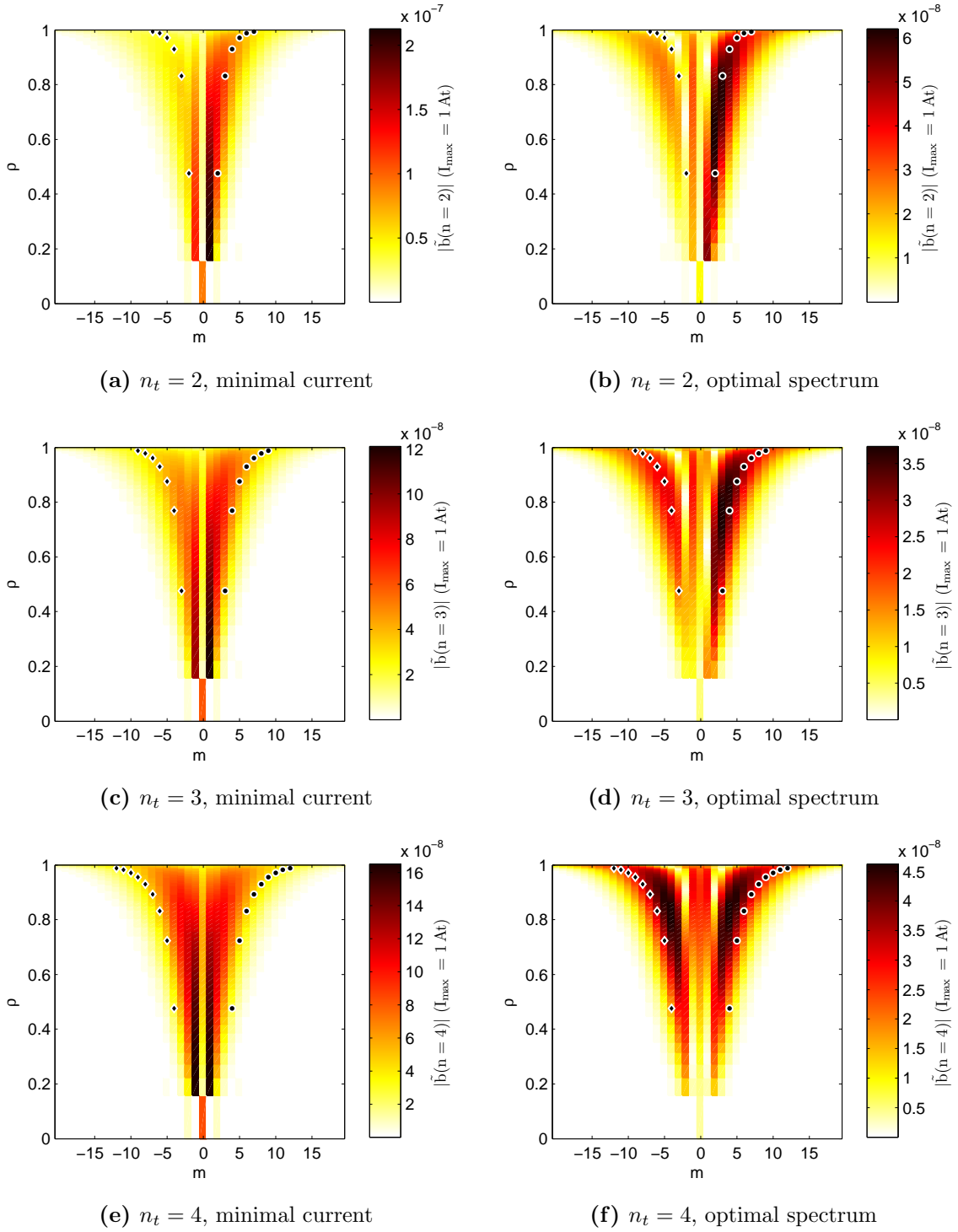
Figure 5.9: $\left|\tilde{b}(\rho, m, n \in \{2; 3; 4\})\right|$. Target: outside $\rho_{\text{lim}} = 0.911$. ● : resonant flux surface locations, ◆ : symmetrical non resonant counterparts. Case: ex-vessel, $z_{\text{mag}} = 0$.

(a) $n_t = 2$, minimal current

(b) $n_t = 2$, optimal spectrum

(c) $n_t = 3$, minimal current

(d) $n_t = 3$, optimal spectrum

(e) $n_t = 4$, minimal current

(f) $n_t = 4$, optimal spectrum
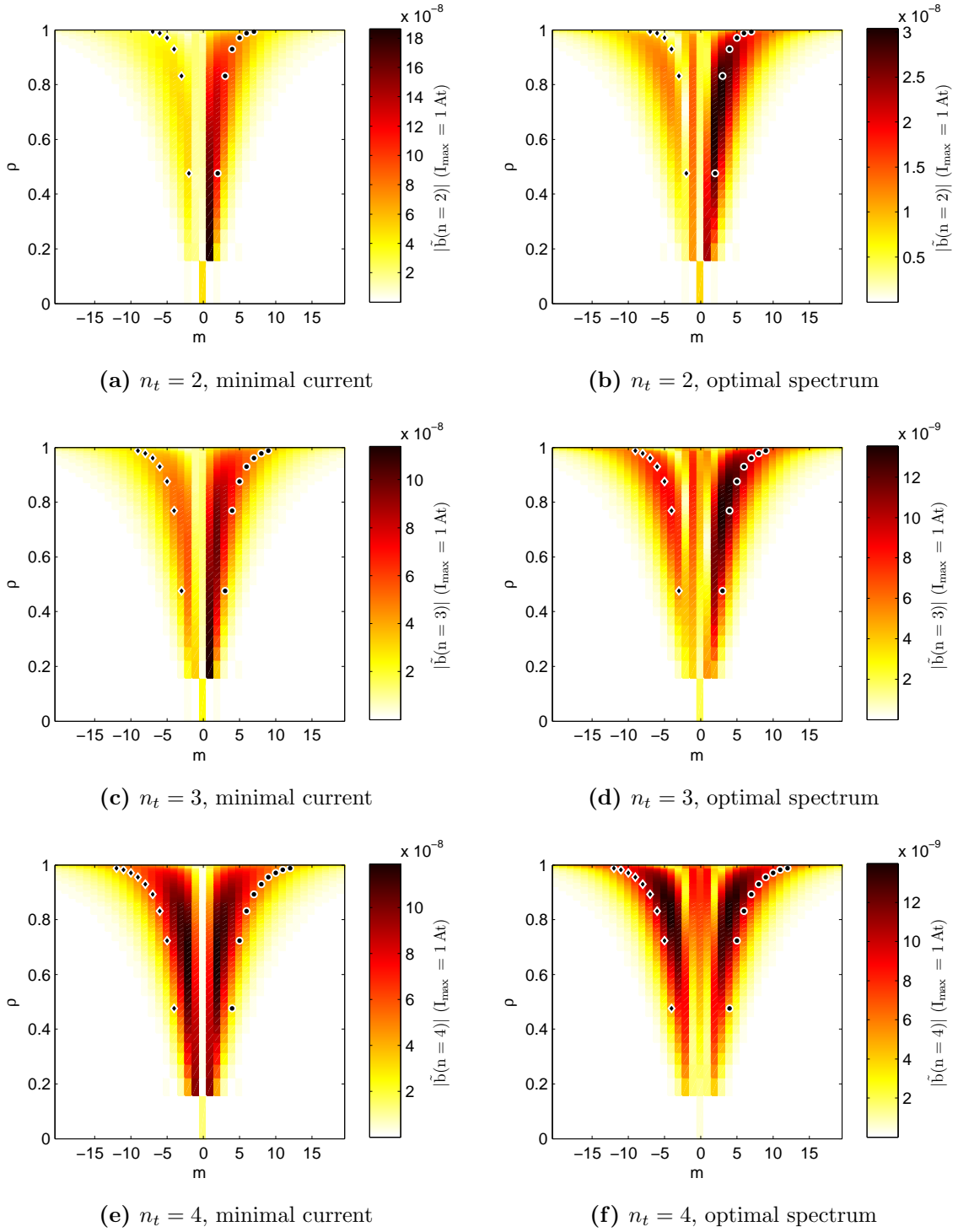
Figure 5.10: $\left| \tilde{b}(\rho, m, n \in \{2; 3; 4\}) \right|$. Target: outside $\rho_{\text{lim}} = 0.911$.   ● : resonant flux surface locations, ♦ : symmetrical non resonant counterparts. Case: ex-vessel, $z_{\text{mag}} = 0.23 \, \text{m}$.

5.2.5.4   Ergodization map

The ergodization maps corresponding to both optimal current distributions, i.e. to both extremes of w_g, for each SCS design and each plasma location are plotted in figures 4.5, 5.11, 5.12 and 5.13. It must be noted that islands corresponding to degenerate modes are also included in these figures (for example $n = 5$ islands for the case $n_t = 3$). Results are very similar for the ex-vessel and the in-vessel case, despite core islands being slightly larger in the ex-vessel case. The maximal current in each plot is given by the condition of equivalence with DIII-D and JET perturbation amplitude at the separatrix. Interestingly, the required current based on a principle of equivalence with DIII-D or JET is often close to the current required to satisfy the Chirikov criterion.

(a) $n_t = 2$, minimal current

(b) $n_t = 2$, optimal spectrum

(c) $n_t = 3$, minimal current

(d) $n_t = 3$, optimal spectrum

(e) $n_t = 4$, minimal current

(f) $n_t = 4$, optimal spectrum
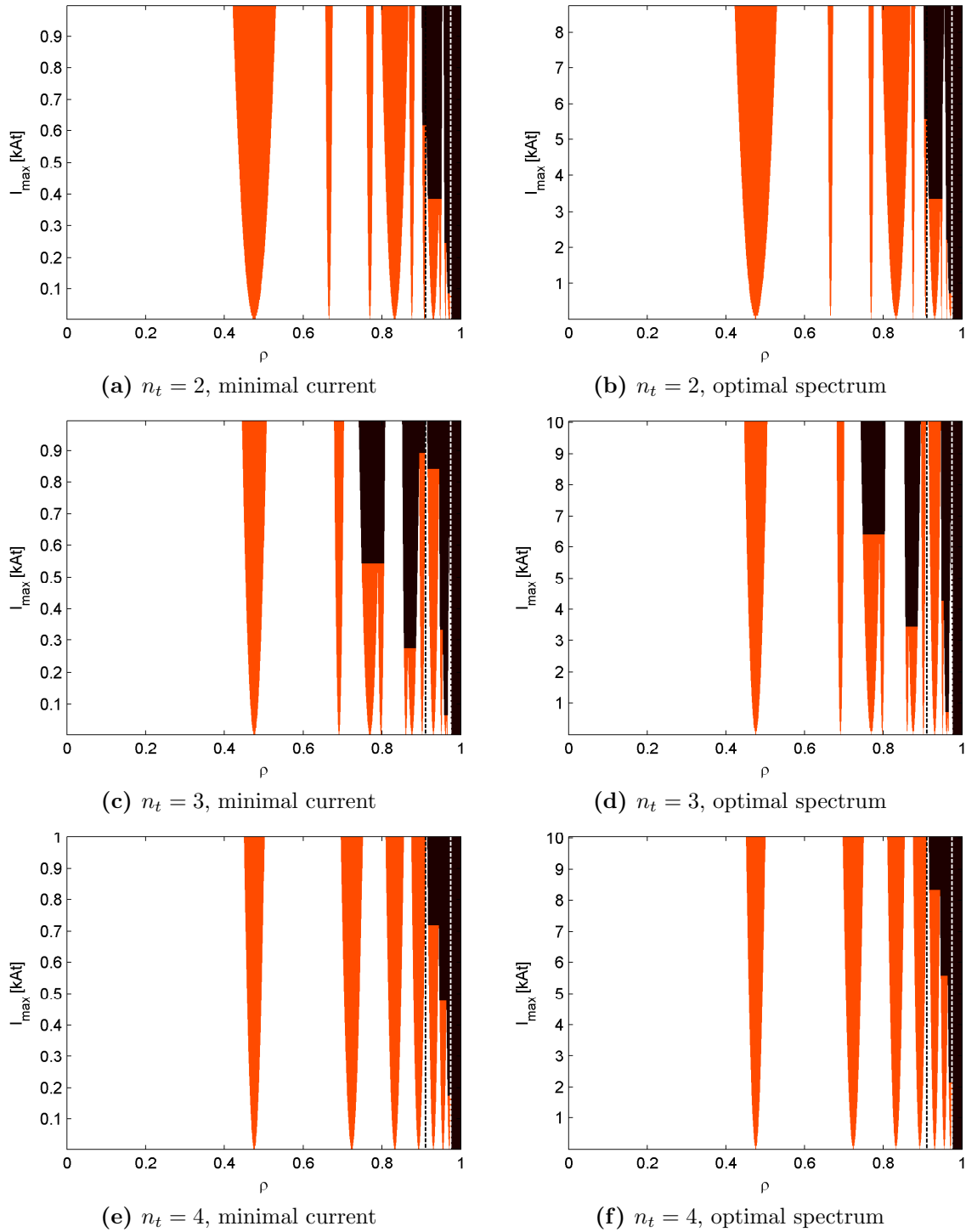
Figure 5.11: Ergodization map. Target: outside $\rho_{\text{lim}} = 0.911$. Island width (red) and ergodic regions (dark brown) shown as a function of the maximal current fed in the SCS. Vertical black dashed line: inner limit of the required ergodic zone according to the $\rho_{\text{lim}} = 0.911$ limit. Vertical white dashed line: $\psi_{01} = 0.95$. Case: in-vessel, $z_{\text{mag}} = 0.23\,\text{m}$.

(a) $n_t = 2$, minimal current

(b) $n_t = 2$, optimal spectrum

(c) $n_t = 3$, minimal current

(d) $n_t = 3$, optimal spectrum

(e) $n_t = 4$, minimal current

(f) $n_t = 4$, optimal spectrum
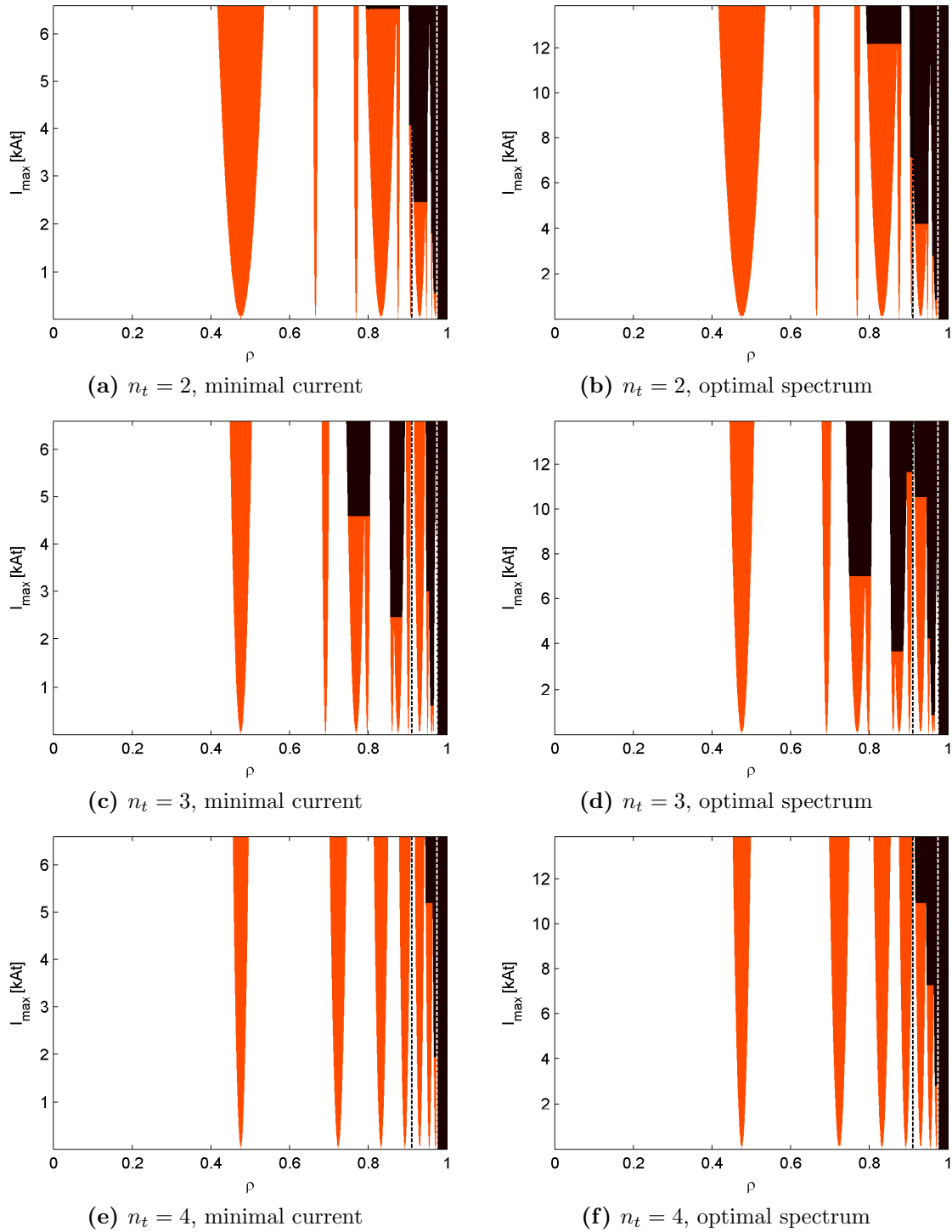
Figure 5.12: Ergodization map. Target: outside $\rho_{\text{lim}} = 0.911$. Island width (red) and ergodic regions (dark brown) shown as a function of the maximal current fed in the SCS. Vertical black dashed line: inner limit of the required ergodic zone according to the $\rho_{\text{lim}} = 0.911$ limit. Vertical white dashed line: $\psi_{01} = 0.95$. Case: ex-vessel, $z_{\text{mag}} = 0$.

(a) $n_t = 2$, minimal current

(b) $n_t = 2$, optimal spectrum

(c) $n_t = 3$, minimal current

(d) $n_t = 3$, optimal spectrum

(e) $n_t = 4$, minimal current

(f) $n_t = 4$, optimal spectrum
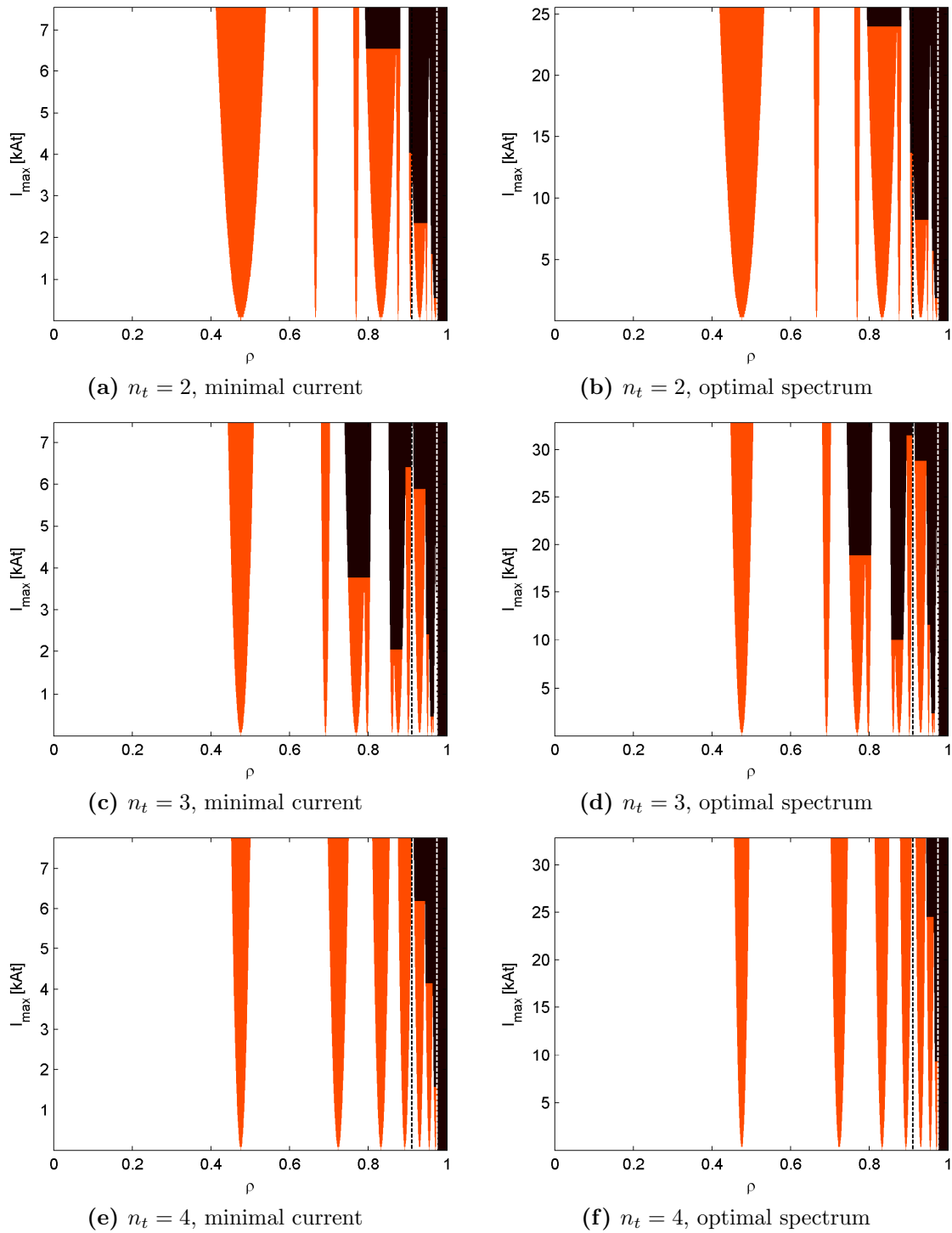
Figure 5.13: Ergodization map. Target: outside $\rho_{\text{lim}} = 0.911$. Island width (red) and ergodic regions (dark brown) shown as a function of the maximal current fed in the SCS. Vertical black dashed line: inner limit of the required ergodic zone according to the $\rho_{\text{lim}} = 0.911$ limit. Vertical white dashed line: $\psi_{01} = 0.95$. Case: ex-vessel, $z_{\text{mag}} = 0.23\,\text{m}$.

(a) Geometrical angle   **(b)** Straight field line angle
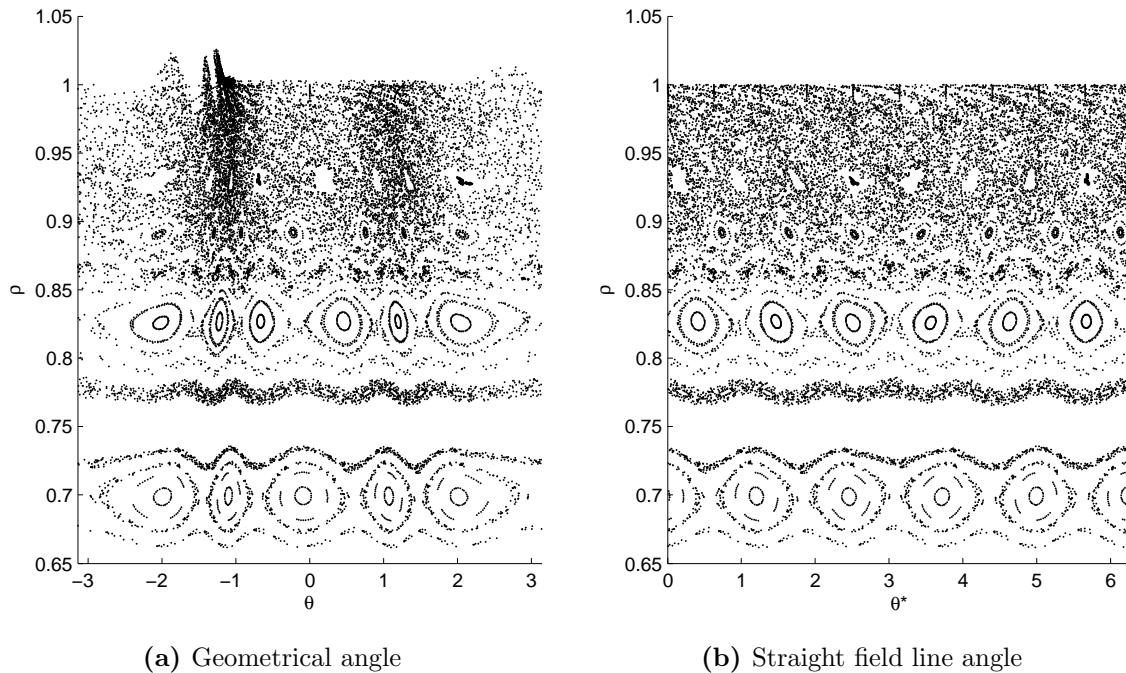
Figure 5.14: Poincaré plot of the magnetic field lines in flux coordinates for the in-vessel design in the $n = 4$ configuration with optimized spectrum, using the $z_{\mathrm{mag}} = 0$ equilibrium. The SCS is powered so that the edge ergodization criterion is satisfied.

5.2.5.5   Poincaré plot

Although Poincaré plots are not directly used in the design study, they provide a point of comparison to verify the results obtained by the analytical island width approach. Indeed, the only common part to both approaches is the total magnetic field in cylindrical coordinates. The Poincaré plot of the $n = 4$ case for the in-vessel system in the optimal spectrum configuration at $z_{\mathrm{mag}} = 0$ is shown in figures 5.14 and 5.15. This figure is the equivalent of figure 4.5(f), but with a maximal current given by the Chirikov criterion (see figure 5.6(a)). When comparing figure 5.14(a) with figure 4.5(f), and recalling that the current used for the Poincaré plot is slightly higher, it can be seen that the island location, width and degree of ergodization is consistent between both figures. In addition, the deformation of the plasma separatrix due to the magnetic perturbation is clearly visible. On figure 5.14(b), the straight field line angle is used to represent the location of the magnetic field lines. As expected, the angular periodicity is restored in the process. Figure 5.15 illustrates the effect of strike point splitting due to the application of RMP. Interestingly, the simple vacuum field approximation is sufficient to account for an experimentally observed phenomenon [86, 107–109].

It can be noted that a core island is missing on figure 5.15. This is due to
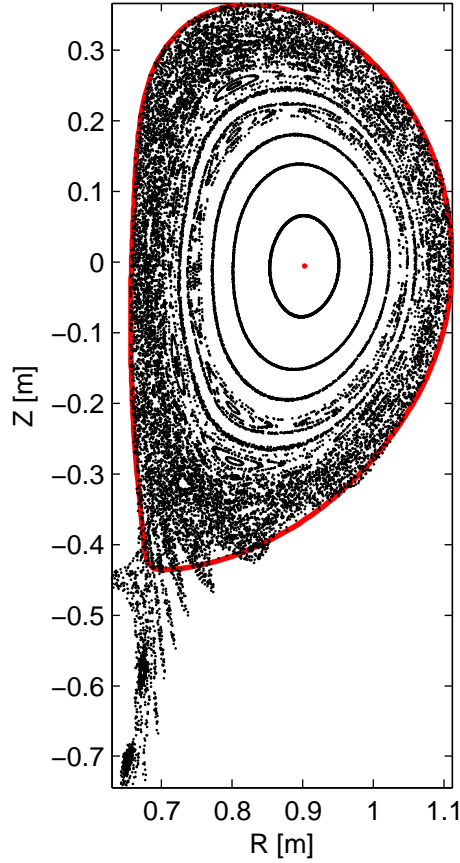
Figure 5.15: Poincaré plot of the magnetic field lines in cylindrical coordinates for the in-vessel design in the $n = 4$ configuration with optimized spectrum, using the $z_{\mathrm{mag}} = 0$ equilibrium. The SCS is powered so that the edge ergodization criterion is satisfied. The equilibrium separatrix and magnetic axis are shown in red. Core islands are not represented.

a small discrepancy between the q-profile given by LIUQE [97] and the q-profile corresponding to field line tracing, although the toroidal field corrected by the plasma contribution has been used in the calculation.

5.3 Error field correction

This section describes the issue of error fields on TCV and how the proposed SCS could correct them. First, the error field situation on TCV is described. Then, the correction principle used in this study is detailed and the SCS design capabilities are discussed. Finally, the question of current requirement is addressed.

5.3.1   Error field on TCV

According to Piras [100], the main source of non-axisymmetric error field on TCV is a tilt of the central coil column corresponding to a misalignment of a maximum of 5 mm of the poloidal field coils located on the central column. This shift corresponds to a $n = 1$ radial perturbation in the range of 1 to 5 mT. The effect of the error field on the plasma is a function of the powering of the different poloidal coils and also a function of the distance between the coils and the plasma.

5.3.2   Error field correction principle

A correction of the error field by a SCS in the entire vacuum chamber is not possible. The SCS can only correct a few spectral components of the error field on a given number of flux surfaces. If the source of error field is known, the resulting magnetic perturbation on the flux surfaces can be calculated for a given magnetic equilibrium. The simplest approach consists in assuming no plasma response to the error field and using the vacuum error field as the error field existing at the flux surfaces. A possible theoretical approach [93] for error field correction (EFC) consists in using a SCS to create a magnetic perturbation that cancels out the most damaging error field components on the resonant flux surfaces (e.g. cancelling out the $(n, m) = (1, 2)$ component on the $q = 2$ surface). Of course, the SCS will itself be a source of error field and its own contribution should be minimized. A more advanced theoretical approach [110, 111], taking into account the amplification of certain components of the error field by the plasma, would possibly give more accurate results, but since the aim here is only to estimate the required current for EFC, the simple vacuum field approach described above is thought to be sufficient.

The experimental approach consists in scanning the parameter space of the $n = 1$ perturbation created by the SCS and correlating the scans with the plasma performances or breakdown robustness. If the number of degrees of freedom of the SCS is large, such an approach might prove extremely resource consuming, especially if the variety of possible magnetic configurations is large, like on TCV.

5.3.3   EFC capabilities with the proposed SCS

Since error field is mainly present for $n = 1$ components, EFC can be obtained independently of other usages of the SCS as long as the combined current requirements do not exceed the design limit value. As described in section 4.3.3.1, the proposed SCS can correct at most 3 modes. Instead of an exact correction of 3 modes, the SCS

can also be fed with a current distribution that minimizes the error field on a larger number of modes, without cancelling them totally. Depending on the experimental program, one could for example correct exactly a particularly strong resonant mode and minimize the amplitude of a set of non-resonant modes. The method described in chapter 4 returns the optimal current distribution for any of the options described above.

5.3.4 Current requirements for EFC on TCV

In order to determine the current requirements for EFC on TCV, the $n = 1$ error field due to a 5 mm radial shift of each poloidal field coil powered at their nominal current of 7.5 kA is calculated on the main resonant flux surfaces $q = 1$ and $q = 2$ of both magnetic equilibria described in section 5.2.5.1. The SCS current distribution is then optimized to cancel this field in different situations: cancellation of the $m = 1$ or $m = 2$ resonant mode only, simultaneous cancellation of both components and, finally, cancellation of one of the resonant modes while minimizing the activation of parasitic modes by the SCS. In all cases, the results are given for the error field phase requiring the largest coil current.

The results for the in-vessel SCS are given in table 5.1(a). As expected, the coils that are close to the magnetic axis have a larger effect. The error fields created by the so-called F-coils also have a larger impact than those created by the E-coils, consistently with the expected larger impact of perturbation coils located on the low field side of the vessel (see section 5.2.3.2). The required current depends strongly on the case under consideration. In the present study, a variation from 0.9 to 16.2 kAt is observed. Following the conclusions of the study of the current requirements for RMP, the required current for EFC increases when an optimal spectrum is required or when several modes are corrected simultaneously. The situation becomes worse when the plasma is located at $z_{\mathrm{mag}} = 0.23$ m and any of both previously stated situations occurs. When considering the values given in table 5.1(a), it seems reasonable to fix the required current at $I_{\mathrm{req,in}} = 3$ kAt since the error field is mainly created by the E-coils in TCV and since special correction scenarios (i.e. multi-mode or optimal spectrum approaches) could use the reserve of current dedicated to RMP (4 kAt in this case). With such a choice, the current limit would be sufficient to cover the standard correction scenario (i.e. one mode with minimal current) with sufficient margin in all the cases and the second limit offered by the RMP reserve would give access to most of the cases of interest. Only multi-mode correction at $z_{\mathrm{mag}} = 0.23$ m would not be possible, but such a scenario would require 9 kAt in addition to the

RMP reserve and therefore represent a large increase of cost with respect to the expected scientific output.

The results for the ex-vessel SCS are given in table 5.1(b). Observations similar to those given for the in-vessel case could be mentioned. Following the arguments given for the in-vessel case, the required current for EFC can be fixed at 7 kAt (recall: the required current for RMP is 14 kAt in that case).

5.4   Inductance and wall currents

The electrical characterization of the SCS requires the calculation of the self and mutual inductances of the coils. For in-vessel coil systems, the electrical coupling of the coils with the vessel wall must also be characterized in order to deduce the frequency response of the coil system and the proportion of screening due to the wall. These aspects are studied in this section.

5.4.1   Mutual and self inductance

The mutual and self inductance calculation of the SCS is based on the Neumann's formula (B.1). When possible, analytical or semi-analytical formulations are used to speed up the calculation. The details of this procedure are given in appendix B.1.

5.4.2   Calculation results in DC mode

When the coils are powered with a constant current, the presence of the vessel wall has no importance. In that case, the coils of the in-vessel design, in a 10-turn configuration, have a self-inductance of $138\,\mu$H while the coils of the ex-vessel design, in a single turn configuration, have a self-inductance of $1.44\,\mu$H. For the in-vessel design, the mutual inductance between direct neighbours on the same row is of $-6\,\mu$H and between direct neighbours one row apart of $-10.6\,\mu$H. The current induced in a coil due to the powering of a neighbouring coil is therefore more than an order of magnitude smaller than the current in the active coil. The mutual inductance between coils located further apart is negligible, as shown in figure 5.16.

5.4.3   Calculation of wall currents

In order to estimate the electromagnetic coupling between the vessel wall and the SCS, the wall is represented by a set of conducting filaments having an imposed

m	z_{mag} [m]	Optimal spectrum	$\max(I_{\mathrm{req,\,E}})$ [kAt]	$\max(I_{\mathrm{req,\,F}})$ [kAt]
1	0	No	0.9 (E3)	1.3 (F5)
1	0	Yes	1.7 (E3)	2.5 (F5)
2	0	No	1.3 (E4)	1.3 (F4)
2	0	Yes	1.7 (E4)	1.8 (F4)
[1,2]	0	No	6.5 (E4)	7.7 (F4)
1	0.23	No	0.9 (E5)	1.3 (F6)
1	0.23	Yes	3.8 (E5)	5.7 (F6)
2	0.23	No	1.1 (E5)	1.2 (F5)
2	0.23	Yes	5.7 (E5)	6.5 (F5)
[1,2]	0.23	No	13.0 (E5)	16.2 (F6)

(a) In-vessel SCS

m	z_{mag} [m]	Optimal spectrum	$\max(I_{\mathrm{req,\,E}})$ [kAt]	$\max(I_{\mathrm{req,\,F}})$ [kAt]
1	0	No	3.2 (E3)	4.8 (F5)
1	0	Yes	4.1 (E3)	6.3 (F5)
2	0	No	4.4 (E4)	4.6 (F4)
2	0	Yes	5.1 (E4)	5.2 (F4)
[1,2]	0	No	24.9 (E4)	29.6 (F4)
1	0.23	No	2.9 (E5)	4.2 (F6)
1	0.23	Yes	8.5 (E5)	12.6 (F6)
2	0.23	No	4.0 (E5)	4.5 (F5)
2	0.23	Yes	13.7 (E5)	15.6 (F5)
[1,2]	0.23	No	26.9 (E5)	33.2 (F5)

(b) Ex-vessel SCS

Table 5.1: Current requirements for EFC with the in- and ex-vessel SCS. The "optimal spectrum" column mentions whether the required current is minimized ("No") or the parasitic modes are minimized ("Yes"). The maximal correction current for each group of poloidal coils is given. The coil for which this current is required is given in brackets. The E-coils are the high field side poloidal coils and the F-coils the low field side ones. Both sets are numbered from 1 to 8 from bottom to top (see figure 2.4).
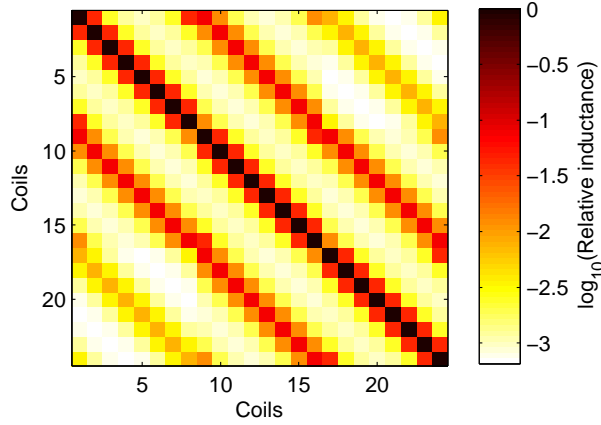
Figure 5.16: Relative mutual inductance between coils of the 10-turn in-vessel SCS. The reference value is the self-inductance of each coil. The coil numbering is done within coil rows first and then from the bottom row to the top row.

geometry. The choice of filament geometry is determined by the expected spatial distribution of the vessel current density, which is in general conforming with the shape of the coils. Particular geometries are proposed below (sections 5.4.3.1 and 5.4.3.2). For the moment, it is sufficient to consider a set of generic vessel filaments. The electromagnetic system formed by the SCS and the wall is then completely described by the resistance and the self and mutual inductances of all the vessel filaments and coil turns. Assuming the time-dependence of the SCS currents to be $\mathbf{I_c}e^{i\omega t}$, the wall currents are given by the vessel filament voltage equations:

$$[i\omega\mathbf{M_{vv}} + \mathbf{R_{vv}}] \cdot \mathbf{I_v} \quad = \quad -i\omega\mathbf{M_{vc}} \cdot \mathbf{I_c} \tag{5.1}$$

$$R_{ij} \quad := \quad R_i\delta_{ij} \tag{5.2}$$

$$R_i \quad := \quad \rho_{vessel}\frac{l_i}{S_i} \tag{5.3}$$

with v the vessel filament index, c the SCS coil index, $\mathbf{I}$ the current vector, $\mathbf{R}$ the electrical resistance matrix, $\mathbf{M}$ the inductance matrix, l the conductor length, S the conductor cross-section and ρ the resistivity. As ω increases, the image currents induced in the vessel wall reduce the magnetic flux created by the SCS and partially cancel the radial magnetic field perturbation. Above a certain frequency, the resistive contribution of the vessel filaments becomes negligible and the relative amplitude of the vessel currents saturates. In theory, the wall screening can therefore be completely compensated by increasing the value of the SCS nominal current, especially for the in-vessel design, but the necessary increase might be very large (a factor 5 to 10) depending on the distance between the coils and the vessel wall (see section 5.4.3.5).

The presence of the wall changes the frequency response of the SCS, effectively replacing the SCS inductance matrix by a frequency-dependent apparent inductance matrix. The latter is identified using the SCS voltage equation:

$$\mathbf{U_c} = \left[\begin{array}{cc} (\mathrm{i}\omega\mathbf{M_{cc}} + \mathbf{R_{cc}}) & \mathrm{i}\omega\mathbf{M_{cv}} \end{array} \right] \cdot \left[\begin{array}{c} \mathbf{I_c} \\ \mathbf{I_v} \end{array} \right] \tag{5.4}$$

Using (5.1) to replace $\mathbf{I_v}$ in (5.4), the vessel contribution can be represented by a frequency-dependent apparent inductance matrix:

$$\mathbf{U_c} = [\mathrm{i}\omega\mathbf{M_{cc,app}}(\omega) + \mathbf{R_{cc}}] \cdot \mathbf{I_c} \tag{5.5}$$

with

$$\mathbf{M_{cc,app}}(\omega) = \mathbf{M_{cc}} - \mathrm{i}\omega\mathbf{M_{cv}}(\mathrm{i}\omega\mathbf{M_{vv}} + \mathbf{R_{vv}})^{-1}\mathbf{M_{vc}} \tag{5.6}$$

From an electrical point of view, the wall decreases the apparent inductance of the SCS as the current frequency is increased. This is consistent with Faraday's equation.

Note that this study is meaningful only in the case of the in-vessel design, since the ex-vessel design would not be powered at frequencies exceeding the wall penetration time.

5.4.3.1 Filament geometry for independent coil powering

In the general case of independent coil powering, the vessel filament geometry is chosen as follows. Each coil of the SCS is matched with a number of geometrically equivalent loops in the wall, taken as an infinite cylinder here. These loops are defined so that wall loops of two neighbouring coils are at most juxtaposed (see figure 5.17). Overlapping of wall loops would be theoretically possible, but certainly of little physical meaning. In addition, the apparent inductance values are nearly insensitive to this aspect. Since the current density in the wall tends to tighten along the projection of the SCS coils as the frequency is increased, the values at the limit $\omega = \infty$ is unaffected by the number of wall filaments outside the coil projection.

Note that the central column, the top and the bottom of the vessel are not taken into account in this representation of the vessel. Since these elements are relatively far away from the coils, neglecting them is certainly not too damaging. The $n = 0$ combination case (section 5.4.3.4) shows that this assumption has no major consequences.
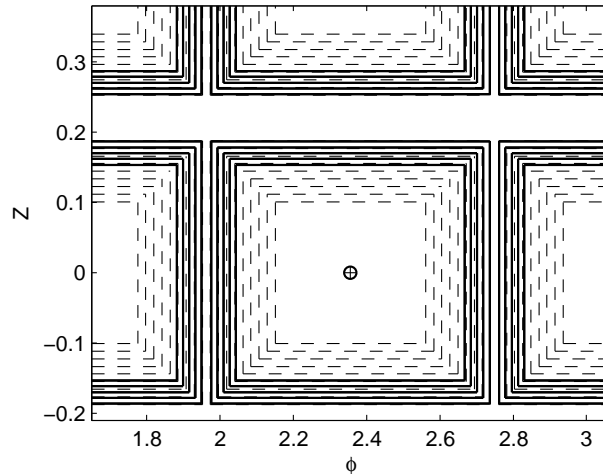
Figure 5.17: Illustration of the vessel filaments (in dashed lines) used in the case of independent coil powering. The number of filaments has been decreased here for the sake of clarity. The coil turns are represented by solid lines. The number of turns per coil in the figure is illustrative only.

5.4.3.2   Filament geometry for $n = 0$ coil combination

The $n = 0$ combination of the in-vessel SCS is of particular interest for vertical control, especially if a dedicated common power supply is used for this task. In order to calculate the magnetic field produced in $n = 0$ configuration, it is easier to replace the rows of the SCS by circular toroidal loops and to also use circular toroidal filaments to describe the wall. Such an assumption allows one to take into account the remaining parts of the vessel (bottom, top and central column). In this context, the general method developed in section 5.4.3 still holds, but the calculation is greatly simplified by the axisymmetric geometry. The results obtained here are also useful to check the validity of the results obtained in the independent coil powering geometry. Note that this approach neglects the contribution from the vertical segments of the SCS and the toroidal gaps between the coils.

5.4.3.3   Apparent inductance as a function of frequency

The apparent self and mutual inductances as a function of frequency of the in-vessel system using the filament geometry for independent coil powering and equation (5.6) is shown in figure 5.18. The relative apparent mutual inductances of the whole system at high frequency are shown in figure 5.19. Similarly to the DC case, coupling between coils at high frequency is weak and becomes negligible for coils that are not direct neighbours. For the sake of clarity, the apparent self-inductance of a single coil is shown separately in figure 5.20. The effect of the wall is not negligible, since the reduction of apparent inductance is close to a factor 2. Therefore, the voltage
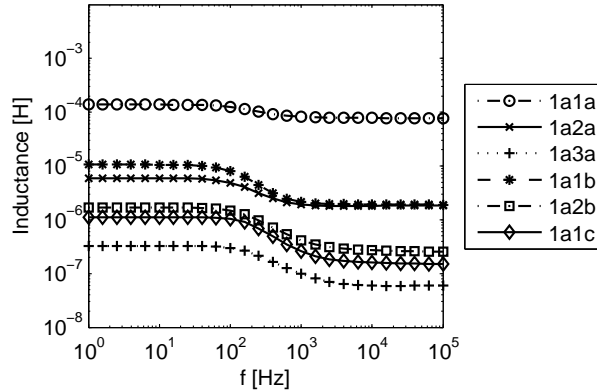
Figure 5.18: Apparent self and mutual inductances of a selection of pairs of coils as a function of frequency for the 10-turn in-vessel SCS, using the wall filament geometry described in section 5.4.3.1. A 2-character alphanumeric code is used to describe the coil locations, the digit indicating the location of a coil in a row and the letter indicating the coil row.

required to reach a given peak current at high frequency is smaller than what could be expected from DC values.

5.4.3.4 $n = 0$ coil combination and wall model consistency

When combining coils in $n = 0$ configurations, the total inductance of the system depends on the relative direction of the current between the coil rows. For the sake of simplicity, we assume that each coil row is either not active ('0') or carry the same current amplitude as the other rows ('+' or '-', depending on the current sign). In this case, the minimal inductance is obtained for the '0+0' configuration while the '+-+' configuration yields the largest inductance. The results for both types of wall filaments can be compared by grouping the apparent inductances obtained with the saddle-shaped wall filaments in $n = 0$ configurations (see figure 5.21). As expected, the DC inductance is slightly higher for the combination of saddle coils because of the contribution of the vertical coil segments. At high frequency, the decrease of apparent inductance due to the presence of the wall is slightly larger for the circular filament model, consistently with a better modelling of the wall screening effect due to a full spatial coverage of the vessel by the filaments. The discrepancy between both results is not significant from the engineering point of view and both approaches will be considered as satisfactory. Nonetheless, when possible, the worst situation results should be used for the power supply design, i.e. the inductance given by the saddle-shaped filament model and the amount of screening given by the circular filament model.
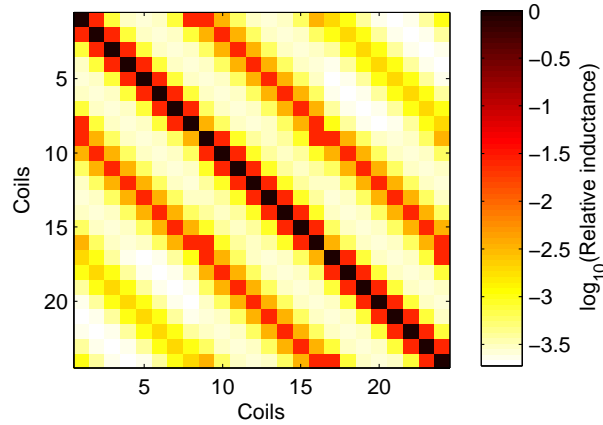
Figure 5.19: Relative apparent mutual inductance between coils of the 10-turn in-vessel SCS at high frequency (100 kHz). The reference value is the apparent self-inductance of each coil. The coil numbering is done within coil rows first and then from the bottom row to the top row.
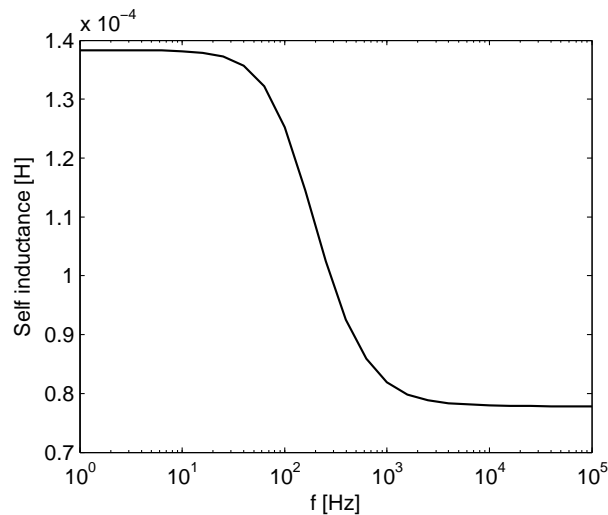
Figure 5.20: Apparent self inductance of a coil of the 10-turn in-vessel SCS as a function of frequency, using the wall filament geometry described in section 5.4.3.1.

5.4.3.5   Magnetic perturbation screening as a function of frequency

The 10-turn in-vessel SCS design is used to quantify the screening of the magnetic perturbation due to the vessel image currents. For that purpose, a single coil of the system is used so that the number of filaments in the wall can be increased both vertically and radially to obtain a more accurate description of the wall. Equation (5.1) is solved for a range of frequencies to obtain the wall currents. The radial magnetic field due to the coil and the wall currents is averaged over an interval of the coil axis limited by the radial extent of the vacuum chamber. This calculation is repeated for a selection of radial locations of the coil, going from 0 to 4 cm between the coil and the wall surface. The results are shown in figure 5.22. Note that the indicated
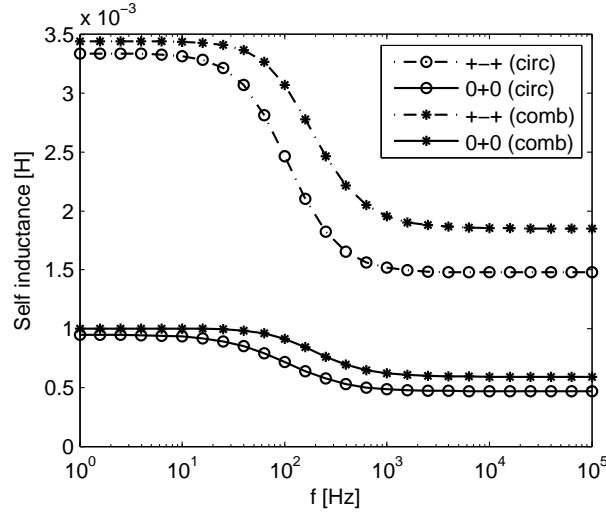
Figure 5.21: Apparent self-inductance of '0+0' and '+-+' $n = 0$ combinations of the 10-turn in-vessel SCS as a function of frequency. The results obtained for the toroidally circular wall filaments ("circ") are compared to the results obtained for the saddle-shaped filaments by combining the apparent inductances of the SCS coils obtained for that geometry ("comb").

distance to wall is measured from the coil center to the wall inner surface. On figure 5.22(a), the saturation of the attenuation at high frequency can be seen. The deviation of the attenuation along the radial coordinate is larger for the case where the coil is further away from the vessel wall, consistently with a larger spreading of the vessel currents and a non negligible distance between both sources of magnetic field with respect to the probed location. Figure 5.22(b) shows that the attenuation is strongly dependent on the distance from the coil to the wall. The coil centers of the 10-turn design are located at 2.5 cm from the wall surface, in which case only approximately 25% of the perturbation remains at high frequency.

5.4.4 SCS response function

Equation (5.5) defines the response functions of the SCS in the presence of a conducting wall. Note that the response functions of the different coils are coupled with one another and with the wall. Although each response function can be represented as a function of frequency in both directions ($I_c(U_c)$ and $U_c(I_c)$), they cannot be described by a simple analytical expression, as would be required to design the power supplies. In order to reduce the complexity of the system, one could think of replacing the wall filaments by an equivalent single-turn loop whose electrical parameters (resistance, self and mutual inductances) are found by fitting the total wall current associated to each coil of the SCS as a function of frequency. Efforts in this

(a) Scan on frequency

(b) Scan on distance to the wall
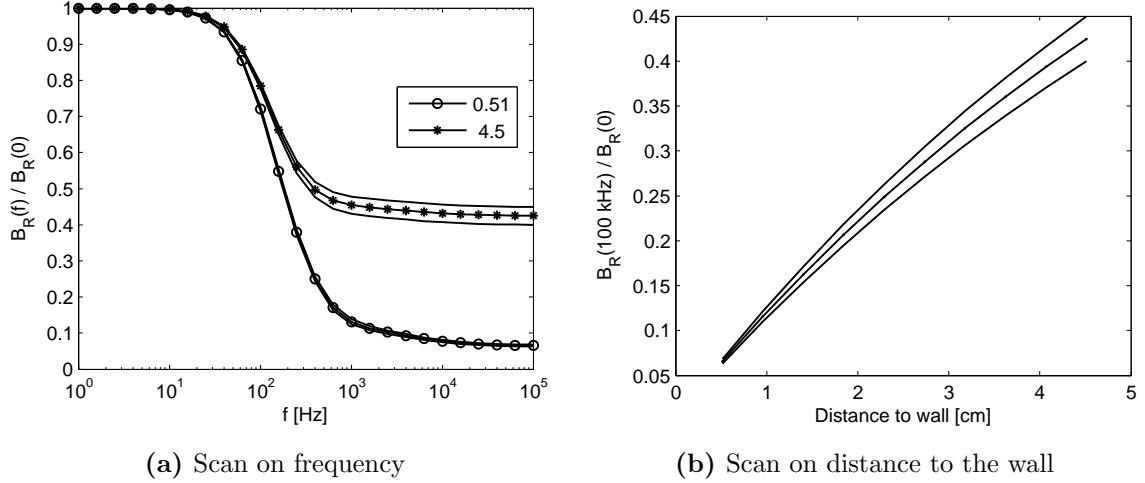
Figure 5.22: Mean attenuation along the coil axis of the magnetic perturbation created by the 10-turn in-vessel SCS. (a) frequency dependence for two different distances from the coil center to the wall surface (in centimeters), including the standard deviation along the radial coordinate. (b) dependence on the distance to the wall at saturation (i.e. $100\,\text{kHz}$), including standard deviation.

direction have been made but even though the wall current has been successfully modelled, the obtained inductances were not physical (self smaller than mutual) and the response functions were not equivalent. One could then think of another similar approach that would consist in finding the electrical parameters of the equivalent single-turn loops by directly fitting the full model response functions. This approach is nonetheless problematic because a non-linear fit would then be required. Finally, simply combining the wall filaments in parallel would be wrong: the voltage on each filament is different, each filament is different and the arbitrary selection of wall filaments would have an important impact. Consequently, a more general approach has to be used. It is described in the next section.

5.4.4.1 System response reduction

Equations (5.1) and (5.4) expressed in a more general form are written:

$$\mathbf{U} = \mathbf{M} \cdot \dot{\mathbf{I}} + \mathbf{R} \cdot \mathbf{I} \tag{5.7}$$

with

$$\mathbf{U} = \begin{bmatrix} \mathbf{U_c} \\ \mathbf{0} \end{bmatrix} \quad \mathbf{I} = \begin{bmatrix} \mathbf{I_c} \\ \mathbf{I_v} \end{bmatrix} \quad \mathbf{M} = \begin{bmatrix} \mathbf{M_{cc}} & \mathbf{M_{cv}} \\ \mathbf{M_{vc}} & \mathbf{M_{vv}} \end{bmatrix} \quad \mathbf{R} = \begin{bmatrix} \mathbf{R_{cc}} & \mathbf{0} \\ \mathbf{0} & \mathbf{R_{vv}} \end{bmatrix}$$

from which the time derivative of the currents is written:

$$\dot{\mathbf{I}} = -\mathbf{M}^{-1} \cdot \mathbf{R} \cdot \mathbf{I} + \mathbf{B} \cdot \mathbf{U_c} \tag{5.8}$$

with $\mathbf{B}$ the first n_c columns of $\mathbf{M}^{-1}$. In this form, the circuit equation is an example of a linear time invariant system (LTI) and the tools developed in the frame of LTI theory are applicable.

LTI theory involves the manipulation of state-space models. A general state-space model formulation is given by:

$$\begin{cases} \dot{\mathbf{x}} = \mathbf{A}\mathbf{x} + \mathbf{B}\mathbf{u} \\ \mathbf{y} = \mathbf{C}\mathbf{x} + \mathbf{D}\mathbf{u} \end{cases} \tag{5.9}$$

where $\mathbf{u}$ is the input, $\mathbf{y}$ the output and $\mathbf{x}$ the space vector of the system. Of course, $\mathbf{u}$ and $\mathbf{y}$ can also be vectors, in which case the system is said to be a MIMO (multiple inputs, multiple outputs). Writing $\dot{\mathbf{x}} = s\mathbf{x}$, the transfer function $\mathbf{G}(s) := \mathbf{y}/\mathbf{u}$ is given by:

$$\mathbf{G}(s) = \mathbf{C}(s\mathbb{1} - \mathbf{A})^{-1}\mathbf{B} + \mathbf{D} \tag{5.10}$$

Note that $\mathbf{G}$ is a matrix of transfer functions in the general case.

In the case of the wall filament model, the state space model is given by comparing equations (5.8) and (5.9): $\mathbf{x} := \mathbf{I}$, $\mathbf{A} := -\mathbf{M}^{-1} \cdot \mathbf{R}$, $\mathbf{B} := \mathbf{B}$, $\mathbf{u} := \mathbf{U_c}$, $\mathbf{y} := \mathbf{I_c}$, $\mathbf{C} = [\mathbb{1_c}, \mathbf{0}]$ and $\mathbf{D} = \mathbf{0}$. In equation (5.9), $\mathbf{x}$ is an internal variable. It is therefore possible to approximate the transfer functions corresponding to the state-space model by reducing the dimensions of the space vector and the state matrix $\mathbf{A}$. In terms of response function, such an approach is equivalent to cancelling close pole-zero pairs. In the formalism of LTI systems, a Hankel singular value decomposition (HSVD) is used to obtain such a system reduction. The wall filament model leads to a problem of degeneracy, each coil and its set of wall filaments being identical or very close to one another. To obtain a correct reduction of the order of the system, the degeneracy must be alleviated beforehand by replacing the multiple input by a single one, so that the system becomes asymmetric. The system order reduction by HSVD is then determined by the desired reduced system order and the conservation of the DC gain of the system. Generally, the reduced system order should be as low as possible and the DC gain should be conserved while keeping a good approximation of the original system. These aspects are studied in the analysis given below. Note that the state-space description of a LTI system is exactly equivalent to a zero-pole-gain description. Therefore, a reduced system can be converted to a set of transfer functions with a number of poles and zeros given by the order of the reduced system.

The numerical analysis is performed on the 10-turn in-vessel SCS. Three questions are addressed: what is the adequate reduced system order, should the equivalent DC gain constraint be used and what is the impact of the choice of the particular

coil used as single input of the system? Due to the symmetry of the SCS, the last question is completely addressed by comparing the transfer functions obtained for a coil of the bottom (or top) row with the transfer functions obtained for a coil of the middle row. This study is presented in figure 5.23, from which it can be concluded that the difference of behaviour is negligible, confirming the small effect of coupling between coils. The study concerning the model reduction is presented in figure 5.24. An order of 3 has been chosen to reduce the model since, as shown, the response function is well approximated in the range of frequencies of experimental interest. A lower order would result in a sufficient approximation quality only on a reduced frequency interval, while a higher order would lead to unnecessary complication of the analytical expression of the transfer functions. In general, system reduction by truncation results in a much better approximation of the transfer functions, at the cost of a small discrepancy on the DC gain. In our case, this discrepancy is negligible and the truncation method should be kept. In that case, the reduction results in:

$$G_{1b1b}(s) = \frac{1.26 \cdot 10^4 \cdot (s + 1.16 \cdot 10^3)(s + 1.69 \cdot 10^2)}{(s + 2.1 \cdot 10^3)(s + 2.04 \cdot 10^2)(s + 1.4 \cdot 10^2)} \text{ A/V} \qquad (5.11)$$

$$G_{1b1c}(s) = \frac{2.73 \cdot 10^2 \cdot (s + 3.86 \cdot 10^3)(s + 1.69)}{(s + 2.1 \cdot 10^3)(s + 2.04 \cdot 10^2)(s + 1.4 \cdot 10^2)} \text{ A/V} \qquad (5.12)$$

$$G_{1b2b}(s) = \frac{3.02 \cdot 10^2 \cdot (s + 2.11 \cdot 10^3)(s - 2.66)}{(s + 2.1 \cdot 10^3)(s + 2.04 \cdot 10^2)(s + 1.4 \cdot 10^2)} \text{ A/V} \qquad (5.13)$$

$$G_{1b2c}(s) = \frac{8.08 \cdot 10^1 \cdot (s + 3.02 \cdot 10^3)(s - 1.59 \cdot 10^1)}{(s + 2.1 \cdot 10^3)(s + 2.04 \cdot 10^2)(s + 1.4 \cdot 10^2)} \text{ A/V} \qquad (5.14)$$

where s is the Laplace variable and each considered coil is labelled by a two-character alphanumeric symbol, the digit representing the toroidal position and the letter indicating the coil row.

Finally, note that the order in which the reduction and sub-system selection (i.e. pairing a single output with the single input) are carried has an influence on the final result. It is not equivalent to reduce the system before or after the sub-system selection. In our case, the difference is stronger for the method conserving the DC gain but remains negligible nonetheless (not presented).

5.5   Vertical control

In the current TCV setup, vertical control (VC) is successfully provided by the internal fast coils, also called G-coils. Since the co-existence of two internal coil systems is problematic in terms of space occupation, not only with the coils themselves but also with feed-throughs and power lines, the questions of replacement of the actual

(a) Self

(b) 1 row apart

(c) 1 column apart

(d) 1 row 1 column apart
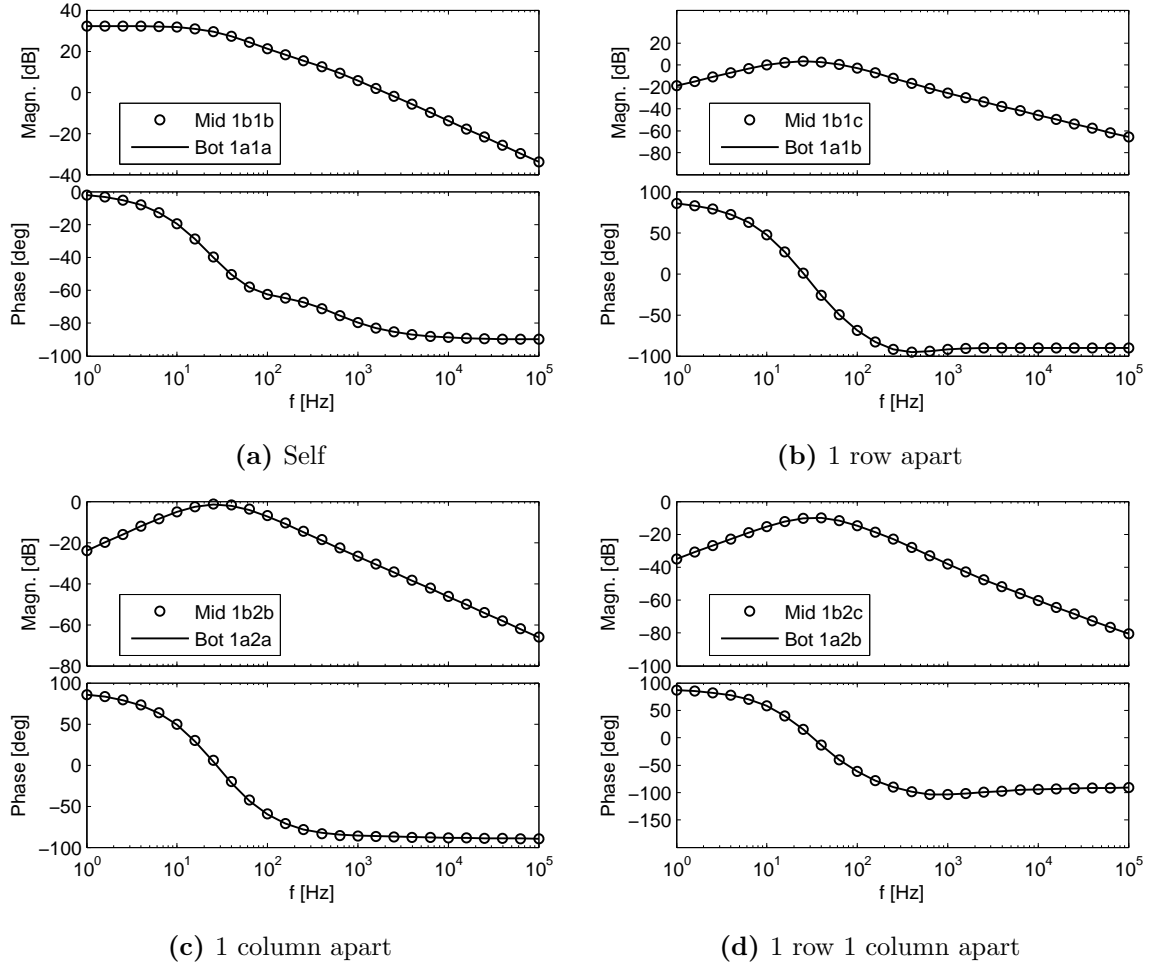
Figure 5.23: Complete model response functions between different pairs of coils of the 10-turn in-vessel SCS using either a middle row coil ('mid') or a bottom row coil ('bot') as system input. Each considered coil is labelled by a two-character alphanumeric symbol, the digit representing the toroidal position and the letter indicating the coil row.

G-coils by the in-vessel SCS and the conditions under which this replacement can occur must be addressed. In this section, the applicability of the in-vessel SCS to vertical control is studied, using a principle of equivalence with the present system, a 3-turn coil whose turns are located in both LFS corners of the vacuum vessel (see figure 5.1) and fed with a maximum current of 2 kA.

5.5.1   Vertical control principle

Vertical control is obtained by applying a magnetic field with a dominant component along the main radial coordinate. Combined with the plasma current, this field gives rise to a vertical Laplace force whose direction and amplitude are adjusted to counteract a vertical displacement of the plasma. Since these corrections must be

(a) Self   **(b)** 1 row apart

(c) 1 column apart   **(d)** 1 row 1 column apart
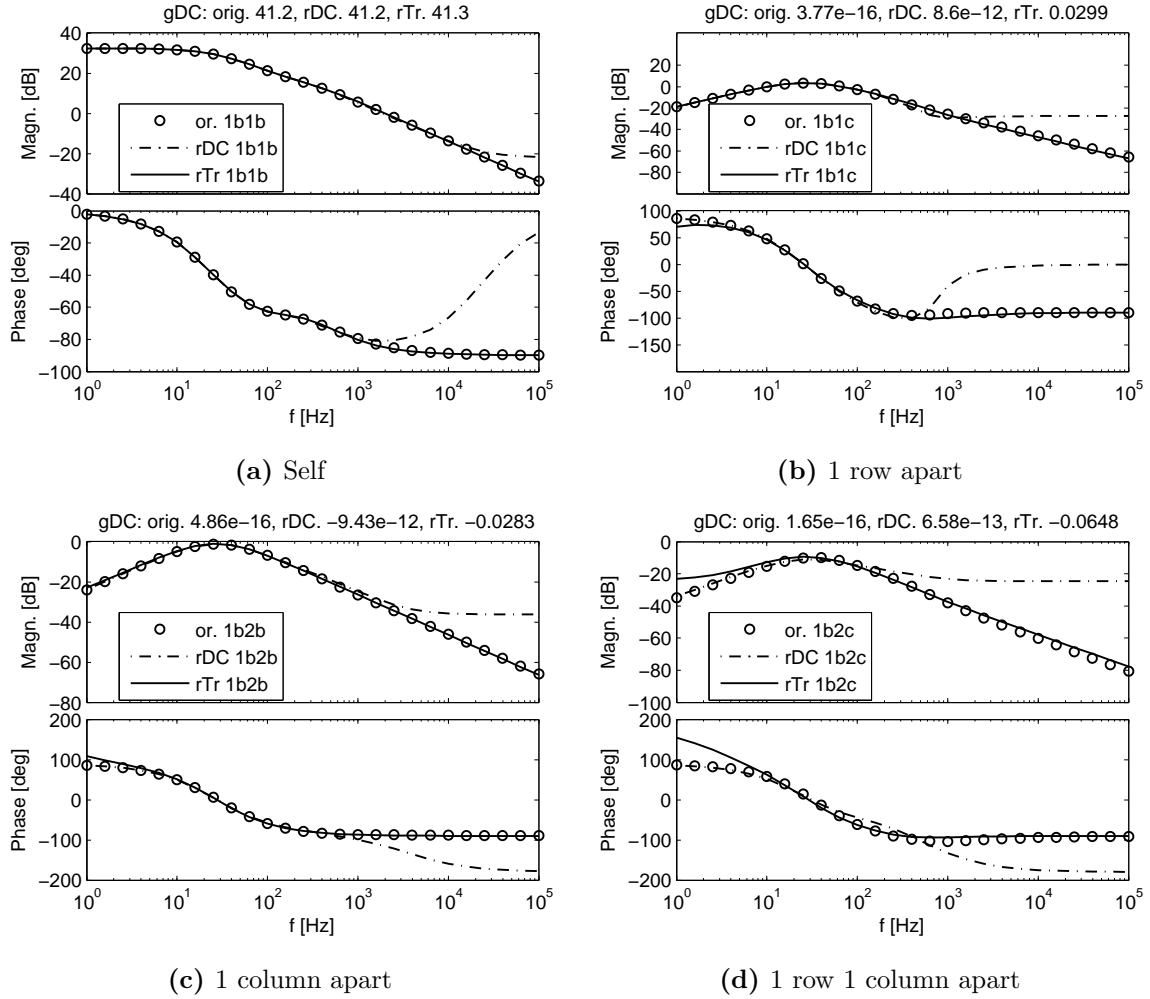
Figure 5.24: Original and reduced (order 3) response functions between different pairs of coils of the 10-turn in-vessel SCS. Original model: 'or'. Reduced model with DC gain constraint: 'rDC'. Reduced model by simple truncation of small singular values: 'rTr'. The DC gains for each case are given in the figure titles. Each considered coil is labelled by a two-character alphanumeric symbol, the digit representing the toroidal position and the letter indicating the coil row.

applied on short time scales, the vessel wall screening currents must be taken into account when dimensioning the amplitude of the control radial field.

5.5.2 Calculation method

Effective radial control field As vertical control is obtained by $n = 0$ combinations of the coils in the case of the SCS, the circular toroidal filament model (section 5.4.3.2) is used to represent the vessel wall. Equation (5.1) is used to get the wall currents as a function of frequency for a given coil combination. The effective radial control field at each point of the Tokamak poloidal cross-section is obtained by adding up the contribution of the coil system with the contribution of the vessel

wall. Note that only the high frequency results are of interest for this study.

Coil row combinations   Since three independent coil rows are available, different row combinations are possible. Using the same labelling as in section 5.4.3.4, the non redundant combinations creating the highest possible radial field are: '+++', '-++', '++-' and '+-+'.

Plasma current distributions   In order to assess the efficiency of the different coil row combinations and to compare them with the control capacity offered by the G-coils, a series of synthetic plasma current distributions is generated to cover a range of typical situations occurring in TCV. The series of synthetic current distributions is expressed as follows:

$$\begin{cases} j_{\mathrm{aux}}(R, Z) = 1 - \left(\frac{R-R_0}{a}\right)^2 - \left(\frac{Z-Z_0}{b}\right)^2 \\ j(R, Z) = j_{\mathrm{mag}} j_{\mathrm{aux}}(R, Z) & j_{\mathrm{aux}} \geq 0 \\ j(R, Z) = 0 & j_{\mathrm{aux}} < 0 \end{cases} \quad (5.15)$$

with

$$\begin{aligned} R_0 &= 0.872 \,\mathrm{m} \\ Z_0 &= 0 \quad \mathrm{or} \quad 0.23 \,\mathrm{m} \\ a &= 0.225 \,\mathrm{m} \\ b &= 2a \quad \mathrm{or} \quad 3a \\ j_{\mathrm{mag}} &= 10^6 \frac{b}{3a} \frac{1}{\int j_{\mathrm{aux}} \mathrm{d}R\mathrm{d}Z} \,\mathrm{A/m^2} \end{aligned} \quad (5.16)$$

In other words, an elliptic cross-section with quadratic current profile is used. $R_0 = 0.872 \,\mathrm{m}$ corresponds to the vessel center, accounting for the new position of the tiles due to the saddle coil system. $b = 3a$ corresponds to an elongated plasma and is used only when $Z_0 = 0$. The current density is scaled to give a total plasma current of $1 \,\mathrm{MA}$ at the largest elongation.

Vertical force   For each current distribution, the vertical component of the Laplace force is calculated and integrated over the plasma poloidal cross-section. The force per unit current serves as a comparison parameter between the different coil row combinations, while the current required to provide a force equal to the force provided by the G-coils gives the equivalent current I_{equiv} for each case.

5.5.3   Optimal coil row combinations

The vertical forces created by the SCS in various row combinations for different plasma current distributions are shown in figure 5.25. The optimal coil row combi-

nation for a given plasma current distribution, defined as the combination delivering the largest vertical force per unit current at high frequency, is used to plot the frequency response of the vertical force for the different plasma current distributions (figure 5.25(d)). In general, the best row combination at high frequency is also the best combination at low frequency. For the elongated plasmas, this is however not the case (see figure 5.25(c)). This is due to an increased importance of the coil segments located in the corners of the vessel for highly elongated plasmas. At low frequency, these segments have a strong contribution to the vertical force, resulting in an optimal combination of type '+++', while at high frequency these segments are more efficiently screened by the vessel than the other coil segments and have a weaker contribution, therefore leading to an optimum given by the '+-+' combination. This effect is shown with more details in figure 5.26, where the results for all the up-down symmetric combinations in the case of a highly elongated plasma located at $z_{\text{mag}} = 0$ are plotted. Since the vertical force obtained for the '+-+' combination dominates above 50 Hz, it can be safely considered as the optimal combination for this kind of plasmas. If lower frequencies are of importance, the '0+0' combination could be a possible consensus between efficiencies at low and high frequencies.

5.5.4   Current requirements

The vertical force provided by the G-coil for the three plasma current distributions is compared to the force provided by the in-vessel SCS in figure 5.27(a). The force ratio displayed in the figure is defined as:

$$r_F = [F_{Z,G}/(I_G N_G)] \, / \, [F_{Z,\text{SCS}}/(I_{\text{SCS}} N_{\text{SCS}})] \tag{5.17}$$

where I is the current and N the number of turns in the respective coils. The SCS current required to obtain $F_{Z,\text{SCS}} = F_{Z,G}$ is given by: $I_{\text{SCS,equiv}} = 6 \cdot 10^3 \cdot r_F \, [\text{At}]$. The most demanding situation, i.e. highly elongated plasmas, corresponds to a required current of $4.05 \, \text{kAt}$. This value might change if the SCS geometry is modified and should therefore be considered as indicative. Based on a 20% safety margin, a current of $5 \, \text{kAt}$ must be considered for vertical control. Note that this value is inferior to the $6 \, \text{kAt}$ of the G-coil system. The SCS provides a much better control for low elongation plasmas located at $z_{\text{mag}} = 0$ (factor 5 at high frequencies), but these plasmas are less vertically unstable than the highly elongated ones.

For the sake of completeness, the results for different sensible coil combinations in the high elongation case are shown in figure 5.27(b). Keeping in mind that the optimal combination is determined by the smallest force ratio, the frequency

(a) $\kappa = 2$, $z_{\mathrm{mag}} = 0$

(b) $\kappa = 2$, $z_{\mathrm{mag}} = 0.23$

(c) $\kappa = 3$, $z_{\mathrm{mag}} = 0$

(d) Optimal combinations
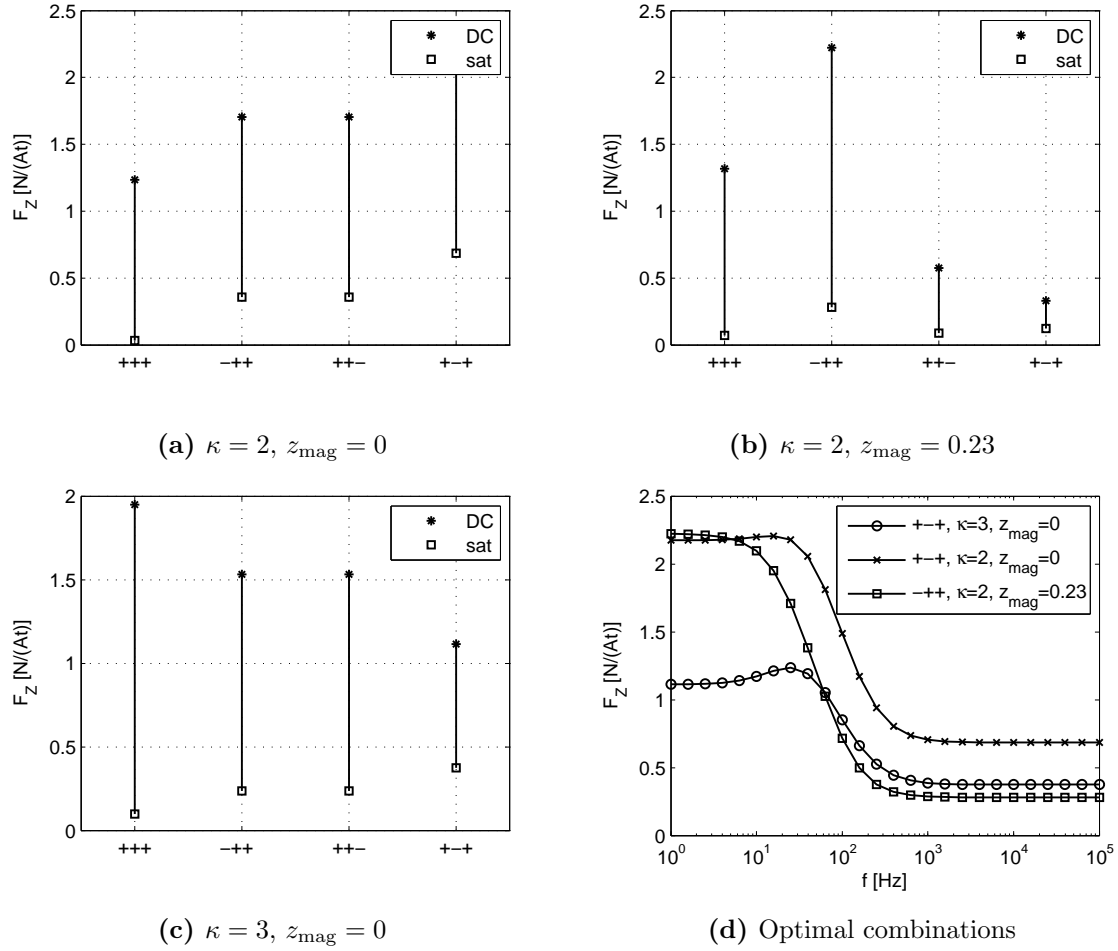
Figure 5.25: Vertical force exerted by the 10-turn in-vessel SCS in different $n = 0$ combinations for a selection of plasma current distributions. (a), (b) and (c) show the DC and high frequency values for the combinations of interest. In (d), the frequency responses of the optimal row combinations for the different plasma current distributions are represented.

response of the vertical force provided by the G-coil does not change the conclusions given previously for the choice of optimal row combination. For high elongation plasmas, the G-coil is better than all the possible combinations at low frequency because it creates a magnetic field that has a radial component of constant sign across the whole plasma.

5.6 Effects of disruptions

Plasma disruptions induce large currents in the Tokamak vessel and in any internal coils. It is therefore necessary to estimate the maximal voltage and current that coils of the SCS will endure during disruptions. This study is presented in this section.
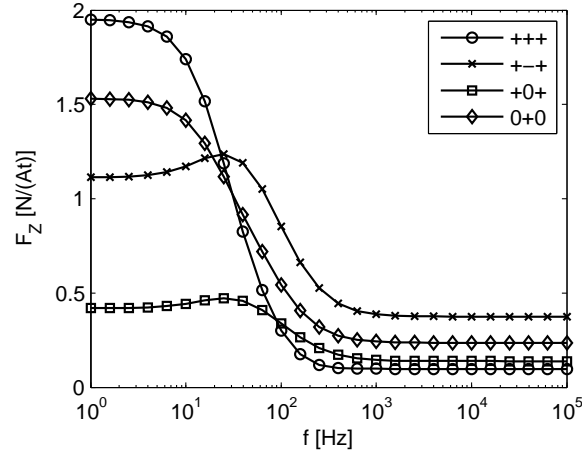
Figure 5.26: Vertical force exerted by the 10-turn in-vessel SCS in different $n = 0$ combinations on a highly elongated plasma located at $z_{\mathrm{mag}} = 0$.

(a) Optimal combinations

(b) High elongation plasma
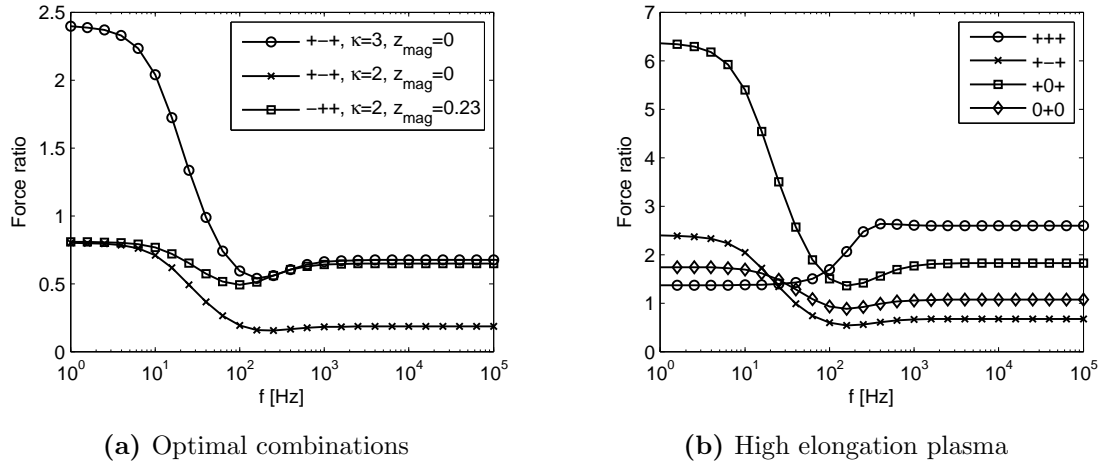
Figure 5.27: Ratio of the vertical forces per unit current per turn of the G-coil and the 10-turn in-vessel SCS in optimal combinations for all the plasma current distributions (a) and in all sensible combinations for the high elongation case (b).

5.6.1   Disruption models

5.6.1.1   Model assumptions

Two kinds of disruptions are considered in this study: vertical disruptions and plasma current quenching. Vertical disruptions are modelled by a 20 cm vertical shift of the plasma on a characteristic time of $250\,\mu$s, at constant velocity. Current quenching disruptions are modelled by a linear decrease of the plasma current from its initial value to zero on a typical time of 1 ms. The different values given here are typical of TCV disruptions. The initial plasma states are described in terms of current density distributions, as defined in section 5.5.2. For this study, the number of distributions is nonetheless increased: Z_0 is scanned from 0 to 0.5 m
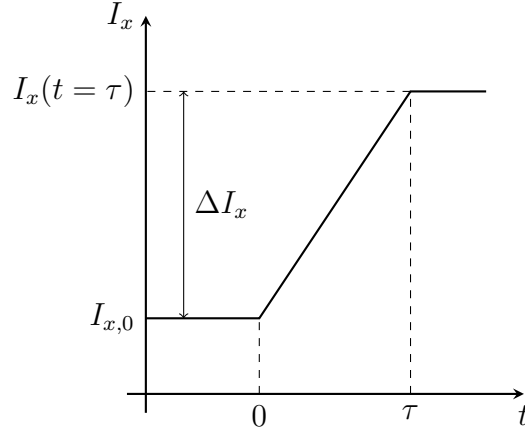
Figure 5.28: Modelled time trace of a plasma filament current $I_x(t)$ during a disruption. τ is the characteristic time of the disruption.

by steps of $0.1\,\mathrm{m}$ and $b = 3a - |Z_0|$. The plasma is represented by toroidal circular current filaments. The vessel wall is modelled by the circular toroidal filament model (section 5.4.3.2), but the real geometry of the SCS coils is used. The wall and coil models are therefore not consistent here, but the small error due to this inconsistency (recall that the perturbation is in $n = 0$) is negligible compared to the benefit of using the correct self-inductance of the coils. For simplicity, the time trace of the plasma filament currents $I_x(t)$ is chosen to be linear by parts, as illustrated in figure 5.28. For vertical disruptions of shift $\Delta Z = \pm 0.2\,\mathrm{m}$, the current variation in the plasma filament is given by $\Delta I_x(Z) = I_{x,0}(Z - \Delta Z) - I_{x,0}(Z)$ where $I_{x,0} = I_x(t = 0)$. For current quenching disruptions, ΔI_x is simply given by $\Delta I_x = -I_{x,0}$.

5.6.1.2   Solution of the circuit equation

In order to find the voltages and currents in the SCS, the coupled voltage equations of the SCS and the vessel wall must be solved for all times, using the plasma current variation as a source term. These equations are written:

$$\mathbf{R_{ss}I_s} + \mathbf{M_{ss}}\partial_t\mathbf{I_s} + \mathbf{M_{sx}}\partial_t\mathbf{I_x} = \mathbf{0} \qquad (5.18)$$

with

$$\mathbf{R_{ss}} = \left[\begin{array}{cc} \mathbf{R_v} & \mathbf{0} \\ \mathbf{0} & \mathbf{R_c} \end{array}\right], \ \mathbf{I_s} = \left[\begin{array}{c} \mathbf{I_v} \\ \mathbf{I_c} \end{array}\right], \ \mathbf{M_{ss}} = \left[\begin{array}{cc} \mathbf{M_{vv}} & \mathbf{M_{vc}} \\ \mathbf{M_{cv}} & \mathbf{M_{cc}} \end{array}\right], \ \mathbf{M_{sx}} = \left[\begin{array}{c} \mathbf{M_{vx}} \\ \mathbf{M_{cx}} \end{array}\right]$$

with c the SCS coil index, v the vessel filament index, $s = c + v$, x the plasma filament index, $\mathbf{M_{ab}}$ the mutual inductance matrix between systems a and b, $\mathbf{R_a}$ the diagonal matrix of resistances of system a and $\mathbf{I_a}$ the current in system a. The

(a) Induced current **(b)** Induced voltage
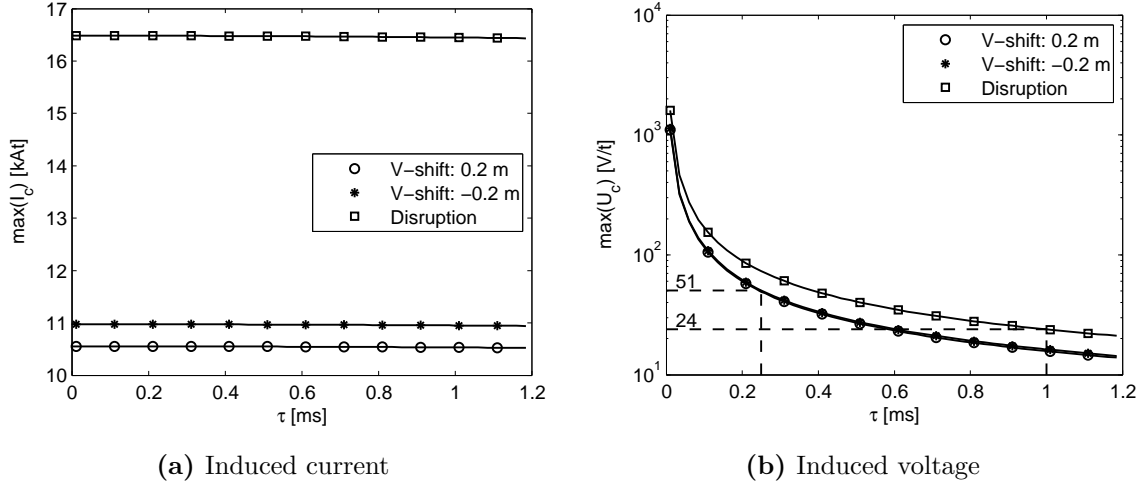
Figure 5.29: Maximal current and voltage induced in the coils of the 10-turn in-vessel SCS for three types of plasma disruptions with characteristic time τ (see section 5.6.1.1). The maxima are taken over a series of plasma current distributions, time evolution and SCS coils.

resolution of equation (5.18) is described in appendix B.2. Knowing $\mathbf{I_c}$, the voltage induced by the plasma disruption in the SCS is given by:

$$\mathbf{U_c} = \mathbf{R_{cc}}\mathbf{I_c} + \mathbf{M_{cc}}\partial_t\mathbf{I_c} \tag{5.19}$$

5.6.2 Induced voltage and current

The maximal voltage and current induced by a plasma disruption in the 10-turn in-vessel SCS is obtained by calculating $\mathbf{I_c}(t)$ (equations (B.15) and (B.16)) and $\mathbf{U_c}(t)$ (equation (5.19)) for each initial plasma current distribution and keeping the maximal value over time, distributions and SCS coils. The results for a scan on τ are shown in figure 5.29. For the studied interval of values of τ, the induced current remains approximately constant and the largest value is obtained for a disruption of type plasma current quenching. The voltage is larger for the same type of disruption at any given characteristic time, but since the characteristic time is smaller for vertical disruptions, their associated voltage is higher. The worst situations therefore result in $16.5\,\mathrm{kAt}$ of induced current and $51\,\mathrm{V/t}$ of induced voltage. Note that only the resistance and the inductance of the SCS coils have been taken into account in this calculation. A more realistic description should also consider the feeding line inductance and resistance, as well as the presence of safety resistances along the current path. In that case, the voltage would remain the same, but the induced current would be decreased.

5.7 Forces

This section describes the aspect of magnetic forces endured by the in-vessel SCS in a worst-case scenario, i.e. the situation leading to the highest force amplitude. The question of linear force density gradient on the coils is also addressed.

5.7.1 Origin of the magnetic forces

Magnetic forces are exerted on the coils when the magnetic field at the coil location has a non zero component perpendicular to the coil segments. They are described by the Laplace force formula:

$$\mathbf{F}_N(s) = I_N \mathbf{e}_s \times \mathbf{B}(s) \, [\text{N/m}] \tag{5.20}$$

where s is a linear coordinate along the coil turns, $\mathbf{F}_N(s)$ is the Laplace force density per turn at s, I_N is the current flowing in the coil, $\mathbf{e}_s$ is the unit vector along the coil turn and $\mathbf{B}(s)$ is the total magnetic field at s.

The current I_N flowing in the coils is given by the sum of the currents required for the desired applications of the SCS and the current induced by a disruption. In the worst-case scenario, all these currents are present simultaneously, so that:

$$I_N = I_{N,\text{nominal}} + I_{N,\text{disr}} = \frac{I_{\text{RMP}} + I_{\text{EFC}} + I_{\text{VC}}}{N} + \frac{I_{\text{disr}}}{N} \tag{5.21}$$

with $I_{\text{RMP}} = 4\,\text{kAt}$, $I_{\text{EFC}} = 3\,\text{kAt}$, $I_{\text{VC}} = 5\,\text{kAt}$, $I_{\text{disr,top}} = 16.5\,\text{kAt}$ and $I_{\text{disr,mid}} = 12.1\,\text{kAt}$ for the $N = 10$-turn in-vessel SCS (coil in short-circuit). Note that the difference between the disruption-induced currents in each coil row is retained in this section.

The relevant sources of magnetic fields are:

- Poloidal coils: $\mathbf{B_a}$
- Toroidal coil: $\mathbf{B_T}$
- Plasma current: $\mathbf{B_p}$
- Vessel currents associated with disruptions: $\mathbf{B_v}$
- Saddle coils (neighbours and coil themselves): $\mathbf{B_c}$

5.7.2 Maximal magnetic field and force calculation

For each source of magnetic field, the worst-case scenario must be considered: the coils must be powered at their maximal current, a series of plasma current distributions must be considered and the disruptions inducing the strongest currents must

be used in the calculation. To simplify the problem, the issue of the simultaneous presence of the magnetic field sources is ignored. The general approach used here goes as follows:

- The magnetic fields due to the different sources are calculated on each point of the SCS.

- Points are considered independently: the worst situation is kept for each point and each source.

- The magnetic fields are combined in absolute value whenever a possible constructive superposition of the fields is encountered.

5.7.2.1 Magnetic field due to the poloidal coils

The magnetic field due to the poloidal coils is given by:

$$\mathbf{B_a}(s) = |\mathbf{G_{sa}^R}|\mathbf{I}_{\text{nom,a}}\mathbf{e_R} + |\mathbf{G_{sa}^Z}|\mathbf{I}_{\text{nom,a}}\mathbf{e_Z} \tag{5.22}$$

with $\mathbf{I}_{\text{nom,a}}$ the maximal currents in the poloidal coils (or system of poloidal coils if there is a fixed connection), $\mathbf{G_{sa}^R}$ and $\mathbf{G_{sa}^Z}$ the (R, Z) components of the magnetic field at s due to a unit current in coil a. The G-coils are not included here since the SCS should replace them.

5.7.2.2 Magnetic field due to the toroidal coil

The magnetic field due to the toroidal coil is given by:

$$\mathbf{B_T}(s) = |G_{sT}^R I_{\text{nom},T}|\mathbf{e_R} + |G_{sT}^\phi I_{\text{nom},T}|\mathbf{e}_\phi \tag{5.23}$$

with $I_{\text{nom},T}$ the maximal current in the toroidal coil, G_{sT}^R and G_{sT}^ϕ the (R, ϕ) components of the magnetic field at s due to a unit current in the toroidal coil. For simplicity, the toroidal coil is modelled by a set of infinite vertical conductors, with two conductors per coil turn (one for each current direction).

5.7.2.3 Magnetic field due to the plasma current

The series of representative plasma current distributions used in the study of disruption effects (section 5.6.1.1) is used to calculate the magnetic field due to the plasma current:

$$\mathbf{B_p}(s) = \max_{Z_0}(|\mathbf{G_{sx}^R} \cdot \mathbf{I_x}(Z_0)|)\mathbf{e_R} + \max_{Z_0}(|\mathbf{G_{sx}^Z} \cdot \mathbf{I_x}(Z_0)|)\mathbf{e_Z} \tag{5.24}$$

with $\mathbf{I_x}(Z_0)$ the currents in the plasma filaments x for the current distribution labelled by Z_0, and $\mathbf{G_{sx}^R}$ and $\mathbf{G_{sx}^Z}$ the (R, Z) components of the magnetic field at s due to a unit current in filament x.

5.7.2.4 Magnetic field due to the vessel wall currents

The worst-case magnetic field due to the currents induced in the Tokamak vessel during a plasma disruption is calculated with:

$$\mathbf{B_v}(s) = \max_{\text{disr.case}} (|\mathbf{G_{sv}^R} \cdot \mathbf{I_v}(\text{disr.case})|)\mathbf{e_R} + \max_{\text{disr.case}} (|\mathbf{G_{sv}^Z} \cdot \mathbf{I_v}(\text{disr.case})|)\mathbf{e_Z} \quad (5.25)$$

with $\mathbf{I_v}(\text{disr.case})$ the matrix of vessel filament currents, each column corresponding to one of the studied disruption cases (see section 5.6.1.1), and $\mathbf{G_{sv}^R}$ and $\mathbf{G_{sv}^Z}$ the (R, Z) components of the magnetic field at s due to a unit current in filament v.

5.7.2.5 Magnetic field due to the saddle coils

The magnetic field due to the saddle coils themselves is also considered in this analysis. The sources are reduced to the direct neighbouring coils (top t, bottom b, left l, right r) and the coil itself i. Due to the symmetry of the system, only two target coils need to be considered: one coil of the middle row and one coil of the top row. The worst case magnetic field per unit current is then given by:

$$\mathbf{G_{c,\text{top}}}(s) = \sum_{k \in \{i,l,r,b\}} (1 + c_{\text{top},k}) \sum_{x \in \{R,Z,\phi\}} |\mathbf{G_{sk}^x}|\mathbf{e_x} \quad (5.26)$$

$$\mathbf{G_{c,\text{mid}}}(s) = \sum_{k \in \{i,l,r,t,b\}} (1 + c_{\text{mid},k}) \sum_{x \in \{R,Z,\phi\}} |\mathbf{G_{sk}^x}|\mathbf{e_x} \quad (5.27)$$

with $\mathbf{G_{sk}^x}$ the x-component of the magnetic field at s due to a unit current in coil k ($k \in \{t, b, l, r, i\}$), $c_{\text{top},k} = \delta_{kb}(\frac{I_{N,\text{mid}}}{I_{N,\text{top}}} - 1)$, $c_{\text{mid},k} = (\delta_{kt} + \delta_{kb})(\frac{I_{N,\text{top}}}{I_{N,\text{mid}}} - 1)$ and δ_{kj} the Kronecker symbol. $c_{\text{top},k}$ and $c_{\text{mid},k}$ are correction factors used to obtain the correct forces when multiplying by $I_{N,\text{top}}^2$ and $I_{N,\text{mid}}^2$ respectively.

5.7.2.6 Force on the saddle coils

The worst-case force density per turn is given by:

$$\mathbf{F}_{\text{turn}}(s) = I_N \mathbf{e_s} \times [\mathbf{B_a} + \mathbf{B_p} + \mathbf{B_v} + \mathbf{B_T}] + I_N^2 \mathbf{e_s} \times \mathbf{G_c} \text{ [N/m]} \quad (5.28)$$

The total force density on the coil is obtained by adding up the forces on each turn. In the process, the variation of the sign of $\mathbf{G_{si}}$ (the magnetic field created by a saddle

coil on itself) on the coil cross-section can be explicitly accounted for:

$$\mathbf{F}_{\text{coil}}(\mathbf{s}) = \sum_{\text{turns}} \left| \left[I_N \mathbf{e_s} \times [\mathbf{B_a} + \mathbf{B_p} + \mathbf{B_v} + \mathbf{B_T}] + I_N^2 \mathbf{e_s} \times (\mathbf{G_c} - |\mathbf{G_{si}}|) \right] \right|$$
$$+ \left| \sum_{\text{turns}} I_N^2 \mathbf{e_s} \times \mathbf{G_{si}} \right| \ [\text{N/m}] \tag{5.29}$$

Note that the force calculated in (5.29) is expressed as a linear density. Its value corresponds to the maximal force that could be exerted independently on each point of the coil, with no information on the sign of this value. Consequently, a direct interpretation in terms of torque would be incorrect (see section 5.7.4 for a discussion on this matter). Also note that each value corresponds to a maximum over a number of combined situations which have little chance of happening simultaneously in reality. For the sake of simplicity, the coil current I_N and the worst-case magnetic field are calculated independently. The worst-case magnetic fields due to the vessel currents and the plasma current are also calculated independently. Finally, the forbidden combinations of the poloidal coils[*] have not been taken into account in this calculation. If the magnetic forces are a major mechanical issue, some assumptions of this approach might therefore need to be revisited.

5.7.3   Results and discussion

5.7.3.1   Maximal magnetic fields

The components of interest of the different contributions to the worst-case magnetic field at the SCS location as calculated with equations (5.22), (5.23), (5.24), (5.25), (5.26) and (5.27) are represented in figures 5.30, 5.31 and 5.32 for the 10-turn in-vessel SCS design. In each case, the maximum over the different layers of coil turns along R is shown. For the R-component, the most important contribution comes from the poloidal coils, the toroidal coil contribution is negligible, the plasma and vessel contributions are in the same range, representing approximately a fifth of the poloidal coil contribution, and the SCS contribution is important on the edge turns of the winding. For the Z-component, similar observations can be made for the poloidal coil contribution with respect to the plasma and vessel contributions. The SCS contribution is nonetheless much smaller. Finally, the ϕ-component contribution of the SCS is comparable to its Z-component contribution and is much smaller than

---

[*]   On TCV, a number of poloidal coil combinations are forbidden. This constraint is due to a limit on the magnetic forces that these coils can withstand. TCV's control system is designed to prevent any operation involving one of these forbidden combinations.

the toroidal coil contribution. Note that the colorbar scales are different in each figure and do not necessarily start at zero.

5.7.3.2 Maximal forces

The contribution of the SCS to the force per turn (last term of equation (5.28)) is represented in figure 5.33 in absolute value. In each case, the maximum over the different layers of coil turns along R is shown. This contribution, integrated over the coil turns as described in equation (5.29), is shown in figure 5.34. Finally, the total force on each coil is shown in figure 5.35. Figure 5.33 shows that the strongest force due to the coil system on itself is located on the edge turns, but figure 5.34 shows that when combining the turns together, most of the contributions cancel out because the force is mostly oriented towards the winding center. According to figure 5.34, the force remains nonetheless strong in the corners of the coil. With that respect, one should keep in mind that the simple model used for these calculations does not deal very well with the coil corners since it assumes a sharp transition in the direction of the current at the corners. In addition, the combination of the different turns does not account for the variation in their spatial extent. Figure 5.35 shows that a maximal force density of $50\,\mathrm{kN/m}$ is to be expected when considering all the possible sources of magnetic field together. The contribution of the SCS itself is therefore of 20% at most.

5.7.4 Spatial variation of magnetic forces

In the approach used above to calculate the maximal magnetic forces, the information on the spatial variation of these forces for a given magnetic configuration is lost. It is nonetheless important to know the typical amplitude of these variations in order to estimate the asymmetry of the forces on the different coil parts. This analysis represents a first step toward the study of the magnetic torques exerted on the coils. To study these aspects, one must start with an analysis of the spatial variation of the magnetic fields creating these forces.

5.7.4.1 Assumptions

The question of spatial variation of magnetic forces is complex since a large number of cases should be considered to identify the worst-case situation, including all the possible combinations of coil current signs, plasma current distributions and disruption types. It is nonetheless possible to limit the field of study by physical arguments

(a) B_a^R

(b) B_T^R

(c) B_p^R

(d) B_v^R

(e) G_c^R
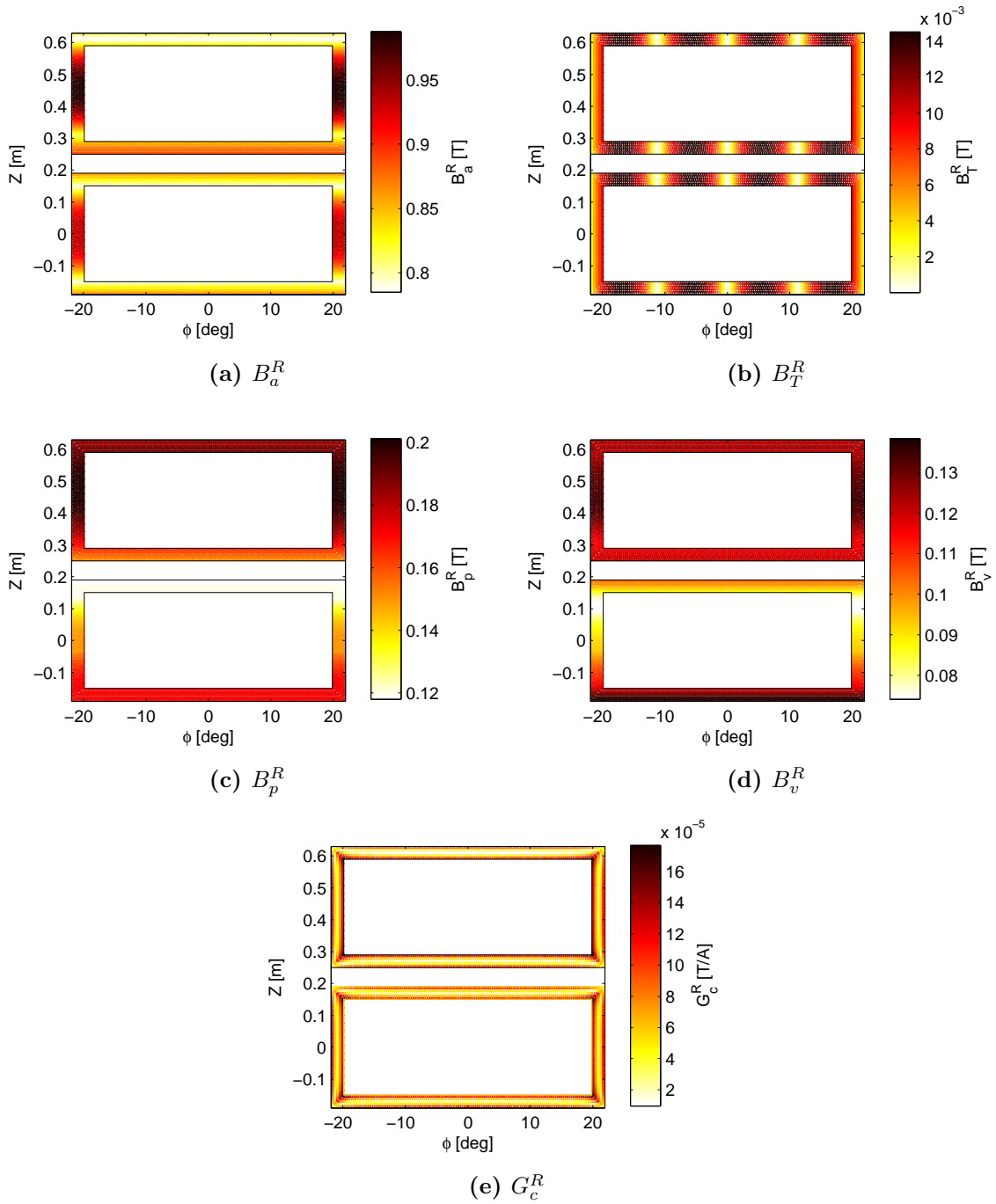
Figure 5.30: Absolute value of the R-component of the worst-case magnetic field produced by the poloidal coils, the toroidal coil, the plasma current, the vessel currents and the SCS. For the SCS, the magnetic field per ampere is given. In each case, the maximum over the different layers of coil turns along R is given.
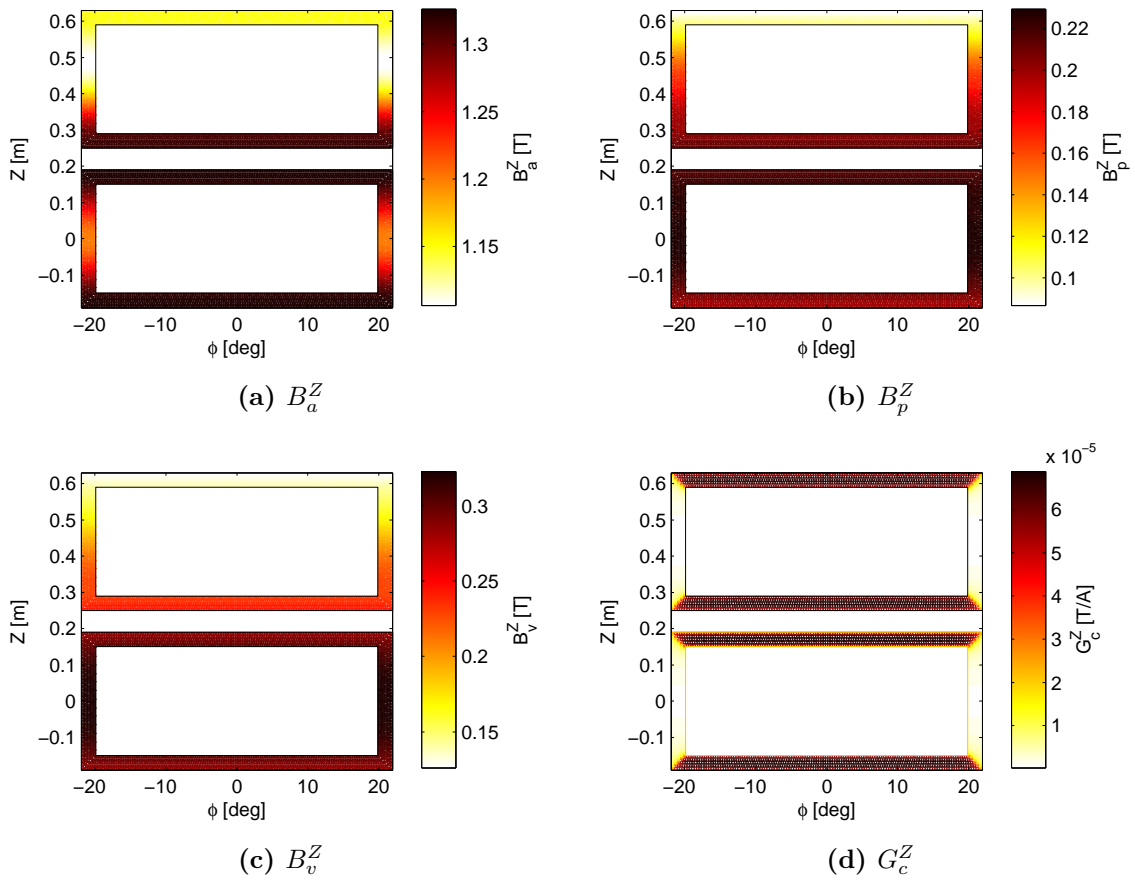
Figure 5.31: Absolute value of the Z-component of the worst-case magnetic field produced by the poloidal coils, the plasma current, the vessel currents and the SCS. For the SCS, the magnetic field per ampere is given. In each case, the maximum over the different layers of coil turns along R is given.
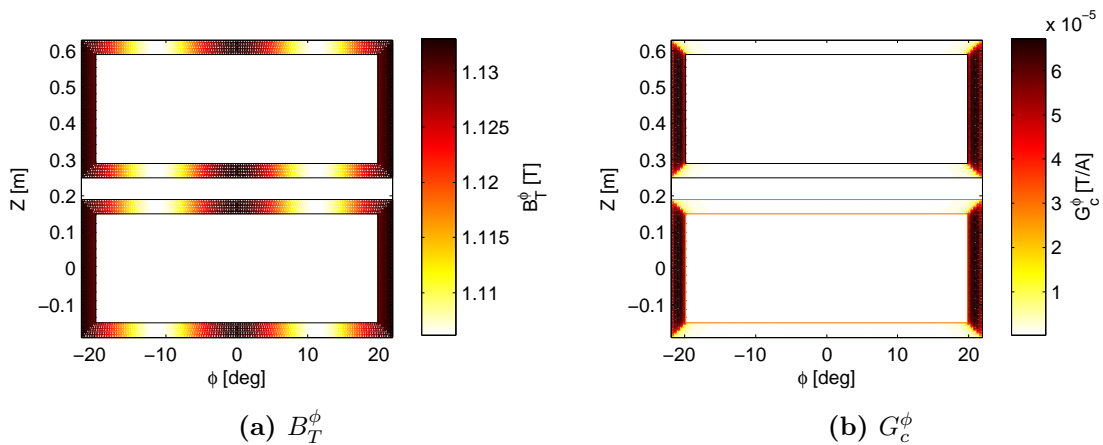
Figure 5.32: Absolute value of the ϕ-component of the worst-case magnetic field produced by the toroidal coil and the SCS. For the SCS, the magnetic field per ampere is given. In each case, the maximum over the different layers of coil turns along R is given.

(a) $F_{\text{turn},c}^R$

(b) $F_{\text{turn},c}^Z$

(c) $F_{\text{turn},c}^\phi$
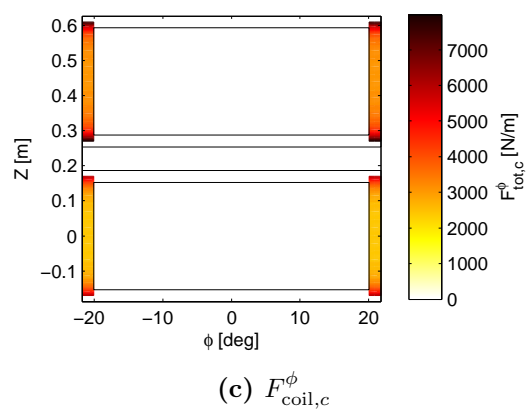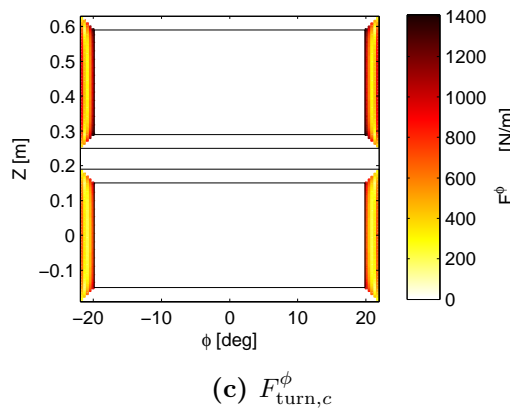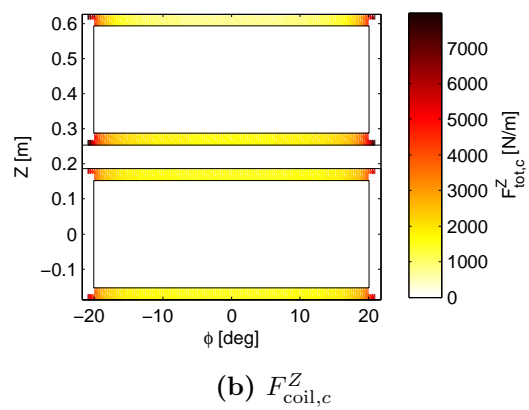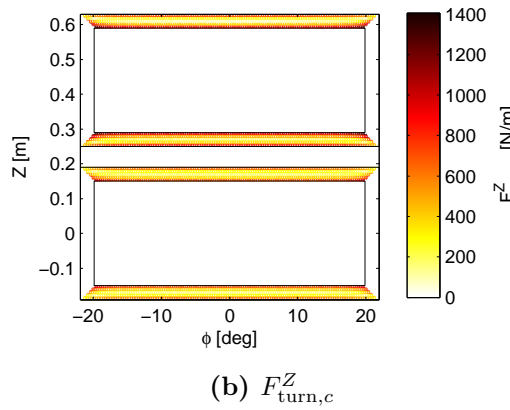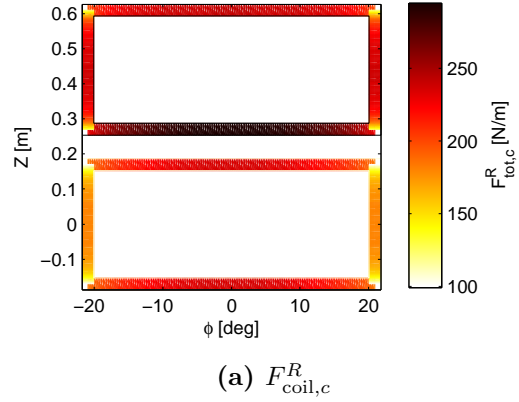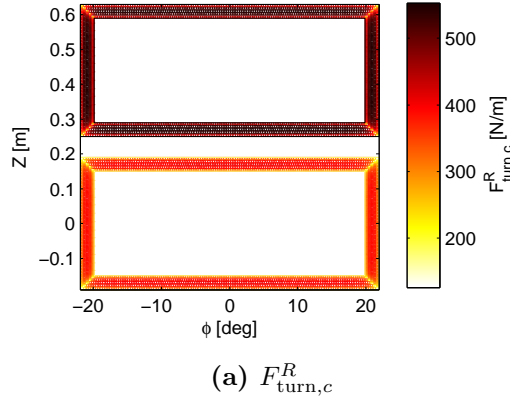
Figure 5.33: Absolute value of the SCS contribution to the force per turn in each direction. In each case, the maximum over the different layers of coil turns along R is given.

(a) $F_{\text{coil},c}^R$

(b) $F_{\text{coil},c}^Z$

(c) $F_{\text{coil},c}^\phi$

Figure 5.34: Absolute value of the SCS contribution to the total force on the coils in each direction.

(a) F_{coil}^R

(b) F_{coil}^Z

(c) F_{coil}^ϕ
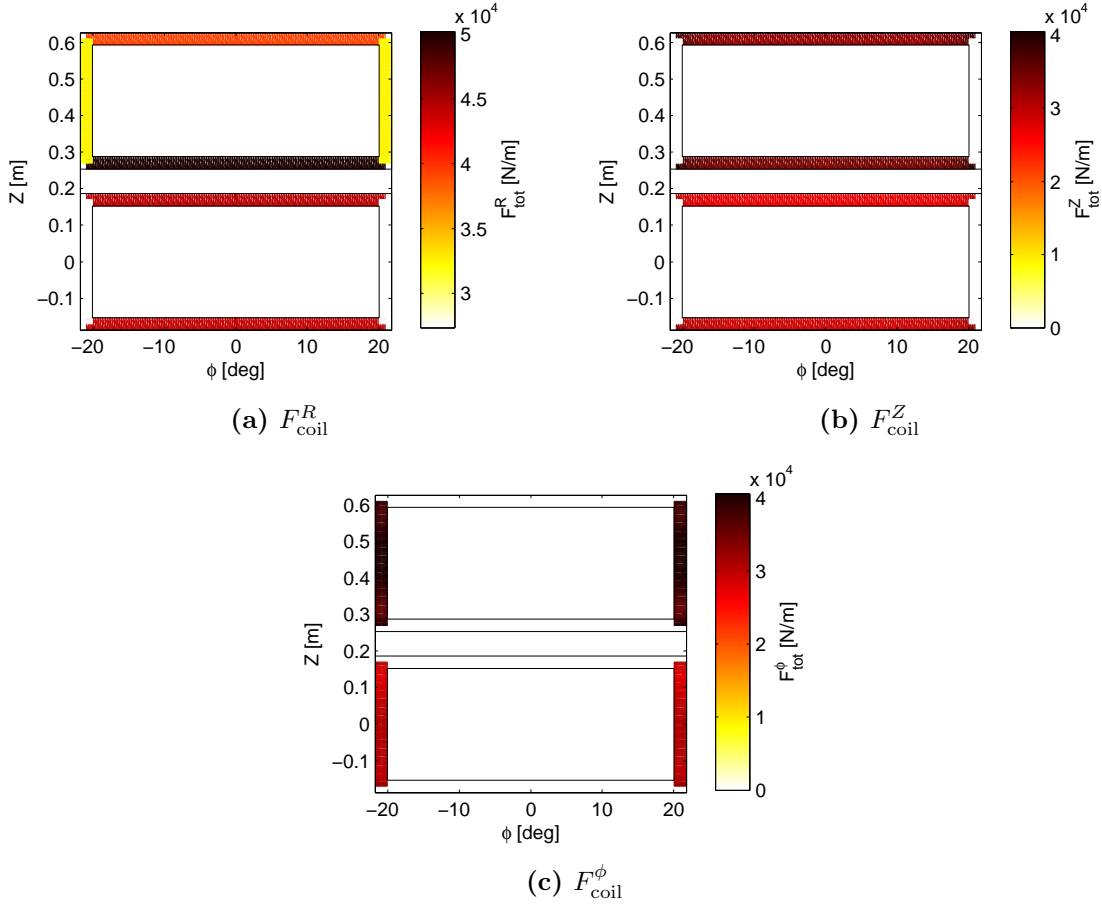
Figure 5.35: Absolute value of the total force on the coils in each direction.

and reasonable assumptions. For example, thanks to the results presented in section 5.7.3.2, the complex contribution of the SCS on itself can be neglected and replaced by a 20% safety margin. Since the toroidal field ripple is small, axisymmetry can also be assumed. In addition, the radial extent of the SCS is small enough to consider that B^ϕ is constant. Therefore, only the spatial variations of B^R and B^Z must be considered. The radial dependence of these fields could be of importance, especially for the contribution of the vessel currents. In the cases where these fields are strong, their sign will remain constant across the radial extent of the SCS, so that even if the forces on each turn might be of different amplitudes, they will all add up constructively. Consequently, it is sufficient to study the gradient of these fields along Z at the SCS mid-radius.

Note that the torques are not directly studied here, since the coil fixation points are not known yet. The study is therefore limited to the spatial variation of the forces. The definition of the worst-case situation in that case is not obvious. A bad situation would occur when both a strong gradient and a strong field amplitude are simultaneously present, bad meaning asymmetric torques. Among all the possible

situations, both the ones leading to the strongest fields and the strongest gradients at the coil locations will therefore be studied.

5.7.4.2   Calculation method

Thanks to the assumptions described above, the number of points where the fields must be calculated is greatly reduced. B^R is calculated on $\{(R, Z) \mid R = \langle R_c \rangle,\, Z = Z_c\}$ where $\langle R_c \rangle$ is the mean coil radius and Z_c describes the vertical position of the points in the SCS. B^Z is only calculated at the vertical position of the horizontal coil segments, since it only contributes to the force exerted on the horizontal segments.

Contrary to the approach used in the maximal force calculation, the SCS points are not considered independently in this worst-case seeking process, so that the obtained gradients have a physical meaning. The worst-case identification is therefore done after having fully calculated each case separately. The plasma current, vessel currents and poloidal coils are nonetheless still considered as independent sources of B^R and B^Z. The same plasma current distributions and disruption cases are used in this calculation as those used in the maximal force calculation. For the poloidal coils, all the coils are powered at their maximal current and all the possible sign combinations of these currents are considered. This choice does not guarantee to obtain the largest gradient of the magnetic field, but is consistent with the large field amplitude requirement and is tractable in terms of computer resources. The worst-cases are first sought independently for each source of magnetic field and then sought for all the possible combinations of the different sources.

5.7.4.3   Results and discussion

The worst-cases $B^R(Z)$ and $B^Z(Z)$ for each source of magnetic field and all their possible combinations are given in figures 5.36 and 5.37. Note that the gradient worst-case for $B^Z(Z)$ is defined as the largest gradient between the lower and upper horizontal segments of the coils and not within the coil winding itself since the value of interest is the asymmetry of the force between both horizontal windings. The obtained results show that the gradient worst-case is either the same as the amplitude worst-case or not too different in terms of maximal amplitude. As expected, the largest variation of amplitude and the largest amplitudes across the SCS coils are due to the poloidal coils. Nonetheless, when combined with the other sources of magnetic field, the selected worst-cases are different, which shows that these sources cannot be ignored. Concerning B^R, the variation of amplitude across a coil can
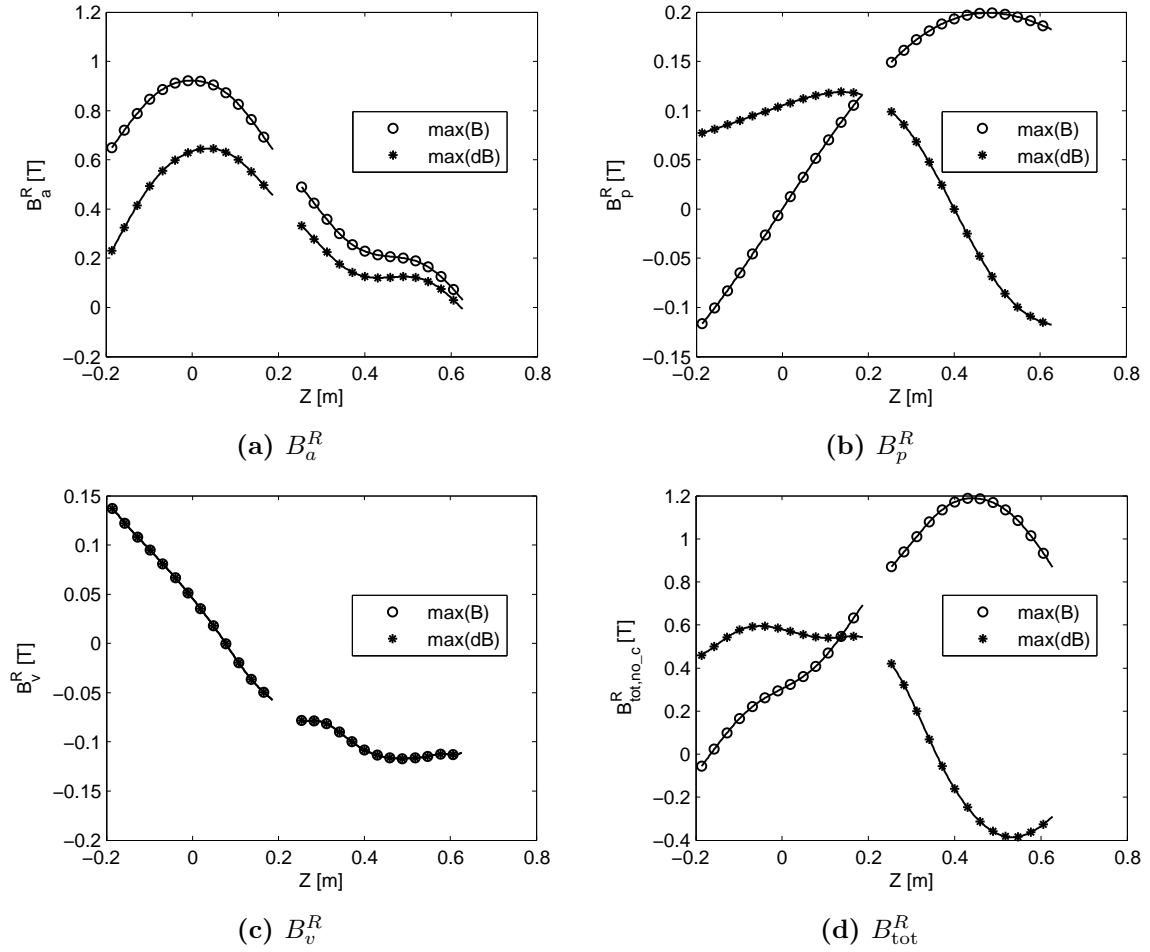
Figure 5.36: Worst-cases $B^R(Z)$ for the poloidal coils (a), the plasma current (b), the vessel currents (c) and the combination of all three (d). The worst-cases are defined as the current configurations leading to the highest field amplitude or the largest field gradient on one of the SCS points.

be as much as two third of the maximum field amplitude. Note however that a strong gradient generally means that the corresponding maximal amplitude is lower. Concerning B^Z, similar observations can be made. In that case, the variation of amplitude across a coil can even reach the maximal field amplitude. This study therefore shows that the variation of magnetic field amplitude on the coil segments is important and that one should account for a variation equal to the maximum of the magnetic field amplitude.

5.7.5 Summary

The study of the magnetic forces exerted on the SCS can be summarized as follows. The maximal force densities that can be expected are:

- Radial component on horizontal coil parts: $50\,\mathrm{kN/m}$

(a) B_a^Z

(b) B_p^Z

(c) B_v^Z

(d) B_{tot}^Z
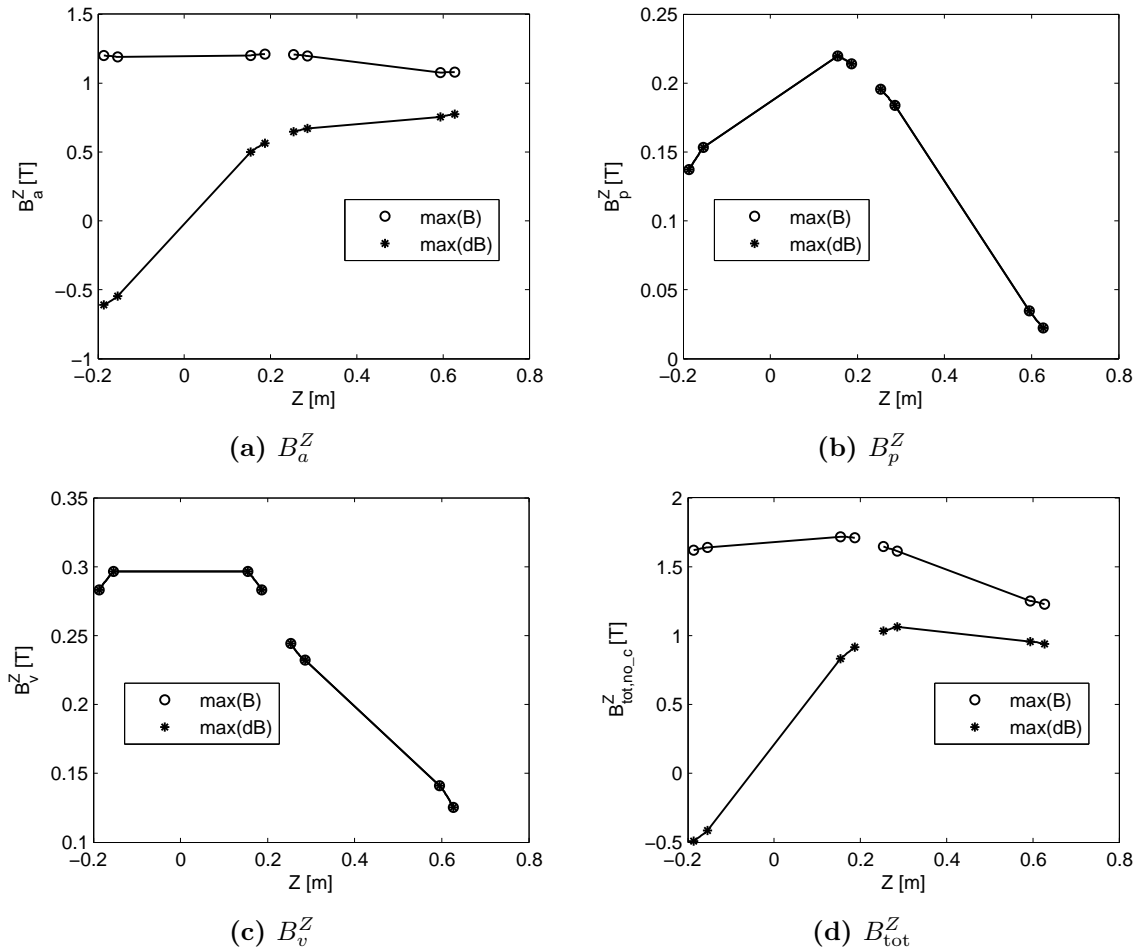
Figure 5.37: Worst-cases $B^Z(Z)$ for the poloidal coils (a), the plasma current (b), the vessel currents (c) and the combination of all three (d). The worst-cases are defined as the current configurations leading to the highest field amplitude on one of the horizontal segments of the SCS or the largest field gradient between the lower and upper horizontal segments of each coil.

- Radial component on vertical coil parts: $35\,\text{kN/m}$

- Vertical component on horizontal coil parts: $40\,\text{kN/m}$

- Toroidal component on vertical coil parts: $40\,\text{kN/m}$

Keeping a 20% margin for the contribution of the SCS on itself, the force densities are constant along ϕ, but the components that are related to B^R or B^Z may vary along Z with a variation amplitude that may reach the amplitude of the maximal force. An illustrated summary of the characteristics of the magnetic forces exerted on the SCS is given in appendix B.3.

5.8 Number of turns per coil

Although the number of turns per coil is not a relevant issue from the point of view of the physical applications of the SCS, it is an important aspect when discussing engineering constraints. This section gathers a number of arguments related to the number of turns per coil and details how the main electrical parameters scale with it.

5.8.1 Mechanical aspects

- For a small number of turns (1 to 3), a rigid material (e.g. GlidCop) can be chosen so that each turn is self-supporting. In that case, the insulating material would be limited to coil supports.

- For a large number of turns (more than 3), the turns must be packed together to ensure rigidity. In that case, each turn must be coated with an insulating material. This material must be able to withstand the thermal expansion due to vessel baking and Joule effect and be vacuum compatible.

- In the case of a large number of turns per coil, a smaller cross-section is allowed for the connection lines from the feed-throughs to the coils. In addition, smaller magnetic forces would be exerted on these conductors, so that their mounting point could be less resistant mechanically.

5.8.2 Electrical aspects

Note: In the following, the index N corresponds to a N-turn coil while the index 1 corresponds to an equivalent single-turn coil.

Required current : The electrical specifications of the coils of the SCS are given in terms of effective required current: $I_{\mathrm{req},1} = N I_{\mathrm{req},N}$. $I_{\mathrm{req},1}$ itself is made of a near DC component for RMP and EFC ($I_{\mathrm{req,DC}} = I_{\mathrm{RMP}} + I_{\mathrm{EFC}}$) and a high frequency component for vertical control ($I_{\mathrm{req,hf}} = I_{\mathrm{VC}}$).

Cross-section : The effective conductor cross-section is determined by the allowed increase of temperature during a duty cycle of the SCS due to Joule effect. The current value used for this calculation might depend on the exact physical application, but in general $I_{\mathrm{req,DC}}$ should be used. The adiabatic temperature variation ΔT of a conductor due to Joule effect is given by:

$$\Delta T = \frac{\rho_{\mathrm{el}}}{\rho_m c} \frac{\int I^2 \mathrm{d}t}{S^2} \tag{5.30}$$

where ρ_{el} is the electric resistivity, ρ_m the mass density, c the heat capacity, I the current and S the cross-section. In order to maintain a constant temperature variation with N, the current density must remain constant: $S_N = S_1/N$. S_1 must be chosen so that ΔT remains tolerable. Note that even though the overall conducting cross-section remains constant with N, the coil cross-section increases with N due to the thickness of the insulator between the turns.

Skin effect : For small values of N, the skin effect might become a problem at high frequency, leading to a non uniform distribution of temperature on the conductor cross-section. The skin depth δ at frequency f is given by $\delta = \sqrt{\rho_{\mathrm{el}}/(\pi f \mu_0 \mu_r)}$ where μ_r is the relative permeability of the conductor. Writing f_{skin} the effective fraction of conducting surface and considering an AC current, equation (5.30) becomes:

$$\Delta T = \frac{\rho_{\mathrm{el}}}{\rho_m c} \frac{\int I_{\mathrm{peak}}^2 \mathrm{d}t}{2 f_{\mathrm{skin}}^2 S^2} \qquad (5.31)$$

The contribution of the skin effect, appearing through $1/f_{\mathrm{skin}}^2$, might therefore be important. It must however be noted that the temperature variation of the whole conductor, after diffusion from the edge to the core, only goes as $1/f_{\mathrm{skin}}$. In addition, the time integral of the AC current results in the presence of a factor $1/2$ which lessens the importance of the skin effect. Finally, since most of the temperature increase is related to $I_{\mathrm{req,DC}}$, this high frequency issue should usually not be important. In advanced applications, like RWM or rotation control, it might however be relevant. Note that the *proximity effect* related to the juxtaposition of coil turns in AC mode has not been accounted for here.

Resistance : The resistance of a N-turn coil is given by $R_N = N^2 R_1$.

Inductance : The mutual inductance between the turns of a coil is at most equal to the self-inductance of each turn. Therefore: $L_N \simeq N^2 L_1$. At high frequency, the apparent inductance can be approximated by $L_N(\omega \to \inf) \simeq N^2(L_1 - C_1)$ where C_1 is the coupling term of a single-turn coil with an ideal wall (see equation (5.6)).

Voltage : The power supply voltage U is determined by the time required to reach a given current in the coils. The step response of RL-circuits can be approximated by $I(t) \simeq (U/L)t$ as long as t is small compared to the characteristic time $\tau_{\mathrm{RL}} = L/R$. The error between the approximation and the exact solution is smaller than 10% if $t \leq 0.19\tau_{\mathrm{RL}}$, i.e. in the first 20% of the current ramp.

For a N-turn coil, it gives:

$$U_N = \frac{1}{\tau_{\text{req}}} I_{\text{VC},N} L_N(\omega) \simeq N \frac{1}{\tau_{\text{req}}} I_{\text{VC},1} \left(L_1 - \alpha(\omega) C_1 \right) \qquad (5.32)$$

with τ_{req} the time required to reach $I_{\text{VC},1}$ and $\alpha(\omega)$ the proportion of wall coupling. If τ_{req} is small enough, $\alpha = 1$. In addition, $\tau_{\text{req}} \leq 0.19\tau_{\text{RL}}$ and $U \geq N R_1 (I_{\text{RMP},1} + I_{\text{EFC},1} + I_{\text{VC},1})$ must be satisfied.

Magnetic forces : During normal operation, the total force on a coil of the SCS is given by the sum of the forces on each turn of the coil and is therefore independent of N. In case of disruption, the induced voltage is proportional to N and the induced current is consequently going as $1/N$. The total force on the coil is hence independent of N in that case as well.

5.8.2.1 Numerical applications

The different parameters described above are calculated here in the case of the 10-turn in-vessel SCS. In order to assess the robustness of the scaling with N, the results are also given for a single-turn SCS equivalent to the 10-turn system in terms of dimensions, cross-section and location. For both cases, the coils are assumed to be made of GlidCop (see table 5.3). Calculation results for $\tau_{\text{req}} = 250\,\mu\text{s}$ are given in table 5.2. The disruption-induced voltage and current have been added to the list of parameters, as well as the maximal magnetic force density exerted on the coil. The cross-section is slightly different between both cases because of the room left for the insulator in the 10-turn case. The most noticeable deviation from the scalings given above occurs for the self-inductance calculation. A multi-turn coil has a lower self-inductance than what would be predicted by the N^2 scaling because the spatial spreading of the turns with respect to one another results in mutual inductances smaller than the self of each turn. The voltages obtained for each case satisfy the conditions stated above: $0.19\tau_{\text{RL}}$ is well above τ_{req} and U is sufficient to reach the total DC current. Note that the inductance and resistance of the power lines have not been accounted for in the given results.

Given the required raise time of $250\,\mu\text{s}$, the maximal frequency in AC mode is of $1\,\text{kHz}$. Using GlidCop parameters and a relative magnetic permeability of 1 (copper and aluminium values), the skin depth at $1\,\text{kHz}$ is $2.7\,\text{mm}$. For $N \geq 10$, the increase of resistance due to skin effect should be negligible, especially if the conductor cross-section aspect ratio is large. Nonetheless, the proximity effect should be assessed on the final coil design. For a smaller number of turns, the skin effect will be

Parameter	1-turn	10-turns
I_{RMP} [kA]	4	0.4
I_{EFC} [kA]	3	0.3
I_{VC} [kA]	5	0.5
S_N [mm²]	300	28.9
ΔT (2s I_{DC}) [K]	9.6	10.3
R [Ω]	$2.4 \cdot 10^{-4}$	$2.4 \cdot 10^{-2}$
L_{DC} [μH]	1.58	138
L_{sat} [μH]	0.96	77.8
$\tau_{\text{RL,DC}}$ [ms]	6.5	5.7
$\tau_{\text{RL,sat}}$ [ms]	4.0	3.2
$U(\alpha = 0)$ [V]	32	277
$U(\alpha = 1)$ [V]	19	156
I_{disr} [kA]	16.9	1.65
U_{disr} [V]	58	510
$F_{\text{coil,max}}$ [kN/m]	51	50

Table 5.2: Various parameters of the 10-turn in-vessel SCS system and its single-turn equivalent. The symbols and the mathematical approaches are described in sections 5.6, 5.7 and 5.8.2.

important. Note that the resistance can increase by a factor 4 before an adaptation of the required voltage is needed.

5.9 Coil cooling

Due to Joule effect, the coils of the SCS will heat up during operation. This section addresses the issue of coil heating and cooling in a generic approach. Its aim is to quantify the main thermal parameters in order to identify relevant engineering issues and deduce physical arguments to orient the coil design. A detailed calculation of heat transport, if relevant, should be done once the final coil design is known. This study is based on a work done by Jean-Marc Moret.

5.9.1 Lamellar structure model

The SCS coils are modelled here by a linear lamellar structure described in figure 5.38. As shown, the coil folding is ignored (each turn has the same length even though the turns remain conceptually connected in series), turns are piled only in
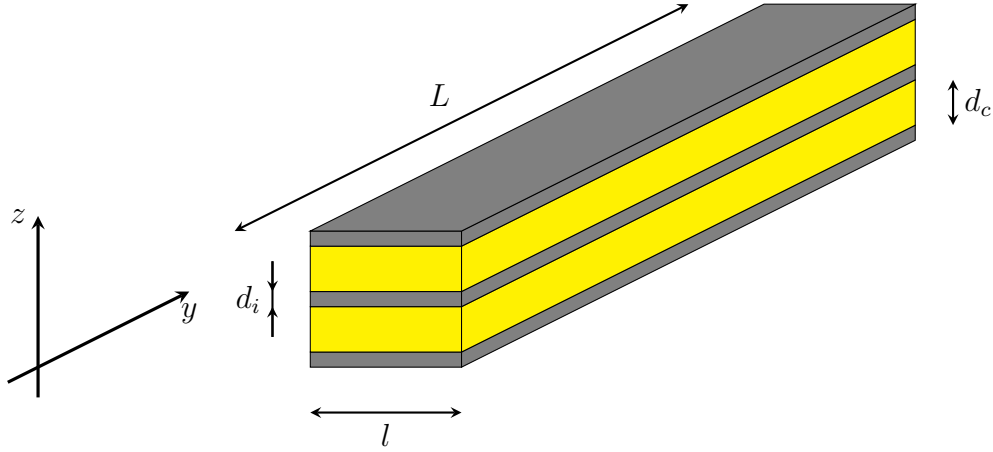
Figure 5.38: Coil model for heat transport calculation. L is the length of the coil, l its width, d_i the thickness of an insulator layer, and d_c the thickness of a conductor layer. The z axis defines the perpendicular conduction direction and the y axis the parallel one.

the z direction and layers of each type of material are respectively of constant thickness. The y direction corresponds to parallel heat transport while the z direction corresponds to perpendicular heat transport.

5.9.2 Thermal properties of lamellar structures

When dealing with composite structures, as the lamellar structure used here, it is convenient to reduce the physical constants of the different components to average values valid for the whole structure. This operation is detailed here for the specific heat capacity and the thermal conductivity. Considering a structure made of N_j layers of thickness d_j of material j (here $j \in \{i, c\}$), the total thickness of material j is $D_j = N_j d_j$, its volume fraction $f_j = D_j/D$ and the overall total thickness $D = \sum D_j$. Writing $\rho_{m,j}$ the mass density of material j and c_j its specific heat capacity, its volumetric heat capacity is given by $C_j = \rho_{m,j} c_j$. The average volumetric heat capacity is then given by:

$$C = \sum f_j C_j \tag{5.33}$$

When considering thermal conductivity, the combination of materials must account for the orientation of the layers with respect to the direction of heat transport. By extensivity of the heat flux, the average parallel thermal conductivity (i.e. along the y axis on figure 5.38) is obtained by simple averaging of the contribution of each layers:

$$K_\parallel = \sum f_j K_j \tag{5.34}$$

where K_j is the thermal conductivity of material j. When considering perpendicular thermal conductivity (i.e. along the z axis on figure 5.38), the resistance to heat transport of each layer, proportional to $1/K_j$, must be used in the average process to ensure conservation of heat flux across the layers. It yields:

$$\frac{1}{K_\perp} = \sum \frac{f_j}{K_j} \tag{5.35}$$

Note that in $K_\perp$, the *interfacial thermal resistance* related to the interface between different materials on an atomic scale and the *contact thermal resistance* related to the mechanical homogeneity of the contact between the coil turns have not been accounted for. $K_\perp$ is therefore overestimated.

5.9.3   Joule heating of lamellar structures

Writing I_1/N_c the current circulating in each layer of conductor and using the expression of the total resistance of the coil $R_c = (\rho_{el}LN_c)/(d_c l)$, the total dissipated Joule power is given by:

$$P = \frac{\rho_{el}LN_c}{d_c l} \left(\frac{I_1}{N_c} \right)^2 \tag{5.36}$$

where ρ_{el} is the electrical resistivity of the conductor. If a constant current is applied during a time t_{on}, the resulting temperature variation of the coil is given by:

$$\Delta T = \frac{Pt_{on}}{LlDC} = \frac{\rho_{el}I_1^2 t_{on}}{D_c l^2 DC} \tag{5.37}$$

5.9.4   Cooling time constants and asymptotic temperature

The parallel and perpendicular cooling time constants are determined by solving the 1D form of the heat equation. This calculation is detailed in appendix B.4. The obtained expressions are recalled here:

$$\tau_\parallel = \frac{L^2 C}{\pi^2 K_\parallel} \tag{5.38}$$

and

$$\tau_\perp = \frac{D^2 C}{\pi^2 K_\perp} \tag{5.39}$$

In general, $K_\perp \ll K_\parallel$ because of the insulator layers, but $L \gg D$ by construction. Since the square of the length is used in the cooling time calculation, the final ordering is $\tau_\parallel \gg \tau_\perp$.

For an infinity of duty cycles $t_{on}+t_{off}$ with $\tau_\parallel \gg \tau_\perp \sim t_{off} \gg t_{on}$ and a temperature increase ΔT after each t_{on}, the coil temperature increases up to an asymptotic

Parameter	GlidCop	Kapton HN	*Copper*
ρ_m [kg/m^3]	9000	1420	8920
c [J/kg/K]	400	1090	390
C [J/m^3/K]	$3.6 \cdot 10^6$	$1.5 \cdot 10^6$	$3.5 \cdot 10^6$
K [W/m/K]	342	0.12	390
ρ_{el} [Ωm]	$3 \cdot 10^{-8}$	-	$1.7 \cdot 10^{-8}$

Table 5.3: Physical constants of the materials used to build the coils: GlidCop as conductor and Kapton as insulator. Copper is also given as a reference.

temperature T_{as} derived in appendix B.4 and given by:

$$T_{\mathrm{as}}(L/2) \simeq \frac{4}{\pi} \Delta T \frac{\tau_{\parallel}}{t_{\mathrm{off}}} + T_b \tag{5.40}$$

with T_b the temperature of the power lines (considered as ideal heat sinks in the derivation of T_{as}).

5.9.5 Numerical applications

The choice of material for the coils is GlidCop as conductor and Kapton as insulator. The physical constants of these materials are given in table 5.3. As a reference, the values for copper are also given.

As in section 5.8, the 10-turn design and its equivalent 1-turn design are used for the numerical applications. Due to the simple lamellar model used here, the 10-turn design cross-section must nonetheless be adapted to the lamellar design. The coil duty cycle is defined by $I_1 = 7\,\mathrm{kA}$ with a typical TCV duty cycle: $t_{\mathrm{on}} = 2\,\mathrm{s}$ and $t_{\mathrm{off}} = 20\,\mathrm{min}$. In addition, the numerical application for a G-coil equivalent is also given. For the G-coil equivalent, since turns are non conjoint, a single turn of length equal to the total winding length and fed with $I_1 = 2\,\mathrm{kA}$ is used to match the coil specifications. In addition, G-coil results are obtained with copper instead of GlidCop. In each case, the first and last layer of the lamellar structure is an insulation layer, so that the insulated mounting points are correctly modelled. The parameters for the different cases are given in table 5.4. The calculation results are given in table 5.5.

5.9.6 Discussion

- Parallel conduction is not sufficient to ensure cooling of the coils between two heating cycles but the asymptotic temperature might be tolerable depending

Parameters	1-turn	10-turns	G-coil equivalent
L [m]	2.42	2.33	20.7
l [m]	0.01	0.01	$8.86 \cdot 10^{-3}$
d_c [m]	0.03	0.003	$8.86 \cdot 10^{-3}$
N_c [m]	1	10	1
D_c [m]	0.03	0.03	$8.86 \cdot 10^{-3}$
d_i [m]	0.0005	0.0005	0.0005
N_i [m]	2	11	2
D [m]	0.031	0.0355	$9.86 \cdot 10^{-3}$
I_1 [kA]	7	7	2

Table 5.4: Parameters of the different coil designs used in the coil cooling study. L is the coil length, l its width, d_c and d_i the thicknesses of a layer of conductor and insulator respectively, N_c and N_i the numbers of layers of each material, D_c the total conductor thickness, D the coil thickness, and I_1 the sum of the currents in each turn. For the 10-turn design, L is obtained by averaging the length of the individual coil turns.

Parameters	1-turn	10-turns	G-coil equivalent
f_c	97%	85%	90%
f_i	3%	15%	10%
$K_\parallel$ [W/m/K]	331	289	350
$K_\perp$ [W/m/K]	3.68	0.77	1.18
C [J/m^3/K]	$3.53 \cdot 10^6$	$3.28 \cdot 10^6$	$3.28 \cdot 10^6$
$\tau_\parallel$ [s]	6342	6252	407109
$\tau_\perp$ [s]	93.6	542.7	27.4
ΔT [K]	8.9	8.4	6.0
$T_{\mathrm{as}} - T_b$ [K]	60	56	2611

Table 5.5: Results of the thermal characterization of the various coil designs used in the coil cooling study. f_c is the fraction of conductor in the coil, f_i the fraction of insulator, $K_\parallel$ and $K_\perp$ the parallel and perpendicular thermal conductivity, C the volumetric heat capacity, $\tau_\parallel$ and $\tau_\perp$ the parallel and perpendicular cooling time constants, ΔT the temperature variation after t_{on}, and $T_{\mathrm{as}} - T_b$ the temperature variation of the center of the coil after an infinite number of heating cycles.

on the exact coil design.

- The perpendicular cooling time is much shorter than the parallel one, so that temperature uniformity across the coil is guaranteed. Note that the lamellar design studied here is the worst case situation for perpendicular heat transport since the number of insulator layers that must be crossed is maximal.

- For coils with multiple turns in contact with one another, the effective length is reduced and the parallel cooling is faster, but not sufficient.

- The worst case is the G-coil. This coil has been successfully used in TCV without cooling for years, but only with short pulses of current in the active part of the cycle.

- The adiabatic temperature increase reaches $9\,\mathrm{K}$ per cycle for GlidCop coils and is almost independent of the coil design if the total conductor cross-section is kept constant. Using copper would be beneficial with that respect.

- If the coils can be operated between 100°C and 150°C, the values obtained for the asymptotic temperatures show that no active cooling is necessary for the saddle coils. However, the calculation assumes a constant temperature at the coil ends, which may result in an underestimation of the asymptotic temperature, and assumes no perpendicular conduction (e.g. at the mounting points), which may result in an overestimation of the asymptotic temperature. If the assumption of negligible heat conduction is made, 10 to 12 consecutive cycles at maximal current will be tolerated. It might therefore be concluded that no active cooling is necessary but that thermocouples should be included in the coil design to monitor the coil temperature.

- If the design of the coil mounting points results in good thermal contacts between the coil and the vacuum vessel, the length between two mounting points could be used in the calculation of $\tau_{\parallel}$ instead of the whole coil length, as long as $\tau_{\parallel}$ remains much larger than $\tau_{\perp}$.

- Proposed materials are adequate for baking temperature (250°C to 300°C).

- The overall evacuation of heat from the vacuum vessel or portholes should be taken into account in the system design.

5.10   Conclusion

In this chapter, two saddle coil system designs have been proposed, namely the in-vessel and the ex-vessel SCS. A number of physical arguments have been given to justify the proposed designs in the perspective of applications including RMP, EFC and VC, and the current requirements have been established for the different applications. A wide range of engineering issues have been addressed for the in-vessel design, including the electrical and thermal characterization of the coil system, the magnetic force calculation and an assessment of the consequences of plasma disruptions. While the electromagnetic characterization of the in-vessel design should be of sufficient accuracy, the magnetic forces might have been slightly overestimated in the worst-case approach used in this study. The thermal characterization of the coils has shown that active cooling is not required and that simple monitoring of the coil temperature should be sufficient, thereby loosening the coil engineering complexity. The RMP, EFC and VC calculations are based on vacuum magnetic field calculation, i.e. excluding the plasma response from the model. While this assumption is reasonable and probably necessary from an engineering point of view, there is no guarantee that it is sufficient to obtain the desired effects on the plasma. The only justification of this assumption is that the SCS design provides features that are similar to other systems (G-coil for vertical control, DIII-D or JET for RMP) when applying the same assumption to these systems. When addressing the question of the choice between an in-vessel and an ex-vessel design, one should keep in mind that although a number of technical challenges have been identified with the in-vessel design, it offers a wider range of experimental applications than the ex-vessel design. In addition, the ex-vessel design also encounters important problems related to space occupation, complex coil geometry and availability of mounting points.

Chapter 6

Summary and conclusions

This thesis primarily presents experimental and design studies regarding the important matter of ELM control in H-mode Tokamak plasmas, and applied to the particular case of TCV.

On the experimental side, the unique flexibility of TCV and its ECRH system has opened an access to a barely studied research domain, ELM control by application of ECRH in the pressure pedestal region of a type I ELMing plasma, leading to a rich variety of significant experimental results. In particular, these experiments have shown that the ELM frequency increases and the relative plasma energy loss per ELM decreases significantly when the ECRH beam is moved toward the plasma separatrix, an effect that is independent of the total input power. This result is opposite to the expected one for type I ELMs, since the absorbed power progressively decreases when approaching the separatrix, and constitutes a promising tool for ELM control and mitigation in reactor-relevant scenarios. It also puts into question the common assumption that heating methods and deposition location are not important with regards to ELMing H-mode physics, and might lead to a reassessment of the scaling laws used to predict ITER scenarios. Contrary to RMP, ELM control by plasma edge ECRH does not lead to a complete ELM suppression, but only lowers the ELM amplitude by a factor 2 in our setup. However, the range of plasma parameters for which this technique of ELM mitigation works is yet unknown and might be less restrictive than that of RMP, in particular in terms of value of q_{95}. In addition, contrary to in-vessel coils, which represent a significant engineering problem in a burning plasma environment, ECRH systems have been present in Tokamaks for a long time and have always been considered as essential parts of ITER. ELM control by plasma edge ECRH, only requiring a dedicated launcher

and sufficient input power, is therefore a technically interesting solution to the ELM problem.

The modulated ECRH experiments, with or without real-time synchronization of the power modulation with the ELM cycle, revealed that ELM pacing is possible with ECRH, but that only real-time synchronized power modulation succeeds in providing a robust pacing of the ELMs. Comparison with various modulation schemes clearly established that the standard deviation of the ELM period depends predominantly on the instantaneous power at the ELM time. The ELM pacing technique, by synchronizing the high power phase with the ELM time, therefore relies on this physical property. Another property revealed by these experiments is the independence of the ELM frequency on the exact waveform of the power in the ELM cycle. The hope of using ECRH power modulation to trigger ELMs with reduced power consumption cannot therefore be realized, at least in the conditions of our experiments. While the standard deviation of the ELM amplitude is not affected by a stabilization of the ELM period, rare transient events with large ELM amplitudes are observed to be less frequent in real-time controlled phases. Although no systematic study has been done on this particular aspect, a reliable avoidance of large amplitude ELMs by real-time ELM pacing would be of significant value for Tokamaks of fusion reactor scale. In addition, the fact that each ELM period can be individually controlled by combining a controlled level of average power delivered during the ELM cycle with a high power phase at the ELM time has been experimentally demonstrated. Finally, the adequacy of these experimental results with a simple 0D model of the ELMs, where the plasma edge is described as a finite confinement time energy integrator with variable energy threshold, has been qualitatively detailed.

Thanks to these experiments, a new ELM control method is now available on TCV. This new method nicely completes the set of methods already existing in the past: plasma shape and input power tuning, or application of fast vertical kicks. Diverse paths of experimental research are thereby opened. Amongst them, the identification of the mechanism at the root of the dependence of the ELM frequency and amplitude on power deposition location certainly is of major interest.

On the design side, an important part of this thesis has been dedicated to the study of ELM control by RMP coil systems, and how such a system could be implemented on TCV. A list of possible physical applications additional to RMP has been drawn, and a number of physical arguments guiding the design choices have been

gathered. From them, two designs have been proposed: a very versatile in-vessel one, and a less expensive external one. These systems have then been qualified with respect to a number of engineering issues: current requirements for the applications in view (RMP, EFC and VC), electrical and thermal characterization, magnetic force calculation, and assessment of the consequences of plasma disruptions. This qualification required the development of an optimization method to determine the optimal coil current distribution with respect to a presumably optimal magnetic perturbation spectrum. The optimization method can handle a large variety of optimization requests for any coil system topology, providing in particular the mean to balance the quality of the magnetic perturbation spectrum optimization with the coil current requirement.

The various calculations involved in this design study are based on vacuum magnetic field calculation, i.e. excluding the plasma response from the model. While this assumption is reasonable and probably necessary from an engineering point of view, there is no guarantee that it is sufficient to obtain the desired effects on the plasma, as its degree of physical relevance is yet unclear. The only justification of this assumption is that the saddle coil system designed here provides features that are similar to other systems (G-coil for vertical control, DIII-D, ASDEX Upgrade or JET for RMP) when applying the same assumption to these systems. As the saddle coil system project is currently on hold, we can only hope that future experiments, if any, will confirm the validity of the models and calculations involved in its design.

Appendix A

Additional experimental aspects

A.1 Experimental recipe

It might be useful for a researcher interested in continuing the edge heating experiments to have more information on the typical phenomenology, to know how the shot scenario is prepared and why, and to be informed on a few useful tricks. This section is devoted to these aspects and complements the information given in section 3.2.

A.1.1 Optimal density time trace

In general, a large puff of gas is injected in the first phase of the discharge in order to avoid a locked-mode disruption due to the crossing of $q = 3$ at the plasma edge at the time of the X-point formation during the plasma current ramp-up. The transition to H-mode generally happens a few milliseconds later, immediately followed by an ELM-free phase leading to an even higher plasma density. The density is then much larger than that required for a stable type I ELMing phase, and one must delay X2 ECRH injection until the ELMs occurring spontaneously after the ELM-free phase have lowered the density sufficiently. Sometimes, the density remains above the type I threshold and the ELMs remain in type III regime, even with X2 ECRH. A reliable solution for better density control consists in increasing the duration of the inter-shot glow plasma discharge cleaning to 10 minutes, so that gas retention in the vessel wall is decreased. Apart from special operation circumstances, in particular when the TCV vessel was baked during operation, this approach always led to satisfactory density control.

It is possible to avoid the initial gas puff altogether by dissociating the current

ramp and the X-point formation. In this approach, the plasma current is ramped to a safe value ($200\,\mathrm{kA}$) and maintained there while the X-point is formed. After the final plasma shape is reached, an additional current ramp to the target value is performed. This approach has the advantage of reaching the H-mode transition from below, in terms of density. Nonetheless, the transition still leads to an ELM-free phase, irrespective of the various X2 pre-heating scenarios attempted. The resulting large excursion in density being similar to that in the gas puff approach, this strategy has been abandoned.

Once in type I ELMing phase, density control remains necessary. If the density increases too much, ELMs become less regular and an ELM-free phase might even be triggered. If it decreases too much, the H-mode is usually lost.

A.1.2   Optimal X2 launcher angles

Beam refraction strongly limits the range of toroidal angles allowed in these experiments. Nonetheless, using a small but finite toroidal angle is usually an effective way of limiting the stray power on the vessel portholes. According to TORAY-GA simulations, a toroidal angle of $3°$ to $5°$ with respect to perpendicular injection for $\theta_l = 8°$ and an angle of $11°$ to $13°$ for $\theta_l = 25°$ are tolerable. In practice, toroidal deviations of $3°$ to $5°$ have been used successfully, with no significant effect of ECCD (see section A.2).

When trying to reach extreme launcher angles (i.e. in the neighbourhood of $\theta_l = 8°$ or $\theta_l = 25°$), it is usually recommended to start heating at a location less sensitive to density variations, for example with $\theta_l = 17°$, at a time when density is already sufficiently low thanks to the ELMing regime maintained by X3 heating alone. θ_l can then be safely swept to the desired value.

A.2   ECCD contribution

In the series of plasma edge heating experiments reported in chapter 3, a small toroidal angle of the X2 beam is often present to avoid large stray power on the portholes of TCV in case of unexpected excursions of density. Using TORAY-GA simulations and comparing experimental results in different situations, it is demonstrated here that this finite toroidal angle has no significant effect, either on the level of current drive it induces or on the location of the power deposition.

(a) Current density profiles **(b)** Power density profiles
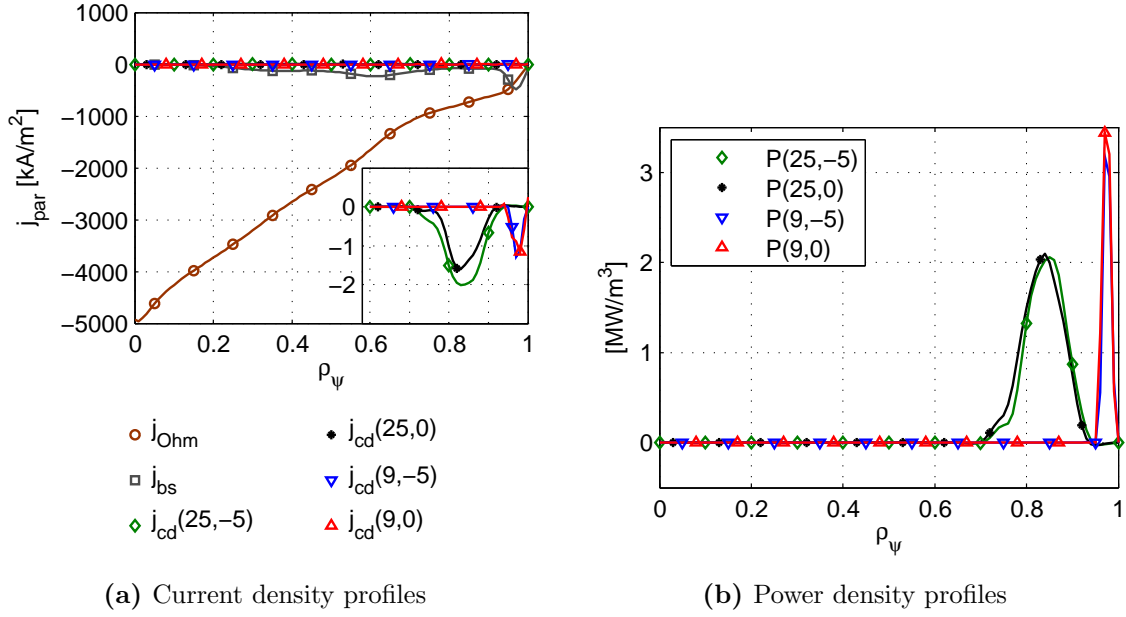
Figure A.1: (a) ohmic, bootstrap and EC-driven current density profiles and (b) absorbed X2 power density profiles for power deposition closer to the core ($\theta_l = 25°$) or to the edge ($\theta_l = 9°$) and orthogonal ($\phi_t - 180° = 0$) or finite toroidal angle ($\phi_t - 180° = -5$) injection. Results are based on T_e and n_e profiles given by the Thomson diagnostics for shot 42062 at 1.15 s and $Z_{\text{eff}} = 2$ is assumed. For the sake of clarity, the ECCD profiles are plotted with an *ad hoc* y-scale in the inset of figure (a).

A.2.1 TORAY-GA simulations

The ohmic and bootstrap [112, 113] current densities are compared in figure A.1(a) to the ECCD current density calculated with TORAY-GA, using typical T_e and n_e profiles measured with the Thomson diagnostics. The situations presented in the figure correspond to experimental limit cases in terms of launcher angle (i.e. poloidal angle in this context) and beam toroidal angle. ϕ_t is the standard TORAY angle, but expressed in the [0°,360°] domain instead of the [-180°,180°] domain, and corresponds to the angle between the orthogonal projection of the X2 beam on a horizontal plane and the major radius unit vector. For the small values of ϕ_t used in the experiments, $\theta_l \simeq 90 - \theta_t$ where θ_t is the TORAY poloidal angle. TORAY-GA simulations show that the current drive is negligible compared to the ohmic and bootstrap currents. Indeed, the maxima of the ratios of j_{cd} to the other current densities are given by: $\max(j_{\text{cd}}/j_{\text{Ohm}})(25, -5) = 0.3\%$, $\max(j_{\text{cd}}/j_{\text{bs}})(25, -5) = 2.6\%$, $\max(j_{\text{cd}}/j_{\text{Ohm}})(9, -5) = 0.5\%$, $\max(j_{\text{cd}}/j_{\text{bs}})(9, -5) = 0.3\%$. Figure A.1(b) shows that the location of power deposition is not affected by ϕ_t in the range of angles used experimentally.

(a) Intermediate power
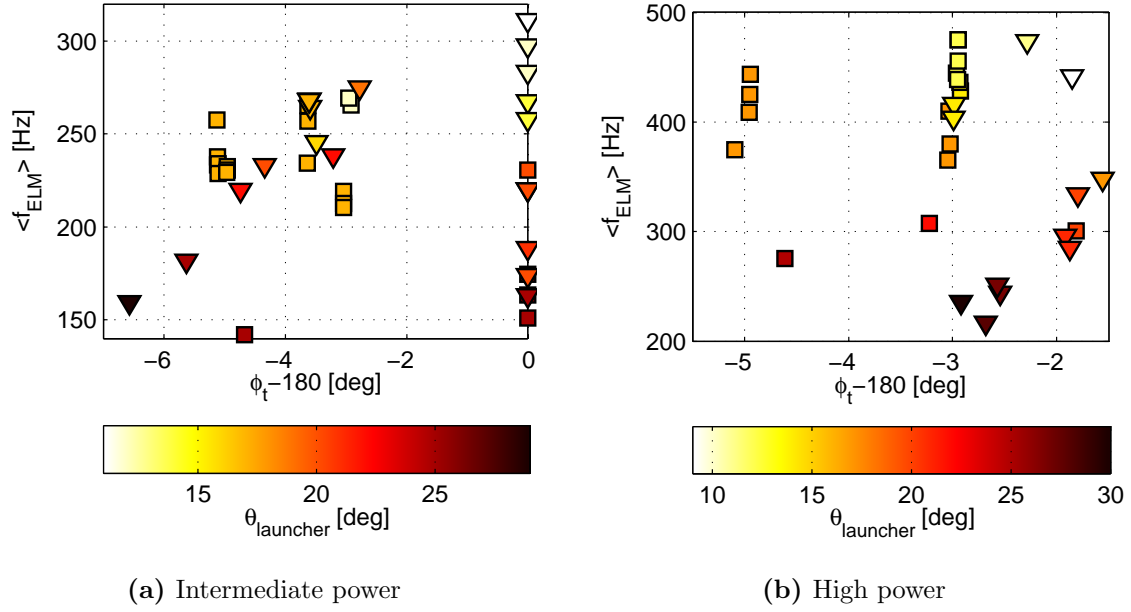
(b) High power

Figure A.2: f_{ELM} as function of $\phi_t - 180°$ and θ_l for stationary (squares) and scanned (triangles) heating modes at intermediate power ($P_{\mathrm{input,X2}} \in [410, 520]\,\mathrm{kW}$) and high power ($P_{\mathrm{input,X2}} \in [850, 1000]\,\mathrm{kW}$). For the sake of clarity, points indicating power or angle scans are not connected.

A.2.2 ELM frequency versus launcher angle and beam toroidal angle

The ELM frequency is plotted as a function of ϕ_t and θ_l for two ranges of input power in figures A.2(a) and A.2(b). Taking into account the natural data scattering, no significant difference is observed between points with orthogonal ECRH injection and points with finite toroidal angle injection. In particular, the dependence of f_{ELM} on θ_l described in section 3.3 is present for both situations.

Appendix B

Specific considerations for the TCV SCS design

B.1 Mutual and self inductance calculation

B.1.1 Mutual inductance calculation in general geometry

In general, the mutual inductance between circuits C_i and C_j at a distance r_{ij} from one another is given by Neumann's formula:

$$M_{ij} = \frac{\mu_0}{4\pi} \oint_{C_i} \oint_{C_j} \frac{\mathbf{ds_i} \cdot \mathbf{ds_j}}{|\mathbf{r_{ij}}|} \tag{B.1}$$

where $\mathbf{ds_i}$ and $\mathbf{ds_j}$ are line elements along C_i and C_j. The integral appearing in (B.1) allows a splitting of the circuits in sensible pieces and a reduction of the mutual inductance calculation to these pieces, for example using ad hoc analytical formulae. Such an approach greatly reduces the numerical cost of inductance calculation and is used in the case of the SCS.

Note that Neumann's formula assumes thin conductors. In general, reducing the conductors to the path followed by their centers is a good assumption if the minimal distance between both conductors is larger than the cross-section dimensions of the conductors. Calculation shows that this condition can be alleviated and that Neumann's formula remains valid when conductors are in contact if the cross-section of the conductors has an aspect ratio equal to 1 (i.e. square or circular). Practically, this means that rectangular cross-section conductors must be split in a subset of square cross-section conductors before performing inductance calculation.

B.1.2   Mutual and self inductance of saddle coils

The mutual inductance between two turns of a saddle coil or between two turns of two different coils is calculated by dividing the turns into horizontal arcs of circles and vertical segments. The mutual inductances are calculated between each pair of segments/arcs and the results are combined to obtain the mutual inductances between the turns. Note that the inductance between a vertical segment and a horizontal arc is zero because they are orthogonal to one another. Mathematically, the mutual inductance M is written:

$$M = M_{t_1 t_2} + M_{l_1 l_2} + M_{b_1 b_2} + M_{r_1 r_2} - M_{t_1 b_2} - M_{b_1 t_2} - M_{l_1 r_2} - M_{r_1 l_2} \qquad \text{(B.2)}$$

where turn segments are labelled with t: top, b: bottom, l: left (higher toroidal angle ϕ), r: right (lower toroidal angle ϕ) and $1, 2$ label the turns. The methods used to calculate each terms in equation (B.2) are given in the following sections.

Note that the coils of the ex-vessel SCS design have a particular geometry which involves a number of additional terms in equation (B.2) to account for the horizontal radial segments. These terms are calculated by numerical integration of Neumann's formula and are therefore not described below.

B.1.2.1   Mutual inductance between parallel segments

A general analytical formula is given in Grover [114, p. 45] to calculate the mutual inductance between parallel segments. Two segments a and b of lengths l_a and l_b, separated by a perpendicular distance d and having an algebraic length h from the top of a to the bottom of b (h can be negative) have a mutual inductance given without approximation by:

$$M = 10^{-7}\left(\alpha \,\mathrm{asinh}\frac{\alpha}{d} - \beta\,\mathrm{asinh}\frac{\beta}{d} - \gamma\,\mathrm{asinh}\frac{\gamma}{d} + h\,\mathrm{asinh}\frac{h}{d}\right.$$
$$\left. - \sqrt{\alpha^2 + d^2} + \sqrt{\beta^2 + d^2} + \sqrt{\gamma^2 + d^2} - \sqrt{h^2 + d^2}\right) \qquad \text{(B.3)}$$

with

$$\alpha = l_a + l_b + h$$
$$\beta = l_a + h \qquad \qquad \text{(B.4)}$$
$$\gamma = l_b + h$$

If the segments are aligned ($d = 0$) but have no contact point, another formula is available:

$$M = 10^{-7}(\alpha \ln \alpha - \beta \ln \beta - \gamma \ln \gamma + h \ln h) \qquad \text{(B.5)}$$

Finally, if the segments are aligned and juxtaposed ($h = 0$ or $h = -l_a - l_b$), the mutual inductance is given by:

$$M = 10^{-7}(l_a \ln(\frac{l_a + l_b}{l_a}) + l_b \ln(\frac{l_a + l_b}{l_b})) \tag{B.6}$$

If the segments are overlapping, the mutual inductance can be found by calculating the self-inductance of the overlapping bit and combining it with the mutual inductances of the non-overlapping bits afterwards.

B.1.2.2   Self inductance of a straight segment

The self inductance of a conductor can be understood as the average of the mutual inductances of all the filaments it is made of. The value of the inductance is dominated by a term going as $\ln(1/d)$ where d is defined above. The average of the mutual inductances can thus be replaced by the mutual inductance of two segments separated by a distance given by the average of the logarithm of the distances between the filaments, also called the *geometrical mean distance*. Therefore, the self inductance of a segment can be determined through equation (B.3) with $d_{\text{gmd}} = 0.2235(w + t)$, $l_a = l_b$ and $h = -l_a$ where w is the width and t the thickness of the segment.

B.1.2.3   Mutual inductance between concentric arcs of circles

In the case of arcs of circles, the presence of elliptic integrals in the mutual inductance calculation prevents the formulation of analytical solutions. The best approach consists in using the concentricity of the arcs and the well studied elliptic integrals to simplify the calculation of the mutual inductance. Leduc [115] gives:

$$M_{12} = \frac{\mu_0}{4\pi} \sqrt{r_1 r_2} \int_{\varphi_1}^{\varphi_2} \left[g(k, \frac{\theta}{2} - \frac{\phi_1 + \pi}{2}) - g(k, \frac{\theta}{2} - \frac{\phi_2 + \pi}{2}) \right] d\theta \tag{B.7}$$

with

$$\begin{aligned}
k &= \sqrt{\frac{4r_1 r_2}{(z_1 - z_2)^2 + (r_1 + r_2)^2}} \\
g(k, \theta) &= (\frac{2}{k} - k)F(k, \theta) - \frac{2}{k}E(k, \theta) \\
F(k, \theta) &= \int_0^\theta \frac{1}{\sqrt{1 - k^2 sin^2 \alpha}} d\alpha \\
E(k, \theta) &= \int_0^\theta \sqrt{1 - k^2 sin^2 \alpha} d\alpha
\end{aligned} \tag{B.8}$$

where $(r_1, z_1, \varphi_1, \varphi_2)$ define the position of the first arc of circle in cylindrical coordinates and $(r_2, z_2, \phi_1, \phi_2)$ the position of the second arc. The elliptic integrals E and F can be calculated with an *AGM* method and a Landau transform. The integral on θ is then performed with a standard Simpson method. The implementation of

this formulation can be checked with full circle cases and nearly straight segment cases (large radius and small angle).

As in the straight segment case, if the arcs are overlapping, the mutual inductance can be found by calculating the self-inductance of the overlapping bit and combining it with the mutual inductances of the non-overlapping bits afterwards. However, the 2π-periodicity involved in the calculation leads to a higher level of complexity.

B.1.2.4   Self inductance of an arc of circle

As in the straight segment case, the self inductance is calculated with the mutual inductance formulation and the geometrical mean distance.

B.1.3   Inductance of turns connected in series

Once the self and mutual inductances of individual turns are known, the effective inductances of individual coils or serial combination of coils can be calculated. If the individual inductances are gathered in a matrix $\mathbf{M}$ with M_{ij} the mutual inductance between turns i and j, the effective inductance of the combined system is given by:

$$M_{\text{eff}} = \mathbf{T}\mathbf{M}\mathbf{T}^{\mathbf{T}} \tag{B.9}$$

with $\mathbf{T}$ a line vector defined by $T_i = \pm 1$, depending on the sign of the current in the turns.

B.2   Resolution of the voltage equation of the disruption model

In order to solve equation (5.18), the equation system must be diagonalized to decouple the differential equations. Following an approach developed by Jean-Marc Moret, the first terms of equation (5.18) are written:

$$\mathbf{R_{ss}}\mathbf{I_s} + \mathbf{M_{ss}}\partial_t\mathbf{I_s} = \mathbf{R_{ss}}^{1/2}\mathbf{R_{ss}}^{1/2}\mathbf{I_s} + \mathbf{R_{ss}}^{1/2}\underbrace{\mathbf{R_{ss}}^{-1/2}\mathbf{M_{ss}}\mathbf{R_{ss}}^{-1/2}}_{\mathbf{K_{ss}}}\mathbf{R_{ss}}^{1/2}\partial_t\mathbf{I_s} \tag{B.10}$$

with $\mathbf{R_{ss}}^{1/2}$ defined as the element-wise square root of the resistance matrix. Since $\mathbf{M_{ss}}$ is symmetric and $\mathbf{R_{ss}}$ is diagonal, $\mathbf{K_{ss}}$ is symmetric. It can therefore by diagonalized by an orthogonal matrix $\mathbf{T}$: $\mathbf{D_{ss}} = \mathbf{T_{ss}^T}\mathbf{K_{ss}}\mathbf{T_{ss}}$ and $\mathbf{K_{ss}} = \mathbf{T_{ss}}\mathbf{D_{ss}}\mathbf{T_{ss}^T}$. The columns of $\mathbf{T_{ss}}$ corresponds to the eigenvectors of $\mathbf{K_{ss}}$ and are found by standard

algebraic methods. Using the property that $\mathbf{T_{ss}^T} = \mathbf{T_{ss}^{-1}}$, equation (B.10) is expressed as:

$$\mathbf{R_{ss}I_s} + \mathbf{M_{ss}}\partial_t\mathbf{I_s} = \underbrace{\mathbf{R_{ss}}^{1/2}\mathbf{T_{ss}}}_{\mathbf{A_{ss}}}\underbrace{\mathbf{T_{ss}^T}\mathbf{R_{ss}}^{1/2}}_{\mathbf{A_{ss}^T}}\mathbf{I_s} + \mathbf{R_{ss}}^{1/2}\mathbf{T_{ss}}\mathbf{D_{ss}}\mathbf{T_{ss}^T}\mathbf{R_{ss}}^{1/2}\partial_t\mathbf{I_s} \quad \text{(B.11)}$$

giving

$$\mathbf{R_{ss}I_s} + \mathbf{M_{ss}}\partial_t\mathbf{I_s} = \mathbf{A_{ss}}\mathbf{A_{ss}^T}\mathbf{I_s} + \mathbf{A_{ss}}\mathbf{D_{ss}}\mathbf{A_{ss}^T}\partial_t\mathbf{I_s} \quad \text{(B.12)}$$

Multiplying (5.18) to the left by $\mathbf{A_{ss}^{-1}} = \mathbf{T_{ss}^T}\mathbf{R_{ss}}^{-1/2}$ therefore gives:

$$\mathbf{I_D} + \mathbf{D}\partial_t\mathbf{I_D} + \mathbf{M_{Dx}}\partial_t\mathbf{I_x} = \mathbf{0} \quad \text{(B.13)}$$

with

$$\mathbf{I_D} = \mathbf{A_{ss}^T}\mathbf{I_s} \qquad \mathbf{D} = \mathbf{D_{ss}} \qquad \mathbf{M_{Dx}} = \mathbf{A_{ss}^{-1}}\mathbf{M_{sx}} \quad \text{(B.14)}$$

In equation (B.13), the unknowns are decoupled and each differential equation can be solved separately. The solution of (B.13) with the plasma current time traces described in figure 5.28 is given by:

$$\mathbf{I_D}(t) = -\frac{1}{\tau}\mathbf{M_{Dx}}\Delta\mathbf{I_x} \cdot \begin{cases} 1 - e^{-t/\mathbf{D}} & t \leq \tau \\ (e^{\tau/\mathbf{D}} - 1)e^{-t/\mathbf{D}} & t > \tau \end{cases} \quad \text{(B.15)}$$

Numerically, the product of exponential terms appearing for $t > \tau$ might be problematic. This difficulty can be avoided by solving for the logarithm of equation (B.15). Once $\mathbf{I_D}(t)$ is known, $\mathbf{I_s}(t)$ is found with:

$$\mathbf{I_s} = \mathbf{R_{ss}}^{-1/2}\mathbf{T_{ss}}\mathbf{I_D} \quad \text{(B.16)}$$

B.3   Illustrated summary of the magnetic forces exerted on the SCS

Keeping a 20% margin for the contribution of the SCS on itself, the magnetic force densities are constant along ϕ, but the components that are related to B^R or B^Z may vary along Z with a variation amplitude that may reach the amplitude of the maximal force. The illustrations given in figures B.1, B.2 and B.3 detail the different characteristics of the forces: origin of the different components on the different coil parts, spatial dependency and presence of symmetry constraints between coil parts.
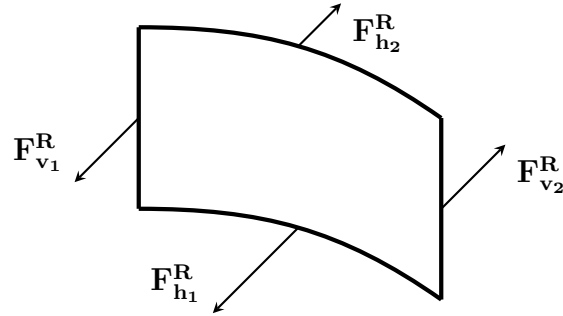
$$F_{v_1}^R = -F_{v_2}^R$$
$$F_{v_1}^R \propto B^\phi$$
$$F_{h_1}^R \quad \text{indep. of} \quad F_{h_2}^R$$
$$F_{h_i}^R = F_{h_i}^R(Z) \propto B^Z(Z)$$

Figure B.1: Illustration of the radial component F^R of the magnetic force exerted on the vertical and horizontal segments of the SCS. The main properties of F^R for the different cases are also given. Note that the represented direction of the forces is arbitrary.
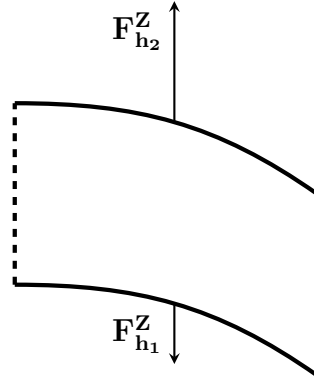
$$F_{h_1}^Z \quad \text{indep. of} \quad F_{h_2}^Z$$
$$F_{h_i}^Z = F_{h_i}^Z(Z) \propto B^R(Z)$$

Figure B.2: Illustration of the vertical component F^Z of the magnetic force exerted on the horizontal segments of the SCS. The main properties of F^Z are also given. Note that the represented direction of the force is arbitrary.
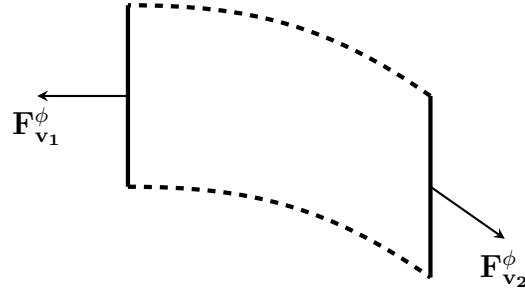
$$F_{v_1}^\phi = -F_{v_2}^\phi$$
$$F_{v_1}^\phi = F_{v_1}^\phi(Z) \propto B^R(Z)$$

Figure B.3: Illustration of the toroidal component F^ϕ of the magnetic force exerted on the vertical segments of the SCS. The main properties of F^ϕ are also given. Note that the represented direction of the force is arbitrary.

B.4 Cooling time constants and asymptotic temperature

Based on the lamellar model described in section 5.9 and the distinction between parallel and perpendicular heat transport, the 1D form of the heat equation can be used:

$$\frac{\partial T}{\partial t} - \frac{K}{C}\frac{\partial^2 T}{\partial x^2} = 0 \tag{B.17}$$

If both edges of the considered dimension are in contact with a heat sink at constant temperature T_b, the solution of the heat equation is given by:

$$\begin{cases} T(x,t) & = \sum_{n=1}^\infty D_n \sin\left(\frac{n\pi x}{L}\right) e^{-t/\tau_n} + T_b \\ D_n & = \frac{2}{L}\int_0^L (T(x,0) - T_b) \sin\left(\frac{n\pi x}{L}\right) \mathrm{d}x \\ \tau_n & = \frac{L^2}{n^2\pi^2}\frac{C}{K} \end{cases} \tag{B.18}$$

Note that D_n is a Fourier component of $T(x,0) - T_b$ on the basis of sine functions compatible with the boundary conditions. The longest-lived mode is the $n = 1$ mode. It defines the cooling time constant $\frac{L^2 C}{\pi^2 K}$. In the particular case of the lamellar model, it yields:

$$\tau_\parallel = \frac{L^2 C}{\pi^2 K_\parallel} \tag{B.19}$$

and

$$\tau_\perp = \frac{D^2 C}{\pi^2 K_\perp} \tag{B.20}$$

In general, $K_\perp \ll K_\parallel$ because of the insulator layers, but $L \gg D$ by construction. Since the square of the length is used in the cooling time calculation, the final ordering is $\tau_\parallel \gg \tau_\perp$.

For an infinity of duty cycles $t_{\text{on}} + t_{\text{off}}$ with $\tau_\parallel \gg \tau_\perp \sim t_{\text{off}} \gg t_{\text{on}}$ and a temperature increase ΔT after each t_{on}, the coil temperature increases up to an asymptotic temperature T_{as}. T_{as} is found by using the conditions $T(x,0) = T_{\text{as}} + \Delta T$ and $T(x, t_{\text{off}}) = T_{\text{as}}$ in (B.18):

$$T_{\text{as}}(x) = \sum_{n=1}^{\infty} \left[\sin\left(\frac{n\pi x}{L}\right) e^{-t_{\text{off}}/\tau_n} \frac{2}{L} \int_0^L (T_{\text{as}} + \Delta T - T_b) \sin\left(\frac{n\pi x}{L}\right) dx \right] + T_b \quad \text{(B.21)}$$

Using the ansatz

$$T_{\text{as}}(x) = \sum_{n=1}^{\infty} B_n \sin\left(\frac{n\pi x}{L}\right) + T_b, \quad \text{(B.22)}$$

the orthogonality of the basis of sine functions and the space invariance of ΔT, equation (B.21) results in:

$$B_n = \frac{2\Delta T}{n\pi} \frac{(1 - (-1)^n) e^{-t_{\text{off}}/\tau_n}}{1 - e^{-t_{\text{off}}/\tau_n}} \quad \text{(B.23)}$$

Again, the $n = 1$ component dominates the space dependence of T_{as}. One can therefore write:

$$T_{\text{as}}(x) \simeq \frac{4\Delta T}{\pi} \frac{e^{-t_{\text{off}}/\tau_{\text{cooling}}}}{1 - e^{-t_{\text{off}}/\tau_{\text{cooling}}}} \sin\left(\frac{\pi x}{L}\right) + T_b \quad \text{(B.24)}$$

where τ_{cooling} is the coil cooling time constant. The correct choice for τ_{cooling} depends on the coil design. The heat dissipation at the coil mounting points and the heat transport through the power lines, for example, may have a significant impact on the cooling time. Ignoring the heat transport through mounting points, assuming that the power lines are ideal heat sinks and recalling that $\tau_\perp \ll \tau_\parallel$, the choice $\tau_{\text{cooling}} = \tau_\parallel$ is a good upper limit candidate, even though $\tau_\parallel$ gathers all the coil turns while only one turn is in fact connected to the power lines. If $\tau_\parallel \gg t_{\text{off}}$, equation (B.24) gives:

$$T_{\text{as}}(L/2) \simeq \frac{4}{\pi} \Delta T \frac{\tau_\parallel}{t_{\text{off}}} + T_b \quad \text{(B.25)}$$

Glossary

C

CAS   Conditional Average Sampling, p. 48.

CRPP   Centre de Recherches en Physique des Plasmas, EPFL, Lausanne, Switzerland, p. 16.

CXRS   Charge Exchange Recombination Spectroscopy, p. 31.

D

DML   DiaMagnetic Loop. Diagnostics used to measure the total plasma energy (see section 2.4.3.6), p. 24.

E

ECCD   Electron Cyclotron Current Drive, p. 21.

ECRH   Electron Cyclotron Resonant Heating, p. 17.

EFC   Error Field Correction, p. 132.

ELM   Edge Localized Mode, p. 12.

F

fb-RT   Particular case of RT mode where Δt_L is determined in real-time by a control algorithm that adjusts the value of Δt_L until a predefined value of f_{ELM} is reached (feed-back mode), p. 43.

FF   Feed-forward power modulation. The power is modulated with a predefined frequency and duty cycle, irrespectively of the ELM cycle, p. 29.

ff-RT   Particular case of RT mode where Δt_L is set *a priori*, irrespectively of the plasma response (feed-forward mode), p. 43.

FIR   Far InfraRed interferometer. Diagnostics measuring the line integrated plasma density (see section 2.4.3.4), p. 23.

H

H-mode   Plasma regime in which the energy and particle confinement are enhanced by a transport barrier located at the plasma edge and forming a pedestal in the plasma pressure profile (as opposed to the L-mode), p. 11.

I

invRT   Equivalent to RT mode but with inverted modulation phase (i.e. ELMs trigger high power phases), p. 29.

L

L-mode   Plasma regime in which confinement of particle and energy is low (as opposed to the H-mode), p. 11.

LTI   Linear Time Invariant system, p. 143.

M

MHD   Magnetohydrodynamics, the 1-fluid theory of plasmas, particularly suited to describe slow and large scale events, p. 5.

R

RMP   Resonant Magnetic Perturbation, p. 14.

RT   X2 power modulated between a low and a high power level with low power phases triggered by the ELMs, p. 29.

RWM   Resistive Wall Modes; ideal MHD instabilities that are not stabilized by the vessel wall because their growth rate is slower than the resistive time of the vacuum vessel, p. 109.

S

SCD Système de Contrôle Distribué (real-time digital Distributed Control System), p. 24.

SCS Saddle Coil System, p. 107.

T

TCV Tokamak à Configuration Variable (CRPP, Lausanne), p. 16.

V

VC Vertical control, p. 108.

X

XTE Diagnostics measuring the core electron temperature by the 2-filter method applied to soft X-ray emissivity (see section 2.4.3.2), p. 22.

Bibliography

[1] BP Company. (2011) **Statistical review of World Energy**. URL: www.bp.com (Cited on page 1.)

[2] K. Kok, **Nuclear engineering handbook**, ser. *Mechanical engineering series*, K. Kok, Ed. CRC Press, 2009. URL: http://books.google.de/books?id=EMy2OyUrqbUC (Cited on page 2.)

[3] J. Wesson and D. J. Campbell, **Tokamaks**, J. Wesson, Ed. Clarendon Press, 2004. (Cited on page 3.)

[4] R. A. Pitts, R. J. Buttery, and S. D. Pinches, **Fusion: the way ahead**, *Physics World*, vol. 19, p. 20, 2006. URL: http://www.physicsweb.org/articles/world/19/3/7/1 (Cited on page 4.)

[5] V. Smirnov, **Tokamak foundation in USSR/Russia 1950–1990**, *Nuclear Fusion*, vol. 50, no. 1, p. 014003, 2010. URL: http://stacks.iop.org/0029-5515/50/i=1/a=014003 (Cited on page 4.)

[6] G. Federici, A. Loarte, and G. Strohmayer, **Assessment of erosion of the ITER divertor targets during type I ELMs**, *Plasma Physics and Controlled Fusion*, vol. 45, no. 9, p. 1523, 2003. URL: http://stacks.iop.org/0741-3335/45/i=9/a=301 (Cited on pages 5 and 13.)

[7] R. Hawryluk, D. Campbell, G. Janeschitz *et al.*, **Principal physics developments evaluated in the ITER design review**, *Nuclear Fusion*, vol. 49, no. 6, p. 065012 (15pp), 2009. (Cited on pages 5 and 13.)

[8] N. Klimov, V. Podkovyrov, A. Zhitlukhin *et al.*, **Experimental study of PFCs erosion and eroded material deposition under ITER-like transient loads at the plasma gun facility QSPA-T**, *Journal of Nuclear Materials*, vol. 415, no. 1, Supplement, pp. S59 – S64, 2011, proceedings of the 19th International Conference on Plasma-Surface Interactions in

Controlled Fusion. URL: http://www.sciencedirect.com/science/article/pii/S0022311511000250 (Cited on pages 5 and 13.)

[9] A. Degeling, Y. Martin, J. Lister *et al.*, ***Magnetic triggering of ELMs in TCV***, *Plasma Physics and Controlled Fusion*, vol. 45, no. 9, pp. 1637–1655, 2003. (Cited on pages 5, 13 and 14.)

[10] T. E. Evans, R. A. Moyer, P. R. Thomas *et al.*, ***Suppression of Large Edge-Localized Modes in High-Confinement DIII-D Plasmas with a Stochastic Magnetic Boundary***, *Phys. Rev. Lett.*, vol. 92, no. 23, p. 235003, Jun 2004. (Cited on pages 5, 13, 14, 83 and 107.)

[11] W. Suttrop, T. Eich, J. C. Fuchs *et al.*, ***First Observation of Edge Localized Modes Mitigation with Resonant and Nonresonant Magnetic Perturbations in ASDEX Upgrade***, *Phys. Rev. Lett.*, vol. 106, no. 22, p. 225004, Jun 2011. (Cited on pages 5, 13, 14, 83, 84 and 107.)

[12] T. Evans, M. Fenstermacher, R. Moyer *et al.*, ***RMP ELM suppression in DIII-D plasmas with ITER similar shapes and collisionalities***, *Nuclear Fusion*, vol. 48, no. 2, p. 024002, 2008. URL: http://stacks.iop.org/0029-5515/48/i=2/a=024002 (Cited on pages 6, 14 and 108.)

[13] F. Piras, S. Coda, B. P. Duval *et al.*, ***"Snowflake" H Mode in a Tokamak Plasma***, *Phys. Rev. Lett.*, vol. 105, p. 155003, Oct 2010. URL: http://link.aps.org/doi/10.1103/PhysRevLett.105.155003 (Cited on pages 6 and 30.)

[14] J. Freidberg, ***Ideal magnetohydrodynamics***. Plenum Press, New York, NY, 1987. (Cited on page 9.)

[15] I. Classen, ***Imaging and Control of Magnetic Islands in Tokamaks***, Ph.D. thesis, Technische Universiteit Eindhoven, 2007. (Cited on page 11.)

[16] G. Bateman, ***MHD instabilities***. Cambridge, Mass., MIT Press, 1978. (Cited on page 10.)

[17] F. Wagner, G. Becker, K. Behringer *et al.*, ***Regime of Improved Confinement and High Beta in Neutral-Beam-Heated Divertor Discharges of the ASDEX Tokamak***, *Phys. Rev. Lett.*, vol. 49, no. 19, pp. 1408–1412, Nov 1982. (Cited on page 11.)

[18] Y. R. Martin, M. A. Henderson, S. Alberti *et al.*, ***Accessibility and properties of ELMy H-mode and ITB plasmas in TCV***, *Plasma Physics and Controlled Fusion*, vol. 45, no. 12 A, pp. A351–A365, 2003. URL: www.scopus.com (Cited on page 11.)

[19] F. Wagner, ***A quarter-century of H-mode studies***, *Plasma Physics and Controlled Fusion*, vol. 49, no. 12B, p. B1, 2007. URL: http://stacks.iop.org/0741-3335/49/i=12B/a=S01 (Cited on page 11.)

[20] F. Ryter, K. Buchl, C. Fuchs *et al.*, ***H-mode results in ASDEX Upgrade***, *Plasma Physics and Controlled Fusion*, vol. 36, no. 7A, p. A99, 1994. URL: http://stacks.iop.org/0741-3335/36/i=7A/a=011 (Cited on pages 11 and 13.)

[21] H. Zohm, ***Edge localized modes (ELMs)***, *Plasma Physics and Controlled Fusion*, vol. 38, no. 2, pp. 105–128, 1996. (Cited on pages 12 and 30.)

[22] H. Zohm, ***The physics of edge localized modes (ELMs) and their role in power and particle exhaust***, *Plasma Physics and Controlled Fusion*, vol. 38, no. 8, p. 1213, 1996. (Cited on pages 12 and 36.)

[23] J. W. Connor, ***A review of models for ELMs***, *Plasma Physics and Controlled Fusion*, vol. 40, no. 2, p. 191, 1998. URL: http://stacks.iop.org/0741-3335/40/i=2/a=003 (Cited on page 12.)

[24] W. Suttrop, ***The physics of large and small edge localized modes***, *Plasma Physics and Controlled Fusion*, vol. 42, no. 5A, p. A1, 2000. URL: http://stacks.iop.org/0741-3335/42/i=5A/a=301 (Cited on page 12.)

[25] G. T. A. Huysmans, ***ELMs: MHD instabilities at the transport barrier***, *Plasma Physics and Controlled Fusion*, vol. 47, no. 12B, pp. B165–B178, 2005. URL: http://stacks.iop.org/0741-3335/47/B165 (Cited on page 12.)

[26] E. Doyle, W. Houlberg, Y. Kamada *et al.*, ***Progress in the ITER Physics Basis Chapter 2: Plasma confinement and transport***, *Nuclear Fusion*, vol. 47, no. 6, p. S18, 2007. URL: http://stacks.iop.org/0029-5515/47/i=6/a=S02 (Cited on pages 12, 27, 33, 34 and 80.)

[27] S. Y. Medvedev, A. A. Martynov, Y. R. Martin *et al.*, ***Edge kink/ballooning mode stability in tokamaks with separatrix***, *Plasma*

Physics and Controlled Fusion, vol. 48, no. 7, p. 927, 2006. URL: http://stacks.iop.org/0741-3335/48/i=7/a=003 (Cited on page 12.)

[28] M. Greenwald, J. Terry, S. Wolfe *et al.*, ***A new look at density limits in tokamaks***, *Nuclear Fusion*, vol. 28, no. 12, p. 2199, 1988. URL: http://stacks.iop.org/0029-5515/28/i=12/a=009 (Cited on page 13.)

[29] P. Lang, J. Neuhauser, L. Horton *et al.*, ***ELM frequency control by continuous small pellet injection in ASDEX Upgrade***, *Nuclear Fusion*, vol. 43, no. 10, p. 1110, 2003. URL: http://stacks.iop.org/0029-5515/43/i=10/a=012 (Cited on page 13.)

[30] P. Lang, K. Lackner, M. Maraschek *et al.*, ***Investigation of pellet-triggered MHD events in ASDEX Upgrade and JET***, *Nuclear Fusion*, vol. 48, no. 9, p. 095007, 2008. URL: http://stacks.iop.org/0029-5515/48/i=9/a=095007 (Cited on page 13.)

[31] P. T. Lang, A. W. Degeling, J. B. Lister *et al.*, ***Frequency control of type-I ELMs by magnetic triggering in ASDEX Upgrade***, *Plasma Physics and Controlled Fusion*, vol. 46, no. 11, p. L31, 2004. URL: http://stacks.iop.org/0741-3335/46/i=11/a=L02 (Cited on page 14.)

[32] S. Gerhardt, J.-W. Ahn, J. Canik *et al.*, ***First observation of ELM pacing with vertical jogs in a spherical torus***, *Nuclear Fusion*, vol. 50, no. 6, p. 064015, 2010. URL: http://stacks.iop.org/0029-5515/50/i=6/a=064015 (Cited on page 14.)

[33] R. Maingi, T. H. Osborne, B. P. LeBlanc *et al.*, ***Edge-Localized-Mode Suppression through Density-Profile Modification with Lithium-Wall Coatings in the National Spherical Torus Experiment***, *Phys. Rev. Lett.*, vol. 103, p. 075001, Aug 2009. URL: http://link.aps.org/doi/10.1103/PhysRevLett.103.075001 (Cited on page 14.)

[34] D. P. Boyle, R. Maingi, P. B. Snyder *et al.*, ***The relationships between edge localized modes suppression, pedestal profiles and lithium wall coatings in NSTX***, *Plasma Physics and Controlled Fusion*, vol. 53, no. 10, p. 105011, 2011. URL: http://stacks.iop.org/0741-3335/53/i=10/a=105011 (Cited on page 14.)

[35] T. Evans, R. Moyer, J. Watkins *et al.*, ***Suppression of large edge localized modes with edge resonant magnetic fields in high confinement***

DIII-D plasmas, *Nuclear Fusion*, vol. 45, no. 7, p. 595, 2005. URL: http://stacks.iop.org/0029-5515/45/i=7/a=007 (Cited on pages 14 and 83.)

[36] Y. Liang, H. R. Koslowski, P. R. Thomas *et al.*, ***Active control of type-I edge-localized modes with*** $n = 1$ ***perturbation fields in the JET Tokamak***, *Physical Review Letters*, vol. 98, no. 26, p. 265004, Jun 2007. (Cited on pages 14, 83 and 107.)

[37] A. Kirk, Y. Liu, E. Nardon *et al.*, ***Magnetic perturbation experiments on MAST L- and H-mode plasmas using internal coils***, *Plasma Physics and Controlled Fusion*, vol. 53, no. 6, p. 065011, 2011. URL: http://stacks.iop.org/0741-3335/53/i=6/a=065011 (Cited on pages 14, 84 and 107.)

[38] S. J. Fielding, R. J. Buttery, A. R. Field *et al.*, ***ELM control in COMPASS-D***, in *28th EPS Conference on Controlled Fusion and Plasma Physics, Funchal*, vol. 25A, June 2001, pp. 1825 – 1828. (Cited on page 14.)

[39] D. A. Gates, ***Overview of Results from the National Spherical Torus Experiment (NSTX)***, in *22nd IAEA Fusion Energy Conference, Geneva*, vol. OV. IAEA, October 2008, pp. 3–1. (Cited on page 14.)

[40] H. Meyer, R. J. Akers, F. Alladio *et al.*, ***Overview of physics results from MAST***, *Nuclear Fusion*, vol. 49, no. 10, 2009. (Cited on page 14.)

[41] T. E. Evans, K. H. Burrell, M. E. Fenstermacher *et al.*, ***The physics of edge resonant magnetic perturbations in hot tokamak plasmas***, *Physics of Plasmas*, vol. 13, no. 5, p. 056121, 2006. URL: http://link.aip.org/link/?PHP/13/056121/1 (Cited on pages 14 and 83.)

[42] Y. Liang, C. Gimblett, P. Browning *et al.*, ***Observations of multi-resonance effect in ELM control with magnetic perturbation fields on the JET tokamak***, *Nuclear Fusion*, vol. 51, no. 7, p. 073001, 2011. URL: http://stacks.iop.org/0029-5515/51/i=7/a=073001 (Cited on pages 14 and 84.)

[43] L. D. Horton, G. D. Conway, A. W. Degeling *et al.*, ***ITER-relevant H-mode physics at ASDEX Upgrade***, *Plasma Physics and Controlled Fusion*, vol. 46, no. 12B, p. B511, 2004. URL: http://stacks.iop.org/0741-3335/46/i=12B/a=042 (Cited on pages 14, 15, 27, 41, 64 and 81.)

[44] T. Luce, R. James, A. Fyakhretdinov *et al.*, ***Electron cyclotron heating and current drive results from the DIII-D tokamak***, in *Plasma physics and controlled nuclear fusion research 1990*, vol. 1. Publ by IAEA, Vienna, Austria, 1991, pp. 631–644. (Cited on pages 15 and 27.)

[45] J. Lohr, K. Matsuda, T. C. Luce *et al.*, ***The effect of edge resonant electron cyclotron heating on edge localized modes in a Tokamak***, *General Atomics*, vol. GA-A20182, May 1991. (Cited on pages 15 and 27.)

[46] C. M. Greenfield, K. H. Burrell, J. C. DeBoo *et al.*, ***Quiescent Double Barrier Regime in the DIII-D Tokamak***, *Phys. Rev. Lett.*, vol. 86, pp. 4544–4547, May 2001. URL: http://link.aps.org/doi/10.1103/PhysRevLett.86.4544 (Cited on page 15.)

[47] K. H. Burrell, T. H. Osborne, P. B. Snyder *et al.*, ***Quiescent H-Mode Plasmas with Strong Edge Rotation in the Cocurrent Direction***, *Phys. Rev. Lett.*, vol. 102, p. 155003, Apr 2009. URL: http://link.aps.org/doi/10.1103/PhysRevLett.102.155003 (Cited on page 15.)

[48] D. Whyte, A. Hubbard, J. Hughes *et al.*, ***I-mode: an H-mode energy confinement regime with L-mode particle transport in Alcator C-Mod***, *Nuclear Fusion*, vol. 50, no. 10, p. 105005, 2010. URL: http://stacks.iop.org/0029-5515/50/i=10/a=105005 (Cited on page 15.)

[49] F. Piras, ***Extremely Shaped Plasmas to Improve the Tokamak Concept***, Ph.D. thesis, EPFL, Lausanne, 2011. URL: http://library.epfl.ch/theses/?nr=5015,http://library.epfl.ch/theses/?nr=5015 (Cited on page 16.)

[50] C. Schlatter, ***Turbulent ion heating in TCV tokamak plasmas***, Ph.D. thesis, EPFL, Lausanne, 2009. URL: http://library.epfl.ch/theses/?nr=4479,http://library.epfl.ch/theses/?nr=4479 (Cited on pages 17 and 18.)

[51] F. Hofmann, J. B. Lister, W. Anton *et al.*, ***Creation and control of variably shaped plasmas in TCV***, *Plasma Physics and Controlled Fusion*, vol. 36, no. 12B, p. B277, 1994. (Cited on page 16.)

[52] V. Alikaev, Y. Dnestrovskii, V. Parail *et al.*, ***Outlook for Electron-Cyclotron Heating in Large Tokamaks***, *Sov J Plasma Phys*, vol. 3, no. 2, pp. 127–136, 1977. URL: http://www.scopus.com/inward/record.url?eid=2-s2.0-0017462973&partnerID=40&md5=9c8714ceca5f86c9dced6fda795dacce (Cited on page 17.)

[53] J. I. Paley, F. Felici, S. Coda *et al.*, ***From profile to sawtooth control: developing feedback control using ECRH/ECCD systems on the TCV tokamak***, *Plasma Physics and Controlled Fusion*, vol. 51, no. 12, p. 124041, 2009. URL: http://stacks.iop.org/0741-3335/51/i=12/a=124041 (Cited on page 17.)

[54] T. P. Goodman, F. Felici, O. Sauter *et al.*, ***Sawtooth Pacing by Real-Time Auxiliary Power Control in a Tokamak Plasma***, *Phys. Rev. Lett.*, vol. 106, p. 245002, Jun 2011. URL: http://link.aps.org/doi/10.1103/PhysRevLett.106.245002 (Cited on page 17.)

[55] S. Coda, T. P. Goodman, M. A. Henderson *et al.*, ***High-power ECH and fully non-inductive operation with ECCD in the TCV tokamak***, *Plasma Physics and Controlled Fusion*, vol. 42, no. 12B, p. B311, 2000. URL: http://stacks.iop.org/0741-3335/42/i=12B/a=323 (Cited on page 17.)

[56] T. Goodman and the TCV team, ***Experience in integrated control of the multi-megawatt electron cyclotron heating system on the TCV tokamak: the first decade***, *Nuclear Fusion*, vol. 48, no. 5, p. 054011, 2008. URL: http://stacks.iop.org/0029-5515/48/i=5/a=054011 (Cited on page 19.)

[57] V. Alikaev and V. Parail, ***Current drive by electron cyclotron waves***, *Plasma Physics and Controlled Fusion*, vol. 33, no. 13, pp. 1639–1656, 1991. URL: http://www.scopus.com/inward/record.url?eid=2-s2.0-0001372564&partnerID=40&md5=e9f956bd34be70f69e3eab4b98c5feb4 (Cited on page 21.)

[58] K. Matsuda, ***Ray tracing study of the electron cyclotron current drive in DIII-D using 60 GHz***, *IEEE Transactions on Plasma Science*, vol. 17, no. 1, pp. 6–11, 1989. (Cited on pages 21 and 29.)

[59] L. Curchod, ***High Density Plasma Heating in the Tokamak à Configuration Variable***, Ph.D. thesis, EPFL, Lausanne, 2011. URL: http://library.epfl.ch/theses/?nr=5012,http://library.epfl.ch/theses/?nr=5012 (Cited on page 23.)

[60] R. Behn, ***Brief description of the TCV Thomson scattering system***, 2007, available on the internal wiki server of CRPP. URL: https://crpplocal.epfl.ch/wiki/Thomson (Cited on page 22.)

[61] R. Behn, S. Franke, Z. Pietrzyk *et al.*, ***The Thomson scattering diagnostic on TCV***, in *7th International Symposium on Laser-Aided Plasma Diagnostics*, 1995, 7th International Symposium on Laser-Aided Plasma Diagnostics, Fukuoka, Japan, December 1995. (Cited on page 22.)

[62] S. Franke, ***Application of Thomson scattering at 1.06mm as a diagnostic for spatial profile measurements of electron temperature and density on the TCV tokamak***, Ph.D. thesis, EPFL, Lausanne, 1997. URL: http://library.epfl.ch/theses/?nr=1654,http://library.epfl.ch/theses/?nr=1654 (Cited on page 22.)

[63] A. Pitzschke, ***Pedestal Characteristics and MHD Stability of H-Mode Plasmas in TCV***, Ph.D. thesis, Ecole Polytechnique Fédérale de Lausanne, Lausanne, 2011. URL: http://library.epfl.ch/theses/?nr=4917 (Cited on pages 22 and 31.)

[64] R. Behn, ***Brief description of the TCV Far InfraRed interferometer***, 2007, available on the internal wiki server of CRPP. URL: https://crpplocal.epfl.ch/wiki/FIR (Cited on page 23.)

[65] S. Barry, ***The extension of the FIR interferometer of TCV to a polarimeter and measurements of the Faraday rotation caused by the poloidal magnetic field***, EPFL, Tech. Rep., 1999. (Cited on page 23.)

[66] J.-M. Moret, F. Buhlmann, D. Fasel *et al.*, ***Magnetic measurements on the TCV Tokamak***, *Review of Scientific Instruments*, vol. 69, no. 6, pp. 2333–2348, 1998. URL: http://link.aip.org/link/?RSI/69/2333/1 (Cited on page 24.)

[67] J.-M. Moret, F. Buhlmann, and G. Tonetti, ***Fast single loop diamagnetic measurements on the TCV tokamak***, *Review of Scientific Instruments*, vol. 74, no. 11, pp. 4634–4643, 2003. URL: http://dx.doi.org/doi/10.1063/1.1614856 (Cited on page 24.)

[68] F. Hofmann and G. Tonetti, ***Tokamak equilibrium reconstruction using Faraday rotation measurements***, *Nuclear Fusion*, vol. 28, no. 10, p. 1871, 1988. URL: http://stacks.iop.org/0029-5515/28/i=10/a=014 (Cited on pages 24 and 32.)

[69] J. I. Paley, F. Felici, J. Berrino *et al.*, ***Real time control of plasmas and ECRH systems on TCV***, *Nuclear Fusion*, vol. 49, no. 8, p. 085017,

2009. URL: http://www.iop.org/EJ/journal/NuclFus,http://crpplocal.epfl.ch/pinboard/jpapers/0805404.pdf (Cited on page 25.)

[70] J. I. Paley, S. Coda, B. P. Duval *et al.*, ***Architecture and commissioning of the TCV distributed feedback control system***, in *Real Time Conference (RT), 2010 17th IEEE-NPSS*, 2010. URL: http://iter.ipfn.ist.utl.pt/RT2010,http://crpplocal.epfl.ch/pinboard/papers/103808806.pdf (Cited on page 25.)

[71] F. Felici, ***Real-Time Control of Tokamak Plasmas: from Control of Physics to Physics-Based Control***, Ph.D. thesis, EPFL, Lausanne, 2011. URL: http://library.epfl.ch/theses/?nr=5203,http://library.epfl.ch/theses/?nr=5203 (Cited on page 25.)

[72] R. Sartori, G. Saibene, M. Becoulet *et al.*, ***Edge operational space for high density/high confinement ELMY H-modes in JET***, *Plasma Physics and Controlled Fusion*, vol. 44, no. 9, p. 1801, 2002. (Cited on pages 31 and 35.)

[73] A. Manini, J.-M. Moret, S. Alberti *et al.*, ***Modulated ECH power absorption measurements using a diamagnetic loop in the TCV tokamak***, *Plasma Physics and Controlled Fusion*, vol. 44, no. 2, p. 139, 2002. URL: http://stacks.iop.org/0741-3335/44/i=2/a=301 (Cited on page 32.)

[74] O. Sauter, B. P. Duval, L. Federspiel *et al.*, ***Effects of ECH/ECCD on Tearing Modes in TCV and Link to Rotation Profile***, in *23rd IAEA Fusion Energy Conference*, vol. EXS. IAEA, October 2010, pp. P2–17. URL: http://www-pub.iaea.org/MTCD/Meetings/PDFplus/2010/cn180/cn180_papers/exs_p2-17.pdf (Cited on pages 32 and 109.)

[75] A. Loarte, M. Becoulet, G. Saibene *et al.*, ***Characteristics and scaling of energy and particle losses during Type I ELMs in JET H-modes***, *Plasma Physics and Controlled Fusion*, vol. 44, no. 9, p. 1815, 2002. (Cited on page 35.)

[76] Y. R. Martin, A. W. Degeling, and J. B. Lister, ***Search for determinism in ELM time series in TCV***, *Plasma Physics and Controlled Fusion*, vol. 44, no. 5A, p. A373, 2002. URL: http://stacks.iop.org/0741-3335/44/i=5A/a=340 (Cited on pages 47 and 48.)

[77] A. W. Degeling, Y. R. Martin, J. B. Lister *et al.*, ***ELM Dynamics in TCV H-modes***, *AIP Conference Proceedings*, vol. 669, no. 1, pp. 223–227, 2003. URL: http://link.aip.org/link/?APC/669/223/1 (Cited on pages 47 and 48.)

[78] S. Alberti, J.-P. Hogge, I. Pagonakis *et al.*, ***Design studies of the dual-frequency operation of the W7-X/140GHz/1MW gyrotron at 126GHz for TCV and 168GHz for ITER***, in *Infrared Millimeter and Terahertz Waves (IRMMW-THz), 2010 35th International Conference on*, sept. 2010, pp. 1 –2. (Cited on page 82.)

[79] K. H. Burrell and T. E. Evans, ***ELM suppression in low edge collisionality H-mode discharges using n = 3 magnetic perturbations***, *Plasma Physics and Controlled Fusion*, vol. 47, no. 12B, pp. B37–B52, 2005. (Cited on page 83.)

[80] M. E. Fenstermacher, T. E. Evans, T. H. Osborne *et al.*, ***Effect of island overlap on edge localized mode suppression by resonant magnetic perturbations in DIII-D***, *Physics of Plasmas*, vol. 15, no. 5, p. 056122, 2008. URL: http://link.aip.org/link/?PHP/15/056122/1 (Cited on pages 83 and 92.)

[81] E. Nardon, M. Bécoulet, G. Huysmans *et al.*, ***Magnetohydrodynamics modelling of H-mode plasma response to external resonant magnetic perturbations***, *Physics of Plasmas*, vol. 14, no. 9, p. 092501, 2007. URL: http://link.aip.org/link/?PHP/14/092501/1 (Cited on page 84.)

[82] M. Bécoulet, G. Huysmans, X. Garbet *et al.*, ***Physics of penetration of resonant magnetic perturbations used for Type I edge localized modes suppression in tokamaks***, *Nuclear Fusion*, vol. 49, no. 8, 2009. (Cited on pages 84, 85 and 109.)

[83] H. Strauss, L. Sugiyama, G. Park *et al.*, ***Extended MHD simulation of resonant magnetic perturbations***, *Nuclear Fusion*, vol. 49, no. 5, p. 055025, 2009. URL: http://stacks.iop.org/0029-5515/49/i=5/a=055025 (Cited on page 84.)

[84] Y. Liu, A. Kirk, Y. Gribov *et al.*, ***Modelling of plasma response to resonant magnetic perturbation fields in MAST and ITER***, *Nuclear Fusion*, vol. 51, no. 8, p. 083002, 2011. URL: http://stacks.iop.org/0029-5515/51/i=8/a=083002 (Cited on page 84.)

[85] E. Nardon, P. Tamain, M. Bécoulet *et al.*, ***Quasi-linear MHD modelling of H-mode plasma response to resonant magnetic perturbations***, *Nuclear Fusion*, vol. 50, no. 3, p. 034002, 2010. URL: http://stacks.iop.org/0029-5515/50/i=3/a=034002 (Cited on page 84.)

[86] E. Nardon, A. Kirk, R. Akers *et al.*, ***Edge localized mode control experiments on MAST using resonant magnetic perturbations from in-vessel coils***, *Plasma Physics and Controlled Fusion*, vol. 51, no. 12, 2009. URL: http://www.scopus.com/inward/record.url?eid=2-s2.0-70449727873&partnerID=40&md5=cd67852467ab4cd52502e97c7a04d076 (Cited on pages 84 and 130.)

[87] M. Schaffer, J. Menard, M. Aldan *et al.*, ***Study of in-vessel nonaxisymmetric ELM suppression coil concepts for ITER***, *Nuclear Fusion*, vol. 48, no. 2, 2008. (Cited on pages 84 and 111.)

[88] M. Bécoulet, E. Nardon, G. Huysmans *et al.*, ***Numerical study of the resonant magnetic perturbations for Type I edge localized modes control in ITER***, *Nuclear Fusion*, vol. 48, no. 2, 2008. (Cited on page 84.)

[89] A. Garofalo, K. Burrell, J. Deboo *et al.*, ***Observation of plasma rotation driven by static nonaxisymmetric magnetic fields in a tokamak***, *Physical Review Letters*, vol. 101, no. 19, 2008. (Cited on pages 85 and 109.)

[90] K. Shaing, S. Sabbagh, M. Chu *et al.*, ***Effects of orbit squeezing on neoclassical toroidal plasma viscosity in tokamaks***, *Physics of Plasmas*, vol. 15, no. 8, 2008. (Cited on pages 85 and 109.)

[91] S. M. Wolfe, I. H. Hutchinson, R. S. Granetz *et al.*, ***Nonaxisymmetric field effects on Alcator C-Mod***, *Physics of Plasmas*, vol. 12, no. 5, pp. 1–10, 2005. URL: www.scopus.com (Cited on pages 85 and 108.)

[92] J. D. Hanson, ***Correcting small magnetic field non-axisymmetries***, *Nuclear Fusion*, vol. 34, no. 3, pp. 441–448, 1994. (Cited on pages 85 and 87.)

[93] J. D. Hanson, ***Using external coils to correct field errors in tokamaks***, *Plasma Science, IEEE Transactions on*, vol. 27, no. 6, pp. 1588–1595, Dec 1999. (Cited on pages 85, 87 and 132.)

[94] P. Cahyna, R. Panek, V. Fuchs *et al.*, ***The optimization of resonant magnetic perturbation spectra for the COMPASS tokamak***, *Nuclear*

Fusion, vol. 49, no. 5, p. 055024 (7pp), 2009. URL: http://stacks.iop.org/0029-5515/49/055024 (Cited on pages 87 and 113.)

[95] J.-M. Moret, ***A software package to manipulate space dependencies and geometry in magnetic confinement fusion***, *Review of Scientific Instruments*, vol. 76, no. 7, p. 073507, 2005. URL: http://link.aip.org/link/?RSI/76/073507/1 (Cited on page 87.)

[96] B. V. Chirikov, ***A universal instability of many-dimensional oscillator systems***, *Physics Reports*, vol. 52, no. 5, pp. 263 – 379, 1979. URL: http://www.sciencedirect.com/science/article/pii/0370157379900231 (Cited on page 87.)

[97] F. Hofmann, ***FBT - a free-boundary tokamak equilibrium code for highly elongated and shaped plasmas***, *Computer Physics Communications*, vol. 48, no. 2, pp. 207 – 221, 1988. (Cited on pages 96 and 131.)

[98] W. Suttrop, O. Gruber, S. Günter *et al.*, ***In-vessel saddle coils for MHD control in ASDEX Upgrade***, *Fusion Engineering and Design*, vol. 84, no. 2-6, pp. 290 – 294, 2009, proceeding of the 25th Symposium on Fusion Technology - (SOFT-25). URL: http://www.sciencedirect.com/science/article/B6V3C-4VD81MV-4/2/5c76820e9ba0bf6cdf3609698e3eb5ab (Cited on pages 106 and 110.)

[99] B. Hudson, T. Evans, C. Petty *et al.*, ***Dependence of resonant magnetic perturbation experiments on the DIII-D plasma shape***, *Nuclear Fusion*, vol. 50, no. 6, p. 064005, 2010. URL: http://stacks.iop.org/0029-5515/50/i=6/a=064005 (Cited on page 108.)

[100] F. Piras, J.-M. Moret, and J. Rossel, ***Measurement of the magnetic field errors on TCV***, *Fusion Engineering and Design*, vol. 85, no. 5, pp. 739 – 744, 2010. URL: http://www.sciencedirect.com/science/article/pii/S0920379610001900 (Cited on pages 108 and 132.)

[101] H. Reimerdes, O. Sauter, T. Goodman *et al.*, ***From current-driven to neoclassically driven tearing modes***, *Physical Review Letters*, vol. 88, no. 10, pp. 1 050 051–1 050 054, 2002. URL: http://www.scopus.com/inward/record.url?eid=2-s2.0-0037061220&partnerID=40&md5=c0f0de4721417380b04fb8359d6a8aba (Cited on page 109.)

[102] A. Boozer, *Equations for studies of feedback stabilization*, *Physics of Plasmas*, vol. 5, no. 9, pp. 3350–3357, 1998. URL: http://www.scopus.com/inward/record.url?eid=2-s2.0-17344374323&partnerID=40&md5=0c1c86d0ec90796fe9569652a16721a7 (Cited on page 109.)

[103] J. Bialek, A. Boozer, M. Mauel *et al.*, *Modeling of active control of external magnetohydrodynamic instabilities*, *Physics of Plasmas*, vol. 8, no. 5 II, pp. 2170–2180, 2001. URL: http://www.scopus.com/inward/record.url?eid=2-s2.0-0035334111&partnerID=40&md5=55565ccc789e2f0b3eceb43aeae0de6f (Cited on page 109.)

[104] C. Bishop, *An intelligent shell for the toroidal pinch*, *Plasma Physics and Controlled Fusion*, vol. 31, no. 7, pp. 1179–1189, 1989. URL: http://www.scopus.com/inward/record.url?eid=2-s2.0-36149035920&partnerID=40&md5=5595cbec9707e2fb78f023f3dfcb800f (Cited on page 109.)

[105] T. Bolzonella, M. Cavinato, E. Gaio *et al.*, *Feedback control of resistive wall modes by saddle coils in RFX-mod*, *Fusion Engineering and Design*, vol. 82, no. 5-14, pp. 1064–1072, 2007. URL: http://www.scopus.com/inward/record.url?eid=2-s2.0-34948886715&partnerID=40&md5=49aad9c215dcec4c9b388e550618fa30 (Cited on page 109.)

[106] I. Zatz, R. Baker, A. Brooks *et al.*, *Design of JET ELM control coils for operation at 350°C*, *Fusion Engineering and Design*, vol. 86, no. 9-11, pp. 1980 – 1983, 2011, proceedings of the 26th Symposium of Fusion Technology (SOFT-26). URL: http://www.sciencedirect.com/science/article/pii/S0920379611003619 (Cited on page 111.)

[107] T. E. Evans, R. K. W. Roeder, J. A. Carter *et al.*, *Experimental signatures of homoclinic tangles in poloidally diverted tokamaks*, *Journal of Physics: Conference Series*, vol. 7, no. 1, p. 174, 2005. URL: http://stacks.iop.org/1742-6596/7/i=1/a=015 (Cited on page 130.)

[108] J.-W. Ahn, J. Canik, V. Soukhanovskii *et al.*, *Modification of divertor heat and particle flux profiles with applied 3D*

fields in NSTX H-mode plasmas, *Nuclear Fusion*, vol. 50, no. 4, 2010. URL: http://www.scopus.com/inward/record.url?eid=2-s2.0-77950678730&partnerID=40&md5=7fbc4df60fe28c6ef10cd484c8c16dad (Cited on page 130.)

[109] E. Nardon, P. Cahyna, S. Devaux *et al.*, *Strike-point splitting induced by external magnetic perturbations: observations on JET and MAST and associated modelling*, *Journal of Nuclear Materials*, vol. In Press, Accepted Manuscript, pp. –, 2010. URL: http://www.sciencedirect.com/science/article/B6TXN-51F25W7-8/2/6b15ddca79d0807d80114a7b5ec71e4c (Cited on page 130.)

[110] J.-K. Park, M. Schaffer, J. Menard *et al.*, *Control of asymmetric magnetic perturbations in tokamaks*, *Physical Review Letters*, vol. 99, no. 19, 2007. URL: http://www.scopus.com/inward/record.url?eid=2-s2.0-36048943427&partnerID=40&md5=007654db3b27d888c90ddf50dfbb4ca3 (Cited on page 132.)

[111] J.-K. Park, M. Schaffer, R. La Haye *et al.*, *Error field correction in DIII-D Ohmic plasmas with either handedness*, *Nuclear Fusion*, vol. 51, no. 2, 2011. URL: http://www.scopus.com/inward/record.url?eid=2-s2.0-79751471985&partnerID=40&md5=4faf47648b95b9c8105f5d5cd3ee9526 (Cited on page 132.)

[112] O. Sauter, C. Angioni, and Y. R. Lin-Liu, *Neoclassical conductivity and bootstrap current formulas for general axisymmetric equilibria and arbitrary collisionality regime*, *Physics of Plasmas*, vol. 6, no. 7, pp. 2834–2839, 1999. URL: http://dx.doi.org/doi/10.1063/1.873240 (Cited on page 181.)

[113] O. Sauter, C. Angioni, and Y. R. Lin-Liu, *Erratum: "Neoclassical conductivity and bootstrap current formulas for general axisymmetric equilibria and arbitrary collisionality regime" [Phys. Plasmas 6, 2834 (1999)]*, *Physics of Plasmas*, vol. 9, no. 12, pp. 5140–5140, 2002. URL: http://dx.doi.org/doi/10.1063/1.1517052 (Cited on page 181.)

[114] F. W. Grover, *Inductance Calculations*. DvNC, 1946. (Cited on page 184.)

[115] P. Leduc, A. Schellmanns, D. Magnon *et al.*, *Modeling of integrated inductors with a coplanar ground plane using the PEEC method*, *Mi-*

crowave Conference, 2003. 33rd European, vol. 1, no. n/a, pp. 447–450 Vol.1, Oct. 2003. (Cited on page 185.)

Remerciements

Afin que les personnes concernées puissent bénéficier d'une lecture moins anglo-saxonne, permettez-moi ici de recourir au français. Je profite donc de ces quelques pages cachées en fin de thèse pour remercier les personnes qui m'ont permis d'entreprendre ce travail et de le conduire jusqu'à son terme.

Au sein du cercle de la famille et des amis, je tiens évidemment à commencer par remercier mes parents, non seulement pour l'infaillibilité de leur soutien moral, et parfois gastronomique, voire même matériel, mais également pour leur accueil durant ma première année de thèse. J'en profite également pour remercier mes frère et soeurs pour leurs nombreuses invitations, me permettant de faire quelques exceptions au régime salami-fromage-pizza-noodles habituel du doctorant. J'ai également une pensée pour Marc-Olivier, mon (deuxième) frère de coeur, et sa Maria, la reine de la cuisine, pour les nombreuses soirées passées entre amis à se remplir la panse et à se rincer le gosier, me permettant d'oublier un instant l'austérité de la science. Je ne peux conclure ce paragraphe sans mentionner l'excellentissime Crazy Pub de Cossonay, établissement de référence s'il en est, havre de paix du doctorant, sagement conduit par son brave capitaine, Sascha, que j'ai désormais le plaisir de compter parmi mes amis et dont le soutien moral pour cette thèse mérite d'être ici relevé. Et c'est sans parler de Clarisse, ma petite souris, qui m'a accompagné, soutenu et supporté tout au long de cette dernière année de thèse et sans laquelle celle-ci aurait été certainement des plus ternes !

Au sein du CRPP, je me dois bien sûr de commencer par remercier Jean-Marc Moret, mon superviseur de thèse. Toujours bien disposé, toujours jovial, l'esprit clair et tranquille, il m'a permis de garder pied et de ne pas me noyer sous la masse souvent impressionnante des choses à faire ou à étudier, des trajectoires de recherche possibles et des problèmes rencontrés. Non content d'avoir un esprit brillant, il parvient également à allier un travail sérieux, soigné et pointu à un détachement aussi sain que déconcertant, incarnant une personnalité singulière qui m'aura souvent conduit à la réflexion et à la remise en question, parfois peut-être "à l'insu de son plein gré".

Il y a ensuite une longue liste de personnes que je tiens à remercier pour différentes raisons : Yves Martin pour son engagement dans les premiers développements du projet des bobines RMP ; Laurent Villard pour ses précieux conseils théoriques et sa personnalité joviale et sympathique ; Stephan Brunner pour sa connaissance impressionnante de la physique des plasmas, son cours d'une qualité exceptionnelle et son humilité tout autant admirable ; Stefano Coda pour ses conseils avisés sur le plan expérimental, sa relecture pointue de certains de mes travaux, son dévouement aussi général qu'efficace au bon fonctionnement de TCV et sa confiance dans la pertinence de mes expériences, même lorsque ces dernières déclenchaient quelques feux d'artifice parfois effrayants dans notre Tokamak préféré ; Tim Goodman pour son support technique et scientifique au niveau des gyrotrons, parfois malgré lui (X3 quand tu nous tiens !), pour son enthousiasme communicatif, et parce qu'il a la bonté de rire à mes blagues ; Federico Felici pour avoir programmé et piloté le système de contrôle en temps réel et pour sa contribution significative sur le plan scientifique ; et Olivier Sauter pour sa disponibilité, sa perspicacité et ses nombreuses bonnes idées sur le plan expérimental. Je regretterai probablement notre duo de choc pour le bogage - débogage de codes d'analyse *Matlab*, nos discussions récurrentes sur la meilleure manière d'organiser ces derniers, ainsi que ses leçons privées d'initiation à la pureté du codage *à la Olivier*. Je tiens aussi à remercier Basil Duval pour ses remarques variées, aussi bien sur le plan scientifique, que philosophique ou psychologique, parfois crues, souvent drôles, et jamais dénuées d'intérêt. Je lui dois notamment l'idée de combiner le contrôle en temps réel et la modulation de puissance, idée fructueuse s'il en est et pour laquelle il a toute ma reconnaissance. Bien entendu, mes expériences n'auraient jamais pu aboutir sans le dévouement et la persévérance de notre opérateur gyrotroniste de choc Miguel Silva, que je remercie également chaleureusement. J'ai aussi ici une pensée pour les doctorants (martyrs ?) qui ont dû me supporter durant toutes ces années dans leur bureau : Christian Theiler, Alessandro Bortolon, Francesco Piras, Sébastien Jolliet, et bien d'autres encore. Je regretterai également toutes les personnes du CRPP qui, par leurs conseils, leurs amitiés ou leur simple sympathie, ont contribué à rendre mon passage au CRPP plus agréable : Andreas Pitzschke (merci pour ton aide et vive l'Irlande !), Loïc Curchod, Mattia Albergante, Kees de Meijere, Karim Besseghir, Alexandre Bovet, Fabio Avino, Joaquim Loizu, David Pfefferlé, David Wagner, Lucia Federspiel, Annamaria Mosetto, Kyle Gustafson, Alexander Karpushov, Benoît Labit, Holger Reimerdes, Jonathan Graves, Tony Cooper, Laurie Porte, Gilbert Tonetti, Ambrogio Fasoli, Xavier Llobet, Christian Schlatter, Edith Gruether, Séverine Jaques (et plouf...), Heidi Francelet,

Damien Fasel, Albert Perez, Philippe Marmillod, Ugo Siravo, Pierre-François Isoz, Steve Couturier, Robert Bertizzolo, Jean-Daniel Landis, Guy Pochon, Jean-Claude Magnin, Francisco Sanchez, Mathieu Toussaint, Frédéric Dolizy, Jérémie Dubray, Christian Moura, Pierre Etienne, et tous ceux que j'ai oubliés ! Toute ma gratitude est également décernée à Thibaut Vernay qui, au fil du temps, entre les pizzas à l'Unil et les burgers au Crazy, est devenu un fidèle compagnon et un ami sincère avec lequel le monde n'a jamais fini d'être fait, défait et refait.

Sur le plan administratif, je tiens à remercier particulièrement Jean-Marc Moret, Yves Martin et Laurent Villard pour leur participation à la fois à mon comité de thèse et à mon jury de thèse, ainsi que Stefano Coda et Stefano Alberti pour leur participation à mon comité de thèse. Je suis également grandement reconnaissant envers Eric Nardon et Wolfgang Suttrop, les membres externes de mon jury de thèse, pour leur travail remarquable en cette occasion.

Publications and contributions

A list of the scientific material published or presented by the author, or to which the author contributed, is given below.

Refereed journal articles

Published

[1] J. X. Rossel, J.-M. Moret, Y. Martin *et al.*, **Physics design of a saddle coil system for TCV**, *Fusion Engineering and Design*, vol. 86, no. 12, pp. 2843 – 2864, 2011. URL: http://www.sciencedirect.com/science/article/pii/S0920379611004996

[2] W. A. Cooper, J. P. Graves, O. Sauter *et al.*, **Helical core tokamak MHD equilibrium states**, *Plasma Physics and Controlled Fusion*, vol. 53, no. 12, p. 124005, 2011. URL: http://stacks.iop.org/0741-3335/53/i=12/a=124005

[3] J. X. Rossel, J.-M. Moret, Y. Martin *et al.*, **A 3D multi-mode geometry-independent RMP optimization method and its application to TCV**, *Plasma Physics and Controlled Fusion*, vol. 52, no. 3, p. 035006, 2010. URL: http://stacks.iop.org/0741-3335/52/i=3/a=035006

[4] F. Piras, J.-M. Moret, and J. Rossel, **Measurement of the magnetic field errors on TCV**, *Fusion Engineering and Design*, vol. 85, no. 5, pp. 739 – 744, 2010. URL: http://www.sciencedirect.com/science/article/pii/S0920379610001900

[5] T. P. Goodman, R. Behn, Y. Camenen *et al.*, **Safety factor profile requirements for electron ITB formation in TCV**, *Plasma Physics and Controlled Fusion*, vol. 47, no. 12B, p. B107, 2005. URL: http://stacks.iop.org/0741-3335/47/i=12B/a=S09

To be published

[1] J. X. Rossel, J.-M. Moret, S. Coda *et al.*, ***Edge localized mode control by electron cyclotron waves in a Tokamak plasma***, submitted to Nuclear Fusion.

[2] J. X. Rossel, F. Felici, J.-M. Moret *et al.*, ***Edge localized mode control and pacing by electron cyclotron resonant heating in a Tokamak plasma***, to be submitted to Plasma Physics and Controlled Fusion.

[3] F. Felici, T. Goodman, O. Sauter *et al.*, ***Integrated real-time control of MHD instabilities using multi-beam ECRH/ECCD systems on TCV***, submitted to Nuclear Fusion.

[4] O. Sauter, B. P. Duval, L. Federspiel *et al.*, ***Roles of MHD and Transport on Toroidal Rotation Profiles in TCV***, submitted to Nuclear Fusion.

Conference proceedings

[1] J. X. Rossel, F. Felici, J.-M. Moret *et al.*, ***ELM control by plasma edge ECRH on TCV***, in *53rd Annual Meeting of the APS Division of Plasma Physics in Salt Lake City, Utah, USA*, no. TP9.00128, 2011. URL: http://www.aps.org/units/dpp/meetings/dpp11/

[2] J. X. Rossel, F. Felici, J.-M. Moret *et al.*, ***ELM control in TCV***, in *480th Wilhelm and Else Heraeus seminar: Active Control of Instabilities in Hot plasmas, Bad Honnef, Germany*, 2011. URL: http://www.iek-yig.de/480thWEH/index.htm

[3] W. A. Cooper, J. P. Graves, O. Sauter *et al.*, ***Helical core tokamak MHD equilibrium states***, in *38th EPS Conference on Plasma Physics, 27 June - 1 July 2011, Strasbourg, France*, no. I5.413, 2011. URL: http://stacks.iop.org/0741-3335/53/i=12/a=124005

[4] W. A. Cooper, O. S. J. P. Graves and, J. X. Rossel *et al.*, ***Free Boundary Tokamak MHD Equilibria with 3D Helical Core Structures***, in *2011 International Sherwood Fusion Theory Conference in Austin, Texas*, 2011. URL: http://ptolemy.ph.utexas.edu/Talks/CooperWA.pdf

[5] J. X. Rossel, J.-M. Moret, Y. Martin *et al.*, ***A 3D multi-mode geometry-independent RMP optimization method and its application to TCV***, in *U.S. Transport Task Force Workshop, Annapolis, Maryland, April 13-16, 2010*, 2010. URL: http://ttf2010.ucsd.edu/presentation_files/postersess2/Rossel.pdf

[6] O. Sauter, F. Felici, T. P. Goodman *et al.*, ***Experimental studies of ECRH/ECCD effects on Tearing Mode stability using the new TCV real-time control system***, in *52nd Annual Meeting of the APS Division of Plasma Physics in Chicago, IL, USA 8-12 nov 2010*, 2010.

[7] O. Sauter, B. P. Duval, L. Federspiel *et al.*, ***Effects of ECH/ECCD on Tearing Modes in TCV and Link to Rotation Profile***, in *23rd IAEA Fusion Energy Conference*, vol. EXS. IAEA, October 2010, pp. P2–17. URL: http://www-pub.iaea.org/MTCD/Meetings/PDFplus/2010/cn180/cn180_papers/exs_p2-17.pdf

[8] F. Piras, T. Goodman, J.-M. Moret *et al.*, ***Plasma start-up in the TCV tokamak***, in *37th EPS Conference on Plasma Phys. Dublin, June 21 - June 25, 2010*. European Physical Society, 2010, p. P2.186. URL: http://ocs.ciemat.es/EPS2010PAP/pdf/P2.186.pdf

[9] O. Sauter, B. P. Duval, L. Federspiel *et al.*, ***Effects of ECH/ECCD on Tearing Modes in TCV and Link to Rotation Profile***, in *37th EPS Conference on Plasma Phys. Dublin, June 21 - June 25, 2010*. European Physical Society, 2010, p. P4.145. URL: http://ocs.ciemat.es/EPS2010PAP/pdf/P4.145.pdf

[10] F. Felici, O. Sauter, T. P. Goodman *et al.*, ***Real-time control of tearing modes and current density profile in TCV***, in *15th Workshop on MHD stability control: US-Japan Workshop on 3D Magnetic Field Effects in MHD Control in Univ. Wisconsin, Madison, WI, USA*, 2010.

[11] J. X. Rossel, J.-M. Moret, and Y. Martin, ***A saddle coil system for TCV and RMP spectrum optimisation***, in *36th EPS Conference on Plasma Phys. Sofia, June 29 - July 3, 2009*, vol. 33E, no. 2009 ECA. European Physical Society, 2009, pp. P–2.142, 36th EPS Conference on Plasma Phys. Sofia, June 29 - July 3, 2009 ECA Vol.33E, P-2.142 (2009). URL: http://epsppd.epfl.ch/

Rossel Jonathan
Rue des Etangs 6
1304 Cossonay, VD, CH
Tél. : +41 78 757 29 36
E-mail : jxrossel@yahoo.fr
Date de Naissance :   06.10.1981
Nationalité :   Suisse
Etat civil :   Célibataire

| **Formation** | 2005 – 2006 | Université de Fribourg | Fribourg |

DAES II
- Diplôme d'enseignant du secondaire II.

2000 – 2005   EPFL   Lausanne

Diplôme d'ingénieur physicien EPF
- Prix Adrien Tschumy (meilleure moyenne générale à l'examen propédeutique I).
- 2002 – 2003 échange ERASMUS avec l'université de Nottingham en Angleterre.

1997 – 2000   Gymnase Cantonal de la Cité   Lausanne

Maturité fédérale en voie scientifique
- Prix en physique, mathématiques, français, allemand et philosophie.
- Meilleure moyenne générale du gymnase.

Expérience
professionnelle   2007 – 2011   CRPP, EPFL   Lausanne

Assistant-doctorant en physique des plasmas
- Design d'un système de bobines et modélisation physique.
- Développement d'une suite de programmes d'analyse de signaux avancée.
- Préparation et supervision de sessions expérimentales sur tokamak.
- Assistanat en physique numérique et physique générale.

2006 – 2007   St-Andrew's School   Turi, Kenya

Professeur de physique, mathématiques et français. Développements informatiques.
- Enseignement et activités pastorales au sein d'un établissement anglais privé.
- Développement d'une base de données et d'une interface utilisateur pour la gestion académique de l'école à l'aide de *Microsoft Access* avec programmation en *VBA*.

Autres expériences :
- **Stagiaire R&D**
  - 01.04.05 – 31.07.05 : CRPP, EPFL. Création d'une interface informatique de traitement de données et développement d'une antenne de sécurité.
  - 18.06.03 – 30.08.03 : Biofluid Systems, Nyon. Analyse de faisabilité de trois projets, développement d'un prototype de jouet.
- **Remplaçant de maîtres du secondaire I et II**
  - 24.04.06 – 12.05.06 : ECDD, Fribourg.
  - 10.09.01 – 12.10.01 et 30.08.04 – 17.09.04 : Collège des Trois-Sapins, Echallens.
  - Remplacements à temps plein avec élaboration du programme et des évaluations.

Langues   Allemand au niveau de la maturité. Bonne maîtrise de l'anglais (parlé et écrit).